

**Electrochemical Performance of Lithium-Ion Batteries containing  
Carbon-Silicon Nanocomposite-based Anode Materials  
designed using Low Pressure Chemical Vapour Deposition on Graphite**

vorgelegt von

Master of Science

Kathleen Lamoth

geboren in Berlin

von der Fakultät II - Mathematik und Naturwissenschaften

der Technischen Universität Berlin

zur Erlangung des akademischen Grades

Doktor der Naturwissenschaften

- Dr. rer. nat. -

genehmigte Dissertation

Promotionsausschuss:

Vorsitzender: Prof. Dr. Martin Lerch

Gutachter: Prof. Dr. Robert Schlögl

Gutachter: Prof. Dr. Peter Strasser

Gutachter: Prof. Dr. Matthias Ballauff

Tag der wissenschaftlichen Aussprache: 16. Oktober 2018

Berlin 2018



Ein Abend, an dem sich alle  
Anwesenden völlig einig sind, ist ein  
verlorener Abend.

---

*(Albert Einstein)*





## Acknowledgements

First and foremost, I would like to express my sincere gratitude to my advisor Prof. Dr. Robert Schlögl, director of the department of Inorganic Chemistry at the "Fritz-Haber-Institut" of the "Max-Planck-Gesellschaft" and of the department of Heterogeneous Reactions at the "Max-Planck-Institut für chemische Energiekonversion", for his unconditional support and scientific guidance. Not only he has been an inspiring example, but also I greatly thank him for his patience, encouragement and numerous rewarding scientific discussions.

I would like to particularly acknowledge Prof. Dr. Peter Strasser and Prof. Dr. Matthias Ballauff, who gladly accepted to invest their valuable time in reviewing this work. Additional gratitude goes to Prof. Dr. Martin Lerch for taking the chair of the examination board.

My special thanks and appreciation go to the Electrochemistry Group, headed by Dr. Sébastien Cap. Particularly I appreciate the scientific conversations with Dr. David Klein and Martin Pradel, which played a crucial role in directing my scientific progression, and the unrestricted team spirit I experienced with the PhD candidates.

Also, I would like to thank all my colleagues, among them also sincere friends. I appreciate all the scientific exchange, interpolated measurements, advice and, of course, all the shared lab work, cake, laughter, presentation days, department trips and coffee. Particularly I would like to thank: Jasmin Allan (TG-MS), Daniel Brennecke, Wiebke Frandsen (SEM), Dr. Frank Girgsdies (XRD), Adnan Hammud (FIB), Maike Hashagen (BET), Dr. Walid Hetaba (TEM), Dr. Xing Huang (TEM), Dr. Robert Imlau (TEM), Dr. Gregor Koch, Maximilian Lamoth, Michael Scherzer, Manfred Swoboda, Dr. Detre Teschner (XPS), Dr. Olaf Timpe (XRF), Dr. Juan Velasco Vélez, Elisabeth Wolf and Leon Zwiener (in alphabetical order).

Further acknowledgement goes to Dr. Sylvia Becker for introducing me into the work with hydrothermal carbons and Teresa Bartoldus for the enduring support with chemical analysis (EA and Raman) and anode preparation. In addition, my thanks go to all PhD candidates of the CEC institute for plenty of cheerful moments at presentation days, department trips and (after) work parties.

Also, I would like to thank the colleagues of the precision mechanical workshop, the electronics workshop and our administration for the very pleasant support.

I'm very grateful that I had the possibility to attend several interesting conferences located all over Germany and a striking summer school in marvellous Sicily.

Last but not least, I would like to express heartfelt thanks to my family, friends and my dear husband for his unsurpassed support and extensive day-by-day encouragement.



## Abstract

Within the frame of the energy transition, the storage and transport of renewable energies are crucial issues. Among the nowadays available techniques, especially lithium-ion batteries are desired for wider applications, such as in electric vehicles or as storage units for the electrical grid. However, present lithium-ion batteries with carbonaceous anode materials exhibit certain inadequacies for the requested applications, first of all an insufficient capacity. Because of the high lithium uptake, silicon is one of the most promising anode materials regarding the capacity. Since the reliable application of silicon in lithium-ion battery anodes turned out to be subjected to several challenges, the vital point of the investigations carried out in this work was to correlate the battery capacity fading to the silicon properties and to develop a conceptual approach for the enhancement of the performance of this type of batteries. Therefore, the influence of the anode material properties, the protocol parameters and the solid electrolyte interphase formation on the battery performance were evaluated.

For the synthesis of nanostructured silicon and carbon-based anode materials an in-house designed low pressure chemical vapour deposition reactor with a rotating module was employed. Silicon deposition was achieved by silane decomposition and amorphous carbon deposition by pyrolysis of propene, both on graphite substrates. The methods' precise adjustability enabled reproducible modifications of the deposit content and crystallinity. In this way, it was shown how the initial capacity of the materials scales with the silicon content of the anode and that the battery capacity decay and charge losses are weakened for amorphous silicon depositions. Additional propene treatments featured further improvements of the battery performance. The investigations indicate that the deposited carbon did not serve as a silicon surface protection layer, but the battery performance was rather improved by other beneficial properties of the carbon. Further, adaption of the cycling protocol revealed the relevance of the anode lithiation constant voltage sequence in cycling protocols for continuous and maximised capacities. Moreover, the battery capacity retention was significantly increased by restricted anode lithiation, however, at the expense of the battery capacity. Yet, the most prominent changes in the battery performance, especially regarding the capacity decay over cycling, were achieved in a modified setup, where electrolyte and cycling protocol were adapted. Here, the morphology and elemental ratio of the solid electrolyte interphase, which was formed on silicon-based anodes during cycling, was fundamentally changed.

Altogether it was demonstrated that the optimisation of silicon-based lithium-ion batteries involves dealing with a complex interplay of the anode material, the cycling protocol and the electrolyte. Although the predominant improvement in the capacity retention was achieved by modification of the electrolyte and protocol, and therefore the formed solid electrolyte interphase, it became evident that worthwhile battery performance improvement can only be achieved by iterative variation and balancing of all three factors.



## Kurzfassung

Im Rahmen des Energiewandels sind der Transport und die Speicherung erneuerbarer Energien entscheidende Kernpunkte. Im Zuge dessen wird insbesondere eine umfangreichere Anwendung von Lithium-Ionen-Batterien angestrebt, beispielsweise in elektrischen Fahrzeugen, oder als Speicher zur Einspeisung in das Stromnetz. Für viele solcher Anwendungen sind moderne Lithium-Ionen-Batterien mit Kohlenstoff-basierten Anoden jedoch unzulänglich, allem voran wegen ihrer zu geringen Kapazität. Hinsichtlich der Kapazität ist Silizium eines der vielversprechendsten Anodenmaterialien. Da der zuverlässige Einsatz von Silizium als Anodenmaterial noch vor Herausforderungen steht, war das zentrale Thema dieser Arbeit die Korrelation des Kapazitätsschwunds mit den Siliziumeigenschaften und die Ermittlung eines konzeptuellen Ansatzes zur Verbesserung der Funktionalität solcher Batterien. Dafür wurden der Einfluss der Materialeigenschaften der Anode, der Protokoll-Parameter und der "Solid Electrolyte Interphase" (SEI) Bildung auf die Leistungsfähigkeit der Batterie untersucht.

Zur Herstellung nanostrukturierter Silizium- und Kohlenstoff-basierter Anoden wurde ein hausintern entworfener Reaktor zur chemischen Niederdruck-Gasphasenabscheidung verwendet. Silizium wurde mittels Silan Zersetzung und amorpher Kohlenstoff durch Pyrolyse von Propen auf Graphit-Substraten abgeschieden. Die präzise Regulierbarkeit dieser Synthesemethode ermöglichte reproduzierbare Modifikationen der Menge und der Kristallinität der Abscheidung. Somit konnte gezeigt werden, dass die Anfangskapazität des Materials mit dem Siliziumgehalt skaliert und, dass sowohl die Abnahme der Batterie-Kapazität, als auch der Verlust von Ladungsträgern durch die Verwendung amorphen Siliziums abgeschwächt werden kann. Auch die zusätzliche Behandlung mit Propen führte zu Verbesserungen der Batterie-Funktion. Untersuchungen des zyklisierten Materials indizierten, dass der abgeschiedene Kohlenstoff nicht dauerhaft das Silizium ummantelt und demnach andere vorteilhafte Eigenschaften des Kohlenstoffs der Grund für die Verbesserungen sind. Durch Variation des Zyklisierungs-Protokolls konnte gezeigt werden, dass eine Konstantspannung-Sequenz nach der Lithiierung der Anode Voraussetzung für eine kontinuierliche und maximierte Kapazität ist und, dass der Kapazitätsverlust durch limitierte Lithiierung der Anode deutlich reduziert werden kann, jedoch auf Kosten der Gesamtkapazität der Batterie. Die bedeutendsten Veränderungen der Leistungsfähigkeit der Batterien, insbesondere bezüglich des Kapazitätsverlustes während des Zyklisierens, wurden in einer Versuchsreihe erreicht, bei der Elektrolyt und Zyklisierungs-Protokoll modifiziert wurden. Hier wies die auf den Anoden gebildete SEI sowohl eine andere Morphologie als auch ein anderes Elementverhältnis auf.

Insbesondere wurde gezeigt, dass die Optimierung von Silizium-basierten Lithium-Ionen-Batterien mit einem komplexen Zusammenspiel aus Anodenmaterial, Zyklisierungs-Protokoll und Elektrolyt verbunden ist. Wenngleich die deutlichste Abschwächung des Kapazitätsverlustes durch die Modifizierung von Elektrolyt und Zyklisierungs-Protokoll und der damit gebildeten SEI erreicht wurde, stellte sich heraus, dass eine lohnenswerte Verbesserung der Batterieleistung nur durch iterative Variation und Abstimmung aller drei Faktoren erreicht werden kann.



# Contents

<b>1</b>	<b>Introduction</b>	<b>1</b>
1.1	The role of batteries in the energy transition . . . . .	1
1.2	Replacing graphite with silicon - aims and challenges . . . . .	4
1.2.1	Graphite, the established lithium-ion battery anode material . . . . .	4
1.2.2	Silicon as potential anode material in lithium-ion batteries . . . . .	7
1.2.3	Processes at the anode electrolyte interface - the solid electrolyte inter-phase (SEI) . . . . .	11
1.3	Electrochemical evaluation of lithium-ion batteries . . . . .	14
1.3.1	Battery cycling: anode lithiation – delithiation . . . . .	15
1.3.2	C-rate capability . . . . .	17
1.3.3	Differential capacity analysis . . . . .	18
<b>2</b>	<b>Thesis Aims</b>	<b>21</b>
<b>3</b>	<b>Silicon deposition on carbonaceous powders using LPCVD for high capacity LIB anodes</b>	<b>23</b>
3.1	Introduction . . . . .	23
3.2	Experimental . . . . .	25
3.2.1	Carbonaceous substrates . . . . .	25
3.2.2	Silicon deposition using LPCVD . . . . .	26
3.2.3	Powder characterisation . . . . .	27
3.2.4	Anode preparation and electrochemical tests . . . . .	28
3.2.5	Post-mortem analysis . . . . .	28
3.3	Results and discussion . . . . .	29
3.3.1	Powder characterisation . . . . .	29
3.3.2	Post-mortem analysis of the anode material after electrochemical testing	31
3.4	Conclusion . . . . .	33
<b>4</b>	<b>Graphite-silicon nanocomposites for LIB anodes prepared by methodically varied LPCVD</b>	<b>35</b>
4.1	Introduction . . . . .	35
4.2	Experimental . . . . .	38
4.2.1	Sample preparation . . . . .	38
4.2.2	Silicon characterisation . . . . .	38

4.2.3	Anode preparation and electrochemical tests . . . . .	40
4.2.4	Post-mortem analysis . . . . .	42
4.3	Results and discussion . . . . .	42
4.3.1	Characterisation of the graphite-silicon nanocomposite . . . . .	42
4.3.2	Electrochemical investigation of the anode materials . . . . .	49
4.3.3	Evolution of the anode material upon electrochemical cycling . . . . .	61
4.4	Conclusion . . . . .	64
<b>5</b>	<b>Carbon coverage of the silicon nanocomposite and its effect on the battery performance</b>	<b>67</b>
5.1	Introduction . . . . .	67
5.2	Experimental . . . . .	70
5.2.1	Sample preparation . . . . .	70
5.2.2	Material characterisation . . . . .	71
5.2.3	Anode preparation and electrochemical tests . . . . .	72
5.2.4	Post-mortem analysis . . . . .	74
5.3	Results and discussion . . . . .	74
5.3.1	Characterisation of the G-Si@C nanocomposite . . . . .	74
5.3.2	Influence of the a-C coverage on the battery performance . . . . .	80
5.3.3	Evolution of the anode material upon electrochemical cycling . . . . .	84
5.4	Conclusion . . . . .	88
<b>6</b>	<b>Beyond anode material modification - the effect of battery parameters on LIB performance</b>	<b>89</b>
6.1	Introduction . . . . .	89
6.2	Experimental . . . . .	93
6.2.1	Graphite-silicon anode materials . . . . .	93
6.2.2	Anode preparation and electrochemical tests . . . . .	94
6.2.3	Post-mortem analysis . . . . .	96
6.3	Results and discussion . . . . .	97
6.3.1	Influence of the "Constant Voltage" anode lithiation sequence in a "Constant Current – Constant Voltage" protocol . . . . .	97
6.3.2	The effect of restricted charging on the battery performance . . . . .	101
6.3.3	Investigation of the influence of combined modified battery protocol, electrolyte and housing on the battery performance . . . . .	104
6.4	Conclusion . . . . .	111
<b>7</b>	<b>Summary and final conclusion</b>	<b>113</b>
<b>8</b>	<b>Appendix</b>	<b>117</b>
8.1	A Supporting information of chapter 3 . . . . .	117
8.2	B Supporting information of chapter 4 . . . . .	120



8.3	C Supporting information of chapter 5 . . . . .	131
8.4	D Supporting information of chapter 6 . . . . .	139
<b>List of figures</b>		<b>152</b>
<b>List of tables</b>		<b>154</b>
<b>Bibliography</b>		<b>155</b>



# 1 Introduction

## 1.1 The role of batteries in the energy transition

The simple term "energy transition" involves plenty of cruxes like the continuous supply of energy for electricity, heat and vehicles generated from environmentally friendly systems, or the production of plastics and fertilisers from renewable energy sources. The innovative approaches to accomplish these ambitious targets are complex, as combining energy transition with climate protection means not only phasing out of the well-established energy generation systems and the expansion of new energy systems, but also a concurrent drastic reduction in energy consumption and CO<sub>2</sub> emissions. On top of this sophisticated scientific task the promotion of a specific innovative technology is significantly aggravated by the fact that energy systems are interconnected in complex manner with multiple non-scientific aspects regarding their utilisation, generation and distribution within society.<sup>[1]</sup> Thus, state-of-the-art renewable energy systems, for example, cannot equal the local and time-dependent energy demand without further progress in the storage and transport of energy.

Our repertoire of energy storage systems is already multifaceted, including mechanical, thermal, electrical, thermochemical, chemical and of course electrochemical storage.<sup>[2–4]</sup> These storage technologies possess different attributes regarding the amount of energy or power that can be stored, the time scale of storage and release, the efficiency, the cost, the spacing and the environmental conditions.<sup>[5]</sup> Although battery technology is surpassed in terms of specific power and energy by other techniques, as shown in the Ragone plot (fig. 1.1 a), it is the dominant technology when local flexibility and continuous energy supply is paramount. With commercialisation of the rechargeable lead-acid battery for more than 100 years, the battery belongs to the more mature technologies. From the 1950s to 2010, the energy density of commercial secondary batteries increased by about 3 Wh · kg<sup>−1</sup> on average per year as depicted in figure 1.1 b).<sup>[6]</sup> This trend was significantly increased by lithium-ion batteries (LIBs), which raised the annual growth rate from 1990 – 2010 to about 5.5 Wh · kg<sup>−1</sup>. Among batteries, lead-acid and sodium-sulfur batteries are the most common for large-scale installations, e.g. as back-up power supply for stationary devices, while LIBs are established for personal electronics.<sup>[7,8]</sup> Nevertheless, the wider application of LIBs, such as in electric vehicles or as storage for the electrical grid, is continuously targeted. The appeal of lithium as battery material is evident, since it is the most reducing element and the lightest metal, hence promising high operation voltage and low battery weight.<sup>[7]</sup> Indeed, LIBs are nowadays the batteries with the highest power density on the

commercial market and have a low discharge rate, an energy efficiency from 90 – 100 %, a long cycle life, a low maintenance requirement, a high nominal voltage (around 3.7 V) and energy densities from 80 to 150 Wh · kg<sup>-1</sup> as well as power densities from 50 to 200 W · kg<sup>-1</sup>.<sup>[2,3,5]</sup> The often criticised currently high costs can be foreseen to decrease with cumulative installed nominal capacity.<sup>[9]</sup> Thus, from the described theoretical LIB properties the aimed application would be within the desired goals, however, there are more aspects to the working ability of a battery.

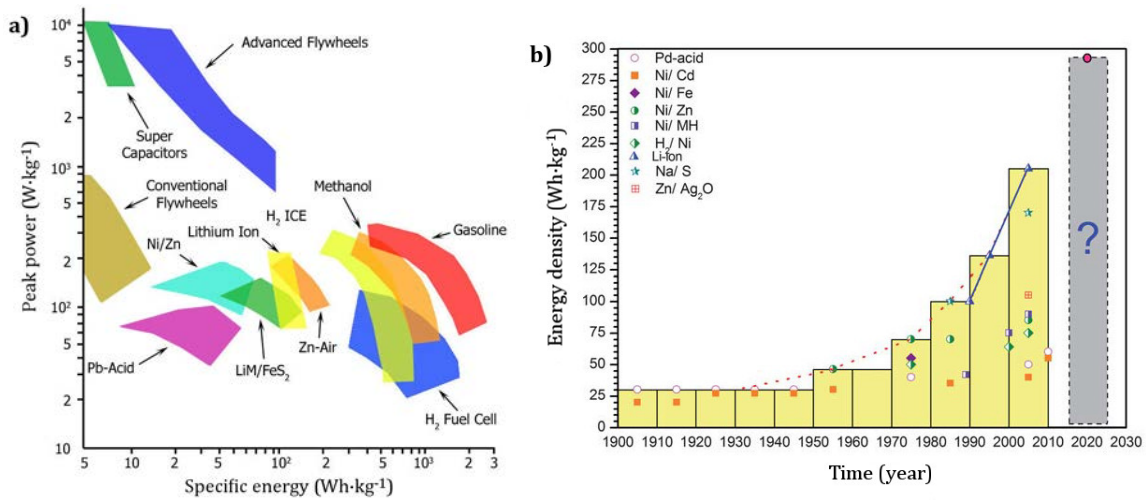


**Figure 1.1:** a) Ragone plot showing power density vs. energy density of different storage technologies adapted from ref. <sup>[10]</sup>; b) History of the development of secondary batteries in view of energy density (dashed line represents progress 1930 – 2010 and solid line represents development of LIBs 1990 – 2010, adapted from ref. <sup>[6]</sup>).

The introduction of new batteries is significantly impeded by the fastidious high demands on the battery cycling stability. A LIB is driven by an electrochemical redox reaction, which entails shuttling of lithium-ions (Li-ions) as illustrated in figure 1.2.<sup>[11]</sup> In the charged state the Li-ions are stored in the anode (negative electrode) and upon discharging they migrate from the anode material, which is at the same time oxidised, to the cathode.<sup>[12,13]</sup> In an ideal case this ion shuttling would happen with 100 % reversibility and without side reactions. However, this is usually not the case. Considering that common preparative chemistry is typically assumed to be sufficient with a product yield of 90 %, yet, even with 99 % efficiency only 37 % of the initial battery capacity would be maintained after 100 cycles.<sup>[12]</sup> This elucidates how high the demands on batteries are. The real battery performance is not only dependent on the main redox-couple, but it is also determined by an interplay of various aspects and side reactions whose fundamental science in operating batteries so far is still subject of investigation.<sup>[14]</sup> The electrode surface, the material density, the electrolyte, the applied cycling protocol and also the battery casing itself cause innumerable side reactions such as overcharge, self-discharge, passivation, phase changes, active material dissolution, electrolyte reduction/oxidation and interfacial film formation.<sup>[15,16]</sup> These side reactions have several effects that need to be avoided, for instance consumption

of active species, by-product deposition and self-heating.<sup>[13]</sup> The latter might cause thermal runaways in case of low thermal stability of the battery components or internal short circuits.

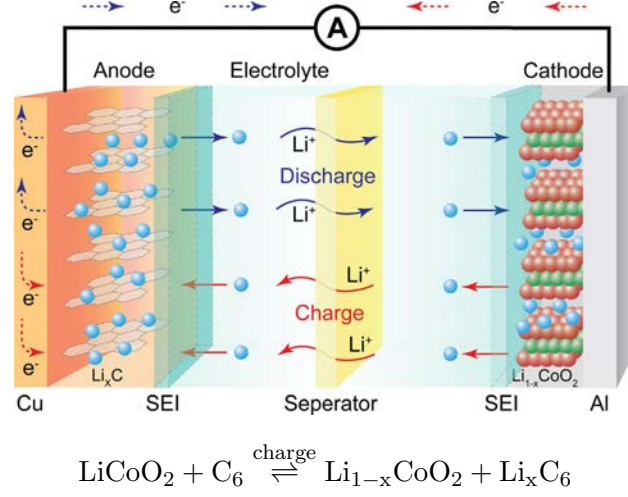


**Figure 1.2:** Schematic of a LIB cell comprised of a graphite anode and a  $\text{LiCoO}_2$  cathode, separated by a membrane and liquid electrolyte.<sup>[11]</sup>

As mentioned before, good progress could be achieved within the last decades regarding the energy density of LIBs. However, for the desired further size decrease of the batteries and to expand on fields like energy storage and automobile applications, further increase of the gravimetric ( $\text{Wh} \cdot \text{kg}^{-1}$ ) and volumetric ( $\text{Wh} \cdot \text{l}^{-1}$ ) energy capacities is necessary.<sup>[17,18]</sup> The energy (Wh) is derived from the capacity (Ah) times the potential (V). The total specific capacity of a battery ( $\text{mAh} \cdot \text{g}^{-1}$ ) in turn is given in eq. 1 with  $C_A$  and  $C_C$  being the theoretical specific capacities of the anode and cathode materials and  $1/Q_M$  being the specific mass ( $\text{g} \cdot \text{mAh}^{-1}$ ) of other cell components (electrolyte, separator, current collectors, case, etc.).<sup>[19]</sup>

$$\text{Total cell capacity} = \frac{1}{\frac{1}{C_A} + \frac{1}{C_C} + \frac{1}{Q_M}} \quad (\text{eq. 1})$$

When only the electrode materials are varied in a specified battery system  $1/Q_M$  is constant, hence eq. 1 can be converted to eq. 2<sup>[20]</sup>:

$$\text{Relative cell capacity} = \frac{C_A C_C}{C_A + C_C} \quad (\text{eq. 2})$$

The evaluation of this equation with nowadays viable cathodic specific capacities ( $C_C$ ) of  $140 - 200 \text{ mAh} \cdot \text{g}^{-1}$  results in the conclusion that the increase of the total battery capacity levels off once  $1200 \text{ mAh} \cdot \text{g}^{-1}$  anode capacity is achieved (fig. 1.3).<sup>[19-21]</sup> Hence, a realistic aim for new anode materials therefore is at least a capacity of  $1000 \text{ mAh} \cdot \text{g}^{-1}$  which would improve a current LIB specific capacity from  $\sim 101 - 117 \text{ mAh} \cdot \text{g}^{-1}$  to  $123 - 145 \text{ mAh} \cdot \text{g}^{-1}$ . This corresponds to an increase by 21 to 25 %.

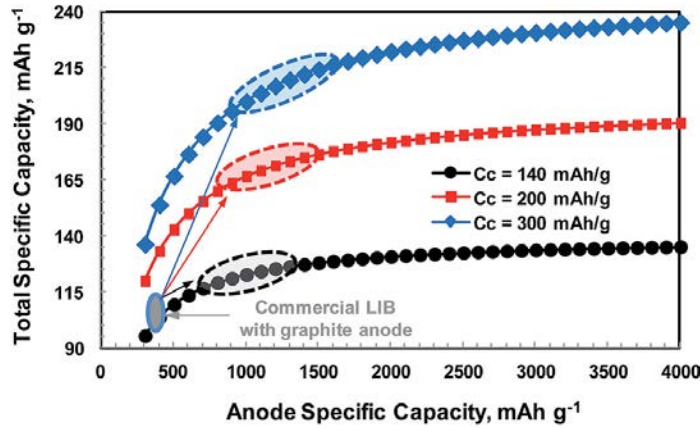


**Figure 1.3:** Total specific capacity of a LIB as a function of the specific capacity of the anode for distinct cathodic specific capacities ( $C_c$ ) based on eq. 2 (fig. adapted from ref. <sup>[21]</sup>).

## 1.2 Replacing graphite with silicon - aims and challenges

### 1.2.1 Graphite, the established lithium-ion battery anode material

When LIBs were commercialised in the 1970s, metallic lithium was used as anode material. Unfortunately, a fatal flaw emerged, namely the nucleation of lithium dendrites at the lithium metal anode upon repeated cycling.<sup>[7]</sup> In consequence the so-called "rocking chair" batteries were developed. They are based on easy Li-ion shuttling between the storage hosts on the cathode and anode side, which can prevent dendrite growth.<sup>[22]</sup> To ensure this migration, the host needs to provide a rather rigid lattice so that the intercalation entails only minor structure and chemical modifications, which are in addition reversible.<sup>[23]</sup> This electrochemical insertion–extraction process is a solid state redox reaction involving electrochemical charge transfer coupled with the insertion and extraction of the mobile guest ions into and from the host.

Carbon materials are up to now the most commonly used "rocking chair" anodes for LIBs due to their outstanding cycling stability.<sup>[12]</sup> In most cases these are graphitic materials, since materials with layered graphite structure exhibit anisotropic electrical conductance and the ability to accommodate ions between the lattice layers with relatively low volume expansion.<sup>[24,25]</sup> Theoretically, common graphite exhibits a gravimetric capacity of  $372 \text{ mAh} \cdot \text{g}^{-1}$  when electrochemically lithiated to  $\text{LiC}_6$ .<sup>[14,26]</sup> The respective lithium accommodation properties, irreversible charge loss and Li-ion (de-)intercalation rate strongly depend on the crystallinity, the microstructure and the micromorphology of the graphite.<sup>[12,27]</sup> The intercalation of lithium is a topotactically controlled reaction and occurs exclusively at prismatic surfaces and the defect sites of the basal planes of graphite.<sup>[28]</sup> Therefore, a high number of structural defects in the graphitic material is beneficial for the performance of graphite.<sup>[12,29]</sup> The regular central intercalation mechanism of ions into graphite includes first the ion penetration into the graphite

under elastic deformation of the graphene layers and then the ion diffusion in between the layers and the stage ordering.<sup>[23]</sup>

In general, the Li-ions can be inserted rather easily through the graphite prismatic sites, since there are no chemical bonds between the graphene layers.<sup>[23,30]</sup> Only the Van-der-Waals forces need to be overcome for a small gap increase between the graphene layers. The Li-ions then spread via solid state diffusion between the graphene layers. It has been shown for highly oriented pyrolytic graphite (HOPG) that the Li-ion diffusivity parallel to the graphene plane is high ( $\sim 10^{-7} - 10^{-6} \text{ cm}^2 \cdot \text{s}^{-1}$ ), while it is decreased along the grain boundaries ( $\sim 10^{-11} \text{ cm}^2 \cdot \text{s}^{-1}$ ).<sup>[31]</sup> It is thus assumed that the solid state diffusion of the ions can restrict the capacity of graphite at high intercalation rates.<sup>[32]</sup> Upon electrochemical Li-ion intercalation the AB stacking, in case of hexagonal graphite, or the ABC stacking, in case of rhombohedral graphite, changes to an AA stacking order and the distance between the layers increases about 10.3 % from 3.4 Å to 3.7 Å (fig. 1.4 a).<sup>[33,34]</sup> The lithiation of graphite is accompanied by a stepwise formation of a periodic array of unoccupied layer gaps. For the labelling the number of the stage addresses the number of layers separating the intercalated layers as illustrated in figure 1.4 c).<sup>[12,30]</sup> Here, stage II is separated into two sub-stages (II and II L) due to different Li-ion packing densities ( $\text{II} \hat{=} \text{Li}_{0.5}\text{C}_6$  and  $\text{II L} \hat{=} \text{Li}_{0.33}\text{C}_6$ ). However, the formed stages should not be considered as densely filled graphite layers over the entire crystal dimension, but considerably smaller stage islands (10 – 1000 nm).<sup>[23]</sup> These intercalated islands are sandwiched by elastic graphene layers and therefore the transition from, e.g. stage III to stage II does not include de- and re-intercalation of the ions, but it includes only motion of the islands over domain boundaries. In general, the staging is related to thermodynamic phenomena including the energy required to expand the gaps between the graphene layers and the repulsive interactions between the guest species. This usually results in few but highly occupied gaps.<sup>[12,23]</sup> Although such staging is energetically favoured, the existence of "diluted stages" where all layers are filled but with diluted Li-ion distribution have recently been suggested as an intermediate between stage I and stage II.<sup>[25,35]</sup> A schematic potential/composition curve for galvanostatic lithiation of graphite can be seen in figure 1.4 c). Its plateaus indicate the two-phase regions where the stages are transformed. When  $\text{LiC}_6$  is reached, all layers are filled and both, the graphene layers and the Li-ions, are stacked on top of each other. This stacking is named A- $\alpha$ -A- $\alpha$  representing  $\text{C}_6\text{-Li-C}_6\text{-Li}$  chains.<sup>[35]</sup> Viewing perpendicular to the basal planes, the Li-ions are arranged in such a manner that they avoid the occupation of the nearest  $\text{C}_6$  neighbour sites (fig. 1.4 b).

For uninterrupted battery performance based on the described Li-ion intercalation process two major processes need to be avoided: firstly, the co-intercalation of solvent into the graphitic structure and secondly, the self-discharge of the battery. The co-intercalation of solvents with Li-ions ( $\text{Li}_x(\text{sol})_y\text{C}_6$ ) is associated with extreme expansion of the graphite matrix around 150 % in contrast to the reported 10 % upon regular  $\text{LiC}_6$  formation.<sup>[12]</sup> This leads to exfoliation of the graphite and therefore to a drastic decrease in the storage capability of the material. Co-intercalation of the solvent can be avoided by the application of ethylene carbonate (EC)

based electrolytes.<sup>[36,37]</sup> The decomposition products of the EC-based electrolytes formed during the first lithiation effectively protect the graphite surface from further excessive solvent co-intercalation. Consequently, graphites with sufficient reactivity towards EC need to be applied.<sup>[38]</sup> However, when lithiated carbonaceous materials in non-aqueous electrolyte are stored in a charged state at elevated temperatures significant self-discharge of batteries can occur.<sup>[39]</sup> This is usually accompanied by self-heating and occurs when intercalated lithium diffuses to the edges of the graphene layers and undergoes exothermic reactions with the non-aqueous electrolyte.<sup>[40,41]</sup> Referring to this it was shown that carbons containing rhombohedral graphite provide a higher thermal stability.<sup>[42]</sup>

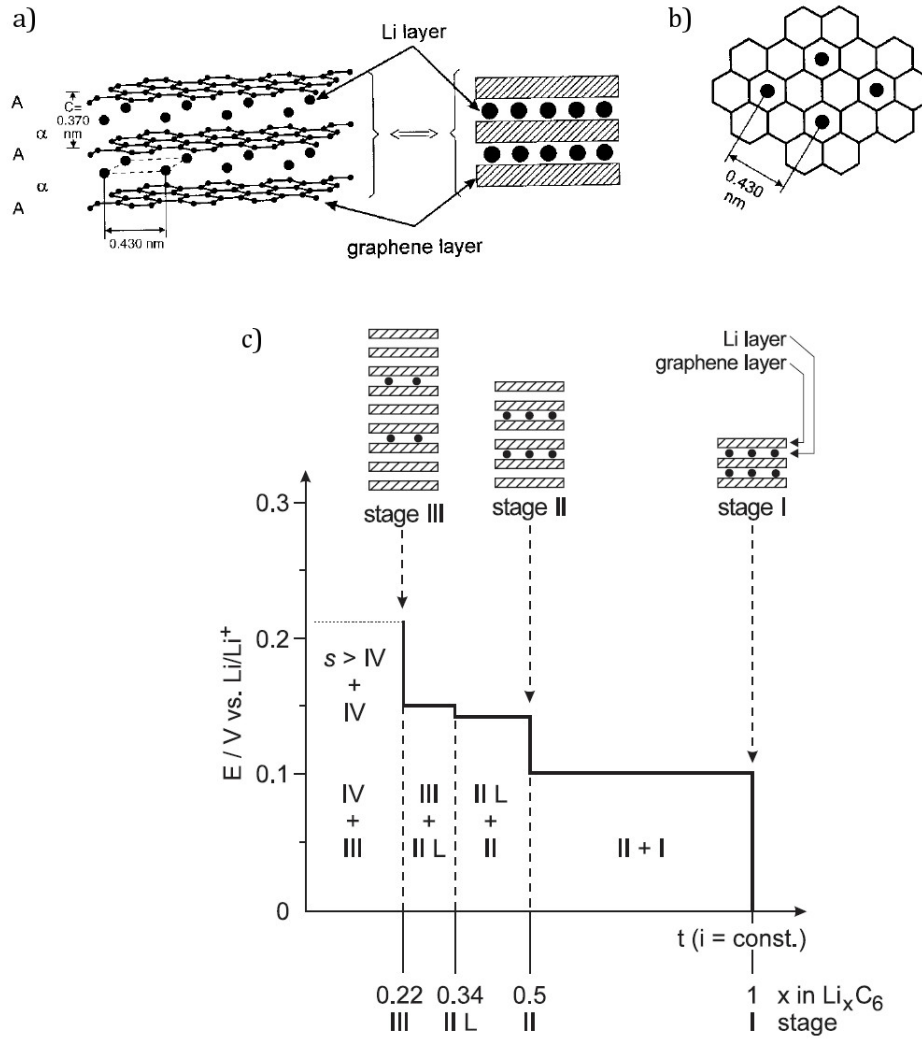


**Figure 1.4:** a) Schematic drawing of  $\text{LiC}_6$  showing the AA layer stacking sequence and the  $\alpha\alpha$  interlayer ordering of the intercalated lithium, b) view perpendicular to the basal plane of  $\text{LiC}_6$  c) schematic galvanostatic curve for stage formation during electrochemical lithiation of graphite (adapted from ref. [12]).



### 1.2.2 Silicon as potential anode material in lithium-ion batteries

In the task of looking for new anode materials with higher capacities, literature agrees on the fact that silicon is one of the most promising candidates.<sup>[14,18,21,43]</sup> Yet, the application of silicon in LIBs includes several challenges, which is why it has been under investigation for four decades now.<sup>[44]</sup> Crystalline silicon (c-Si) is a semiconductor, has the dense diamond cubic crystal structure (face-centered cubic) and forms a self-passivating layer on the surface when exposed to air.<sup>[14,45]</sup> Reflecting the beneficial properties of graphite, which make it a state-of-the-art anode material, namely its electrical conductivity and the facile Li-ion (de-)intercalation in between the graphene layers, silicon does not seem more suitable for the application in LIBs. However, silicon exhibits an outstandingly high theoretical gravimetric capacity when electrochemically lithiated to  $\text{Li}_{15}\text{Si}_4$  ( $3579 \text{ mAh} \cdot \text{g}^{-1}$ ).<sup>[46–48]</sup> Moreover, its abundant supply together with low toxicity make it attractive for processing on industrial scales. A list of characteristics for graphite and silicon applied in LIBs can be found in table 1.1. The table includes the volumetric capacity ( $\text{Ah} \cdot \text{l}^{-1}$ ), which is considered crucial for most battery applications.<sup>[49]</sup> To ascertain the volumetric capacity properly, the volume of the fully lithiated, not the fresh, material is decisive, since this will restrict the applicability in batteries. To obtain a viable impression of the battery capacity improvement Obrovac et al. introduced a full cell model ("stack model"). Compared to the theoretical tenfold gravimetric capacity which silicon exhibits compared to graphite, the model predicts an increased energy (Wh) of 34 %.

**Table 1.1:** Characteristics of graphite and silicon as anode materials in LIBs (adapted from ref.<sup>[12,49]</sup>)

material	reaction with lithium	lithiated phase	gravimetric capacity ( $\text{mAh} \cdot \text{g}^{-1}$ )	volumetric capacity ( $\text{Ah} \cdot \text{l}^{-1}$ )	expansion (%)	"Stack model" energy ( $\text{Wh} \cdot \text{l}^{-1}$ )
graphite	intercalation	$\text{LiC}_6$	372	837	10	726
silicon	alloying	$\text{Li}_{15}\text{Si}_4$	3579	2194	280	976

Silicon is not an intercalation host for Li-ions, like graphite, but reacts to Li-Si alloys of so high stoichiometric lithium content ( $\text{Li}_{15}\text{Si}_4$ ) that it could be considered as silicon dispersed in lithium. The Li-Si phase diagram (see fig. 1.5) depicts various Li-Si phases which are generally understood as Zintl-like phases.<sup>[50,51]</sup> However, these phases are only electrochemically formed when c-Si is lithiated at high temperatures ( $415^\circ\text{C}$ ). At room temperature the formation of equilibrium intermetallic phases is kinetically hindered.<sup>[11]</sup> Instead, the c-Si undergoes electrochemically-driven solid state amorphisation.<sup>[52]</sup>

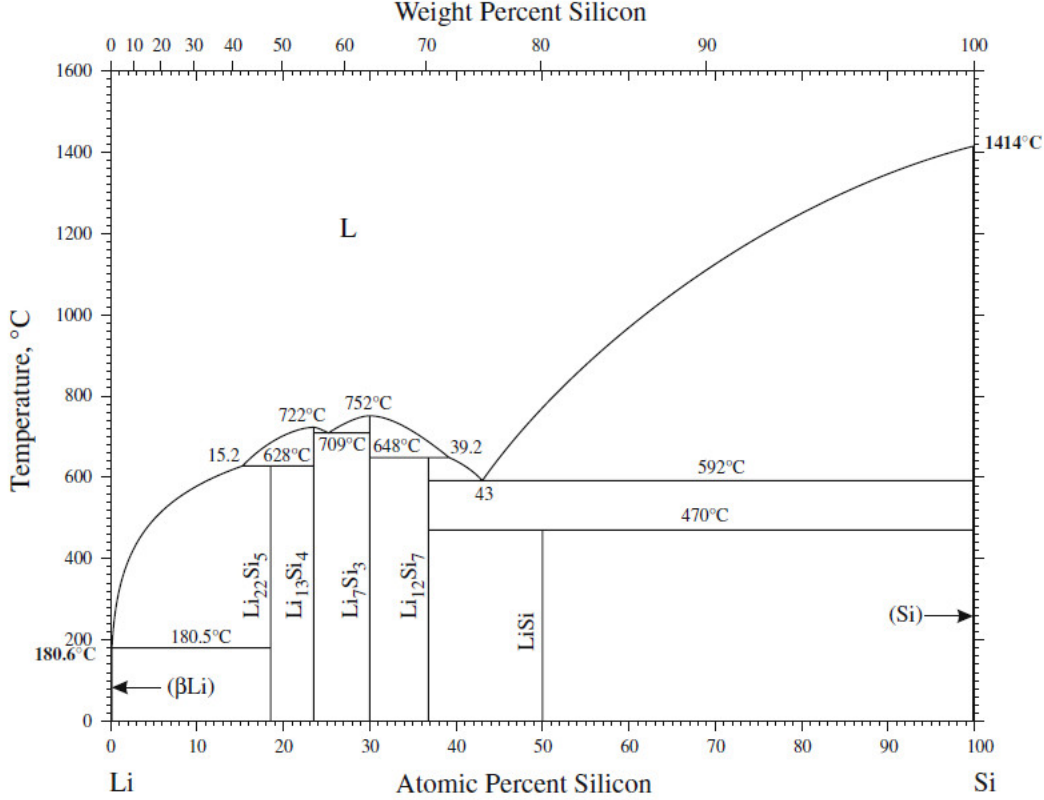
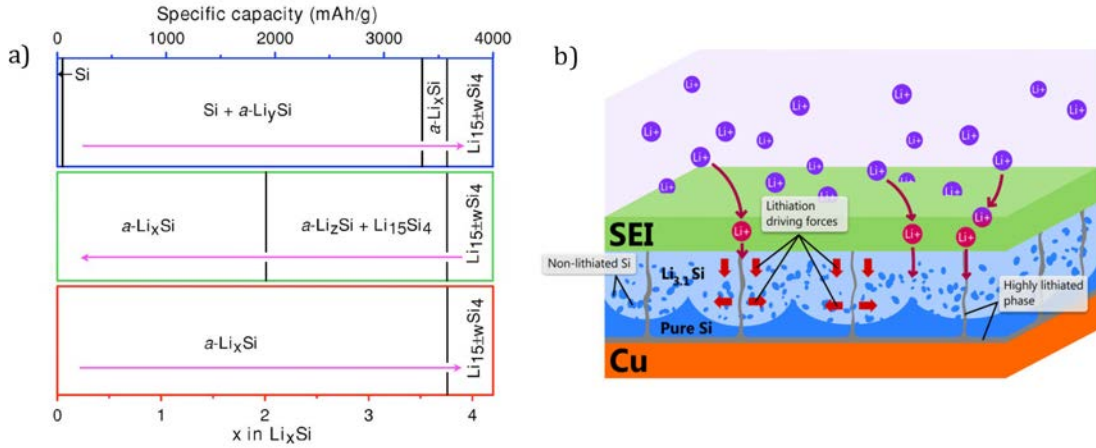


Figure 1.5: Li-Si phase diagram. <sup>[50]</sup>

The investigation of the explicit (de-)lithiation processes in silicon is delicate, since predominantly amorphous Li-Si compounds occur. The associated (de-)lithiation processes are mainly derived from (in-situ) XRD, TEM, EELS, and NMR analysis. Their transitions are illustrated in figure 1.6 a) <sup>[53]</sup>. During the electrochemically-driven solid state amorphisation c-Si is lithiated in a two-phase process to amorphous Li-Si compounds (a- $\text{Li}_y\text{Si}$ ). <sup>[49]</sup> Thereby, the c-Si and the a- $\text{Li}_y\text{Si}$  are separated by a sharp reaction front. <sup>[53]</sup> This reaction front shows a high concentration of Li-ions, which is necessary to weaken the Si-Si bonds and involves a tremendous volume expansion. <sup>[54,55]</sup> The entailed enormous gradients in transformation strain are associated with high internal stress and can lead to material cracking. The resulting highly lithiated amorphous state a- $\text{Li}_x\text{Si}$  can be described as a lithiated metastable glass which contains isolated Si-anions and Si-clusters that are broken apart upon further lithiation. <sup>[56,57]</sup> When lithiation continues, but not before nearly all Si-clusters are broken, and the potential reaches about 50 mV (vs.  $\text{Li}/\text{Li}^+$ ), the highest lithiated phase accessible at room temperature, c- $\text{Li}_{15}\text{Si}_4$ , forms. <sup>[14,47,58,59]</sup> The crystallisation of this metastable phase is assumed to be kinetically favoured, since both, a- $\text{Li}_x\text{Si}$  and c- $\text{Li}_{15}\text{Si}_4$ , contain isolated Si-atoms, which are well dispersed in lithium. <sup>[59,60]</sup> The subsequent delithiation takes place in a two-phase process, in which amorphous  $\text{Li}_{2\pm 0.3}\text{Si}$  replaces the c- $\text{Li}_{15}\text{Si}_4$ . Further delithiation to amorphous silicon (a-Si) occurs in a single phase process. <sup>[61]</sup> The resulting a-Si contains Si-tetrahedron clusters and forms a much more open matrix with less overpotential for the next lithiation processes compared to c-Si. <sup>[59]</sup> However, be-

sides a-Si, crystalline regions and trapped Li-ions are a part of the delithiated state.<sup>[19,62–64]</sup> The incomplete delithiation is attributed to the poor conductivity of silicon and its Li-compounds in combination with the volume contraction which can lead to contact loss of silicon to its conductive partner.<sup>[46,65,66]</sup> In the next and all following cycles the silicon lithiates via a single-phase lithiation reaction until crystallisation of  $\text{Li}_{15}\text{Si}_4$ .<sup>[67]</sup> Nevertheless, these suggested reactions have to be assessed carefully, not least because the lithiation processes strongly depend on the battery parameters. In contrast to the discussed lithiation mechanisms, studies using neutron reflectometry and XPS combined with secondary-ion mass spectrometry reported the existence of regions with divergent lithiation degree.<sup>[62,68]</sup> For the a- $\text{Li}_y\text{Si}$  state occurring during the lithiation of c-Si two time-dependent regions were reported, a skin region with  $\text{Li}_{2.5}\text{Si}$  and growth region with  $\text{Li}_{0.1}\text{Si}$ . Upon lithiation of a-Si highly lithiated phases beyond  $\text{Li}_{15}\text{Si}_4$  were found, which can serve as fast diffusion paths due to a relatively high diffusion coefficient for Li-ions (fig. 1.6 b).<sup>[65,68]</sup>



**Figure 1.6:** a) Diagram for cycling of a Li/Si electrochemical cell with 1<sup>st</sup> lithiation (blue), 1<sup>st</sup> delithiation (green) and 2<sup>nd</sup> lithiation (red); a- $\text{Li}_y\text{Si} \triangleq$  fixed composition that coexists with c-Si, a- $\text{Li}_x\text{Si} \triangleq$  single-phase region of variable composition,  $\text{Li}_z\text{Si} \triangleq$  fixed composition that coexists with  $\text{Li}_{15}\text{Si}_4$  during delithiation,  $\text{Li}_{15\pm w}\text{Si}_4 \triangleq$  variable stoichiometry single-phase region<sup>[53]</sup>; b) schematic view of the lithiation mechanism of an a-Si thin film.<sup>[68]</sup>

During repeated (dis-)charging the capacity of micrometer-sized silicon decays quickly. This decay can mainly be attributed to the low conductivity of silicon and the large volume expansion caused by the lithium uptake.<sup>[20,69]</sup> The combination of both leads to fragmentation and electrical contact loss of the silicon and moreover makes a formation of a stable solid electrolyte interphase (SEI) impossible (fig. 1.7).<sup>[48]</sup> The latter will be discussed in detail in chapter 1.2.3. Upon silicon lithiation to c- $\text{Li}_{15}\text{Si}_4$  the volume of the material expands about 280 %.<sup>[70–72]</sup> Hence, occurrence of stress and vertical displacement is likely, resulting in silicon fracture and irreversible silicon particle detachment.<sup>[71]</sup> Even for small silicon particles (5 – 10  $\mu\text{m}$ ) cracks form while cycling and even at very low current rates not all Li-ions exit from the particles.<sup>[66,73,74]</sup> Owing to the large surface-to-volume ratio, nanostructured materials can facilitate strain relaxation and can prevent the build-up of internal stress.<sup>[11,46]</sup> This makes

them more mechanically stable than their bulk counterparts. In addition, the initial reaction of lithium with silicon takes place at the silicon surface, grain boundaries and planar defects, which are abundant in nanoscale silicon. Moreover, the nanostructure improves the slow Li-ion transport by decreasing the electron/Li-ion diffusion length, which thus enables a higher rate performance and higher capacity utilisation.<sup>[75]</sup> In agreement with this, it has been shown for silicon nanoparticles (Si NPs) that their fracture is size dependent and that Si NPs smaller than 150 nm in size could overcome the cracking upon electrochemical (de-)lithiation.<sup>[76]</sup> Investigations of smaller Si NPs (30 – 50 nm) showed further peculiarities.<sup>[75]</sup> While bulk silicon undergoes nearly linear solid state amorphisation, the lithiation of the Si NPs proceeded in a non-linear process. Moreover,  $c\text{-Li}_{15}\text{Si}_4$  was not formed. Silicon nanowire (Si-NW) battery electrodes were also reported to circumvent pulverisation as they can accommodate large amounts of strain.<sup>[8]</sup> Comparable results were obtained from extensive silicon thin film studies by deposition of a-Si thin films using radio frequency magnetron sputtering, radio frequency glow discharge, vapour evaporation and electron-beam deposition on several substrates (copper foil, stainless steel, nickel foil and beryllium windows).<sup>[58,63,77–80]</sup> The studies agree on higher gravimetric capacities and longer cycle life for thinner films around 250 nm compared to  $\mu\text{m}$ -scale films.

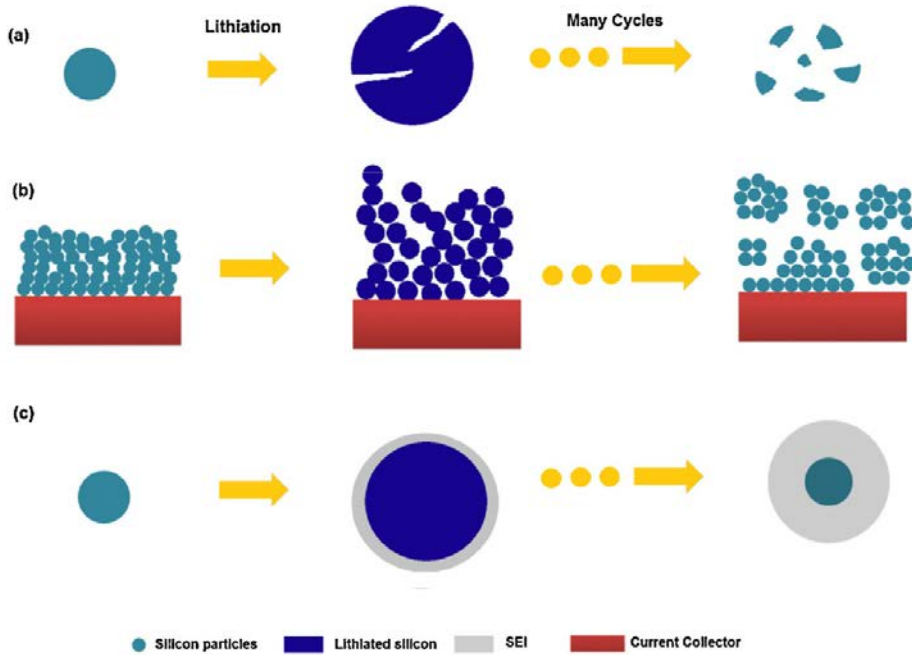


**Figure 1.7:** Silicon anode failure mechanisms: (a) material pulverisation, (b) material vertical displacement and (c) continuous SEI growth.<sup>[81]</sup>

Summarising the last years' research, the basis for the rational design of silicon-based anodes seems to be the application of nanoscale silicon preferably combined with conductive networks.<sup>[48]</sup> Yet, the decreased size and thereby increased surface, entails new challenges like an increased demand for binder, electrochemical sintering of the active material and an en-

larged silicon-electrolyte interface promoting side reactions.<sup>[82,83]</sup> Origins and consequences of the latter are discussed in the next section.

### 1.2.3 Processes at the anode electrolyte interface - the solid electrolyte interphase (SEI)

The purpose of an electrolyte in a LIB is to shuttle the Li-ions between anode and cathode.<sup>[13]</sup> Therefore, electrolytes in LIBs have to be aprotic and should, moreover, provide a good Li-ion conductivity, a low electric conductivity and a high electrochemical stability.<sup>[12,84]</sup> For application in commercial batteries they need to be stable in the working temperature range, safe, inexpensive and have a low toxicity. A mixture of cyclic and linear organic carbonates together with a conductive salt provides the basis for current LIB electrolytes. The cyclic carbonates provide high dielectric constants to reduce ion pairing and increase the ion mobility in the electric field, while the linear carbonates exhibit lower viscosity for faster Li-ion diffusion. The structure formula of electrolyte components discussed in this section are illustrated in figure 1.8.

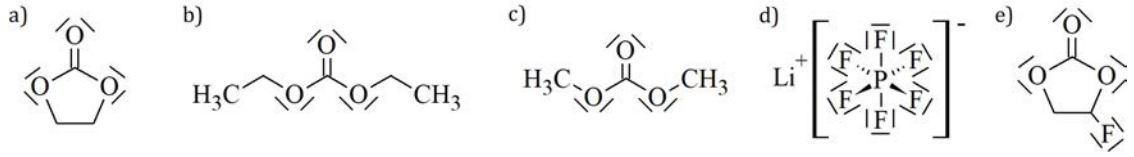
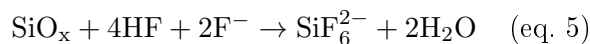
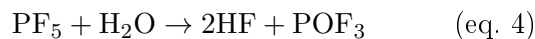


**Figure 1.8:** Structural formula of a) ethylene carbonate (EC), b) diethyl carbonate (DEC), c) dimethyl carbonate (DMC), d) lithium hexafluorophosphate (LiPF<sub>6</sub>) and e) fluoroethylene carbonate (FEC).

In the course of time ethylene carbonate (EC) based electrolytes stood out for application in LIBs due to their good performance.<sup>[85,86]</sup> Despite its comparably high dielectric constant, EC was not considered as electrolyte for a long time due to its high melting-point of 36 °C.<sup>[87]</sup> However, EC was found to form liquid homogeneous mixtures with linear carbonates, e.g. diethyl carbonate (DEC) and dimethyl carbonate (DMC), at room temperature, with the resulting electrolytes providing lower melting temperature, lower viscosity and higher ion conductivity.<sup>[87]</sup> Nevertheless, the conductivity of the mixture needs to be further increased by the addition of a lithium salt. For the salt the requirements are also tough, so that the repertory is small. Most of the salts cannot provide enough solubility in the low dielectric media, or the anions are unstable to oxidation. Among the remaining salts LiPF<sub>6</sub> stands out due to its multifaceted good performance in terms of conductivity, dissociation constant, thermal stability and chemical stability.<sup>[87]</sup> However, even at room temperature LiPF<sub>6</sub> undergoes autocatalytic decomposition (eq. 3). Its products PF<sub>5</sub> and HF from reaction with traces of water further react with EC, DEC and the silicon surface, SiO<sub>x</sub> (eq. 4 and 5).<sup>[84,85,87-89]</sup>



In EC/DEC mixtures the Li-ions of the dissolved lithium salts are rather solvated by EC than DEC.<sup>[90,91]</sup> A favourable coordination number of four EC in the first solvation sphere was found by calculations and spectroscopic methods.<sup>[92–94]</sup> Furthermore, it was determined that a coordination of the Li-ion by the carbonyl-group oxygen in the tetrahedral arrangement is the most favourable. DFT calculations indicate that the solvation is a spontaneous exothermic process and that the solvation of Li-ions with EC exhibits the highest values for the binding energy, enthalpy of solvation and free energy of solvation, which supports the experimental results.<sup>[91]</sup> However, it was also shown that the complex’ coordination number depends on the salt concentration, since  $\text{PF}_6^-$  can be part of the first solvation sphere ( $\text{Li}^+(\text{EC})_2(\text{LiPF}_6^-)$ ) for salt concentrations above 0.5 M.<sup>[95]</sup>

Upon exposure of graphite or silicon anodes in LIBs to these aprotic electrolytes a thermodynamical driving force for the electrochemical reduction of the electrolyte on the anode surface emerges.<sup>[96]</sup> This is due to the fact that the Fermi levels of both materials are higher than the estimated lowest unoccupied molecular orbitals (LUMO) of the electrolyte components. One electron reductive decomposition of EC and DEC leads to various decomposition products, including further reactions with Li-ions, EC and DEC.<sup>[97]</sup> Even though these are parasitic reactions which consume Li-ions and active charges, the result can be self-passivation of the anode surface if the decomposition products form an assistant surface electrolyte interphase (SEI). Such an SEI can contribute to the stabilisation of the battery performance in terms of irreversible charge loss, self-discharge, cyclability, rate capability and safety.<sup>[98]</sup> The SEI can prevent continuous electrolyte reduction by blocking the electron transport and thereby also Li-ion consumption and the formation of decomposition products is avoided.<sup>[96,98]</sup> Moreover, it can protect the active material from exfoliation and co-intercalation of solvent molecules.<sup>[99,100]</sup> A prerequisite is that the SEI is electronically insulating, but Li-ion conductive and, first and foremost, stable.<sup>[101–103]</sup>

A representative example for stable SEI formation is graphite in EC-based electrolytes. When a graphitic anode is lithiated its surface is negatively polarised, initiating the electrolyte decomposition processes.<sup>[98]</sup> EC is reduced in the first cycle at potentials above the lithium intercalation potential to  $(\text{CH}_2\text{OCO}_2\text{Li})_2$ -surface films, which passivate the carbon.<sup>[38,104]</sup> This SEI formation entails gas evolution and a significant irreversible charge loss in the first cycle, with the latter scaling with the surface area and the nature of the graphite.<sup>[33,105,106]</sup> This confirms that the charge consuming process is a surface process and indicates that it differs for prismatic and basal planes. Indeed, it has been shown for HOPG cycled in an EC/DEC mixture that the SEI contained more organic components on the basal planes and more inorganic species on the edges.<sup>[107,108]</sup> It is suggested that the SEI on graphite consists of a dense layer of inorganic components close to the carbon, followed by a more porous organic or polymeric layer.<sup>[98,109,110]</sup> To give a general SEI composition is difficult, since the detailed study of the SEI is difficult due to its nanoscale thickness, amorphous composite structure and air sensitivity.<sup>[111]</sup> Moreover, its precise composition is affected by several factors like the pre-treatment of the carbon ma-

terial, the electrolyte composition and battery operation.<sup>[98]</sup> However, most reports agree on mainly insoluble materials including  $\text{Li}_2\text{O}$ ,  $\text{LiF}$ ,  $\text{Li}_2\text{CO}_3$ ,  $\text{RCO}_2\text{Li}$ , alkoxides,  $\text{C}_x\text{H}_y$ -based fragments, non-conducting polymers and polymers with  $(\text{CH}_2)_n$  sequences.<sup>[109,110,112,113]</sup> Despite EC forming a proper surface film, the SEI thickness and its  $\text{LiF}$  content have been reported to increase with the number of battery cycles, which also entails a gradually increasing overpotential for the anode lithiation.<sup>[114,115]</sup> These observations were attributed to the material dynamics during (de-)lithiation. Both, anode volume and the SEI thickness, were found to be smaller in the delithiated state than in the lithiated state.<sup>[99]</sup> These volume changes can lead to continuous electrolyte reactions caused by small scale surface reactions between lithiated graphite and solution species.

The SEI formation on silicon in comparable electrolytes, however, is more inhomogeneous with single-, double-, and multi-layered, porous and sandwiched structures.<sup>[116]</sup> The formation of the reported underlying polymers and oligomers through degradation of electrolyte solvent is ascribed to be the reason for the irreversible capacity occurring in these batteries.<sup>[117]</sup> Conversely, results from gravimetric analysis showed that the silicon electrode mass continuously increased in close relationships with the irreversible capacity loss.<sup>[118]</sup> Especially low potentials were reported to cause thick SEI layers of large particles, which partially dissolve and form cracks upon delithiation, so that the SEI coverage for the fully discharged silicon is only about 51 %.<sup>[119]</sup> With the continuous growth the characterisation of the SEI gets more complicated, while the components are well-known for the first cycle. The initial SEI formed on silicon in  $\text{LiPF}_6$  EC/DEC-based electrolytes is similar to that on graphite until 0.5 V are reached and consists mainly of  $\text{LiF}$  with further  $\text{LiPF}_6$ ,  $\text{PF}_y$ ,  $\text{Li}_2\text{CO}_3$ ,  $\text{RCO}_2\text{Li}$ .<sup>[119–121]</sup> During further lithiation, penetration of the underlying silicon by Li-ions occurs and  $\text{Si-Li}$ ,  $\text{Si-F}$ ,  $\text{Li}_2\text{O}$  and  $\text{Li}_x\text{SiO}_y$  are formed by reaction with the  $\text{SiO}_2$ -layer (see fig. 1.9). This  $\text{SiO}_2$ -layer caused by silicon oxidation upon air-exposure is reactive enough to form  $\text{SiO}_x\text{F}_y$  ( $y \leq 3$ ) species by simple contact with the electrolyte.<sup>[122]</sup> The described lithiation process goes in line with the reported observation that only after 30 % anode lithiation the SEI layer growth stagnates and the lithiation of the silicon starts to rise significantly.<sup>[68]</sup> Upon delithiation until 0.9 V, the lithium is almost fully extracted, the SEI thickness has decreased and no more  $\text{Li}_2\text{O}$  can be detected.<sup>[121]</sup> The instability of the SEI on silicon is mainly attributed to the large volume expansion ( $\sim 280$  %) of silicon upon lithiation. This leads to cracking of the SEI due to mechanical strain and continuously exposes fresh silicon surface, leading to further SEI formation.<sup>[111]</sup> Indeed, it was shown that decomposition reactions on silicon stop once reaching deep lithiation potentials due to sufficient prevention by the SEI. However, upon delithiation and material shrinking the oxygen content starts to increase in the interior anode region, indicating new exposure of silicon to the electrolyte.<sup>[63]</sup>

As a consequence of the described processes, the charge loss for SEI formation increases with increasing silicon surface.<sup>[123]</sup> This is especially critical since, as discussed in the previous chapter, nanostructured silicons are desired for new anode materials. One approach to maintain the

SEI stable under expansion and contraction of the silicon is to cover the silicon with a flexible, conductive element.<sup>[124]</sup> The surface coatings may act as mechanical constraining layers that buffer volumetric changes during electrochemical cycling, thus helping to maintain good electrical contact of the components.<sup>[11,125]</sup> At the same time such coatings may form a passivation layer that can suppress unwanted reactions between the silicon and the electrolyte. Especially electronically conductive coatings such as carbon, metal and conductive polymers are considered to further enhance the redox reaction kinetics. However, it was reported for conductive polymer coatings that the mechanical protection entailed internal compressive stress leading to self-delithiation.<sup>[126]</sup> Another approach to stabilise the SEI is to alter the electrolyte to generate a thin, flexible and stable SEI that remains in contact to the silicon surface.<sup>[127]</sup> To achieve this, various chemicals such as vinylene carbonate and fluoroethylene carbonate (FEC) have been added to the electrolyte.<sup>[127,128]</sup> Particularly, FEC additives have been proven effective by formation of a stable FEC-derived SEI film, which limited the emergence of large cracks, preserved the original surface morphology and suppressed additional SEI formation from the solvent.<sup>[129,130]</sup> However, it was shown that the FEC is continuously consumed during electrochemical cycling, leading to a rapid capacity drop once all FEC is consumed.<sup>[131]</sup>

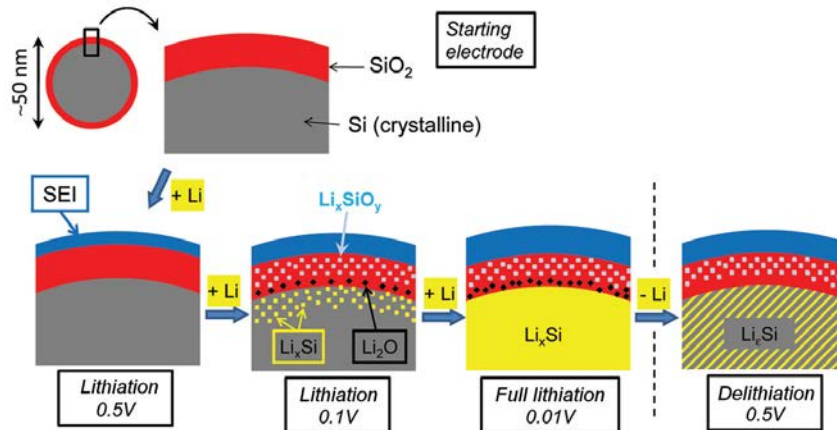


**Figure 1.9:** Schematic view of the mechanisms occurring at the surface of silicon nanoparticles: initial formation of the SEI,  $\text{Li}_x\text{Si}$ ,  $\text{Li}_2\text{O}$  and  $\text{Li}_x\text{SiO}_y$  formation upon further lithiation and the partial reversibility upon delithiation (adapted from ref. <sup>[121]</sup>).

### 1.3 Electrochemical evaluation of lithium-ion batteries

To properly investigate anode materials, the electrochemical test parameters have to be chosen carefully. Already for simple electrochemical tests like "cycling" the experimental parameters can be varied significantly and thereby have a severe influence on the battery performance. Hence, to improve the understanding of the degradation processes in LIBs and moreover investigate the influence of the anode material on parameters like capacity fade and SEI formation,



the experimental parameters should be set thoughtfully and the resulting data must be analysed thoroughly.

### 1.3.1 Battery cycling: anode lithiation – delithiation

The cycling of batteries, meaning the repeated lithiation and delithiation of the electrodes, can be simplest achieved by the application of a constant current (CC) until the battery is charged or discharged. The exact cycling protocol, however, can have a significant influence on the battery performance, in particular when the lithiation sequence is varied.<sup>[132–134]</sup> The variable testing parameters discussed in this work include the cut-off criterion, whether there is a break or constant voltage (CV) sequence after the (dis-)charge and the current rate (C-rate). By variation of the C-rate the material can be charged faster (high C-rate) or more slowly (low C-rate). The C-rate represents the number of hours required for a full (dis-)charge, so with C/2 a complete charge is achieved in 2 hours and with 2C in half an hour.<sup>[46]</sup>

The battery performance in turn is usually defined by the capacity of the battery, the capacity continuity and the coulombic efficiency (CE) of the individual cycles. The capacity can be defined by various parameters like the specific discharge capacity ( $\text{mAh} \cdot \text{g}^{-1}$ ) which is often cited because it can be calculated reliably, gives the reversible capacity and is an important parameter for weight-sensitive applications.<sup>[46]</sup> The CE is defined as the ratio of delithiation to lithiation capacity and therefore describes the loss of charges within one cycle. Low CE values are usually caused by particle fracture and disconnection or electrolyte decomposition. In most cases this entails the consumption of Li-ions, leading inevitably to a continuous loss of capacity.<sup>[49]</sup> Finally, the stability needs to be described for a reasonable number of cycles. A commercially viable electrode must be able to sustain a stable capacity for 100 – 200 cycles for wearable computing and 300 – 1000 for portable electronics.<sup>[46]</sup> Hence, a reasonable capacity stability test needs at least 100 cycles.

To increase the cycle life of batteries with nanostructured silicon-based anodes, the parameters of the protocols are usually set so that the silicon is not lithiated to the maximum. To achieve this, two major techniques are reported: firstly, cycling within a smaller potential window and, secondly, restricting the depth of charge. Both methods are based on the reduction of the amount of volume change to decrease the stress on the material and reduce the fragmentation of the SEI on the silicon surface. By fixing a cycling potential window which is smaller than necessary for complete charging and discharging, a significant improvement of the cycling stability of Si-based LIBs was reported.<sup>[47,53,70,119,135,136]</sup> Here, the most popular method is to increase the cut-off potential border for the lithiation process from 0 – 5 mV to 50 – 70 mV. This avoids the formation of  $\text{c-Li}_{15}\text{Si}_4$ , which is associated with high internal stress and therefore capacity fading.<sup>[47,53]</sup> Moreover, the morphology and composition of the SEI on Si-NWs was found to be voltage dependent.<sup>[119]</sup> However, the shrinkage of the cycling potential window inevitably involves a reduction of the capacity. When the lithiation cut-off border is raised from 0.0 V to

0.2 V for a-Si thin films the gravimetric capacity is reduced from over 3000 to 400  $\text{mAh} \cdot \text{g}^{-1}$ , but remains stable over 400 cycles.<sup>[137]</sup> Another widespread method to improve the performance is the restricted "charging depth" of silicon-based materials. Based on the same idea that less lithium is inserted in the material, usually about 45 % of actual capacity or less are in use. Yet, the cut-off criterion is not the voltage, but the amount of charges. As a result a significant improvement in the cycling stability for a great number of cycles and different current rates was reported.<sup>[63,138,139]</sup> Nevertheless, it has been shown that the restriction of the charging depth simply postpones the battery failure to a higher cycle number.<sup>[123,140]</sup> As can be seen from figure 1.10, the gradually decreased charging depth leads to a successive longer cycle life of the battery. For the batteries cycled with a significantly reduced charging depth the failure point where the capacity suffers from a drastic drop involves a distinct decay in the CE. Furthermore, it was shown for the silicon sample cycled with fixed 1000  $\text{mAh} \cdot \text{g}^{-1}$  how the fresh c-Si was consumed during cycling. This strongly suggests that not all available silicon was lithiated to a small degree from the beginning on, as intended. Instead, only a part of the available silicon was lithiated to inevitably higher lithiation degrees. Thus, the silicon material runs through the same electrochemical processes as in the regular protocol, but stepwise in smaller material regions. Whether such an approach is worthwhile regarding the sum over all charges provided in all cycles remains questionable. From these methods a variety of hybrid protocols can be deduced, which include formation cycles with restricted charging depth entailed by a stable cycling in a respective restricted potential region.<sup>[70]</sup> With this, it is intended to amorphise parts of the silicon and then cycle subsequently only the amorphous parts.

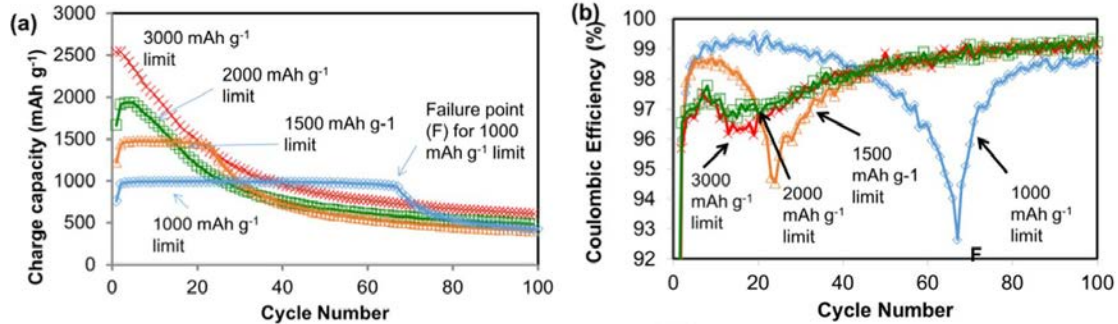


**Figure 1.10:** Diagram of a) the cycle performance of ball-milled silicon with CMC-433 composition and b) the coulombic efficiency as a function of the cycle number.<sup>[123]</sup>

As discussed in the previous paragraphs, a battery cannot be defined by a single property, e.g. the initial gravimetric discharge capacity, but has several key characteristics. Besides the initial capacity it is, for example, of prime importance how long this capacity can be maintained and how the CE develops over cycling. To obtain a more comprehensive impression of several materials or battery compositions simultaneously, radar plots are a reliable representation tool (fig. 1.11).<sup>[7,141–145]</sup> As can be seen from the examples, no fixed defaults for the axes are given, hence radar plots can be adapted for the respective parameters of interest.

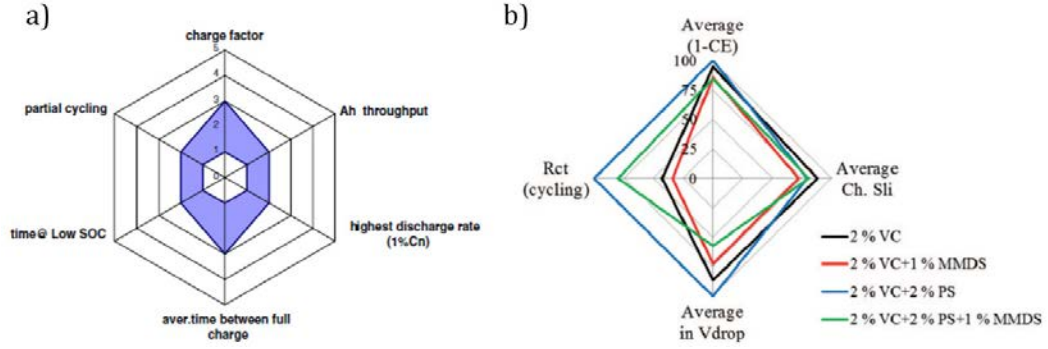


**Figure 1.11:** Radar plot with a) individual stress factors for diverse battery categories<sup>[142]</sup> and b) battery data for varied electrolyte combinations in  $\text{Li}(\text{Ni}_{1/3}\text{Mn}_{1/3}\text{Co}_{1/3})\text{O}_2/\text{graphite}$  pouch cells<sup>[143]</sup>.

### 1.3.2 C-rate capability

By varying the C-rate, the rate capability of a material can be investigated which in turn gives insights on the material's reaction kinetics and inner resistance. There are various protocols for C-rate capability tests, which are based on a stepwise increase of the C-rate over cycling, for example every fifth cycle, to evaluate how the capacity changes with increasing C-rates.<sup>[138,146,147]</sup> In addition, the C-rate of the last set of cycles can be re-decreased to the initial low C-rate to investigate whether the capacity is irreversibly lost or if it can be reobtained.<sup>[124,130,148]</sup> An example for the performance of silicon-carbon electrodes in electrolytes with different content of fluoroethylene carbonate (FEC) is shown in figure 1.12. It is clearly depicted that the battery run without FEC suffers from a stronger capacity decay and is more affected by the increasing C-rate. A stabilised performance as observed for the battery containing 15 wt.-% FEC is an indication for a reduction in the anodes interfacial resistance, which was supported by electrochemical impedance spectroscopy.<sup>[130,148]</sup>

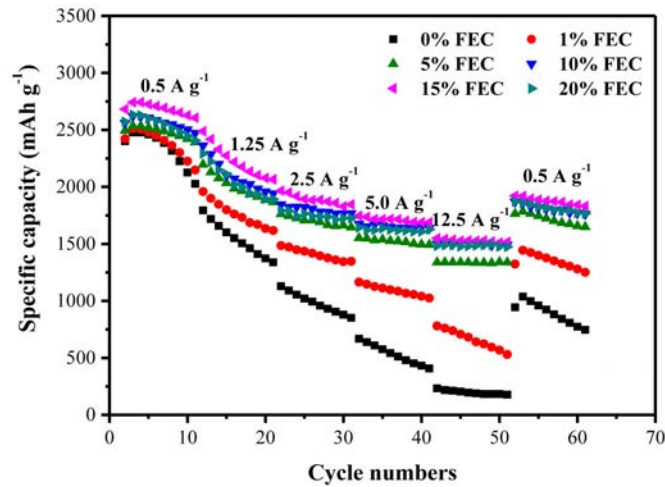


**Figure 1.12:** Specific capacity as a function of the cycle number for Si/C electrodes in electrolytes containing 0, 1, 5, 10, 15 and 20 wt.-% FEC at current densities from 0.5 – 12.5  $\text{A} \cdot \text{g}^{-1}$  to illustrate the C-rate capability.<sup>[130]</sup>

### 1.3.3 Differential capacity analysis

To investigate even small changes in the material function of batteries, constant-current chronopotentiometry is used to collect the voltage versus the charge. Differentiated plots of this data reveal electrochemical reactions as peaks.<sup>[149,150]</sup> The differential capacity plot (DCP) of graphite typically shows six peaks (fig. 1.13 a), three reduction peaks and three oxidation peaks.<sup>[151,152]</sup> The peaks indicate that the reaction consists of at least three solid-state redox reactions.<sup>[153]</sup> The observed peak shift with increasing cycle number is ascribed to an increased resistance of the working electrode with cycling, which leads to successive overpotentials for the staging processes.<sup>[150]</sup> The peaks were assigned to the respective intercalation stage by investigation of the graphene layers' repeated distance using (in-situ) XRD in combination with the anode weight and the state of charge (table 1.2).<sup>[153–155]</sup> An illustration of the connection between the stage transitions  $\text{LiC}_6 \rightleftharpoons \text{LiC}_{12}$  (region I),  $\text{LiC}_{12} \rightleftharpoons \text{LiC}_{18}$  (region II),  $\text{LiC}_{18} \rightleftharpoons \text{LiC}_{27}$  and  $\text{LiC}_{27} \rightleftharpoons \text{LiC}_{36}$  (region III a and b) and  $\text{LiC}_{36} \rightleftharpoons \text{LiC}_{72}$  (region IV) and the potentials is given in figure 1.13 b). Despite the disunities for the highly diluted stage, the reports agree that the three dominant peaks are attributed to the transitions listed in table 1.2. Levi et al. and Dahn et al. additionally reported the appearance of two more peaks in region III, which goes well in line with the missing  $\text{LiC}_{18} \rightleftharpoons \text{LiC}_{27}$  and  $\text{LiC}_{27} \rightleftharpoons \text{LiC}_{36}$  phase transition peaks.<sup>[154,156]</sup>

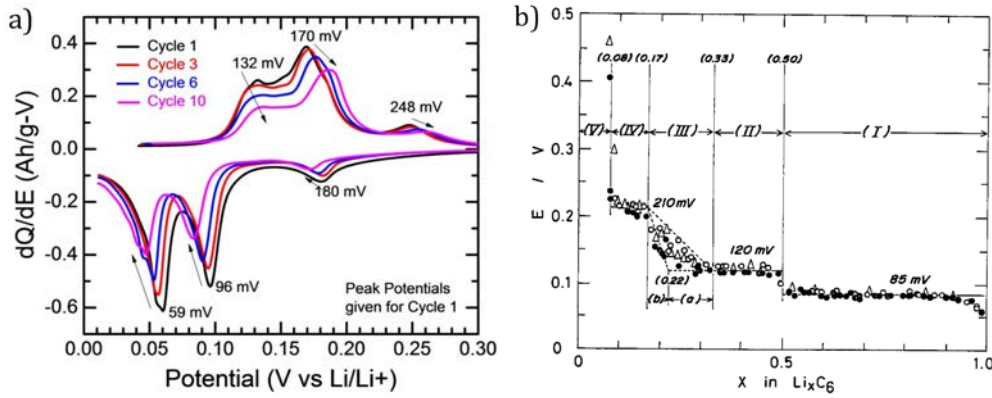


**Figure 1.13:** a) Differential capacity plot of graphite<sup>[150]</sup> and b) reversible potential of a lithium-graphite-intercalation compound as a function of  $x$  in  $\text{Li}_x\text{C}_6$ .<sup>[153]</sup>

**Table 1.2:** Correlation of differential capacity plot peak positions (vs.  $\text{Li}/\text{Li}^+$ ) and lithiation stages of graphite

reference	process	peak position lithiation (mV)	peak position delithiation (mV)	region
Ohzuku et al. <sup>[153]</sup>	$\text{LiC}_{72} \rightleftharpoons \text{LiC}_{36}$	190	230	IV
	$\text{LiC}_{18} \rightleftharpoons \text{LiC}_{12}$	95	140	II
	$\text{LiC}_{12} \rightleftharpoons \text{LiC}_6$	65	105	I
Dahn et al. <sup>[154,155]</sup>	$\text{LiC}_{x \leq 0.04} \rightleftharpoons \text{LiC}_{36}$	$\sim 210$	$\sim 225$	IV
	$\text{LiC}_{18} \rightleftharpoons \text{LiC}_{12}$	$\sim 115$	$\sim 135$	II
	$\text{LiC}_{12} \rightleftharpoons \text{LiC}_6$	$\sim 60$	$\sim 110$	I

In figure 1.14 a) the DCPs of the 1<sup>st</sup> to 5<sup>th</sup> cycle of a graphene-silicon nanocomposite are shown.<sup>[157]</sup> None of the graphite peaks discussed in the previous paragraph is observed, since staging cannot occur in graphene. The DCP of the first lithiation exhibits a very distinct and irreversible peak (A). It is attributed to the dominant conversion process from c-Si to a-Li<sub>x</sub>Si, which can be observed in parallel using in-situ XRD.<sup>[53,138,157–159]</sup> The reduction peaks (E) and (F) correlate with the oxidation peaks (B) and (C) and are widely accepted to be caused by the stepwise lithiation of a-Si to a-Li<sub>2.0</sub>Si and a-Li<sub>3.5</sub>Si and the respective delithiation.<sup>[57,157,158]</sup> The last reduction peak (G) is observable around 50 mV and it indicates the formation of c-Li<sub>15</sub>Si<sub>4</sub>.<sup>[47,58,160,161]</sup> Moreover, peak (G) is linked to the strong oxidation peak (D), meaning, if the battery is cycled above potentials of 50 – 70 mV, it disappears together with peak (D) (fig. 1.14 b). These peaks, correlated to c-Li<sub>15</sub>Si<sub>4</sub>, have been shown to decay over cycling in conjunction with the battery capacity.<sup>[53,157,162]</sup> In table 1.3 the reactions ascribed to the labelled peaks are listed. While the characterisation of crystalline phases was straightforwardly accomplished by in-situ XRD methods the characterisation of the amorphous phases is only possible to a limited extent. Also, the stoichiometric composition of the amorphous Li<sub>x</sub>Si compounds derived from XRD is calculated from the anode lithium content and therefore imprecise.<sup>[53]</sup> The stoichiometric compositions derived from <sup>7</sup>Li NMR and pair distribution studies are based on peak positions attributed to the arrangement of Si-clusters formed around Li in Li<sub>x</sub>Si model compounds.<sup>[56,57,59]</sup> But even though the evaluated transition reactions may be incomplete, the acquired assignments provide a useful basis for the discussion of differential capacity plots. In addition, it is to mention that the first cycle DCP of a-Si looks different compared to that of c-Si (fig. 1.14 c). In contrast to the first cycle DCP of crystalline Si-NWs (green curve), the DCP of a-Si – c-Si core-shell Si-NWs (red curve) shows a distinct peak around 230 mV upon lithiation. Comparable to the first cycle peak of c-Si it indicates a two-phase region and it does not occur in subsequent cycles.<sup>[79]</sup> For silicon-graphite composites DCP features of both materials can be observed at the same time.<sup>[159,163,164]</sup>

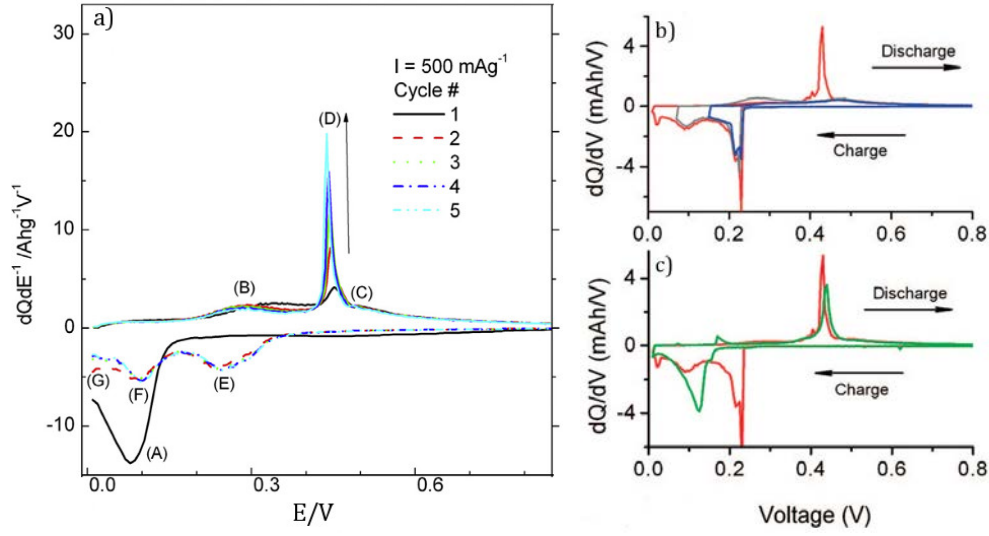


**Figure 1.14:** a) DCP of graphene-silicon nanocomposite<sup>[157]</sup> and first cycle DCPs of b) Si-NWs at different cutoff voltages of 10 mV (red), 70 mV (grey) and 150 mV (blue) and c) crystalline-amorphous core-shell Si-NWs (red) and single crystalline Si-NWs (green)<sup>[165]</sup>.

**Table 1.3:** Correlation of differential capacity plot peak positions (vs.  $\text{Li}/\text{Li}^+$ ) and lithiation processes of silicon; XRD<sup>1</sup> method involved capacity calculations for determination of the  $\text{a-Li}_x\text{Si}$  stoichiometry

peak	reference	peak position (mV)	attributed reaction	concluded from
A	Li et al. <sup>[53]</sup>	~100	$\text{c-Si} \rightarrow \text{a-Li}_{3.5}\text{Si}$	XRD <sup>1</sup>
B	Ogata et al. <sup>[57]</sup>	270	$\text{a-Li}_{3.5}\text{Si} \rightarrow \text{a-Li}_{2.0}\text{Si}$	(in-situ) NMR
	Gauthier et al. <sup>[61]</sup>	300	$\text{a-Li}_{15}\text{Si}_4 \rightarrow \text{a-Li}_{2\pm 0.3}\text{Si}$	EELS
C	Ogata et al. <sup>[57]</sup>	500	$\text{a-Li}_{2.0}\text{Si} \rightarrow \text{a-Si}$	(in-situ) NMR
	Gauthier et al. <sup>[61]</sup>	350 – 1000	$\text{a-Li}_2\text{Si} \rightarrow \text{a-Si}$	EELS
D	Hatchard et al. <sup>[58]</sup>	400	$\text{c-Li}_{15}\text{Si}_4 \rightarrow \text{a-Li}_x\text{Si}$	in-situ XRD
	Li et al. <sup>[53]</sup>	420	$\text{c-Li}_{15}\text{Si}_4 \rightarrow \text{a-Li}_{\sim 2}\text{Si}$	in-situ XRD <sup>1</sup>
	Ogata et al. <sup>[57]</sup>	430	$\text{c-Li}_{15}\text{Si}_4 \rightarrow \text{a-Li}_{\sim 1.1}\text{Si}$	(in-situ) NMR
	Gauthier et al. <sup>[61]</sup>	450	$\text{c-Li}_{15}\text{Si}_4 \rightarrow \text{a-Li}_{2\pm 0.3}\text{Si}$	EELS
E	Ogata et al. <sup>[57]</sup>	300 – 250	$\text{a-Si} \rightarrow \text{a-Li}_{2.0}\text{Si}$	(in-situ) NMR
F	Ogata et al. <sup>[57]</sup>	100	$\text{a-Li}_{2.0}\text{Si} \rightarrow \text{a-Li}_{3.5}\text{Si}$	(in-situ) NMR
G	Obrovac et al. <sup>[47]</sup>	50	$\text{a-Li}_x\text{Si} \rightarrow \text{c-Li}_{15}\text{Si}_4$	XRD
	Hatchard et al. <sup>[58]</sup>	30	$\text{a-Li}_x\text{Si} \rightarrow \text{c-Li}_{15}\text{Si}_4$	in-situ XRD
	Li et al. <sup>[53]</sup>	60	$\text{a-Li}_{3.5}\text{Si} \rightarrow \text{c-Li}_{15}\text{Si}_4$	XRD <sup>1</sup>

## 2 Thesis Aims

In the context of the desired energy transition the objective of this work is to contribute to the understanding of capacity degradation in lithium-ion batteries and to evaluate state-of-the-art concepts, which are adduced for new rationally designed silicon-based lithium-ion batteries. Therefore, decisive parameters for the battery performance were examined by systematic research. This includes both, the modification of the starting anode material and its electrochemical treatment.

Nowadays nanostructured silicon materials like thin films, nanotubes and nanoparticles in combination with carbonaceous materials are used in high capacity lithium-ion batteries to prevent battery capacity decay through silicon fragmentation. To synthesise adjustable nanostructured silicon with good reproducibility an in-house designed low pressure chemical vapour deposition (LPCVD) hot wall reactor with a rotating module, which deposits silicon by pyrolysis of  $\text{SiH}_4$  on particulate and planar systems, is introduced. Using this very clean synthesis technique, the deposition substrates are varied systematically to, firstly, test and validate the technique and, secondly, choose a substrate which is the basis for further systematic research. For chemical and morphological characterisation of the synthesised powders X-ray Fluorescence, Electron Microscopy and Energy Dispersive X-ray analysis are used. Further knowledge on the anode material is obtained through electrochemical testing and post-mortem characterisation using Near Edge X-ray Absorption Fine Structure Spectroscopy and Electron Microscopy. (Chapter 3)

Innumerable materials are imaginable on the basis of nanostructured silicon-carbon composites, hence the publications on specific materials with exceptional structures and morphologies are vast. However, whether the stability is indeed attributed to the described nanocomposite properties is hard to prove without proper comparison. To evaluate the influence of the silicon content and morphology on the nanocomposites' electrochemical performance, silicon is deposited on graphite with systematic variation of the deposition time and temperature. Decisive correlations between the silicon loading determined by Elemental Analysis and Thermogravimetric Analysis, the crystallinity investigated by X-ray Diffraction and Raman Spectroscopy, the morphology evaluated using Electron Microscopy and Energy Dispersive X-ray analysis and the battery performance characteristics are revealed through electrochemical evaluation. Thereby, a beneficial silicon content range for a stable battery performance and distinct correlations between deposition temperature and electrochemical performance are worked out. Moreover, the investigation of cycled anodes using Electron Microscopy and X-ray Photoelectron Spectroscopy

reveals an instructive impression of the solid electrolyte interphase morphology, thickness and content. (Chapter 4)

To examine the battery performance stabilisation by silicon surface coverage with carbon the adaptable LPCVD method is used to synthesise an amorphous carbon covered silicon deposit. Therefore, amorphous carbon is deposited directly after the silicon deposition on the graphite-silicon nanocomposite using propene. The highly crystalline silicon deposit, sintered due to the high carbon deposition temperatures, is then covered with amorphous carbon which can prevent the oxidation of the underlying silicon. The influence on the battery stability is investigated by electrochemical testing and the evolution of the amorphous carbon layer after anode (de-)lithiation is investigated post-mortem using Transmission Electron Microscopy. (Chapter 5)

Due to the high variety in battery constructions, electrolytes and cycling protocols it is difficult to estimate the significance of material modifications compared to variations of the surrounding factors by simply comparing publications from research groups. To gain a conclusive impression of the significance of the achieved improvements by active material modification, the last section refers to the investigation of the cycling protocol, battery housing and electrolyte composition. The influence of the variation and skipping of protocol sequences and the modification of the electrolyte on the battery performance and solid electrolyte interphase formation are investigated by a range of targeted electrochemical experiments and X-ray Photoelectron Spectroscopy, Scanning Electron Microscopy and Energy Dispersive X-ray analysis of the cycled anode materials. (Chapter 6)



# 3 Silicon deposition on carbonaceous powders using LPCVD for high capacity LIB anodes

## Abstract

Silicon represents an attractive material for future high capacity anodes for lithium-ion batteries (LIBs) owing to several appealing properties. To avoid its fragmentation upon electrochemical cycling, nanostructured silicon materials like silicon thin films, nanotubes and nanoparticles in combination with carbonaceous materials are used nowadays. Low pressure chemical vapour deposition (LPCVD) allows the homogeneous deposition of silicon on virtually any substrate. Using the in-house designed LPCVD hot wall reactor, being equipped with a rotating module, silicon can be deposited not only on planar substrates, but also on powders, even simultaneously. Using the LPCVD setup, depositions of silicon by pyrolysis of a  $\text{H}_2/\text{SiH}_4$  gas mixture on several morphologically different carbonaceous materials, e.g. multi-walled carbon nanotubes (MWCNTs), MWCNTs treated with hydrothermal carbon (MWCNT-HTC) and graphite were achieved. The synthesised powders were characterised using SEM and XRF and the anodes were examined ex-situ after 20 and 50 (dis-)charge cycles using SEM and NEXAFS.

## 3.1 Introduction

Nowadays, the usage of nanostructured silicon materials seems to be the most promising way to reliably apply silicon in lithium-ion batteries (LIBs). These materials can accommodate lithiation-induced strain without fracture, provide an improved rate performance and do not suffer from inhomogeneous lithium-ion (Li-ion) distribution within the silicon caused by slow Li-ion diffusion.<sup>[22]</sup> Yet, pristine bulk silicon does not provide a stable cycling performance, hence, silicon is rather applied as coating on a substrate which provides the connection to the current collector. For the generation of silicon coatings vapour processing routes stand out most, since they can provide highly pure, thin and dense coatings with structural control at low temperatures, in contrast to semi-molten processing like plasma or thermal spraying or wet chemical casting routes.<sup>[166]</sup> Various studies were carried out on amorphous silicon (a-Si) thin films deposited by radio frequency magnetron sputtering, radio frequency glow discharge and vapour evaporation on several substrates (copper foil, stainless steel, nickel foil and beryllium

windows).<sup>[58,77–80]</sup> The observations agree on higher gravimetric capacities and cycle life for thinner films around 250 nm, compared to  $\mu\text{m}$ -scale films.

The investigation of the influence of the silicon's physical and chemical properties on the battery performance demands a synthesis method which guarantees clean, reproducible and adjustable silicon. Amongst the vapour techniques, chemical vapour deposition (CVD) meets these requirements best, since physical vapour deposition (PVD) shows significant drawbacks when it comes to deposition on complex structured substrates and larger surfaces.<sup>[166]</sup> The CVD technique generates highly dense, pure and uniform films with good reproducibility and reasonably high deposition rates, even on sophisticated surfaces. Moreover, by adaption of the CVD process parameters the crystal structure, surface morphology and orientation of the deposit can be controlled. In this work low pressure CVD (LPCVD) is used to alter the rate limiting step during the deposition and reduce homogeneous nucleation of solid polymers.<sup>[167]</sup>

The chemical basis of silicon deposition by  $\text{SiH}_4$ -LPCVD is the pyrolysis of silane. Its kinetics have already been studied a century ago.<sup>[168,169]</sup> However, the pyrolysis mechanism of  $\text{SiH}_4$  is complex, since the pyrolysis includes a sophisticated system with an extensive number of possible radical polymers<sup>[170,171]</sup> and various growth mechanisms.<sup>[172]</sup> Nevertheless, the deposition rates for LPCVD of  $\text{SiH}_4$  are precisely investigated and the synthesis is known for its great reproducibility.<sup>[173,174]</sup> Studies show that for silicon nanodroplet deposits the density and size of the droplets are piloted by the nature of the substrate and can be further modified by synthesis conditions like time and temperature.<sup>[175,176]</sup> The deposited silicon can be varied from crystalline to amorphous silicon by decreasing the deposition temperature, increasing the deposition pressure or decreasing the dilution of the source gas.<sup>[177]</sup> Additionally, the hydrogen content of an a-Si deposit can be increased by further decrease in deposition temperature, which entails a decrease in the number of dangling bonds in the a-Si structure.<sup>[167,178]</sup>

Although LIBS with anodes containing plain silicon thin film depositions on planar substrates exhibited the expected capacity, they did not show the desired stability, even when the thin films were decreased to a thickness of 50 nm a-Si.<sup>[137,179]</sup> Yet, it was shown for vacuum deposited a-Si films that an increase of the substrate roughness can stabilise the electrochemical performance significantly.<sup>[180,181]</sup> Hence, tremendous research on the combination of nanostructured silicon with a suitable substrate ensued. Since the late 1990s, the combination of silicon and graphite has been regarded as a promising approach.<sup>[18]</sup> It was recognised as an effective strategy to stabilise the electrode material, since well-chosen carbons can provide mechanical flexibility, electrical conductance, fast ion transport and high chemical stability.<sup>[22]</sup> Already simple mixtures of silicon and carbon have significantly decreased the relative volume changes and improved the electrochemical performance of silicon-based anodes, however, the latter only to a limited extent.<sup>[147,182,183]</sup>

In the pursuit of obtaining an enhanced beneficial effect from the carbonaceous substrate the connection between carbon and silicon was tried to be improved using  $\text{SiH}_4$ -CVD on carbons of

various dimensions. The most popular one dimensional carbon substrate are carbon nanotubes (CNTs), since they constitute a flexible support with high tensile strength and high electric conductivity and can be used binder free.<sup>[183,184]</sup> It has been shown using a fluidised bed reactor that CVD is an appropriate method to deposit silicon on CNTs and that the silicon loading can be controlled by the deposition duration.<sup>[185]</sup> Materials with CNT substrate provided superior performance compared to sputter-on silicon films on metal substrates, with the highest gravimetric capacity reported reaching 2000 – 3000 mAh · g<sup>-1</sup> on regular and vertically aligned CNTs, depending on the silicon to carbon ratio.<sup>[183,186,187]</sup> However, this capacity still decays after 25 – 50 charging-discharging cycles. Comparable results were obtained for silicon CVD on carbon nanofibres, with a capacity of about 2000 mAh · g<sup>-1</sup> for the first 30 cycles.<sup>[160]</sup> For a two-dimensional carbon material, in this case graphene, the comparison of silicon deposited via CVD with a simple mixture showed that the CVD nanocomposite exhibited 2858 mAh · g<sup>-1</sup>, nearly 1.5 times the initial discharge capacity of the mixture reference.<sup>[188]</sup> Furthermore, the CVD material provided a stable performance for fast delithiation (14 A · g<sup>-1</sup>) over 1000 cycles with on average 1103 mAh · g<sup>-1</sup>. This improvement was attributed to the improved silicon-carbon contact and the avoidance of silicon agglomeration. Considering three-dimensional carbons, various types of graphite were taken into account. Silicon LPCVD on SFG graphite resulted in silicon nanodroplets of 5 to 30 nm in diameter, depending on the deposition time, and the material provided a good capacity of 780 mAh · g<sup>-1</sup> for 10.7 wt.-% silicon content.<sup>[189]</sup> Although this material showed a strong fade, Holzapfel et al. reported that a comparable material containing 7 wt.-% silicon with 10 – 20 nm silicon droplets deposited by CVD on KS6 graphite could maintain 500 mAh · g<sup>-1</sup> for a current rate of C/10 over 150 cycles.<sup>[190]</sup> Its stability is attributed to the low silicon particle size, good adherence of silicon to graphite and the homogeneous silicon distribution. KS6 graphite is in addition a well-suited substrate for silicon LPCVD because of its relatively high specific surface area of about 26 m<sup>2</sup> · g<sup>-1</sup>.<sup>[191]</sup>

This chapter addresses silicon depositions from a H<sub>2</sub>/SiH<sub>4</sub> gas mixture carried out with an in-house designed LPCVD reactor on carbonaceous powders. The deposition time and pressure were varied, and their influence on the deposit regarding the silicon content and morphology was investigated using XRF and SEM. Moreover, various carbonaceous substrates were used to validate the flexibility of the LPCVD method. Finally, the graphite-silicon nanocomposite was electrochemically tested for 50 cycles and analysed after electrochemical testing using SEM and NEXAFS to evaluate its transformation during the cycling.

## 3.2 Experimental

### 3.2.1 Carbonaceous substrates

Synthetic graphite (Timrex KS6, Timcal) was used as substrate without further treatment. Multi-walled carbon nanotubes (MWCNTs, Shandong Dazhan Nano Materials Co.) were heated

to 100 °C for 20 h in a large excess of HNO<sub>3</sub> (ROTIPURAN ≥ 65 %, p.a., ISO, Carl Roth) to remove residual traces of catalyst. The MWCNTs were subsequently thoroughly washed with deionised water and dried at 110 °C overnight. MWCNTs covered with hydrothermal carbon (MWCNT-HTC) were obtained by adding 2.5 g of MWCNTs (catalyst free) to a solution of 6 g glucose (Alfa Aesar) dissolved in 30 ml deionised water. The suspension was heated for 6 h at 220 °C in a teflon lined steel autoclave (Berghof DAB-2, 50 ml vessel). The resulting powder was washed with deionised water, dried overnight at 100 °C and thermally annealed in a hot wall oven (RS 80/500/11, Nabertherm) at 900 °C with a dwell time of 5 h in N<sub>2</sub> atmosphere (heating ramp 10 °C · min<sup>-1</sup>). Prior to the silicon deposition the resulting nanocomposite was ground in a planetary micro mill (PULVERISETTE 7, Fritsch) using agate beakers and balls with additional 2-propanol (≥ 99.5 %, Roth) for 15 min at 800 rpm. Subsequently, the material was dried for 18 h at 80 °C and 250 mbars in a vacuum oven (VTR 5022, Heraeus).

#### 3.2.2 Silicon deposition using LPCVD

The silicon depositions were performed using an in-house designed LPCVD reactor setup comprised of a gas supply facility (N<sub>2</sub> and Ar, purity 99.999 %, Westfalen; H<sub>2</sub> (N50)/SiH<sub>4</sub> (N40) mixture, ratio 4:1, Air Liquide), a three zone hot wall oven (HTM Reetz GmbH), and a horizontally placed 1.2 m long by 4.5 cm in diameter quartz tube as the main reaction chamber (fig. 3.1 a). All gases were dried and filtrated using a dry bed cartridge (MC200, MicroTorr) and the deposition parameters were controlled via a LabView interface. The depositions were performed using a rotary feedthrough motion quartz reactor insert (60 cm long by 3.5 cm in diameter) composed of a 10 cm baffled deposition chamber, reaction gas exhaust compartment, a glass frit, a quick connection holder and a rotary sealing (ALMA-M-KF-012-V-U, Alma) mounted on a KF40 “T” piece, as shown in figure 3.1 d). A carbon felt (SGL carbon) which was thermally annealed and covered with silicon prior to the first use, was applied to stabilise the reactor position within the main LPCVD reaction chamber and guide the reactive gas flow through the rotating deposition chamber (fig. 3.1 c). Prior to deposition all gas lines were purged with N<sub>2</sub> at 2 l · min<sup>-1</sup> for 1 h. The reactor insert was filled with 1 g of graphite or MWCNT powder (fig. 3.1 b) or 0.6 g of MWCNT/HTC powder, inserted inside the main LPCVD reaction chamber and rotated at 2 rounds per minute by a controlled electric step motor. The main LPCVD chamber absolute pressure was set to 1 mbar and the oven heating zones were simultaneously heated from room temperature to 550 °C with a ramp of 5 °C · min<sup>-1</sup> under 10 sccm argon flow. The oven temperature was calibrated using a high temperature type K thermocouple, resulting in the following correlation:  $T_{\text{sample}} = (20.80 + T_{\text{oven}} \cdot 0.99)$  (°C) (SI fig. 8.1). In the following, given temperatures represent the set temperature ( $T_{\text{oven}}$ ). The setup was thermally stabilised for 30 min prior to silicon deposition and cooled down to room temperature under a constant flow of argon. The product was stored inside an argon filled glove box (mBraun B790, O<sub>2</sub> ≤ 1 ppm, Ionic System Trace Oxygen Sensor TOS 3.0). The detailed list of samples with their associated deposition conditions is given in table 8.1 (SI).

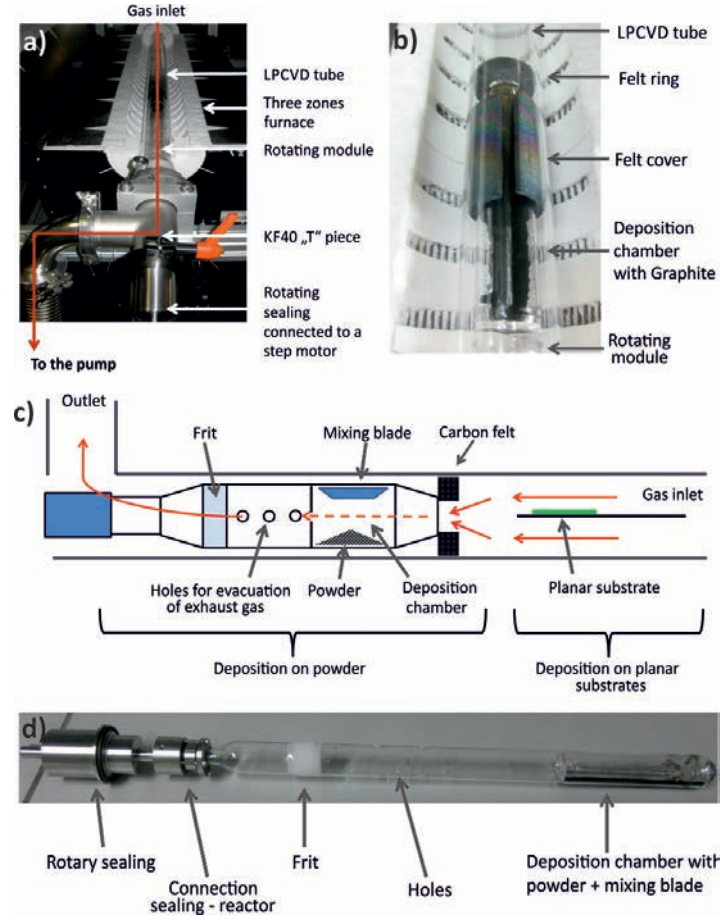


**Figure 3.1:** LPCVD reactor: a) picture of the hot wall LPCVD reactor with the rotary insert, b) picture of the deposition chamber of the rotary insert, c) scheme of the reactor and gas flow and d) picture of the quartz reactor insert connected to the rotary feedthrough sealing.

### 3.2.3 Powder characterisation

**X-ray Fluorescence** The XRF instrument used is a wavelength dispersive device S4-Pioneer, derived from Bruker AXS, equipped with a rhodium anode as radiation source. To enable proper silicon quantification by the  $K_{\alpha}$  line (1.7 keV) calibration series of graphite/ $\text{SiO}_2$  and MWCNT/ $\text{SiO}_2$  (AEROSIL 300, Degussa) mixtures with known silicon content were measured. Via the resulting linear correlation  $[\text{Si}] = 0.5133 \cdot I_{\text{Si}K_{\alpha}}$  the silicon contents were calculated from the measured Si  $K_{\alpha}$  line intensity. All measurements were performed using 20 mg of powder in a 25 mm diameter beaker, which was enclosed with a 6  $\mu\text{m}$  Mylar foil and measured under helium atmosphere.

**Scanning Electron Microscopy** SEM images were acquired on a Hitachi S-4800 microscope using 1.5 kV accelerating voltage and 3 – 4 mm working distance. The samples were prepared on a beryllium holder and energy dispersive X-ray (EDX) analysis was performed using a silicon drift detector (SDD).

**Scanning Transmission Electron Microscopy** STEM images were captured using a Hitachi HD-2700 Cs-corrected dedicated STEM (200 kV, Cold FEG) with Edax Octane T Ultra W 200 mm<sup>2</sup> SDD (Team-Software) at 700.000-fold magnification.

**Nitrogen physisorption** N<sub>2</sub> physisorption was performed in a Quantochrome AUTOSORB-6 machine after degassing 50 mg KS6 graphite at 225 °C for 2.5 h. The resulting isotherms were recorded at -196 °C using an AUTOSORB-6B-MP (Quantachrome). Calculation of the surface area was performed according to the equation of Brunauer, Emmet and Teller (BET equation).<sup>[192]</sup>

### 3.2.4 Anode preparation and electrochemical tests

**Anode preparation** For the preparation of electrodes, polyacrylic acid (PAA,  $\leq 0.5$  % benzene, Sigma-Aldrich) was dispersed in an ethanol (Sigma-Aldrich) : 2-propanol ( $\geq 99.5$  %, Carl Roth) (6.25:1) mixture and stirred for 15 h. Then, carbon black (CB) (Super Conductive P, Alfa Aesar) and the sample were added (PAA : CB : sample = 1 : 1.5 : 10), stirred and treated in an ultrasonic bath. The prepared slurry was cast as a thin film on a 25  $\mu$ m thick copper foil (Cu58, bare, Schlenk) using a 4-sided film applicator (VF2169-013, 60 mm, TQC), set to a film thickness of 120  $\mu$ m, and dried for 15 h at 80 °C in a vacuum oven (VTR 5022, Heraeus). Hereafter, 10 mm anodes were punched out using a lever press, weighed and stored in an argon filled glovebox (mBraun B790, O<sub>2</sub>  $\leq 1$  ppm Ionic System Trace Oxygen Sensor Tos 3.0). The reference slurry with silicon nanoparticles was produced under the same conditions using a mixture of KS6 and silicon nanopowder (purity  $\geq 98$  %, Sigma Aldrich).

**Electrochemical testing** For the two electrode battery system, a modified stainless steel Swagelok tube fitting was electrically insulated by a one-way 75  $\mu$ m Kapton foil (Dr. Dietrich Müller GmbH). The working electrode and counter electrode (metallic lithium, 10 mm diameter, 1.5 mm thickness, Thermo Fisher GmbH) were sandwiched with two 25  $\mu$ m thick separators (C2500, Celgard Inc., USA) in between and wetted with 140  $\mu$ l of a solution of 1 M LiPF<sub>6</sub> dissolved in a mixture of ethylene carbonate : diethyl carbonate 1 : 1 wt.-% (Selectilyte LP40, Battery grade, BASF) electrolyte. The battery cell was sealed inside the argon filled glovebox with nylon ferrules (Swagelok) on both sides. Electrochemical measurements were carried out using an Arbin Instruments BT2000 battery tester applying a constant current – constant voltage (CC-CV) scheme. The current rate was set to one charge per hour (1C), the CV-sequence was set to 1 h and the system was cycled in the borders of 2 V and 5 mV for the respective number of cycles.

### 3.2.5 Post-mortem analysis

After electrochemical testing the batteries were disassembled inside the argon filled glove box, with the anodes being in the delithiated state. Then, the anodes were washed successively in

four flasks filled with 3 ml DEC ( $\geq 99\%$ , anhydrous, Sigma Aldrich) each and prepared for the respective analysis method (SEM and NEXAFS) on transfer holders which provide an airtight seal.

**Scanning Electron Microscopy** SEM images were acquired on a Hitachi S-4800 microscope using 1.5 kV accelerating voltage and 3 – 4 mm working distance. The anodes were mounted on conductive carbon tape (Plano) on a transfer holder. Energy dispersive X-ray (EDX) analysis was performed using a silicon drift detector (SDD).

**Near Edge X-ray Absorption Fine Structure Spectroscopy** The extended absorption fine structure spectra (EXAFS) at the Si and P K-edges were recorded in the beamline BL16A1 of the National Synchrotron Radiation Research Centre (NSRRC), Hsinchu (Taiwan). The photons are sourced from a bending magnet (BM3) with a total flux of  $4.8 \times 10^{11}$  photons  $\cdot$  s $^{-1}$  (measured at 5 keV). In addition, the beamline is equipped with a double-crystal monochromator (InSb(111)) yielding an energy range from 2 keV up to 8 keV. The beam spot size can be resized down to 0.5 mm (horizontal) x 0.4 mm (vertical) using a slit-width control. To avoid changes in the oxidation state by air, the measurements were performed in an inert helium controlled atmosphere using a specially sealed chamber. The spectra were collected in fluorescence yield mode between 1.75 keV and 4 keV with a resolved power of 3000 using a gas ionisation chamber (Lytle) as a detector.

## 3.3 Results and discussion

### 3.3.1 Powder characterisation

LPCVD is known to be a very flexible technique enabling depositions of various materials on all kinds of substrates. To investigate whether this also holds for silicon depositions on different carbonaceous powders, silicon was deposited by SiH<sub>4</sub> pyrolysis from a H<sub>2</sub>/SiH<sub>4</sub> gas mixture on graphite (G), multi-walled carbon nanotubes (MWCNTs) and MWCNTs treated with hydrothermal carbon (MWCNT-HTC). To investigate the influence of the substrate and the deposition parameters, time and pressure, on the silicon loading, the samples were analysed by XRF. The results are listed in table 3.1. Doubling the deposition time (30 to 60 min) of silicon on graphite resulted in nearly the double amount of silicon, in particular 2.4 wt.-% and 5.5 wt.-%. For increasing deposition pressures, namely 1, 5 and 20 mbars, a continuous decrease of the silicon content in the graphite nanocomposite materials was observed. It has been reported that increasing deposition pressures result in a decrease in the gas flow<sup>[193]</sup>, which would be in good agreement with the decreasing silicon content for increasing deposition pressures. For identical deposition parameters the silicon contents of G-Si, MWCNT-Si and MWCNT-HTC-Si were found to be similar, with G-Si providing, by a narrow margin, the highest silicon loading with 5.5 wt.-% silicon after 1 h deposition time.

**Table 3.1:** Silicon content (wt.-%) from XRF analysis for depositions at 550 °C (standard error 8 %)

sample	time (min)	pressure (mbar)	Silicon (wt.-%)
G-Si-30m	30	1	2.35
G-Si	60	1	5.49
G-Si-5	60	5	2.87
G-Si-20	60	20	1.69
MWCNT-Si	60	1	4.62
MWCNT-HTC-Si	60	1	5.01

The morphology of the substrates MWCNTs, MWCNT-HTC and G and the deposited silicon was investigated using SEM (fig. 3.2). Compared to the pristine MWCNT substrate, depicted in figure 3.2 a), the MWCNT-HTC substrate is composed of MWCNTs and spherical hydrothermal carbon (fig. 3.2 b). The G substrate consists of relatively small platelets below 10  $\mu\text{m}$  in diameter and various thicknesses (SI fig. 8.2). After the silicon deposition, the formation of discrete silicon nanodroplets of some few nanometres in size is observed independent of the substrate material (fig. 3.2 a'-c'). This observation goes in line with earlier reported experiments on various carbons.<sup>[187,188,190]</sup>

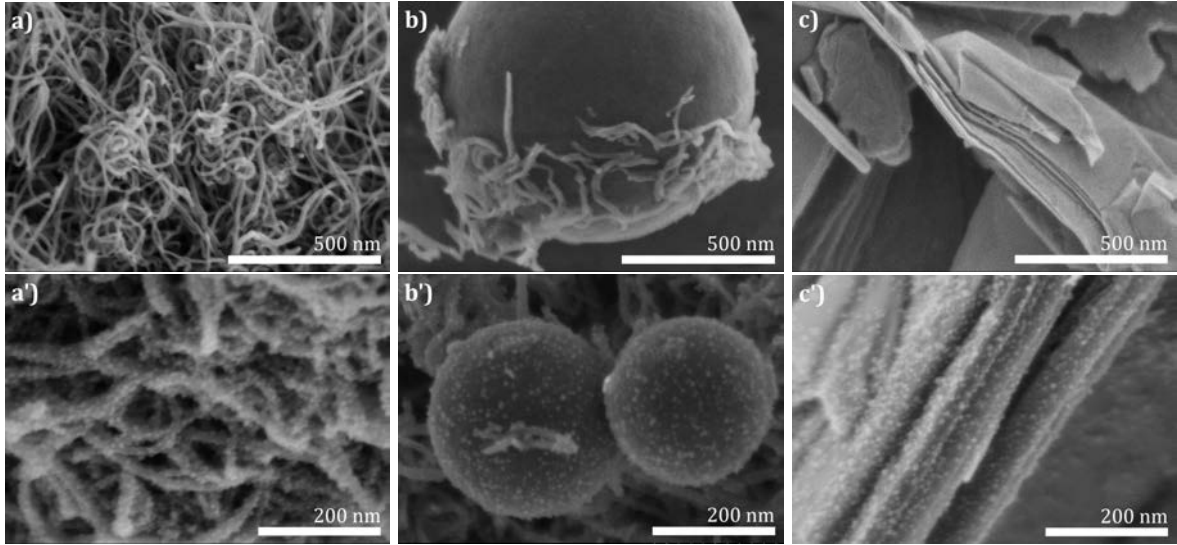


**Figure 3.2:** SEM images of a) MWCNTs, b) MWCNT-HTC and c) G before and a') MWCNTs-Si, b') MWCNT-HTC-Si and c') G-Si after silicon deposition.

STEM combined with the respective silicon elemental map (fig. 3.3) of the MWCNT-HTC-Si sample confirms that the deposited droplets contain silicon. This validates that the visible droplets indeed result from  $\text{SiH}_4$  pyrolysis.



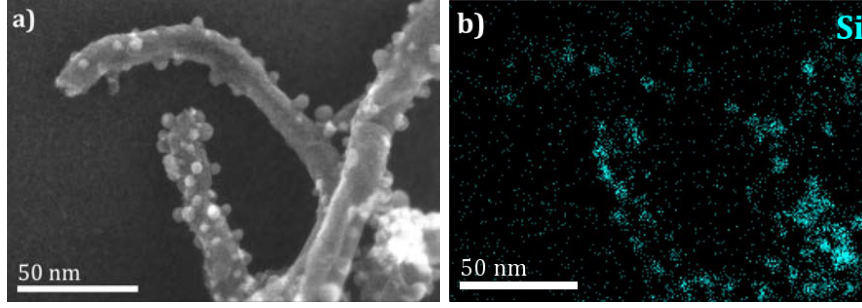


**Figure 3.3:** a) STEM image of MWCNTs with silicon deposition (sample: MWCNT-HTC-Si) with b) respective silicon elemental map obtained from EDX.

In accordance with the flexible handling and the time-proven application of graphite in batteries, it was chosen as the carbonaceous substrate for all following experiments. Compared to other graphites, the used KS6 graphite exhibits a relatively high specific surface area of  $25 \text{ m}^2 \cdot \text{g}^{-1}$ , which is further useful to maximise the silicon content of the nanocomposites while maintaining small dimensions of the deposited silicon.

### 3.3.2 Post-mortem analysis of the anode material after electrochemical testing

The graphite sample with the highest silicon loading, namely G-Si ( $5.5(\pm 0.4) \text{ wt.-% Si}$ ), a reference mixture of graphite with 4 wt.-% silicon nanoparticles (G-SiNP) and a reference graphite anode were electrochemically aged using a CC-CV protocol at 1C between 2 V and 5 mV. The anodes were subjected to 50 (dis-)charge cycles and were dismantled in the delithiated state. The cycling raw data can be found in the SI (fig. 8.3). In figure 3.4 SEM images of tested G-Si anodes are depicted. The anode in figure 3.4 a) was exposed to electrolyte with applied open circuit voltage (OCV), b) was (dis-)charged 20 times and c) (dis-)charged 50 times. Already the exposure of the anode to the electrolyte leads to the generation of tiny droplets of unknown composition, covering the surface in a netlike structure. The deposited silicon droplets, however, appear unchanged. After 20 (dis-)charge cycles, the silicon droplets look "molten". However, it cannot be concluded from SEM analysis whether the shape of the droplets changed or the changed shape is the result of a solid electrolyte interphase (SEI) coverage. Yet, the TEM analysis reported by Yao et al.<sup>[194]</sup> of cycled silicon hollow nanospheres supports the assumption that the shape of the silicon nanodroplets remains the same, and that they are covered with SEI. Notably, this coverage connects the silicon nanodroplets with each other. After 50 cycles, this trend is further enhanced. The presented SEM images in figure 3.4 were captured in silicon rich regions, where the alteration is more pronounced. SEM images of areas with less silicon droplets can be seen in SI (fig. 8.4). Comparable results were also obtained for the G-SiNP reference after 20 cycles (SI fig. 8.5). However, the silicon nanoparticles turned out to be bigger than stated and were highly agglomerated within the slurry (SI fig. 8.6).

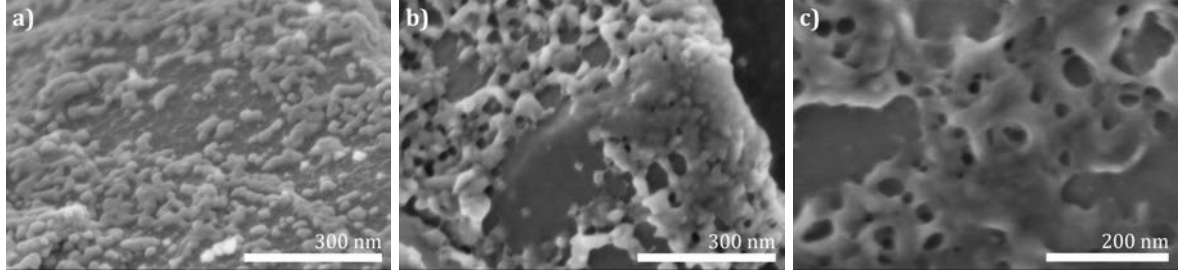


**Figure 3.4:** SEM images of G-Si anodes after a) OCV b) 20 (dis-)charge cycles and c) 50 (dis-)charge cycles.

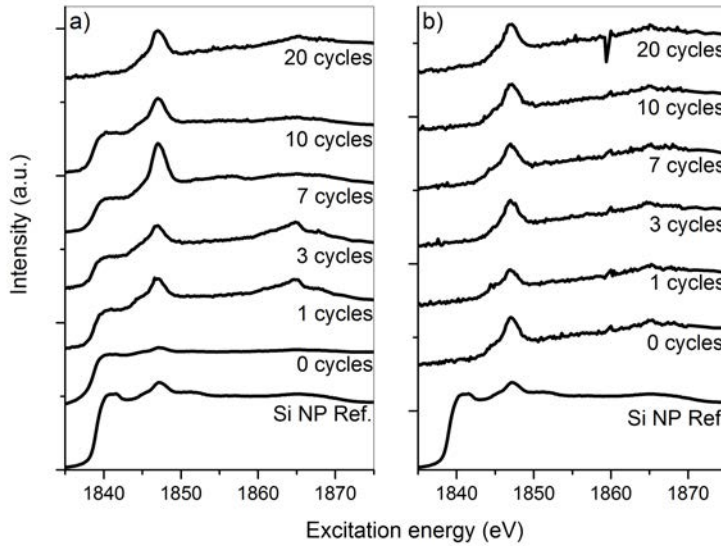


**Figure 3.5:** NEXAFS spectra of a) G-SiNP and b) G-Si anodes after OCV, 1, 3, 7, 10 and 20 cycles with silicon nanoparticle (Si NP) reference.

To gain further insights on the chemical alteration of the silicon deposit, NEXAFS analysis was employed on G-SiNP and G-Si anodes subjected to 1, 3, 7, 10 and 20 (dis-)charge cycles. The cycling raw data can be found in the SI (fig. 8.7 and 8.8). The region of the Si K-edge for G-Si anodes, G-SiNP anodes and the reference silicon nanoparticles is shown in figure 3.5. In literature, the Si K-edge of crystalline silicon was reported between 1838 and 1842 eV, while  $\text{SiO}_2$  exhibits a main feature at 1847 eV.<sup>[195–197]</sup> Both, the silicon nanoparticle reference and the G-SiNP anode solely exposed to electrolyte in OCV (0 cycle) show, besides the Si K-edge, a contribution of the  $\text{SiO}_2$  signal. This indicates that the initial  $\text{SiO}_2$  signal of the anode is attributed to the air exposure of the material during the anode preparation. The Si K-edge, however, shrinks over cycling for the G-SiNP battery at the expense of the  $\text{SiO}_2$  signal, until after 20 cycles the Si K-edge completely vanished (fig. 3.5 a). This observation indicates the generation of  $\text{SiO}_x$  species during cycling, which is most probably due to electrolyte degradation

including silicon oxidation and SEI formation. These processes involve the consumption of charges, which goes in line with the observed smaller coulombic efficiencies of the G-SiNP battery in the first 10 cycles (SI fig. 8.3). The G-Si anode also shows a contribution of the  $\text{SiO}_2$  signal, but no Si K-edge before the (dis-)charging starts and remains unchanged for increasing cycle numbers (fig. 3.5 b). Yet, a XANES spectrum of deposited a-Si:H reported by Mastelaro et al.<sup>[198]</sup> is very similar to the depicted reference silicon nanoparticle spectrum. This indicates that, due to the small droplet size, most of the deposited silicon is oxidised through air contact during preparation of the anode.

### 3.4 Conclusion

Employing the in-house designed rotating LPCVD reactor module, nanometer-sized silicon droplets were deposited on various particulate carbonaceous substrates. The silicon content was adjustable by variation of deposition time and pressure. A synthesised graphite-silicon nanocomposite containing around 5 wt.-% deposited silicon was electrochemically cycled and compared to a graphite/silicon nanoparticle reference. The NEXAFS data illustrated the electrochemical degradation of the silicon nanoparticles upon cycling, while for the LPCVD nanocomposite material neither a Si K-edge nor any changes during cycling were observed, indicating that the silicon was mostly oxidised prior to cycling. Further work in the following chapters will therefore focus on samples with higher silicon loading and bigger silicon droplets.



## 4 Graphite-silicon nanocomposites for LIB anodes prepared by methodically varied LPCVD

### Abstract

The sophisticated application of silicon in anode materials for lithium-ion batteries (LIBs) is widely desired and the publications in this field on specific new materials are innumerable. However, it is difficult to compare the distinct materials' performance, since not only the active material but also various parameters like battery setup, cycling protocol and electrolyte usually vary. Hence, to investigate the influence of the silicon properties on the electrochemical performance of the batteries, this chapter addresses graphite-silicon nanocomposites synthesised by low pressure chemical vapour deposition (LPCVD) with systematically varied deposition time (30 – 180 min) and temperature (435 – 550 °C). Additionally, a graphite-silicon nanocomposite sample was annealed at 800 °C to create an intermediate sample between the LPCVD nanocomposites and the established graphite/silicon nanoparticle mixtures. This annealed silicon deposit meets the silicon nanoparticles in size and morphology, but is connected to the graphite surface. By systematic characterisation (TGMS, XRD, Raman, SEM, EDX and TEM) of the graphite-silicon nanocomposites their silicon contents (7 – 30 wt.-% Si), morphology and crystallinity were evaluated and thus correlated with the deposition parameters. Combined with electrochemical tests it was revealed that for a stable battery performance the silicon content should be less than 30 wt.-% and that the crystallinity of the silicon deposit affects especially the coulombic efficiency of the batteries. The post-mortem analysis of the cycled anodes using SEM and XPS contributed to a more thorough understanding of the anode ageing processes by providing information about the morphology and chemical composition of the evolved solid electrolyte interphase.

### 4.1 Introduction

Significant efforts have been undertaken to develop silicon-based batteries with superior energy and power densities. However, such a huge capacity entails correspondingly large volume changes, namely a 280 % increase when crystalline silicon (c-Si) is lithiated to c-Li<sub>15</sub>Si<sub>4</sub>.<sup>[11,70]</sup> Together with the intrinsic low electrical conductivity of silicon, these are the main reasons for

mechanical degradation and lithium-ion (Li-ion) trapping. Both, material degradation and Li-ion trapping, can be counteracted by the combination of nanostructured silicon with carbon.<sup>[199]</sup> Beyond the simple mixing of silicon nanoparticles (Si NPs) and carbonaceous powders, the deposition of silicon via chemical vapour deposition (CVD) on carbon proved to be a promising route. One of the main advantages of the CVD process is its flexibility, so that silicon can be deposited as crystalline or amorphous silicon (a-Si) on all kinds of substrates. Results from Forney et al. showed that only LPCVD generates a purely a-Si deposition on single-walled carbon nanotubes (SWCNTs) for various deposition times, while for plasma-enhanced CVD partial crystallisation occurs.<sup>[200]</sup> This degree of control is fundamental to deposit precisely defined silicon, which enables to draw correlations between the battery performance and the silicon properties like content, morphology and crystallinity.

The silicon content of silicon-carbon nanocomposite materials produced by CVD using  $\text{SiH}_4$  can be varied with the deposition time.<sup>[186]</sup> The silicon content affects three major battery properties: the gravimetric capacity, the battery cycling stability and the first cycle coulombic efficiency (CE). An increase in the silicon content for silicon depositions on graphite and SWCNTs entails, on the one hand, an increase of the gravimetric capacity and, on the other hand, a faster capacity decay.<sup>[189,200]</sup> This indicates that there is a balance of the gravimetric capacity and a stable cycling performance for silicon-carbon composite batteries. Yet, as introduced in chapter 1.1, a gravimetric capacity of  $1000 - 1200 \text{ mAh} \cdot \text{g}^{-1}$  should be striven for to achieve a reasonable improvement of the LIB capacity.<sup>[19-21]</sup> While the battery cycling stability decreases with increasing silicon content, the CE of the very first cycle has been shown to increase with increasing silicon content.<sup>[147,200]</sup> This is attributed to the formation of a stable solid electrolyte interphase (SEI) on carbonaceous materials in the first cycle, which is known to entail an irreversible loss of charges and simultaneous gas evolution, leading to low CEs. Both have been reported to decrease with increasing silicon coverage of carbonaceous substrates which indicates that the SEI formation on silicon proceeds via a different mechanism.

LPCVD does not only allow a precise tuning of the silicon content, but also of the silicon morphology in the silicon-carbon composite. By variation of the  $\text{SiH}_4$  partial pressure for silicon deposition on CNTs, either silicon droplets or thin films are formed.<sup>[201]</sup> It was reported that the droplet deposition showed a significantly better cycling performance, which was mainly attributed to a more free silicon expansion for the silicon droplets compared to the silicon thin film upon lithiation. Moreover, the droplets were found to be tethered to the CNT surface by an amorphous carbon layer, which formed between the silicon droplets and the CNT during the deposition.<sup>[186]</sup> Although the deposition temperature was not reported to visibly affect the deposit morphology, Hatalis et al. showed that upon thermal annealing of a-Si thin films deposited at various temperatures, lower deposition temperatures lead to bigger c-Si grains.<sup>[193]</sup> This was attributed to a decreased nucleation rate for lower deposition temperatures which led to the increased grain sizes upon annealing.

Besides the influence of the morphology of the nanostructured silicon on the battery performance, the impact of the silicon crystallinity is widely discussed in this research field. The crystallinity of the silicon deposit usually is controlled by the deposition temperature, with the transition from a-Si to c-Si deposition being dependent on the substrate. For silicon (LP)CVD on carbonaceous substrates the most common reported deposition temperature is 500 °C, leading to amorphous or amorphous and nanocrystalline silicon deposits.<sup>[160,184,185,200,201]</sup> Only few report higher (540 – 650 °C)<sup>[187–189]</sup> or lower (450 °C)<sup>[202]</sup> deposition temperatures. Indeed, both materials, c-Si and a-Si, are lithiated in a two-phase reaction and show a phase boundary observable using in-situ TEM.<sup>[54,67,203]</sup> However, c-Si undergoes anisotropic lithiation with irregular velocity and the lithium concentration required for the Si-bond breaking is assumed to be higher. This goes in line with a-Li<sub>3.5</sub>Si being reported as a-Li<sub>y</sub>Si phase for the lithiation of c-Si, while a-Li<sub>2.5</sub>Si, containing less lithium, being reported for a-Si, before further single phase lithiation is initiated.<sup>[53,203]</sup> That c-Si and a-Si undergo the first lithiation in diverging ways is also clearly visible in differential capacity analysis.<sup>[165]</sup> The final lithiation product for both materials, c-Si and a-Si, at room temperature was reported to be c-Li<sub>15</sub>Si<sub>4</sub>. The delithiation product for both materials is a-Si, which is of bigger volume than regular a-Si. Its subsequent lithiation follows a one phase reaction, in contrast to the previously observed two phase reaction of the pristine a-Si.<sup>[11,67]</sup> This indicates an essential difference in the microstructure of delithiated a-Si compared to its pristine form. Hence, the assumption arises that for all subsequent cycles the initially used material is irrelevant, as illustrated in figure 4.1. Nevertheless, it has been reported for silicon particles that c-Si particles bigger than 150 nm in diameter fractured during cycling, while a-Si spheres did not fracture even with a diameter of 870 nm.<sup>[67,76]</sup> Consistent with this it has been shown that batteries with anodes based on continuous a-Si films and a-Si nanowires provide higher capacities and better cycle life than their nanocrystalline counterparts.<sup>[204,205]</sup> Whether this is caused solely by the first cycle is part of ongoing research on the lithiation processes in silicon-based anode materials.

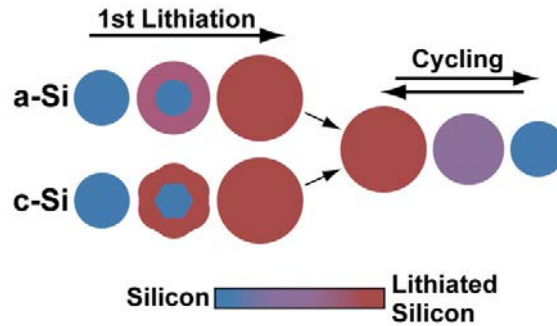


**Figure 4.1:** Summary of 1<sup>st</sup> lithiation and subsequent cycling as suggested by McDowell et al.<sup>[67]</sup>

For the development of new rationally designed silicon-carbon-based anode materials for application in LIBs, CVD is often the method of choice, since it combines clean nanostructured silicon with every desired carbonaceous substrate. However, the comparison of the reported materials regarding the battery performance is difficult, because the silicon loading, crystallinity and the

battery setup are often varied at the same time. Hence, this chapter presents a systematic study on the influence of the silicon content, morphology and crystallinity for an LPCVD synthesised graphite-silicon nanocomposite on the battery performance. Additionally, informative insights into the SEI morphology, growth and chemical composition by post-mortem analysis are given.

## 4.2 Experimental

### 4.2.1 Sample preparation

The silicon depositions were performed using an in-house designed LPCVD reactor setup comprised of a gas supply facility ( $\text{N}_2$  and Ar, purity 99.999 %, Westfalen;  $\text{SiH}_4$ , UHP, Air Liquide), a three zone hot wall oven (HTM Reetz GmbH), and a horizontally placed 1.2 m long by 4.5 cm in diameter quartz tube as main reaction chamber. All gases were dried and filtrated using a dry bed cartridge (MC200, MicroTorr). The depositions were performed using a rotary feedthrough motion quartz reactor insert (60 cm long by 3.5 cm in diameter) composed of a 10 cm baffled deposition chamber, reaction gas exhaust compartment, a glass frit, a quick connection holder and a rotary sealing (ALMA-M-KF-012-V-U, Alma) mounted on a KF40 “T” piece. Prior to deposition all gas lines were purged with  $\text{N}_2$  at  $2 \text{ l} \cdot \text{min}^{-1}$  for 1 h. The reactor insert was typically filled with 1.5 g of graphite powder (KS6, Timcal) inserted inside the main reaction chamber and rotated at 2 rounds per minute. The main chamber absolute pressure was set to 1 mbar and the oven heating zones were simultaneously heated from room temperature to the silicon deposition temperature with a ramp of  $5 \text{ }^\circ\text{C} \cdot \text{min}^{-1}$  under 10 sccm argon flow. The oven calibration revealed a  $T_{\text{sample}} = (20.80 + T_{\text{oven}} \cdot 0.99) \text{ (}^\circ\text{C)}$  correlation. In the following, given temperatures represent the set temperature ( $T_{\text{oven}}$ ). The setup was thermally stabilised for 30 min prior to silicon deposition and cooled down to room temperature under a constant flow of argon. The depositions were varied in time (30 – 240 min) and temperature (435 – 550  $^\circ\text{C}$ ) and were performed with a  $\text{SiH}_4$  flow of 10 sccm (list of samples in SI table 8.2). The product was ground in an agate mortar and stored inside an argon filled glove box (mBraun B790,  $\text{O}_2 \leq 1 \text{ ppm}$  Ionic System Trace Oxygen Sensor Tos 3.0).

### 4.2.2 Silicon characterisation

**Elemental Analysis** For silicon quantification, elemental analysis was executed by the analysis laboratory Kolbe (Höhenweg 17, 45470 Mülheim an der Ruhr, Germany) using a Vario EL CHNOS-Analyser (Elementar) and photometric silicon determination.

**Thermogravimetric analysis – mass spectrometry** TG-MS measurements were carried out using a simultaneous TG–DSC on a Netzsch STA 449C Jupiter thermoanalyzer equipped with an electromagnetic micro balance (resolution 0.1  $\mu\text{g}$ ; relative error of the mass determination 0.5 %) with top-loading. The sample was placed in an open corundum crucible (85  $\mu\text{l}$ ) and placed on



the sample holder whose temperature change was monitored via Pt/Pt-Rh thermocouples. The samples were heated in a  $100 \text{ ml} \cdot \text{min}^{-1}$  flow of a gas mixture consisting of 21 %  $\text{O}_2$  : 79 % Ar (both 99.999 %, Westfalen) with  $10 \text{ }^\circ\text{C} \cdot \text{min}^{-1}$  to  $650 \text{ }^\circ\text{C}$ , then  $2 \text{ }^\circ\text{C} \cdot \text{min}^{-1}$  to  $1000 \text{ }^\circ\text{C}$  and finally with  $5 \text{ }^\circ\text{C} \cdot \text{min}^{-1}$  to  $1500 \text{ }^\circ\text{C}$ . The evolved gases were monitored with a quadrupole mass spectrometer (QMS200 Omnistar, Balzers) coupled to STA via a quartz capillary heated to  $40 \text{ }^\circ\text{C}$ . The experiments were performed with an electron ionisation energy of 60 eV and a dwell time per mass of 0.2 s.

**X-ray diffraction and Rietveld refinement** The X-ray diffraction measurements were performed in Bragg-Brentano geometry (Bruker AXS D8 Advance II) using Ni filtered Cu  $\text{K}_\alpha$  radiation and a position sensitive energy dispersive LynxEye silicon strip detector. Rietveld refinement was carried out using the TOPAS software (TOPAS version 5, copyright 1999-2014 Bruker AXS). Finding a reasonable fit model was complicated by the properties of the graphite support, which exhibits a mixture of 2H and 3R polytypes with anisotropic peak broadening and strong preferred orientation effects, as well as the deposited only partially crystalline silicon. Thus, a coupled refinement of all sample data was carried out to reduce the number of freely refined parameters without making the model too inflexible. The anisotropic peak shapes and the preferred orientation parameters of the 2H and 3R graphite phases within each sample were restricted to be the same but allowed to vary between different samples. In contrast, the lattice parameters of each phase were coupled between all sample data. The silicon diffraction signals were represented by superposition of two silicon "phases", one of them with extreme peak broadening to approximate the diffuse signal from the a-Si fraction. Due to strong correlations with the background polynomial, the peak width of this phase was restricted to be the same for all samples. To index the XRD patterns the references listed in table 4.1 were used.

**Table 4.1:** XRD reference patterns

phase	chemical formula	database #
Graphite 2H	C	PDF 89-7213
Graphite 3R, syn	C	PDF 26-1079
Silicon, syn	Si	PDF 27-1402
Cristobalite, syn	$\text{SiO}_2$	PDF 39-1425

**Raman spectroscopy** Raman measurements were carried out on a Thermo Fischer Scientific DXR spectrometer with a 532 nm laser in the measurement range from  $100 - 4000 \text{ cm}^{-1}$  applying an incident light power of  $0.5 - 1 \text{ mW}$ . For comparison of the Raman spectra the silicon TO-band was normalised.

**Scanning Electron Microscopy** SEM images were acquired on a Hitachi S-4800 microscope using 1.5 kV accelerating voltage and 3 – 4 mm working distance. The samples were prepared on a beryllium holder and energy dispersive X-ray (EDX) analysis was performed using a silicon drift detector (SDD).

**Focused Ion Beam** For TEM lamella preparation a Helios NanoLab G3 FIB/SEM system was used. First, ca. 300 nm of platinum were deposited as a protection layer on the surface of a particle by electron beam induced deposition, then a second layer of ca. 700 nm platinum was deposited by focused ion beam deposition. Afterwards, the lamella was cut, transferred to a TEM grid via a micromanipulator and subsequently thinned to less than 100 nm from both sides by 30 kV ion beam treatment. Finally, the lamella was cleaned by low ion beam voltage at 5 keV and 2 keV in sequence to reduce the thickness of the amorphous damage layer.

**X-ray Photoelectron Spectroscopy** XPS spectra were recorded at room temperature using non-monochromatised Al  $K_{\alpha}$  (1486.6 eV) excitation and a hemispherical analyser (PHOIBOS 150, Specs). The binding energy scale was calibrated by the standard Au 4f<sub>7/2</sub> and Cu 2p<sub>3/2</sub> procedure. The elemental composition was determined using the theoretical cross sections from Yeh and Lindau.<sup>[206]</sup>

#### 4.2.3 Anode preparation and electrochemical tests

**Anode preparation** For the preparation of electrodes, polyacrylic acid (PAA,  $\leq 0.5$  % benzene, Sigma-Aldrich) was dispersed in an ethanol (Sigma-Aldrich) : 2-propanol ( $\geq 99.5$  %, Carl Roth) (6.25:1) mixture and stirred for 15 h. Then, carbon black (CB) (Super Conductive P, Alfa Aesar) and the ground sample were added (PAA : CB : sample = 1 : 1.5 : 10), stirred and treated in an ultrasonic bath. The prepared slurry was cast as a thin film on a 25  $\mu\text{m}$  thick copper foil (Cu58, bare, Schlenk) using a ZUA 2000 universal applicator (Zehntner) or a 4-sided film applicator (VF2169-013, 60 mm, TQC), respectively set to a film thickness of 120  $\mu\text{m}$ . Subsequently, the film was dried for 15 h at 80 °C in a vacuum oven (VTR 5022, Heraeus). Hereafter, anodes of 10 mm in diameter were punched out using a lever press, weighed and stored in an argon filled glovebox (mBraun B790, O<sub>2</sub>  $\leq 1$  ppm Ionic System Trace Oxygen Sensor Tos 3.0). The reference anodes with silicon nanoparticles were produced under the same conditions using a mixture of KS6 and silicon nanopowder (Hongwu international group Ltd). Solely the carbon black reference slurry was prepared differently by adding 8.7 mg PAA to 2.9 ml N-Methyl-2-pyrrolidone ( $\geq 99.8$  %, Carl Roth) and stirring for 1 h. Subsequently, 100 mg of CB were added, the mixture was stirred and cast on the copper foil. Then, the film was dried for 15 h at 80 °C in a vacuum oven (Heraeus Vacutherm, Thermo Scientific).

**Electrochemical testing** For the two electrode battery system, a modified stainless steel Swagelok tube fitting was electrically insulated by a one-way 75  $\mu\text{m}$  Kapton foil (Dr. Dietrich Müller GmbH). The working electrode and counter electrode (metallic lithium, 10 mm diameter, Xiamen Tob New Energy Technology Co.) were sandwiched with two 25  $\mu\text{m}$  thick separators (C2500, Celgard Inc., USA) in between and wetted with 140  $\mu\text{l}$  of a solution of 1 M LiPF<sub>6</sub> dissolved in a mixture of ethylene carbonate : diethyl carbonate 1 : 1 wt.-% (Selectilyte LP40, Battery grade, BASF) electrolyte. The battery cell was sealed with nylon ferrules (Swagelok) on both sides inside the argon filled glovebox. Electrochemical measurements were carried out

using an Arbin Instruments BT2000 battery tester or a Biologic MPG-2 battery cycler. The regular cycling protocol with differential capacity analysis in the 1<sup>st</sup>, 2<sup>nd</sup> and 103<sup>rd</sup> cycle is given in table 4.2 and the C-rate variation protocol without CV-sequences in table 4.3.

**Table 4.2:** Cycling protocol

cycle	current (C-rate)	final lithiation potential (V)	CV-sequence (min)	final delithia- tion potential (V)	CV-sequence (min)
1-2	C/20	0.005	90	2	60
3-102	C	0.005	90	2	60
103	C/20	0.005	90	2	60

**Table 4.3:** Current rate (C-rate) variation protocol applied between 5 mV and 2 V

cycle	1 - 10	11 - 20	21 - 30	31 - 40	41 - 50	51 - 60
C-rate	C/10	C/5	C	5 C	10 C	C/10

To calculate the gravimetric capacities of the anode materials the measured capacities were divided by the mass of the active material. Since the weight of the copper foil varies strongly while the mass of active material varies only slightly due to the casting process, the mass of the active material could not be accurately determined by weighing of the entire anode. Therefore, except for occasional cases, the precise investigation of the gravimetric capacity was accomplished as follows. For new anode materials with unknown gravimetric capacity, the theoretical capacity was calculated based on  $372 \text{ mAh} \cdot \text{g}^{-1}$  gravimetric capacity for graphite and  $3579 \text{ mAh} \cdot \text{g}^{-1}$  for silicon. The anode was cycled following the protocol in table 4.2 with the current congruous with the theoretical 1C C-rate, employing 50 instead of 100 cycles. Afterwards, the anode was dismounted, washed and the active material was removed by ultrasonification in ethanol. The left-over copper foil was weighed and the difference to the anode weight prior to cycling, i.e. the amount of removed material, was set off against the binder and thereby resulted in the amount of active material including graphite, silicon and carbon black. The gravimetric discharge capacities of the subsequently cycled anodes were then pinned in the 5<sup>th</sup> cycle to the same gravimetric discharge capacity as the previously dispersed anode. This procedure is illustrated for CB and graphite in the SI (fig. 8.9). Samples were exempted from this procedure when they were not used for post-mortem analysis, in this case the weight of the active material was directly determined by dissolving the anode material. For evaluation of the capacity normalised per silicon and averaged over 100 cycles the scattered capacity outliers were linearly interpolated, before the discharge capacities were added over 100 cycles and normalised for cycle and wt.-% silicon.

#### 4.2.4 Post-mortem analysis

After electrochemical testing the batteries were disassembled inside the argon filled glove box, with the anodes being in the delithiated state. Then, the anodes were washed successively in four flasks filled with 3 ml DEC ( $\geq 99\%$ , anhydrous, Sigma Aldrich) each and prepared for the respective analysis method (SEM, FIB and XPS) on transfer holders which provide an airtight seal.

**Scanning Electron Microscopy** SEM images were acquired on a Hitachi S-4800 microscope using 1.5 kV accelerating voltage and 3 – 4 mm working distance. The anodes were mounted on conductive carbon tape (Plano) on a transfer holder. Energy dispersive X-ray (EDX) analysis was performed using a silicon drift detector (SDD).

**Focused Ion Beam** For the preparation a Helios NanoLab G3 FIB/SEM system was used. First, ca. 500 nm of platinum were deposited as a protection layer on the surface of a cycled anode by electron beam induced deposition, then a second layer of ca. 1000 nm platinum was deposited by focused ion beam deposition. Subsequently, a bigger section of the material was removed by FIB to have a view on the cross-section of the cycled anode.

**X-ray Photoelectron Spectroscopy** XPS spectra were recorded at room temperature using non-monochromatised Al  $K_{\alpha}$  (1486.6 eV) excitation and a hemispherical analyser (PHOIBOS 150, Specs). The binding energy scale was calibrated by the standard Au 4f<sub>7/2</sub> and Cu 2p<sub>3/2</sub> procedure. The elemental composition was determined using the theoretical cross sections from Yeh and Lindau.<sup>[206]</sup>

### 4.3 Results and discussion

#### 4.3.1 Characterisation of the graphite-silicon nanocomposite

The proper quantification of the silicon content of the graphite-silicon nanocomposites is of significant relevance to grade the samples reliably. Therefore, the silicon loading was evaluated by two distinct methods: thermogravimetry coupled with mass spectrometry (TG-MS) and elemental analysis (EA). For all samples, TG-MS showed a mass loss at around 650 – 675 °C with a corresponding CO<sub>2</sub> signal (SI fig. 8.10 and 8.11), caused by the burning of the graphite substrate. The samples reach the mass minimum at around 760 – 815 °C followed by a subsequent increase. This increase can be attributed to the oxidation of the deposited silicon to SiO<sub>2</sub>. This assumption was supported by XRD and SEM/EDX analysis of the TG-MS exit sample of G-550C-22% Si, which showed no significant carbon signal and clear reflections of cristobalite (SI fig. 8.12). Assuming that all silicon is oxidised and with disregard of the initial oxidation layer on the silicon surface, the silicon content can be estimated by  $m(\%)_{\text{Si}} = \frac{m(\%)_{\text{TG}}}{M_{\text{SiO}_2}} \cdot M_{\text{Si}}$ , with  $m(\%)_{\text{TG}}$  being the final mass evaluated by TG-MS and  $M_{\text{Si}}$  and  $M_{\text{SiO}_2}$  being the molar

masses of silicon and  $\text{SiO}_2$ , respectively. The resulting silicon contents are compared to the results from EA in figure 4.2 a) and the values are listed in table 8.2 in SI. The silicon content of the nanocomposites increases proportionally with the deposition time and is independent of the deposition temperature between 485 °C and 550 °C. For example, depositions at 550 °C for 30, 60, 120 and 180 min lead to a silicon content of 8, 13, 22 and 30 wt.-%, respectively. In good agreement with this, depositions at 485 °C for 60, 120 and 180 min result in a silicon content of 11, 22 (or 19) and 30 wt.-%. For temperatures below 485 °C the deposition rate decreases significantly and also the linear correlation between deposition time and silicon content deviates strongly, such that depositions at 450 °C for 120, 180 and 240 min gave 18, 27 and 30 wt.-% silicon content. As can be seen from the comparison of the masses derived from TG-MS and EA (fig. 4.2 b), both methods are in good agreement up to 20 wt.-% silicon content. On average, the TG-MS method gives slightly higher silicon contents, however, only in a significant scale for higher silicon contents exceeding 27 wt.-%. This is probably due to two effects, firstly, the aforementioned initial silicon oxidation layer and secondly, insufficient graphite burning. The silicon content is also integrated in the sample name, for example silicon deposited at 550 °C for 1 h, resulting in 14.6 wt.-% silicon determined by TG-MS analysis and 12.7 wt.-% silicon determined by EA is named G-550C-13% Si.

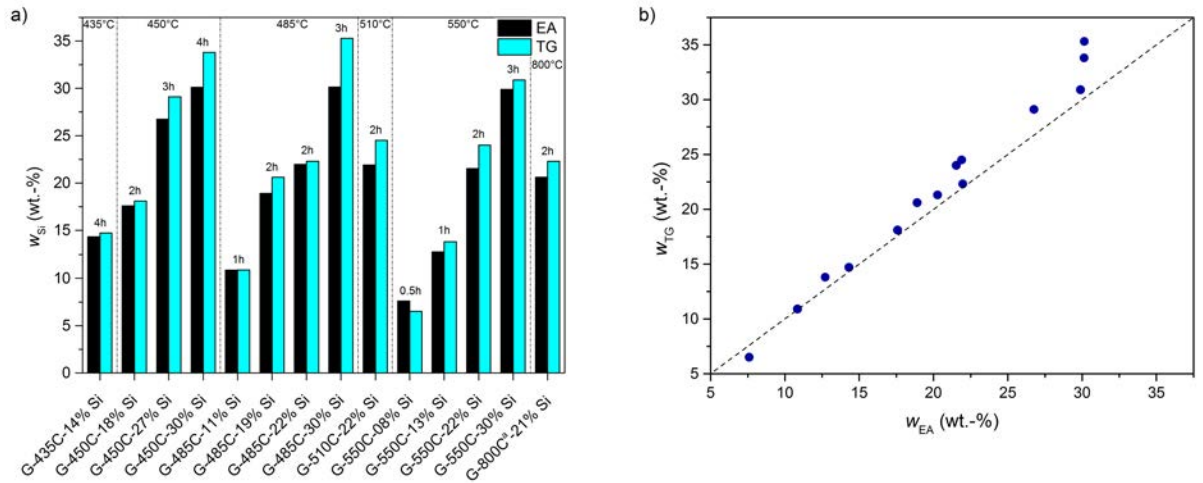


**Figure 4.2:** Graph of a) silicon content according to TG-MS and EA analysis for respective samples; b) silicon content according to TG-MS as a function of the silicon content according to EA.

For the following evaluations the samples are divided into four series, namely silicon depositions A: at 550 °C for 30 – 180 min resulting, in 8 – 30 wt.-% silicon, B: at 485 °C for 60 – 180 min, resulting in 11 – 30 wt.-% silicon, C: between 435 – 550 °C, resulting in ~13 wt.-% silicon and D: between 450 – 550 °C, resulting in ~21 wt.-% silicon (table 4.4). Series B contains a replica, namely G-485C-19% Si, which was synthesised using identical deposition parameters as for G-485C-22% Si, to evaluate the reproducibility of the method. The series C and D in addition contain reference samples consisting of mixtures of graphite and silicon nanoparticles

(Si NPs) with 13 and 20 wt.-% silicon, respectively. To investigate the impact of the anchoring of the deposited silicon on the graphite surface, a "bridging" sample synthesised by LPCVD but more similar to the Si NPs in regard to morphology and crystallinity is also introduced here. The silicon was deposited at 485 °C for two hours and was subsequently annealed at 800 °C (G-800C<sup>a</sup>-21% Si).

**Table 4.4:** Sample series

series	characteristic	series	characteristic
A	$t = 30 - 180$ min at 550 °C 8 – 30 wt.-% Si	C	$T = 435 - 550$ °C ~13 wt.-% Si
B	$t = 60 - 180$ min at 485 °C 11 – 30 wt.-% Si	D	$T = 450 - 550$ °C ~21 wt.-% Si

To evaluate the crystallinity of the deposited silicon, X-ray diffractometry was carried out for the deposition series A – D. In fig. 4.3 a) the XRD patterns for samples with silicon deposited at 550 °C for 30, 60, 120 and 180 min are shown (series A). All diffractograms reveal crystalline silicon reflections, which increase with increasing deposition time. Rietveld refinement indicates that the average crystallite size for all four samples is similar and that the ratio of crystalline to amorphous silicon is solely significantly increased for the G-550C-30% Si sample (SI fig. 8.13). Hence, the continuous increase of the silicon reflection intensities mainly reflects the increasing total silicon content. For depositions at 485 °C for 60, 120 and 180 min (series B), illustrated in fig. 4.3 b), independent of the deposition time all samples are XRD amorphous, only showing a slight shoulder at the angle where the *Si* 111 reflection would appear.

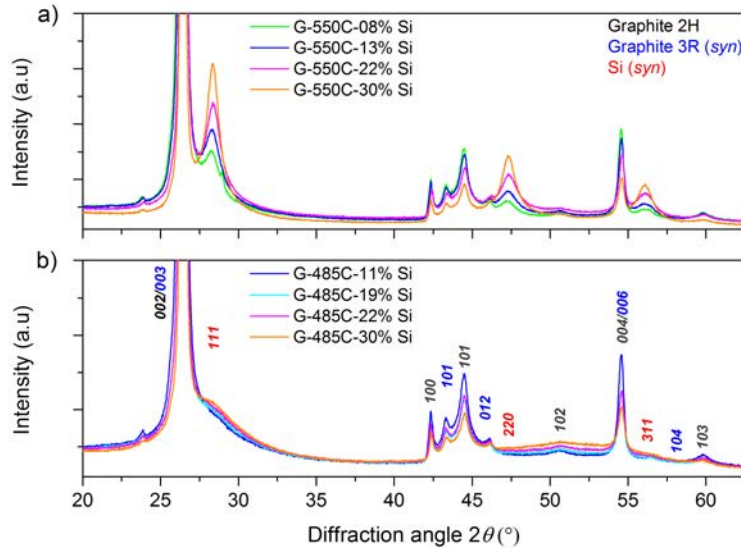


**Figure 4.3:** Powder XRD patterns of sample series a) A and b) B.

In agreement with this observation, the diffraction patterns in the figures 4.4 a) and b) for the varied temperature series C and D depict XRD amorphous patterns for all samples with silicon deposited below 510 °C for both 13 and 21 wt.-% silicon loading. Additionally, the diffraction

pattern of a graphite/Si NP mixture with 21 wt.-% Si NPs is shown in figure 4.4 b). Compared to the samples with the highest deposition temperature, namely 550 °C, the graphite/Si NP mixture shows significantly more distinct silicon reflections. However, to evaluate whether the direct connection of the silicon to the graphite substrate affects the battery performance, all other properties, such as crystallinity, should be as similar as possible. The annealed sample (G-800C<sup>a</sup>-21% Si) meets this requirement. Its diffraction pattern is very similar to the one of the graphite/Si NP mixture. From the Rietveld refinement of the crystalline samples of series D it turns out that by increasing the deposition temperature from 510 °C to 550 °C the average crystallite domain size remains constant, while the crystalline volume fraction increases significantly. For the annealed sample (G-800C<sup>a</sup>-21% Si) both the evaluated silicon domain size and the crystalline volume fraction increased substantially, which indicates a significant increase of the average silicon crystallite domain size.

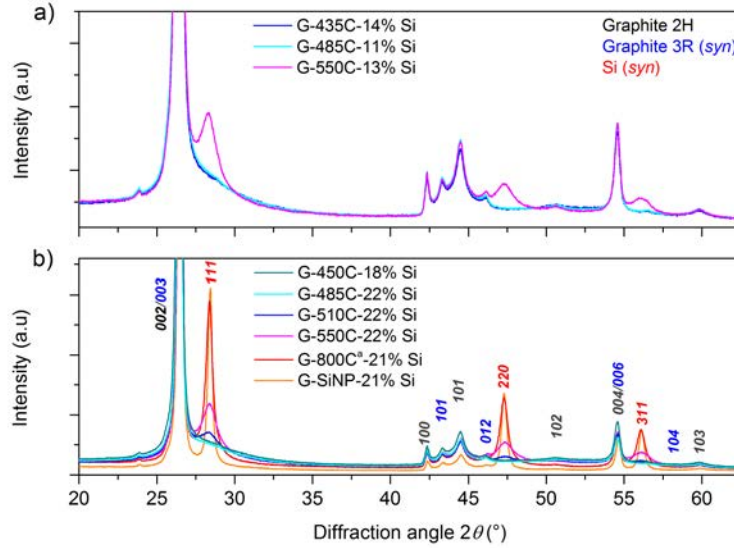


**Figure 4.4:** Powder XRD patterns of sample series a) C and b) D with additional G-800C<sup>a</sup>-21% Si and G/Si NP mixture (G-SiNP-21% Si).

Additionally, Raman analysis was carried out for the sample series A and D to verify the silicon crystallinity inferred from XRD analysis. In fig. 4.5 a) the Raman spectra of silicon depositions at 550 °C (series A) for 30, 60, 120 and 180 min is depicted. Comparable to the results from XRD analysis, an increase in the silicon crystallinity with increasing deposition time can also be deduced from the Raman spectra. This is indicated by a reduction of the TA, LA and LO bands with increasing deposition time. These bands are characteristic for a-Si.<sup>[207,208]</sup> The TO band can be deconvoluted into three Gaussian components, namely the a-Si contribution (460-490 cm<sup>-1</sup>), the intermediate component from grain boundaries (500 cm<sup>-1</sup>) and the TO mode of silicon crystal grains of different sizes (512-520 cm<sup>-1</sup>).<sup>[207,209,210]</sup> With increasing silicon content, caused by longer deposition time, the TO band sharpens indicating that the amorphous and intermediate contributions decrease. In fig. 4.5 b) the Raman spectra of series D are depicted.

All samples exhibit a silicon content around 21 wt.-% while the applied deposition temperature varies from 450 – 550 °C. Also, the spectra of the annealed sample (G-800C<sup>a</sup>-21% Si) and the Si NPs are shown. At deposition temperatures below 510 °C only bands of a-Si (TA, LA, LO) appear, while at 510 °C the crystalline fraction of the TO band starts to form at 515 cm<sup>-1</sup>. For 550 °C deposition temperature the contributions of a-Si decrease further, while the TO band becomes sharper and more pronounced. The Raman spectra of the annealed sample (G-800C<sup>a</sup>-21% Si) and the Si NPs are very similar. Both exhibit no a-Si bands, but a clear sharp TO band, indicating the existence of pure c-Si, and additional bands around 305 and 942 cm<sup>-1</sup>. These are attributed to the multiphonon 2TA and 2TO Raman bands of c-Si.<sup>[211–213]</sup> In conclusion, the trends derived from XRD analysis go well in line with the results from Raman spectroscopy. For increasing deposition times at 550 °C, the measurable crystallinity of the silicon increases with the silicon content. Moreover, at deposition temperatures below 510 °C only a-Si and for higher temperatures a mixture of c-Si and a-Si is deposited. A crystallinity similar to the one of the Si NPs was only achieved by thermal annealing of the silicon deposit.

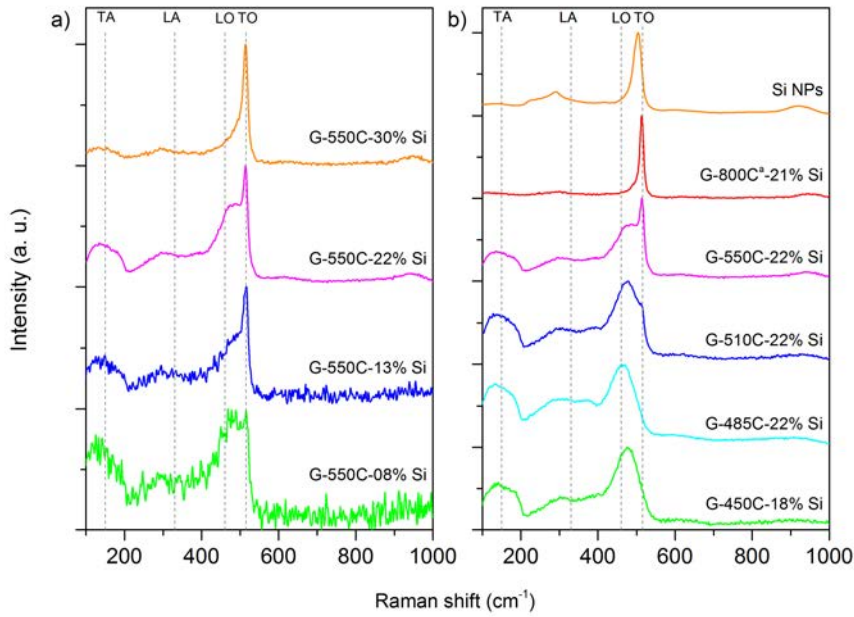


**Figure 4.5:** Raman spectra normalized to TO-band of sample series a) A and b) D with additional spectra of G-800C<sup>a</sup>-21% Si and Si NPs. For full range spectra see SI (fig. 8.14).

The SEM images in figure 4.6 depict graphite flakes (fig. 4.6 a) with silicon deposited at 435 – 550 °C leading to silicon contents from 8 – 30 wt.-% (fig. 4.6 b-k). It is notable that the silicon deposited on the graphite basal planes forms nanodroplets, while the silicon deposited on the graphite edges looks denser and therefore film-like (fig. 4.6 c, d and h). For the samples deposited at 550 °C with 8, 13, 22 and 30 wt.-% silicon content (series A, fig. 4.6 g-k) the captured images illustrate that the graphite surface is increasingly covered with silicon droplets with increasing silicon content. When a silicon content of 30 wt.-% is reached, continuous layers of silicon droplets are observed for deposition temperatures of 550 and 485 °C (fig. 4.6 f



and k). In general, no difference for varied silicon deposition temperature is perceptible using SEM analysis. However, sintering of the silicon droplets is found for the annealed sample (G-800C<sup>a</sup>-21% Si, fig. 4.6 l). This sample exhibits both very small and big silicon droplets, with the latter ones being in the dimension of the reference Si NPs (fig. 4.6 m). This observation goes in line with the observed similarities of the annealed sample and the Si NPs regarding the silicon crystallinity in Raman and XRD analysis. Further SEM images at lower magnification are given in the SI (fig. 8.15).

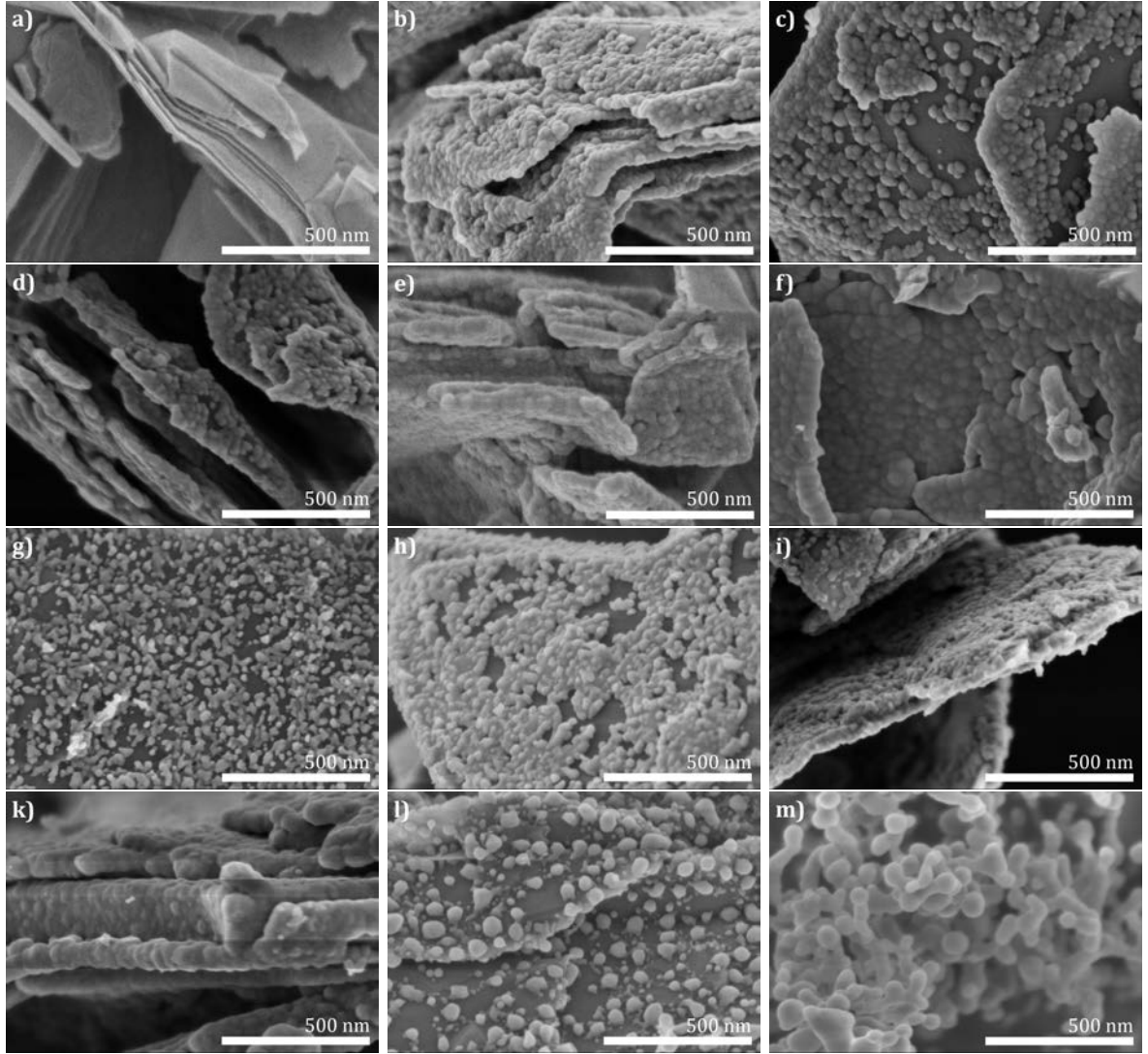


**Figure 4.6:** SEM images of a) G, b) G-435C-14% Si, c) G-450C-18% Si, d) G-485C-19% Si, e) G-485C-22% Si, f) G-485C-30% Si, g) G-550C-08% Si, h) G-550C-13% Si, i) G-550C-22% Si, k) G-550C-30% Si, l) G-800C<sup>a</sup>-21% Si and m) Si NPs.

To gain a better insight into the graphite-silicon interface, a TEM cross section of the sample G-485C-22% Si was prepared using FIB technique. TEM images of the cross section (fig. 4.7) reveal a layered structure of graphite with an a-Si coverage of about 20 nm thickness. Again, the silicon deposit exhibits the shape of partially connected droplets on the basal planes of the

graphite, while on the edges and kinks the silicon forms a continuous layer. This agrees well with the results from SEM analysis. The STEM image (fig. 4.8 a) exposes that the silicon droplets are definite from the graphitic substrate. This is supported by single element maps of C and Si (fig. 4.8 c and d) revealing the elemental distribution. Moreover, the oxygen map indicates an oxidation layer on the silicon droplets, which is caused by air exposure of the sample (fig. 4.8 e).

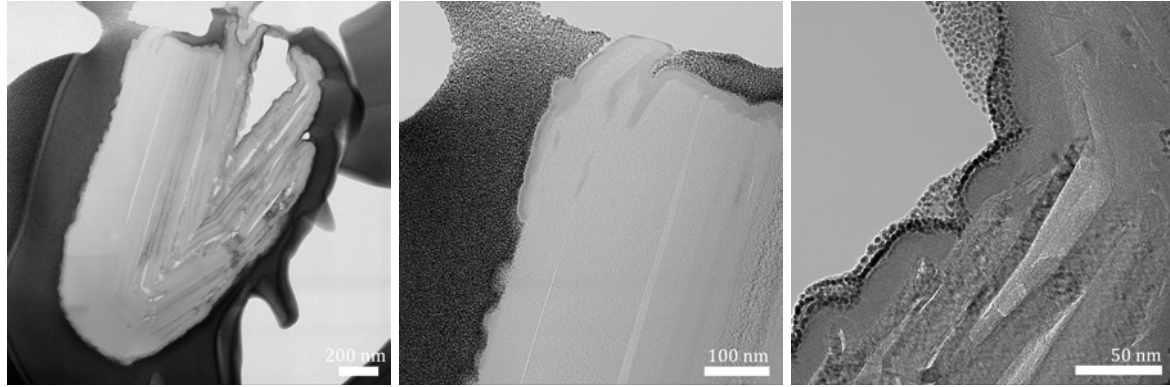


**Figure 4.7:** BF-TEM images of the G-485C-22% Si cross section.

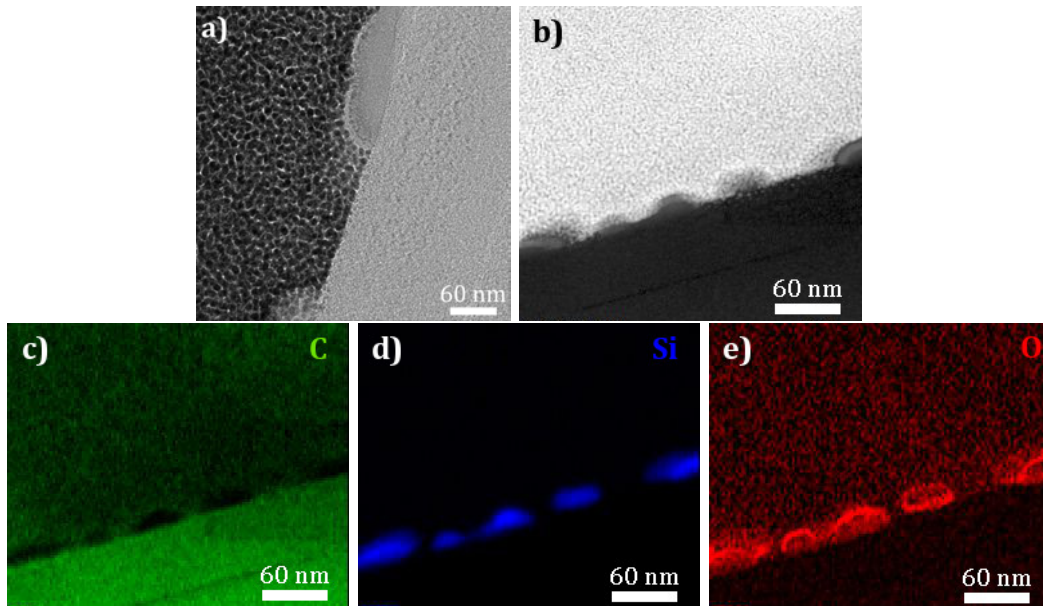


**Figure 4.8:** a) HRTEM image, b) HAADF image and STEM-EDX single element maps for c) carbon, d) silicon and e) oxygen of the G-485C-22% Si cross section.

Altogether silicon was effectively deposited on graphite flakes with the silicon crystallinity and content being reproducibly controlled by the deposition time and temperature. The silicon was deposited in droplets on the graphite basal planes, layer-like on the graphite edges and covered by a thin oxidation layer due to air exposure.

### 4.3.2 Electrochemical investigation of the anode materials

All anode materials were cycled with the "cycling protocol" and the "C-rate variation protocol" as described in the experimental section. Since all anodes contain graphite as deposition substrate and CB added in the slurry, pure CB anodes and reference graphite anodes were cycled as references. From the cycling data (SI fig. 8.9), a gravimetric capacity of  $254 \text{ mAh} \cdot \text{g}^{-1}$  is calculated for CB, resulting in  $346 \text{ mAh} \cdot \text{g}^{-1}$  for the graphite reference material including CB. The evaluated capacity of the graphite reference material is close to the theoretical gravimetric capacity of graphite of  $372 \text{ mAh} \cdot \text{g}^{-1}$ .<sup>[153]</sup>

#### Influence of the deposition time and temperature on the battery performance during cycling

Graphite without (G) and with silicon deposition at  $550^\circ\text{C}$  for 30 min (G-550C-08% Si), 60 min (G-550C-13% Si), 120 min (G-550C-22% Si) and 180 min (G-550C-30% Si) were cycled to determine the influence of the silicon deposition time on the battery performance. The resulting gravimetric discharge capacities and coulombic efficiencies (CEs) of the batteries and their replica are shown in figure 4.9. The reference graphite sample cycles steadily at a gravimetric discharge capacity of  $346 \text{ mAh} \cdot \text{g}^{-1}$ . With increasing silicon content the gravimetric capacity is increased in the first cycles, however, with increasing cycle number the capacity decays for the silicon containing samples, so that finally after 100 cycles nearly all samples meet the gravimetric capacity of the graphite reference. Moreover, the 22 and 30 wt.-% silicon containing samples show additional outliers in the gravimetric capacity, which exceed the actual gravimetric capacity of the material significantly. These outliers are caused either by a continuous current flow in the delithiation constant voltage protocol sequence (at 2 V) or by the failure to reach the 2 V border within the constant current protocol sequence. As a consequence, the current then is applied until a safety cutoff is initiated after 2 – 3 hours. It can be seen from the replica that these outliers are not reproducible and do not have a significant influence on the overall cycling performance of the battery. Another interesting feature of the batteries is the capacity change in the 103<sup>rd</sup> cycle compared to the 102<sup>nd</sup> cycle. The 103<sup>rd</sup> cycle is, just like the 1<sup>st</sup> and 2<sup>nd</sup> cycle, run at a lower current rate (C-rate), namely C/20 instead of 1C. The capacity is higher in the 103<sup>rd</sup> cycle than in the 102<sup>nd</sup>, while the first two cycles do not show an increased capacity compared to the 3<sup>rd</sup> cycle. This could have two reasons. On the one hand, the applied C-rate is constant over cycling and determined for the initial capacity of the battery. With continuous capacity loss the amount of active material decreases, which leads to real C-rates of up to  $\sim 2\text{C}$  for the higher cycle numbers, which could be too fast for appropriate (dis-)charging. On the other hand, the kinetics of the active material lithiation might change over cycling, such that thorough lithiation can only occur when charging more slowly. Moreover, it is noteworthy that the graphite reference battery exhibits lower CE values in the first cycles. With increasing silicon loading the samples show not only over-all lower CE values but also a

different distribution over the cycle number accumulating to a significant CE minimum from cycle 20 – 30 for G-550C-30% Si.

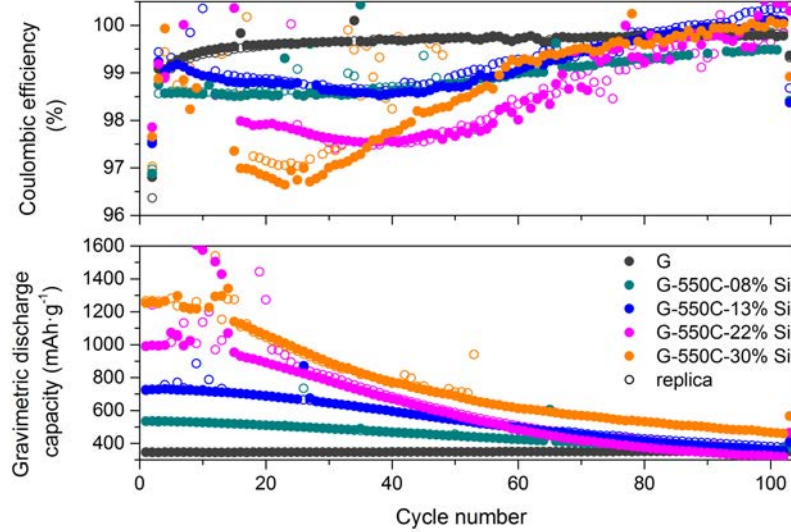


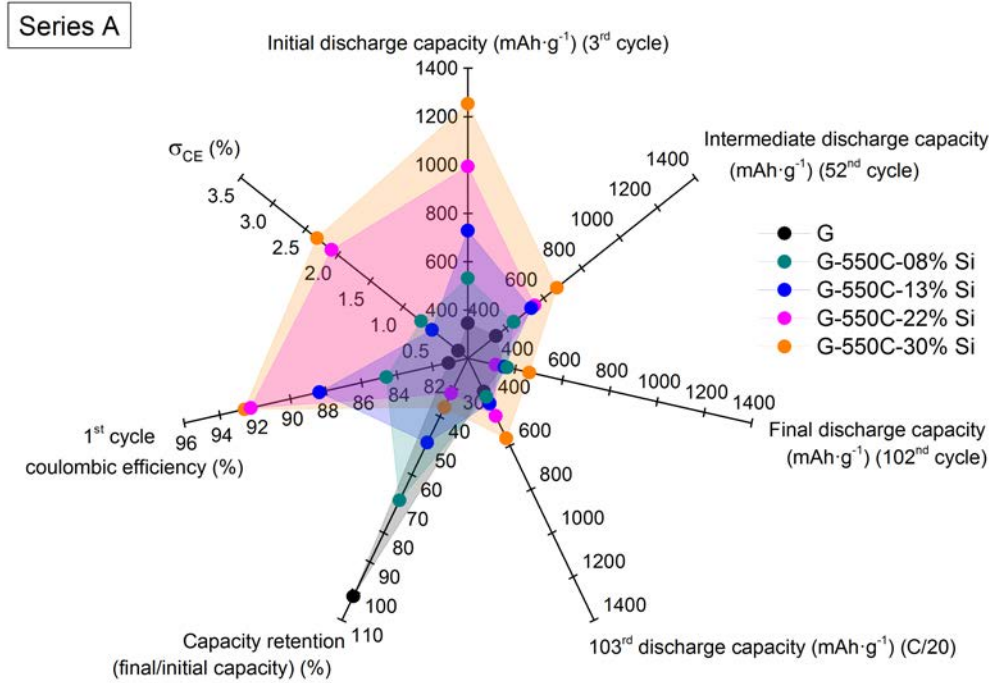
**Figure 4.9:** Gravimetric discharge capacity and CE as a function of the cycle number for batteries containing anodes obtained from silicon deposited at 550 °C for 30 – 180 min (series A).

In order to facilitate the comparison of these samples, seven performance metrics, listed in table 4.5, were chosen to represent the battery performance in radar plots. By comparing the 3<sup>rd</sup>, 52<sup>nd</sup> and 102<sup>nd</sup> cycle gravimetric discharge capacity the capacity fade can be evaluated more precisely. These axes illustrate how much capacity is provided by the battery in the beginning and how much is lost after 50 and 100 cycles. Matching the 102<sup>nd</sup> and 103<sup>rd</sup> cycle gravimetric discharge capacity indicates how strongly the battery capacity depends on the applied C-rate after the electrochemical testing. The capacity retention (CR) is the ratio of the final to the initial capacity and therefore is a direct indication for how much capacity is lost over cycling. The 1<sup>st</sup> cycle CE gives the amount of charges lost in the very first cycle at C/20 and therefore reveals differences in the reaction of the fresh anode material with the electrolyte. The standard deviation of the CE ( $\sigma_{\text{CE}}$ ) was derived from the CE generated at 1C, excluding all CE outliers above 120 %. It illustrates the steadiness of the CE over cycling. Higher  $\sigma_{\text{CE}}$  values are an indication for either outliers in the CE or occurring local decays in the CE.

The radar plot resume for figure 4.9 is given in figure 4.10. Comparing initial, intermediate and final discharge capacity reveals that the capacity decay is stronger exhibited in the first half of the cycling than in the second half. Moreover, the 103<sup>rd</sup> cycle discharge capacity shows that after the cycling test the batteries with higher silicon content still provide higher capacities, but significantly less pronounced. The capacity re-increase in the 103<sup>rd</sup> cycle indicates that the losses in the final capacity are not exclusively caused by irreversible material degradation, but also kinetic hindrance of the (de-)lithiation process.

**Table 4.5:** Overview over radar plot axes

axis	information
3 <sup>rd</sup> cycle gravimetric discharge capacity	initial gravimetric discharge capacity at 1C
52 <sup>nd</sup> cycle gravimetric discharge capacity	intermediate gravimetric discharge capacity at 1C
102 <sup>nd</sup> cycle gravimetric discharge capacity	final gravimetric discharge capacity at 1C
103 <sup>rd</sup> cycle gravimetric discharge capacity (C/20)	influence of the C-rate on the capacity after the cycling test
capacity retention (CR)	ratio of discharge capacity in 102 <sup>nd</sup> to 3 <sup>rd</sup> cycle
1 <sup>st</sup> cycle CE	loss of charges in the very first cycle at C/20
$\sigma_{CE}$	illustrates steadiness of CE at 1C


**Figure 4.10:** Radar plots of the performance of batteries containing anodes from silicon deposited at 550 °C for 30, 60, 120 and 180 min, leading to 8, 13, 22 and 30 wt.-% silicon content (series A).

The proportionality to the silicon content suggests that silicon is involved in these processes. Despite the fact that the capacity of the G-550C-30% Si battery maintained highest over the whole cycling, the capacity retention (CR) reveals that its capacity decay is comparatively high. The G-550C-08% Si and G-550C-13% Si batteries provide significantly higher CRs, however, they are still significantly lower than the graphite reference battery CR. The 1<sup>st</sup> cycle CE increases with increasing silicon loading, which goes well in line with graphite being known to have a very low 1<sup>st</sup> cycle CE due to SEI formation<sup>[147,200]</sup>. Hence, this correlation can be attributed to the fact that with increasing silicon content also the coverage of the graphite surface with silicon is increased, as depicted by the SEM images (fig. 4.6). The increased 1<sup>st</sup> cycle

CE represents the reduced SEI formation due to the smaller graphite-electrolyte interface. On the contrary, the standard deviation of the CE ( $\sigma_{CE}$ ) was larger for higher silicon loadings, caused firstly by an increased incidence of outliers and secondly by a stronger pronounced CE minimum.

The electrochemical evaluation for the series deposited at 485 °C (series B) for 60 min (G-485C-11% Si), 120 min (G-485C-19% Si and G-485C-22% Si) and 180 min (G-485C-30% Si) is depicted in figure 4.11. The cycling raw data can be found in the SI (fig. 8.16 a). The sample G-485C-19% Si is a reproduction of G-485C-22% Si, meaning they were synthesised using the same deposition parameters to verify the reproducibility of the method. Except for the differing silicon content of 3 wt.-%, which entails a corresponding difference in the gravimetric capacity, the respective batteries perform similarly. In comparison to series A the series B shows similar trends. Specifically, the initial gravimetric discharge capacity increases proportionally with the silicon content, the capacity decay is more pronounced in the first than in the second half of the cycling, the 103<sup>rd</sup> cycle discharge capacity increases with the silicon content, the CR is higher and the 1<sup>st</sup> cycle CE and  $\sigma_{CE}$  are lower for lower silicon contents.

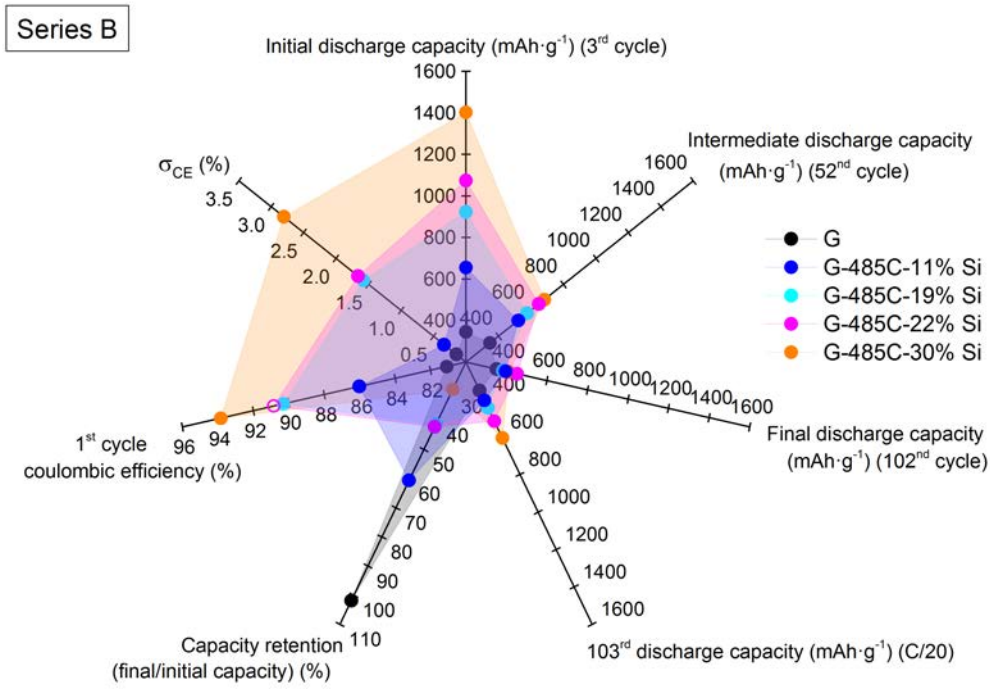


**Figure 4.11:** Radar plots of the performance of batteries containing anodes from silicon deposited at 485 °C for 60, 120 and 180 min, leading to 11, 19, 22 and 30 wt.-% silicon content (series B). The 1<sup>st</sup> cycle CE for G-485C-22% Si was taken from a replica battery.

The radar plots in figure 4.12 depict the electrochemical performance of series C, which includes batteries containing anodes obtained from silicon depositions at 435 (G-435C-14% Si), 485 (G-485C-11% Si) and 550 °C (G-550C-13% Si), resulting in ~13 wt.-% silicon content. Additionally, reference anodes from a mixture of graphite and Si NPs (G-SiNP-13% Si) were evaluated. The



cycling raw data can be found in the SI (fig. 8.16 b). The initial discharge capacities are similar, solely the G-485C-11% Si battery provides a slightly lower capacity, which can be attributed to the lower silicon content. As observed for the series A and B, the capacity decay is stronger for the first half of the cycling than the second half. The final discharge capacity is highest for the G-SiNP-13% Si and G-485C-11% Si batteries, which is also visible in the higher CRs. The similar CRs for the G-485C-11% Si and the G-SiNP-13% Si batteries implies that the superior final discharge capacity of the G-SiNP-13% Si battery is rather caused by the higher silicon content, than by a superior stability. The differences in the final capacity are small and further decreased when the C-rate is reduced to C/20 in the 103<sup>rd</sup> cycle. This indicates that the differences in the final capacity are not exclusively caused by irreversible material degradation, but also kinetic hindrance of the (de-)lithiation process. The measured 1<sup>st</sup> cycle CE is in good agreement with the previously observed trend of increasing 1<sup>st</sup> cycle CE values for higher graphite surface coverage. The batteries containing materials with higher silicon loadings provide a higher 1<sup>st</sup> cycle CE, while the G-SiNP-13% Si battery provides a lower 1<sup>st</sup> cycle CE compared to the G-550C-13% Si battery containing the CVD anode with similar silicon content. This can be attributed to the fact that the graphite surface is not continuously covered by the Si NPs to the same extent as it is by the deposit. The high  $\sigma_{CE}$  of the G-345C-14% Si battery is caused by unsteady cycling as can be seen from the raw data. Regarding the other samples the  $\sigma_{CE}$  increases with increasing silicon content and crystallinity.

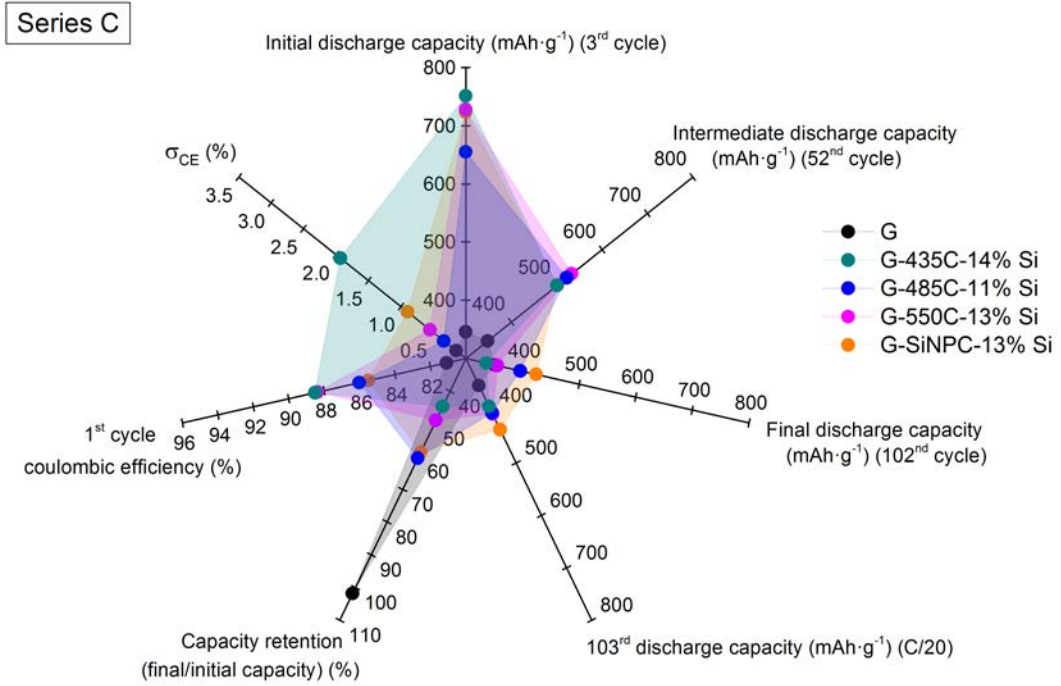


**Figure 4.12:** Radar plots of the performance of batteries containing anodes from silicon deposited at 435 °C, 485 °C and 550 °C, resulting in ~13 wt.-% silicon content (series C) and additionally a graphite/Si NP mixture with 13 wt.-% silicon.

The radar plots (fig. 4.13) of series D reveal clearer trends. The figure includes batteries containing anodes with a silicon content of  $\sim 21$  wt.-% deposited at 450 (G-450C-18% Si), 485 (G-485C-22% Si), 510 (G-510C-22% Si) and 550 °C (G-550C-22% Si). Moreover, also a reference anode produced from a mixture of graphite and 20 wt.-% Si NPs (G-SiNP-20% Si) and the annealed sample (G-800C<sup>a</sup>-21% Si) anode are included in this radar plot resume. The respective raw data is depicted in the SI (fig. 8.17). In contrast to series C, in this series the initial gravimetric capacity decreases with increasing silicon crystallinity. Sole exception is the G-450C-18% Si battery, providing the lowest initial capacity. However, this can be attributed to the significantly lower silicon content. The G-485C-22% Si battery provides the highest intermediate, final and 103<sup>rd</sup> discharge capacity. Despite the minor differences between the individual batteries, batteries containing anodes with crystalline silicon tend to perform poorer. The same applies to the CR. For this series, too, the capacity re-increases and differences between the batteries nearly vanish when the C-rate is decreased to C/20 in the 103<sup>rd</sup> cycle. As observed for series C, the battery containing the Si NP anode provides, with a slight distance, the lowest 1<sup>st</sup> cycle CE, while for the other batteries the differences are small and the order does not follow a clear trend. The  $\sigma_{CE}$  shows high values for the Si NP sample and the annealed sample due to a substantial and reproducible CE loss in the first 20 – 40 cycles visible in the raw data. This loss is presumably dependent on the crystallinity and particle size, which were shown to be similar for these two samples using XRD, Raman and SEM. In contrast, the high  $\sigma_{CE}$  for the G-550C-22% Si battery is caused by unsteady cycling as can be deduced from the raw data.

To give an overview of how much current the samples could accumulate over 100 cycles, the discharge capacities were added over 100 cycles and normalised for cycle and wt.-% silicon. Taking into consideration that the capacity outliers do not affect the overall cycling performance of the batteries, they were linearly interpolated. The results are listed in the SI (table 8.3). The resulting contour plot (fig. 4.14) illustrates how much capacity was provided per silicon averaged over 100 cycles subject to the silicon content and the deposition temperature, with darker regions marking high and brighter regions indicating lower capacities. Maxima of the capacity are revealed for the samples with amorphous silicon deposited at 485 °C. The batteries G-485C-11% Si and G-485C-22% Si provide  $1616$  and  $1536 \text{ mAh} \cdot \text{g}_{\text{Si}}^{-1}$ , respectively. Minima of the capacity are found for batteries containing crystalline silicon deposited at 550 °C or annealed silicon. More precisely the batteries G-550C-08% Si and G-550C-22% Si, and G-800C<sup>a</sup>-21% Si provided only  $1198$ ,  $1147$  and  $1112 \text{ mAh} \cdot \text{g}_{\text{Si}}^{-1}$ , respectively.



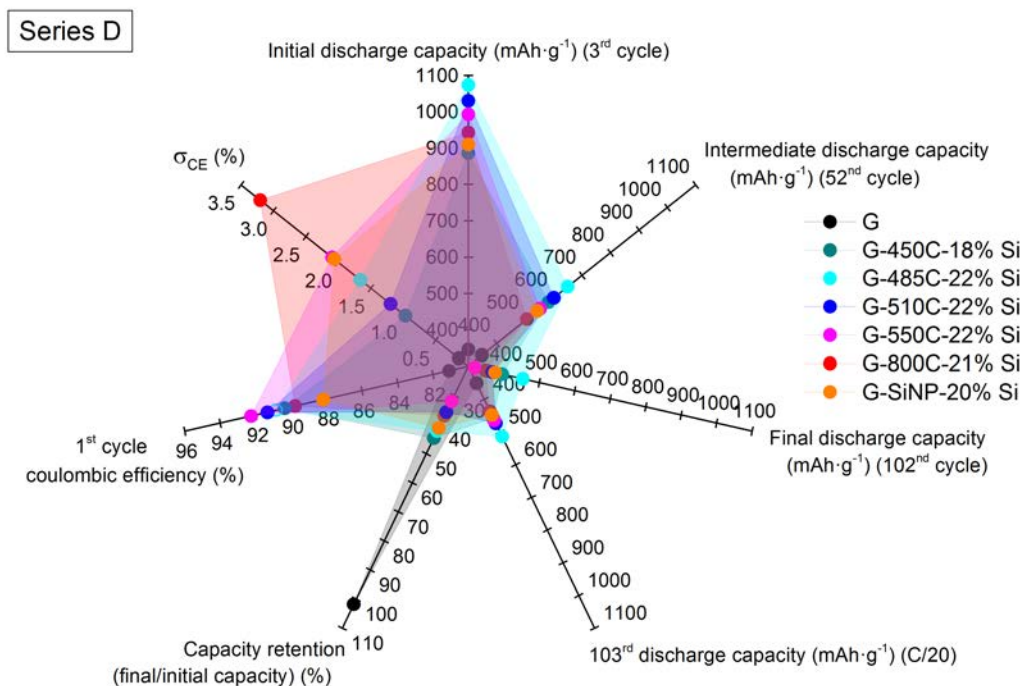


**Figure 4.13:** Radar plots of the performance of batteries containing anodes from silicon deposited at 450 °C, 485 °C, 510 °C and 550 °C, resulting in ~21 wt.-% silicon content (series D) with additional the sample annealed at 800 °C and a graphite/Si NP mixture with 20 wt.-% silicon. The 1<sup>st</sup> cycle CE for G-485C-22% Si was taken from a replica battery.

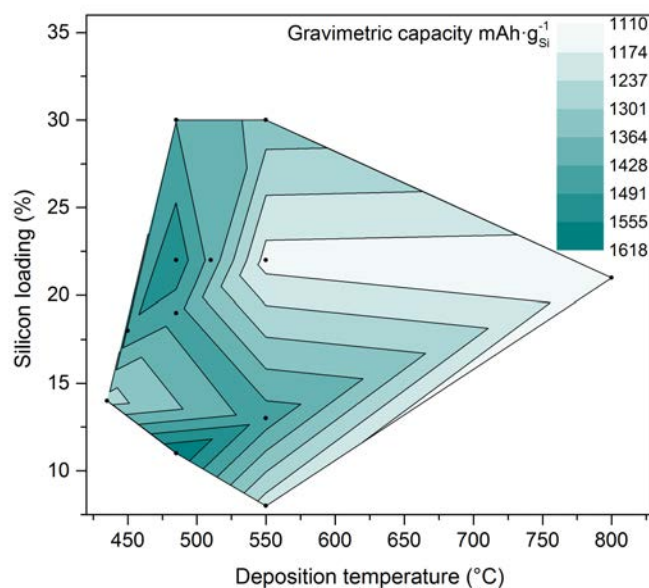


**Figure 4.14:** Contour plot illustrating the gravimetric discharge capacity per silicon and cycle as a function of the silicon loading and the deposition temperature (dots = data points; dark areas indicate higher capacities, bright areas lower capacities).

### Characterisation of electrochemical processes using differential capacity analysis

To distinguish between peaks of electrochemical processes caused by graphite, CB and silicon, the differential capacity plots (DCP) of graphite and CB for the 2<sup>nd</sup>, 53<sup>rd</sup> and 103<sup>rd</sup> cycle were evaluated (SI fig. 8.18). The broad peaks measured for the CB anode battery are small compared to the ones of the graphite reference and therefore they are not observable in the graphite reference DCP, although the anode also contains CB. In agreement with the stable electrochemical performance, the DCP peaks related to electrochemical processes of graphite in LIBs look similar in the 1<sup>st</sup>, 2<sup>nd</sup>, 53<sup>rd</sup> and 103<sup>rd</sup> cycle.

In the former section it was shown that the capacities of the batteries decay over cycling. To clarify the reasons for this decay, the DCPs in the 2<sup>nd</sup>, 53<sup>rd</sup> and 103<sup>rd</sup> cycle of batteries containing G-550C-22% Si anodes are compared in figure 4.15. Additionally, the DCP of graphite is plotted to distinguish the processes caused by graphite. The graphitic peaks observed in the 2<sup>nd</sup> cycle of the G-550C-22% Si battery maintain their intensity during the cycling. The additional reduction peaks at 290, 240, 90 and 40 mV and oxidation peaks at 300, 430 and 490 mV decay (fig. 4.15 a). The broad double-peak between 240 – 290 mV and the peak at 90 mV observed in the 2<sup>nd</sup> cycle lithiation correspond to the broad oxidation peaks around 300 and 490 mV. They are attributed to (de-)lithiation between a-Si and a-Li<sub>x</sub>Si.<sup>[57,157,158]</sup> The distinct oxidation peak at 430 mV (fig. 4.15 b) is attributed to the delithiation of c-Li<sub>15</sub>Si<sub>4</sub> and relates to the reduction peak at 40 mV.<sup>[47,58,160,161]</sup> Consistent with literature<sup>[53,157,162]</sup>, these peaks decrease significantly with cycling, so that in the 52<sup>nd</sup> cycle they were not detectable anymore, while the broad peaks attributed to processes caused by amorphous compounds remained more constant. However, the latter peaks also continuously shrink, so that in the 103<sup>rd</sup> cycle mainly graphite (de-)lithiation processes are observable in the DCPs. This is in good agreement with the observed gravimetric capacity being close to the one of the graphite reference.

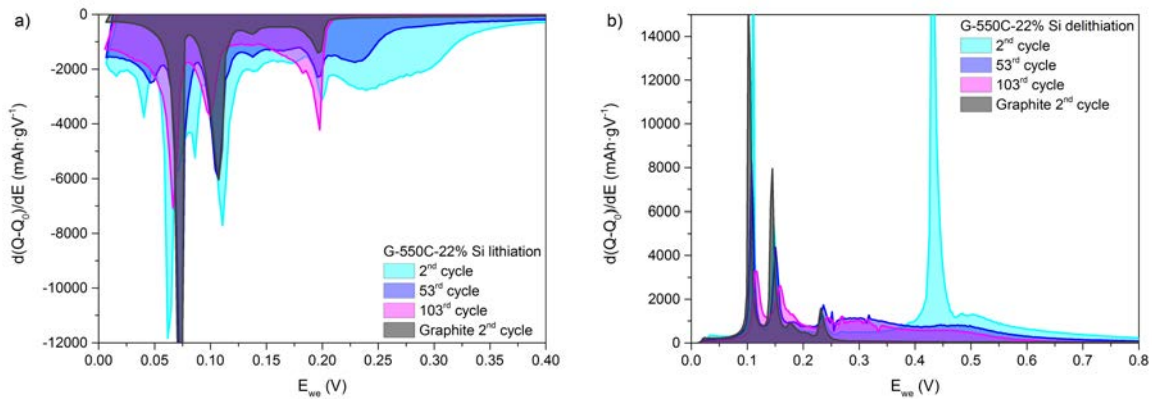


**Figure 4.15:** Differential capacity plots of G-550C-22% Si batteries at 2<sup>nd</sup>, 53<sup>rd</sup> and 103<sup>rd</sup> cycle for a) lithiation and b) delithiation.

In figure 4.16 the DCPs for the 2<sup>nd</sup> and 103<sup>rd</sup> cycle of batteries cycled with anodes obtained from silicon deposition at 550 °C for 30 min (G-550C-08% Si), 60 min (G-550C-13% Si), 120 min (G-550C-22% Si) and 180 min (G-550C-30% Si) (series A) are shown. The broad double-peak between 240 – 290 mV, and peaks around 86 mV and 40 mV are clearly visible in the 2<sup>nd</sup> lithiation (fig. 4.16 a). These peaks are characteristic for the lithiation of silicon and were observed to increase with increasing silicon content, which also is consistent with the increased gravimetric capacity. However, in the 103<sup>rd</sup> cycle only the characteristic graphite (de-)lithiation peaks are visible, which goes in line with the gravimetric capacity of the sample being close to the one of the graphite reference.

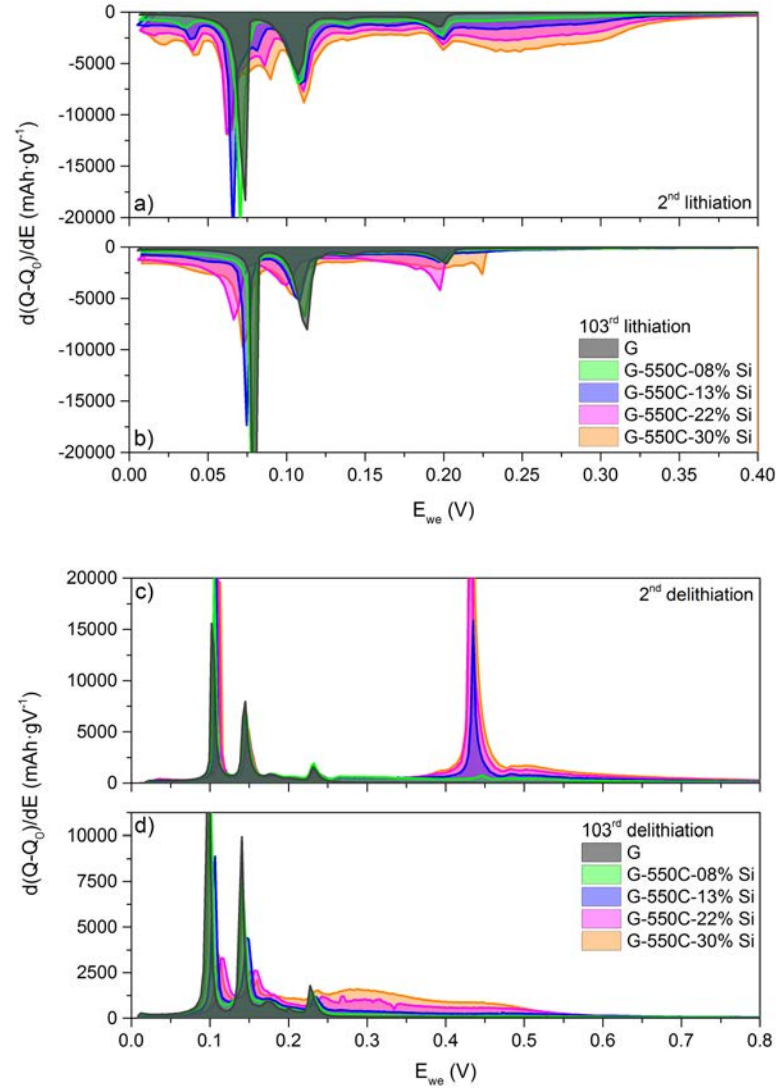


**Figure 4.16:** Differential capacity plots of batteries containing anodes from silicon deposited at 550 °C for 30 – 180 min (series A): a) 2<sup>nd</sup> lithiation, b) 103<sup>rd</sup> lithiation, c) 2<sup>nd</sup> delithiation and d) 103<sup>rd</sup> delithiation.

A similar trend can be observed for the delithiation peaks at 300, 430 and 490 mV (fig. 4.16 c and d). Yet, the broad delithiation peaks of a-Li<sub>x</sub>Si at 300 and 490 mV are still visible after 100 cycles for the G-550C-22% Si and G-550C-30% Si batteries. This suggests that some silicon is still (de-)lithiated. Similar trends were observed for DCPs of batteries cycled with anodes obtained from silicon deposition at 485 °C for 60 – 180 min (series B), which are depicted in the SI (fig. 8.20).

Several reports on the 1<sup>st</sup> cycle DCPs of c-Si and a-Si state irreversible significant peaks upon lithiation around 0.1 V and 0.2 V for c-Si and a-Si, respectively.<sup>[79,157,159,165]</sup> These peaks are attributed to two-phase lithiation processes and do not occur for all subsequent cycles. Figures 4.17 a) and b) show the 1<sup>st</sup> cycle lithiation DCPs for batteries containing anodes obtained from silicon depositions between 450 – 550 °C, resulting in around 21 wt.-% silicon content (series D). It was concluded from XRD and Raman analysis that samples deposited at temperatures below 510 °C consist of a-Si, while for deposition temperatures at or above 510 °C also polycrystalline silicon is formed. In agreement with this, the DCPs of the G-450C-18% Si and G-485C-22% Si batteries show a strong lithiation peak around 0.2 V, while the DCPs of the G-800C<sup>a</sup>-21% Si and G-SiNP-20% Si batteries, containing highly crystalline silicon, exhibit a sharp lithiation peak around 0.1 V. The DCPs of batteries with anodes of minor crystallinity, namely G-510C-22% Si and G-550C-22% Si, however, do not show a strongly distinct lithiation peak. For the delithiation the DCPs look similar, except for the ones of batteries containing highly crystalline silicon (G-800C<sup>a</sup>-21% Si, G-SiNP-20% Si) (fig. 4.17 c) and d). For these two, a significantly smaller peak around 0.45 V is observed. This indicates that either less c-Li<sub>15</sub>Si<sub>4</sub> is formed in the first lithiation, or less of the c-Li<sub>15</sub>Si<sub>4</sub> is delithiated. This trend is also maintained in the second cycle (SI fig. 8.19). These observations imply that, in comparison to the c-Si, the a-Si is accessible for lithium to a larger extent from the beginning on. This could be an explanation for the observed lower initial capacity of the G-800C<sup>a</sup>-21% Si and G-SiNP-20% Si batteries. Similar trends are observed for the DCPs of series C, comprised of batteries containing anodes obtained from silicon deposited at 435 – 550 °C and an average silicon content of 13 wt.-% (see SI fig. 8.21).

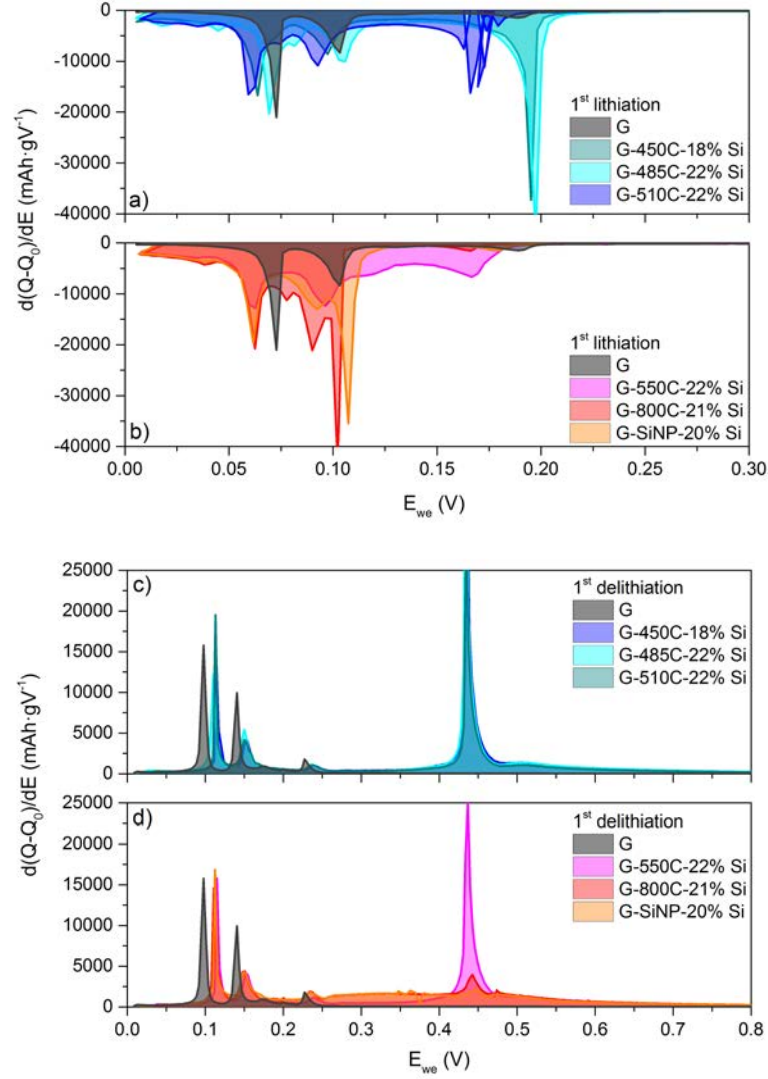


**Figure 4.17:** Differential capacity plots of batteries containing anodes with ~21 wt.-% silicon (series D) in the 1<sup>st</sup> cycle, a) lithiation of silicon deposited at 450, 485 and 510 °C, c) respective delithiation, b) lithiation of silicon deposited at 550 °C, annealed sample at 800 °C and graphite/Si NP mixture and d) respective delithiation.

### C-rate capability test

To gain an impression of the (de-)lithiation kinetics, the batteries were subjected to a C-rate capability test. This test reveals how much of the initial capacity achieved at low C-rates can, firstly, be maintained under faster C-rates and, secondly, be re-obtained after the stress test. For proper comparison, the results of the C-rate capability test on batteries containing graphite and CB reference anodes are shown in SI (fig. 8.22 a). Figure 4.18 depicts the results of the C-rate capability test for the batteries series A and B (series A: silicon deposition at 550 °C for 30 – 180 min; series B: silicon deposition at 485 °C for 60 – 180 min). Most of the samples exhibit a comparable performance. Only samples with 30 wt.-% silicon show a faster capacity

decay for higher C-rates and an extensive capacity loss after the stress test. This might be attributed to the morphology. The silicon is deposited in droplet shape on the graphite surface, however, for the 30 wt.-% silicon samples the droplets are so densely packed, that they locally form films. These films could be more stress-sensitive, hence fracture during the stress test. Also, the electrolyte with the charge carriers may have significantly less contact to the graphite leading to the reaction kinetics being slowed down by the low conductivity of the silicon, which is assumed to lead to less lithiation and further irreversible lithium trapping within the silicon. Whether the samples initially contained c-Si or a-Si does not affect the performance. The C-rate capability tests for the series C and D are given in the SI (fig. 8.22 b) and c). Again, all batteries containing anodes obtained from silicon deposition exhibit a similar performance. Remarkably, for the Si NP containing batteries, a little less of the initial capacity can be re-obtained after the stress test. This might be attributed to the missing silicon-carbon connection.

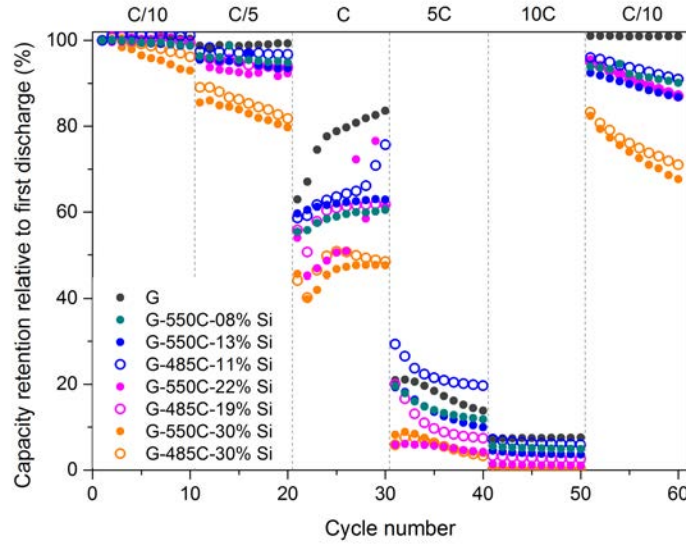


**Figure 4.18:** Capacity retention relative to first discharge as a function of the cycle number for C-rate capability tests conducted on batteries containing silicon anodes obtained from silicon deposition at 550 °C for 30 – 180 min (series A) and at 485 °C for 60 – 180 min (series B).

In summary, batteries containing anodes with higher silicon contents provided higher initial capacities, but simultaneously also a more pronounced capacity decay and standard deviation of the CE. Batteries comprising anodes which contain c-Si exhibited reproducible significant CE losses in the first half of the cycling and batteries containing anodes obtained from silicon deposition at 485 °C stood out with the highest capacity per silicon over 100 cycles. Moreover, the capacity decay during cycling was shown to go in line with the decrease of the peaks attributed to silicon (de-)lithiation in DCPs. C-rate capability tests revealed that silicon contents of 30 wt.-% significantly diminish the battery performance and that batteries containing anodes obtained from LPCVD provide superior performance compared to batteries containing similar anodes obtained from graphite/Si NP mixtures.

### 4.3.3 Evolution of the anode material upon electrochemical cycling

A more thorough understanding of the anode evolution during cycling and the reasons for the capacity decay can be obtained from post-mortem analysis. In figure 4.19 SEM images of an anode made from G-550C-22% Si are shown before cycling, after 52 cycles and after 103 cycles. Before cycling, the anode exhibits a fluffy structure. Particulate graphite flakes with silicon deposition and carbon black are pictured. After 52 cycles, the anode surface is covered by a solid electrolyte interphase (SEI) layer. The visible cracks in the SEI layer are most probably induced by the drying process of the anode after the cycling. After 103 cycles the SEI layer appears thicker and from EDX analysis of the spots A (on SEI) and B (in cracks) two fundamentally different spectra were collected (fig. 4.20). On spot A no silicon signal and in decreasing intensity order oxygen, carbon, fluorine and phosphorous signals are obtained. While the intensity of the oxygen peak is similar for the spectrum of spot B, the carbon signal is increased and the fluorine and phosphorous peaks are decreased significantly. Moreover, a considerable silicon signal appears. From this it can be concluded that the formed SEI mainly consists of fluorine, oxygen, phosphorous and carbon, resulting from electrolyte decomposition products and that its thickness and density avoids the detection of the underlying silicon with an EDX interaction depth of 700 nm.

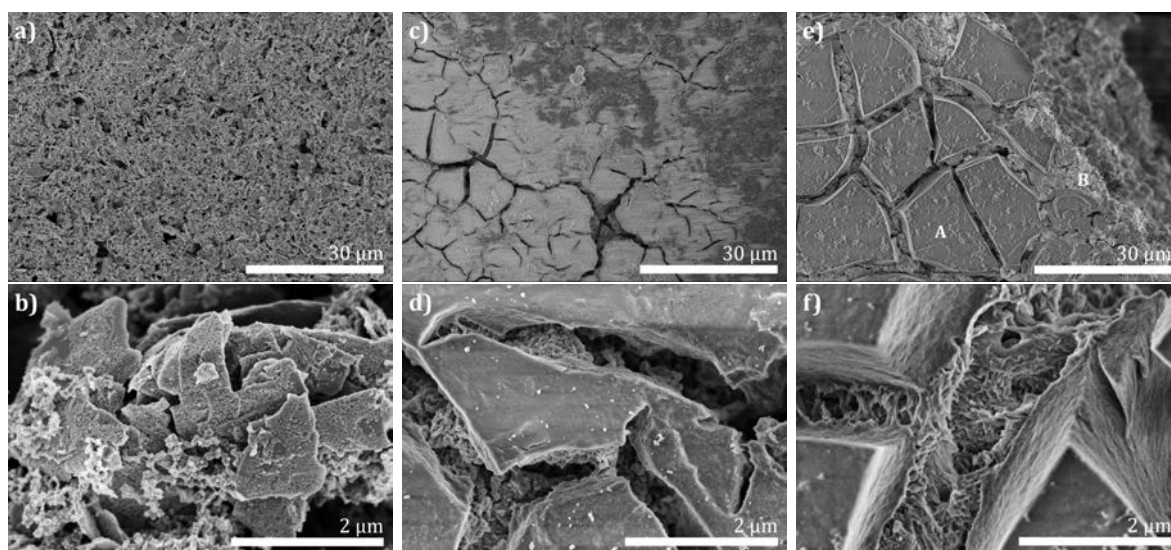


**Figure 4.19:** SEM images of G-550C-22% Si anodes a, b) before cycling, c, d) after 52 cycles and e, f) after 103 cycles.



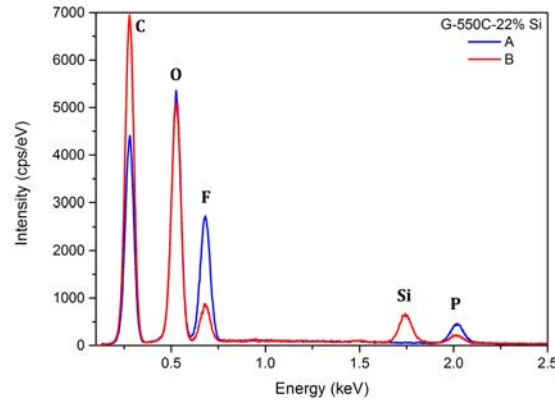


**Figure 4.20:** EDX spectra for spots A and B in SEM image 4.19 e).

Additionally, a G-485C-19% Si anode, containing exclusively the a-Si phase was investigated after 103 cycles by SEM, to evaluate whether the SEI is formed differently on a-Si compared to c-Si. The corresponding SEM images convey a similar SEI on both anode types (SI fig. 8.23). The single element maps of the cycled G-485C-19% Si anode are depicted in figure 4.21. They go in line with the EDX analysis from the c-Si sample, meaning that on the SEI no significant silicon signal can be detected with 700 nm interaction depth, while fluorine and oxygen are the dominant species. Also, a significant silicon signal is detectable in the SEI cracks. Importantly, the SEI coverage is not present to this extent on the entire anodes. Images of less SEI covered regions for anodes made from G-550C-22% Si and G-485C-19% Si after 103 cycles can be found in the SI (fig. 8.24).

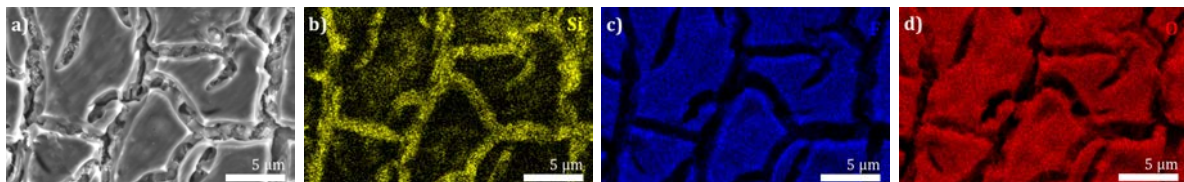


**Figure 4.21:** a) Secondary electron image of G-485C-19% Si anode after 103 cycles and corresponding single element maps of b) silicon, c) fluorine and d) oxygen (700 nm interaction depth).

For a better insight into the interphase between SEI and material, a cross section of the cycled G-485C-19% Si anode was prepared perpendicular to the surface (fig. 4.22, SI fig. 8.25). In the bottom region of the image, the graphite flakes with silicon deposition and carbon black are identifiable. On top of it, the SEI layer of around 630 nm thickness can be seen. This thickness goes well in line with the impossibility to detect a silicon signal on the SEI layer with 700 nm EDX interaction depth. In agreement with the previous results, for spot A (SEI) no silicon, but fluorine and phosphorous signals are detected. However, the EDX analysis of the cross section depicts salient peak intensities for carbon and oxygen in the SEI region. On the anode material at the bottom of the image, spot B, a distinct silicon signal, but no significant fluorine or phosphorous and considerably smaller oxygen and carbon signals are quantifiable.



The corresponding EDX spectra for the denoted spots A (SEI) and B (material) are given in the SI (8.26 a).

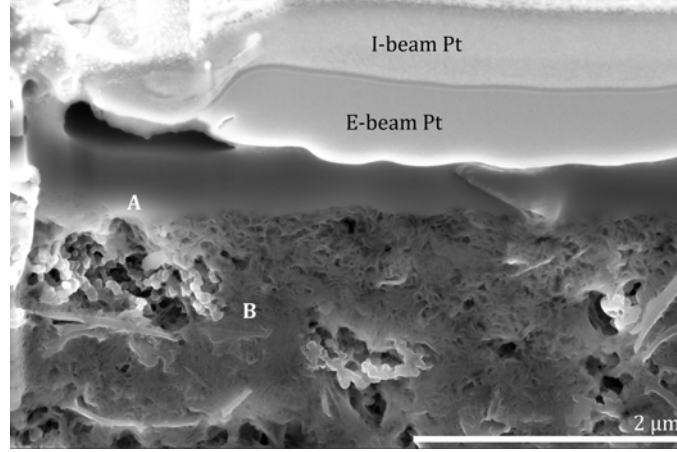


**Figure 4.22:** SEM image of the cross section of a G-485C-19% Si anode after 103 cycles.

The same anode was investigated using XPS before and after cycling. The resulting elemental compositions are presented in table 4.6. In good agreement with the SEM investigations, an increase in oxygen, fluorine and phosphorous content in the near surface region is detectable after 103 cycles. Referring to the carbon content, XPS analysis indicates that the SEI layer contains less carbon than the anode material. Mere traces of silicon can be detected on the cycled anode surface, which goes in line with the results from the EDX measurements on the SEI layer. Moreover, XPS analysis reveals a significant lithium content in the SEI. This is consistent with the Li-ion consumption during SEI formation described in literature.<sup>[68,97,119,120]</sup>

**Table 4.6:** Near surface composition according to XPS (mol %) for G-485C-19% Si anodes before and after electrochemical testing

cycling	O	F	Li	C	Cu	N	Si	P
before	25.3	-	-	56.3	0.1	0.3	18.0	-
after	32.8	7.6	19.2	38.9	0.1	0.1	0.1	1.3

For comparison, a reference graphite anode was also investigated after cycling using SEM. The cycled graphite anode is not covered with a similarly thick SEI (fig. 4.23 a, b), however, a thin coverage of the graphite flakes is visible at higher magnifications (fig. 4.23 c, d). In agreement with this representative EDX spectra revealed a small fluorine signal on the anode surface (SI fig. 8.26 b). This indicates the formation of a thin SEI on the graphite surface, which is consistent with the reported stable SEI layer formation on graphite in EC-based electrolytes.<sup>[38,104]</sup> Moreover, it confirms that the inhomogeneous and several hundred nanometers thick SEI layer comprised of oxygen, lithium, fluorine, carbon and phosphorous observed for the previous two anodes, is truly caused by the contained silicon.

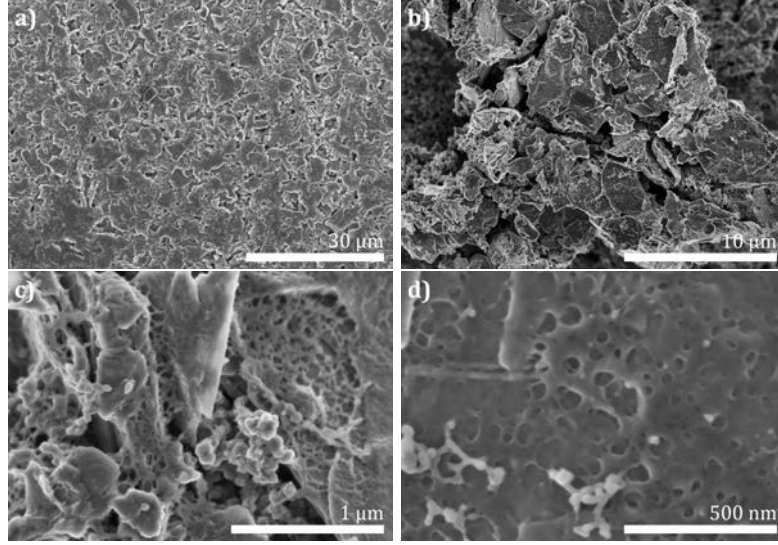


**Figure 4.23:** SEM images of a graphite reference anode after 103 cycles.

## 4.4 Conclusion

In this chapter, the influence of the silicon content and crystallinity in graphite-silicon nanocomposite-based anodes on the lithium-ion battery performance was investigated. The silicon was deposited on a graphite substrate with methodically varied deposition times ranging from 30 – 180 min and temperatures ranging from 435 – 550 °C. The samples were classified in four series according to their silicon content and crystallinity: A) crystalline silicon (c-Si) deposited at 550 °C containing 8 – 30 wt.-% silicon, B) amorphous silicon (a-Si) deposited at 485 °C containing 11 – 30 wt.-% silicon, C) amorphous and crystalline silicon deposited at 435 – 550 °C containing around 13 wt.-% silicon and D) amorphous and crystalline silicon deposited at 450 – 550 °C containing around 21 wt.-% silicon. The transition temperature for amorphous to crystalline silicon deposition was observed to occur between 485 °C and 510 °C deposition temperature. SEM and TEM analysis revealed that the silicon is deposited in the shape of droplets on the basal planes and film-like on the edges of the graphite. The film-like deposit containing spherical shapes indicated a similar nucleation process, but a faster silicon growth rate on the graphite edges than on the basal planes. Samples with lower silicon content showed more distinct silicon droplets on the basal planes, while samples with a high silicon content of 30 wt.-% exhibited graphite surfaces which were fully covered with silicon. Yet, no visible morphological differences for a-Si and c-Si depositions were observed. Electrochemical cycling of the samples revealed a stronger capacity decay for higher silicon contents and increasing silicon crystallinity. Moreover, depositions at 485 °C provided the highest averaged capacity per silicon and for the samples with either 30 wt.-% silicon content or high crystallinity a characteristic reproducible decay of the coulombic efficiency within the first 40 cycles occurred. Differential capacity analysis depicted that the peaks reported for silicon (de-)lithiation scaled

proportionally with the silicon content and decayed over cycling. Furthermore, differential capacity analysis confirmed different lithiation behaviours of c-Si and a-Si in the very first cycle. Employing post-mortem analysis it was shown that thick layers of solid electrolyte interphase (SEI) of around 630 nm thickness were formed on silicon containing samples during electrochemical testing. In the SEI no silicon, but lithium, fluorine, phosphorous, oxygen and carbon were detected.

Hence, for the design of new silicon-graphite-based anode materials, the presented results point at the application of a-Si. LPCVD turned out to be a suitable synthesis method for such nanostructured composites, since both silicon crystallinity and content can be reliably determined. Moreover, batteries containing anodes made from LPCVD exhibited superior performance regarding the coulombic efficiency and C-rate capability compared to the graphite/Si NP mixtures. However, the batteries still exhibit a significant capacity decay and inhomogeneous SEI formation on the anodes. Whether this can be avoided by employing further deposition of amorphous carbon, is discussed in the following chapter.



# 5 Carbon coverage of the silicon nanocomposite and its effect on the battery performance

## Abstract

It is widely discussed in literature that the performance decay of lithium-ion batteries (LIBs) containing silicon-based anodes is dominantly caused by the electrochemical degradation of electrolyte on the silicon surface. An approach to avoid the direct silicon-electrolyte contact is to cover the silicon surface with carbonaceous materials. In this section the amorphous carbon (a-C) coverage of the previously introduced graphite-silicon nanocomposite and its effect on the battery performance are examined. The graphite-silicon-a-C nanocomposite (G-Si@C) was synthesised using an adaptable low pressure chemical vapour deposition (LPCVD) reactor setup. Specifically, silicon was deposited on graphite flakes using LPCVD and subsequently covered with a-C using  $C_3H_6$ . The  $C_3H_6$  treatment time of the graphite-silicon nanocomposite was varied from 15 – 90 min. The resulting samples contained highly crystalline sintered silicon droplets covered with a-C, which avoided the formation of  $SiO_x$ -surface layers when the samples were exposed to air. A treatment with  $C_3H_6$  before and after the silicon deposition was used to achieve an encapsulation of silicon inside a-C. Yet, results from post-mortem TEM investigations of the materials after electrochemical testing indicated that the a-C coverage could not be maintained during cycling. Nevertheless, especially the coulombic efficiency was improved compared to batteries containing anodes without a-C coverage. A battery comprising an anode made from the a-C encapsulated sample also exhibited significantly improved capacity stability. Moreover, the evolution of the solid electrolyte interphases formed on the anodes during electrochemical testing was investigated using SEM.

## 5.1 Introduction

In the past decades great efforts have been made to introduce silicon in anode materials for lithium-ion batteries (LIBs). This is mainly due to the high theoretical gravimetric capacity of silicon ( $3579 \text{ mAh} \cdot \text{g}^{-1}$ ) compared to the currently mainly used anode material graphite ( $372 \text{ mAh} \cdot \text{g}^{-1}$ ).<sup>[22,47,124]</sup> To provide such a high gravimetric capacity, silicon is alloyed to  $Li_{15}Si_4$  and thereby undergoes a large volume expansion of 280 %, which entails material stress

and rearrangement of the material.<sup>[70,71]</sup> Although the often resulting silicon fracturing can be mostly prevented by the application of silicon nanostructuring, still silicon-based batteries do not achieve the required performance. They exhibit a fast capacity decay and low coulombic efficiency (CE) when cycled to their maximum capacity. This is mainly attributed to the insufficiently stable solid electrolyte interphase (SEI) formation on and lithium-ion trapping inside the silicon.<sup>[19,64,116]</sup> A stable SEI provides the basis for the stabilisation of battery performance regarding irreversible charge loss, self-discharge, cyclability, rate capability and safety.<sup>[98]</sup> It is formed by reduction of electrolyte components on the anode surface. In case of graphite anodes this occurs in the first battery cycle and the formed SEI then prevents further electrolyte reduction, graphite exfoliation and co-intercalation of solvent molecules.<sup>[96,99,100]</sup> In contrast, the SEI formed on silicon was reported to be multi-layered and porous.<sup>[116]</sup> Such an SEI formation process is assumed to continuously consume charges and is attributed to the mentioned large volume expansion of silicon during (de-)lithiation.<sup>[63,111,118]</sup>

The addition of carbonaceous materials to silicon-based anodes, e.g. by mixing and milling, has been reported to improve the performance of batteries by providing a conductive network inside the anode.<sup>[19]</sup> Hence, the dedicated carbonaceous surface coverage of silicon is expected to cope with three particular tasks:<sup>[11,85,124,214]</sup> Firstly, a carbon coverage is supposed to act as mechanical constraining layer, which accommodates the silicon's volumetric changes, thus avoiding electrochemical sintering and deterioration of the silicon in order to maintain good electrical contact. Secondly, the carbon is to function as a passivation layer which suppresses unwanted reactions between electrode and electrolyte, such as anode reaction with fluorine species. Thirdly, the carbon is intended to enhance the redox reaction kinetics and improve the current collection efficiency due to its superior electrical conductivity. However, too thick and stable surface coatings can lead to large stress upon the silicon volume expansion and slow down the reaction kinetics, resulting in incomplete silicon lithiation.<sup>[215,216]</sup> Hence, it is important to select an elaborated synthesis method which generates a thin, homogeneous and controllable carbon layer.<sup>[125]</sup> Several routes have been reported to cover silicon with various carbons, e.g. straightforward processes using hydrothermal carbonization, pyrolysis or heating with precursors or more elaborated approaches including several intermediate steps.<sup>[124,125,217–219]</sup> Among these approaches especially chemical vapour deposition (CVD) of amorphous carbon (a-C) on nanostructured silicon gave promising results.

Common deposition gases are propene ( $\text{C}_3\text{H}_6$ ) or ethene ( $\text{C}_2\text{H}_4$ ) and deposition temperatures are usually between 700 and 900 °C.<sup>[220–225]</sup> Higher deposition temperatures result in carbon depositions with a higher degree of graphitization and more reduction of  $\text{SiO}_x$  surface species, which was reported to improve the 1<sup>st</sup> cycle CE and high-rate performance of the battery.<sup>[225]</sup> During the deposition of a-C the precursors propene and ethene undergo pyrolysis reactions. Hereby, both alkanes result in five common major compounds, namely hydrogen, ethyne ( $\text{C}_2\text{H}_2$ ), methane ( $\text{CH}_4$ ), 1,3-butadiene ( $1,3\text{-C}_4\text{H}_6$ ), and benzene ( $\text{C}_6\text{H}_6$ ).<sup>[226]</sup> The pyrolysis of  $\text{C}_3\text{H}_6$ , however, is a bit more complex and furthermore includes propyne ( $\text{C}_3\text{H}_4$ ) and propadiene

( $\text{H}_2\text{CCCH}_2$ ) as major pyrolysis species (fig. 5.1). Thus, the coverage of ball-milled silicon with a-C by ethene pyrolysis was reported to lead to a significant improvement in the cycling stability, which was attributed to the formation of an a-C network.<sup>[227]</sup>

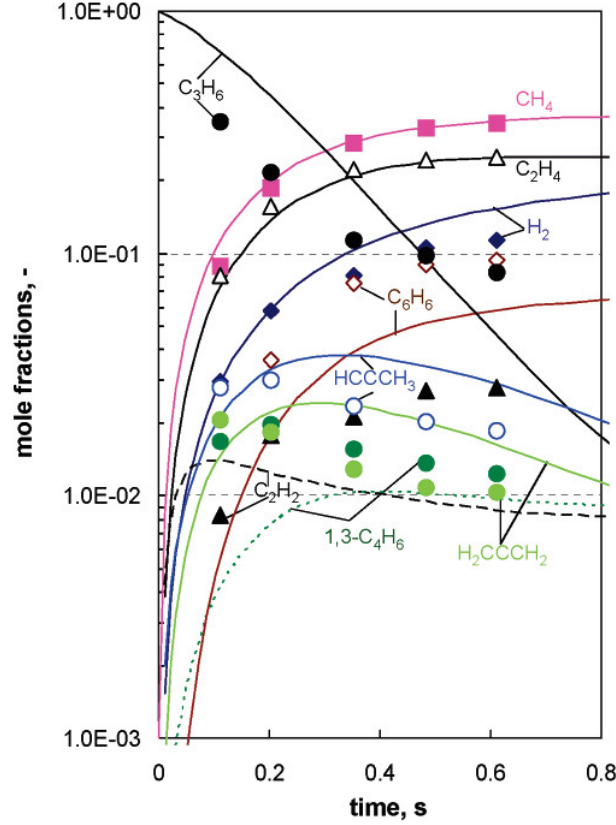


**Figure 5.1:** Comparison of model predictions (lines) with experimental mole fraction profiles (symbols) of major species during propylene pyrolysis at 900 °C and 8 kPa.<sup>[226]</sup>

Nevertheless, it was reported that there is not only a minimum, but also a maximum a-C thickness which should not be exceeded, since a too thick a-C film is assumed to limit the lithium-ion diffusion.<sup>[223]</sup> Batteries obtained from ethene pyrolysis on silicon nanoparticles (Si NPs) with about 20 wt.-% a-C in the resulting nanocomposite exhibited a stable cycling performance providing a capacity of  $1200 \text{ mAh} \cdot \text{g}^{-1}$  over 600 cycles.<sup>[225]</sup> Also, the cycling performance of more complex nanostructured silicons like hollow silicon nanotubes and sponge silicon, were significantly improved by a-C coverage.<sup>[220,228]</sup> In addition, there are several promising bottom-up approaches which use the CVD processes, first for silicon deposition and subsequently for a-C coverage. Batteries containing anodes obtained from silicon deposition on spherical natural graphite with additional coverage with a-C by ethene pyrolysis provided an outstanding performance in C-rate capability tests with only 3 wt.-% a-C.<sup>[224]</sup> However, the system turned out to be unstable for silicon contents above 6 wt.-%, therefore it is limited to a gravimetric capacity of  $517 \text{ mAh} \cdot \text{g}^{-1}$ . In contrast, material obtained from pyrolysis of propene on carbon black or graphene with silicon deposits provided the base for batteries which exhibited stable gravimetric capacities of 1400 and  $1000 \text{ mAh} \cdot \text{g}^{-1}$  for 100 and 150 cycles, respectively.<sup>[221,222]</sup>

Due to its buffering properties, a-C films were reported to also stabilise the performance of silicon thin films when deposited between the silicon and the current collector.<sup>[229]</sup>

In this chapter, the synthesis, characterisation and electrochemical performance of graphite-silicon-amorphous carbon nanocomposites (G-Si@C) is discussed. The G-Si@C composites were obtained from LPCVD of silicon on graphite with subsequently performed coverage with a-C using pyrolysis of propene. It was investigated how the propene treatment time affects the a-C deposit, the silicon deposit and the battery performance. Moreover, it was probed whether the a-C coverage is able to outlast the electrochemical cycling and if the SEI formation is affected by the a-C coverage.

## 5.2 Experimental

### 5.2.1 Sample preparation

Silicon was deposited using an in-house designed LPCVD reactor setup comprised of a gas supply facility (N<sub>2</sub> and Ar, purity 99.999 %, Westfalen; SiH<sub>4</sub>, UHP, Air Liquide; C<sub>3</sub>H<sub>6</sub> containing 5 vol.-% 5.0 O<sub>2</sub>, 10 vol.-% 2.5 C<sub>3</sub>H<sub>6</sub> and 5.0 N<sub>2</sub> balance, Westfalen), a three zone hot wall oven (HTM Reetz GmbH), and a horizontally placed 1.2 m long by 4.5 cm in diameter quartz tube as main reaction chamber. All gases were dried and filtrated using a dry bed cartridge (MC200, MicroTorr). The depositions were performed using a rotary feedthrough motion quartz reactor insert (60 cm long by 3.5 cm in diameter) composed of a 10 cm baffled deposition chamber, reaction gas exhaust compartment, a glass frit, a quick connection holder and a rotary sealing (ALMA-M-KF-012-V-U, Alma) mounted on a KF40 “T” piece. Prior to deposition all gas lines were purged with N<sub>2</sub> at 2 l · min<sup>-1</sup> for 1 h. The reactor insert was typically filled with 1.5 g of graphite powder (KS6, Timcal) inserted inside the main reaction chamber and rotated at 2 rounds per minute. The main chamber absolute pressure was set to the required pressure and the oven heating zones were simultaneously heated from room temperature to the deposition temperature with a ramp of 5 °C · min<sup>-1</sup> under 10 sccm argon flow. The oven calibration revealed a  $T_{\text{sample}} = (20.80 + T_{\text{oven}} \cdot 0.99)$  (°C) correlation. In the following, given temperatures represent the set temperature ( $T_{\text{oven}}$ ). The setup was thermally stabilised for 30 min prior to deposition and cooled down to room temperature under a constant flow of argon after the deposition process. Silicon was deposited at 485 °C or 550 °C for 1 – 2 h at 1 mbar and 10 sccm SiH<sub>4</sub> flow. Carbon was deposited at 800 °C for 15 – 90 min at 9 mbar and 15 sccm C<sub>3</sub>H<sub>6</sub> flow. The prepared samples are presented in table 5.1. The samples were ground in an agate mortar and stored inside an argon filled glove box (mBraun B790, O<sub>2</sub> ≤ 1 ppm Ionic System Trace Oxygen Sensor Tos 3.0).



**Table 5.1:** List of sample names and varied deposition parameters

sample	C <sub>3</sub> H <sub>6</sub> <i>t</i> (min)	SiH <sub>4</sub> <i>t</i> (min)	SiH <sub>4</sub> <i>T</i> (°C)	C <sub>3</sub> H <sub>6</sub> <i>t</i> (min)	remark
G-Si(21%)-60m	-	120	485	60	annealing under vacuum
G-Si(20%)-C15m	-	120	485	15	-
G-Si(17%)-C30m	-	120	485	30	-
G-Si(19%)-C60m	-	120	485	60	-
G-Si(19%)-C90m	-	120	485	90	-
G-Si(12%)-C30m	-	60	550	30	1 h Si deposition
G-Si(O)(24%)-C30m	-	120	485	30	exposed to air before a-C deposition
G-C-Si(20%)-C30m	30	120	485	30	C <sub>3</sub> H <sub>6</sub> treatment before and after Si deposition

### 5.2.2 Material characterisation

**Elemental Analysis** For silicon quantification, elemental analysis was executed by the analysis laboratory Kolbe (Höhenweg 17, 45470 Mülheim an der Ruhr, Germany) using a Vario EL CHNOS-Analyser (Elementar) and photometric silicon determination.

**Thermogravimetric analysis – mass spectrometry** TG-MS measurements were carried out using a simultaneous TG–DSC on a Netzsch STA 449C Jupiter thermoanalyzer equipped with an electromagnetic micro balance (resolution 0.1 µg; relative error of the mass determination 0.5 %) with top-loading. The sample was placed in an open corundum crucible (85 µl) and placed on the sample holder whose temperature change was monitored via Pt/Pt-Rh thermocouples. The samples were heated in a 100 ml · min<sup>-1</sup> flow of a gas mixture consisting of 21 % O<sub>2</sub> : 79 % Ar (both 99.999 %, Westfalen) with 10 °C · min<sup>-1</sup> to 650 °C, then 2 °C · min<sup>-1</sup> to 1000 °C and finally with 5 °C · min<sup>-1</sup> to 1500 °C. The evolved gases were monitored with a quadrupole mass spectrometer (QMS200 Omnistar, Balzers) coupled to STA via a quartz capillary heated to 40 °C. The experiments were performed with an electron ionisation energy of 60 eV and a dwell time per mass of 0.2 s.

**X-ray diffraction** The X-ray diffraction measurements were performed in Bragg-Brentano geometry (Bruker AXS D8 Advance II) using Ni filtered Cu K<sub>α</sub> radiation and a position sensitive energy dispersive LynxEye silicon strip detector. To index the XRD patterns the references listed in table 5.2 were used.

**Table 5.2:** XRD reference patterns

phase	chemical formula	database #
Graphite 2H	C	PDF 89-7213
Graphite 3R, syn	C	PDF 26-1079
Silicon, syn	Si	PDF 27-1402

**Raman spectroscopy** Raman measurements were carried out on a Thermo Fischer Scientific DXR spectrometer with a 532 nm laser in the measurement range from 100 – 4000  $\text{cm}^{-1}$  applying an incident light power of 0.5 mW. For comparison of the Raman spectra the G-band was normalised. For the Raman fitting the five bands G ( $\sim 1580 \text{ cm}^{-1}$ ), D1 ( $\sim 1350 \text{ cm}^{-1}$ ), D2 ( $\sim 1620 \text{ cm}^{-1}$ ), D3 ( $\sim 1500 \text{ cm}^{-1}$ ) and D4 ( $\sim 1200 \text{ cm}^{-1}$ ) reported by Sadezky et al.<sup>[230]</sup> were used as starting alignment. The D4 band needed to be fixed to values  $\leq 1208 \text{ cm}^{-1}$  to avoid convergence with the D1 band.

**Scanning Electron Microscopy** SEM images were acquired on a Hitachi S-4800 microscope using 1.5 kV accelerating voltage and 3 – 4 mm working distance. The samples were prepared on a beryllium holder and energy dispersive X-ray (EDX) analysis was performed using a silicon drift detector (SDD).

**Transmission Electron Microscopy** The powder samples were prepared on a 200 mesh lacey carbon copper grid. The TEM images of the sample G-Si(12%)-C30m were acquired using an aberration-corrected JEOL JEM-ARM 200F microscope operated at 200 kV acceleration voltage. The elemental maps were recorded using a high angle silicon drift EDX detector. The samples G-Si(19%)-C60m and G-Si(O)(24%)-C30m were investigated using an FEI Talos F200X microscope. Scanning transmission electron microscope bright field (STEM-BF) images were acquired using a 200 kV acceleration voltage and 98 mm camera length. EDX analysis was performed using the Super-X system comprised of four Bruker SDDs.

### 5.2.3 Anode preparation and electrochemical tests

**Anode preparation** For the preparation of electrodes, polyacrylic acid (PAA,  $\leq 0.5 \%$  benzene, Sigma-Aldrich) was dispersed in an ethanol (Sigma-Aldrich) : 2-propanol ( $\geq 99.5 \%$ , Carl Roth) (6.25:1) mixture and stirred for 15 h. Then, carbon black (CB) (Super Conductive P, Alfa Aesar) and the ground sample were added (PAA : CB : sample = 1 : 1.5 : 10), stirred and treated in an ultrasonic bath. The prepared slurry was cast as a thin film on a 25  $\mu\text{m}$  thick copper foil (Cu58, bare, Schlenk) using a ZUA 2000 universal applicator (Zehntner) or a 4-sided film applicator (VF2169-013, 60 mm, TQC), respectively set to a film thickness of 120  $\mu\text{m}$ . Subsequently, the film was dried for 15 h at 80  $^{\circ}\text{C}$  in a vacuum oven (VTR 5022, Heraeus). Hereafter, anodes of 10 mm in diameter were punched out using a lever press, weighed and stored in an argon filled glovebox (mBraun B790,  $\text{O}_2 \leq 1 \text{ ppm}$  Ionic System Trace Oxygen Sensor TOS 3.0).

**Electrochemical testing** For the two electrode battery system, a modified stainless steel Swagelok tube fitting was electrically insulated by a one-way 75  $\mu\text{m}$  Kapton foil (Dr. Dietrich Müller GmbH). The working electrode and counter electrode (metallic lithium, 10 mm diameter, Xiamen Tob New Energy Technology Co.) were sandwiched with two 25  $\mu\text{m}$  thick separators (C2500, Celgard Inc., USA) in between and wetted with 140  $\mu\text{l}$  of a solution of 1 M  $\text{LiPF}_6$  dissolved in a mixture of ethylene carbonate : diethyl carbonate 1 : 1 wt.-% (Selectilyte LP40,

Battery grade, BASF) electrolyte. The battery cell was sealed with nylon ferrules (Swagelok) on both sides inside the argon filled glovebox. Electrochemical measurements were carried out using an Arbin Instruments BT2000 battery tester or a Biologic MPG-2 battery cycler. The regular cycling protocol with differential capacity analysis in the 1<sup>st</sup>, 2<sup>nd</sup> and 103<sup>rd</sup> cycle is given in table 5.3 and the C-rate variation protocol without CV-sequences in table 5.4.

**Table 5.3:** Cycling protocol

cycle	current (C-rate)	final lithiation potential (V)	CV-sequence (min)	final delithia- tion potential (V)	CV-sequence (min)
1-2	C/20	0.005	90	2	60
3-102	C	0.005	90	2	60
103	C/20	0.005	90	2	60

**Table 5.4:** Current rate (C-rate) variation protocol applied between 5 mV and 2 V

cycle	1 - 10	11 - 20	21 - 30	31 - 40	41 - 50	51 - 60
C-rate	C/10	C/5	C	5 C	10 C	C/10

To calculate the gravimetric capacities of the anode materials the measured capacities were divided by the mass of the active material. Since the weight of the copper foil varies strongly while the mass of active material varies only slightly due to the casting process, the mass of the active material could not be accurately determined by weighing of the entire anode. Therefore, except for occasional cases, the precise investigation of the gravimetric capacity was accomplished as follows. For new anode materials with unknown gravimetric capacity, the theoretical capacity was calculated based on  $372 \text{ mAh} \cdot \text{g}^{-1}$  gravimetric capacity for graphite and  $3579 \text{ mAh} \cdot \text{g}^{-1}$  for silicon. The anode was cycled following the protocol in table 5.3 with the current congruous with the theoretical 1C C-rate, employing 50 instead of 100 cycles. Afterwards, the anode was dismounted, washed and the active material was removed by ultrasonification in ethanol. The left-over copper foil was weighed and the difference to the anode weight prior to cycling, i.e. the amount of removed material, was set off against the binder and thereby resulted in the amount of active material including graphite, silicon and carbon black. The gravimetric discharge capacities of the subsequently cycled anodes were then pinned in the 5<sup>th</sup> cycle to the same gravimetric discharge capacity as the previously dispersed anode. Samples were exempted from this procedure when they were not used for post-mortem analysis, in this case the weight of the active material was directly determined by dissolving the anode material. For evaluation of the capacity normalised per silicon and averaged over 100 cycles the scattered capacity outliers were linearly interpolated, before the discharge capacities were added over 100 cycles and normalised for cycle and wt.-% silicon.

### 5.2.4 Post-mortem analysis

After electrochemical testing the batteries were disassembled inside the argon filled glove box, with the anodes being in the delithiated state. Then, the anodes were washed successively in four flasks filled with 3 ml DEC ( $\geq 99\%$ , anhydrous, Sigma Aldrich) each and prepared for the respective analysis method (SEM and TEM) on transfer holders which provide an airtight seal.

**Scanning Electron Microscopy** SEM images were acquired on a Hitachi S-4800 microscope using 1.5 kV accelerating voltage and 3 – 4 mm working distance. The anodes were mounted on conductive carbon tape (Plano) on a transfer holder. Energy dispersive X-ray (EDX) analysis was performed using an SDD.

**Transmission Electron Microscopy** For TEM investigations, cycled material was scraped off the anode and mounted on 200 mesh lacey carbon copper grids. The TEM images of the sample G-Si(12%)-C30m after 27 cycles were acquired using an aberration-corrected JEOL JEM-ARM 200F microscope operated at 200 kV acceleration voltage. The elemental maps were recorded using a high angle silicon drift EDX detector. The samples G-Si(12%)-C30m after 7 cycles and G-Si(19%)-C60m after 103 cycles were investigated using an FEI Talos F200X microscope. Scanning transmission electron microscope bright field (STEM-BF) images were acquired using a 200 kV acceleration voltage and 98 mm camera length. EDX analysis was performed using the Super-X system comprised of four Bruker SDDs.

## 5.3 Results and discussion

### 5.3.1 Characterisation of the G-Si@C nanocomposite

The samples examined in this chapter can be classified as listed in table 5.5. The sample names are derived from the deposition conditions and the silicon content determined by elemental analysis (EA), for example: G-Si(19%)-C60m represents graphite covered with 19 wt.-% silicon deposit treated with propene for 60 min.

**Table 5.5:** Classification of samples

classification	samples
group of 15, 30, 60 and 90 min C <sub>3</sub> H <sub>6</sub> treatment	G-Si(20%)-C15m, G-Si(17%)-C30m, G-Si(19%)-C60m, G-Si(19%)-C90m
◇ 60 min annealing at 800 °C under vacuum	G-Si(21%)-60m
◇ lower Si content and 30 min C <sub>3</sub> H <sub>6</sub> treatment	G-Si(12%)-C30m
◇ exposed to air before 30 min C <sub>3</sub> H <sub>6</sub> treatment	G-Si(O)(24%)-C30m
◇ C <sub>3</sub> H <sub>6</sub> treatment before and after Si deposition	G-C-Si(20%)-C30m

The silicon contents of the Si-G@C nanocomposites listed in table 5.5 were quantified by thermogravimetric analysis coupled with mass spectrometry (TG-MS) in synthetic air and EA. The masses and ion currents of CO and CO<sub>2</sub> during TG-MS analysis of samples with propene treatment for 15 min (G-Si(20%)-C15m), 30 min (G-Si(17%)-C30m), 60 min (G-Si(19%)-C60m), 90 min (G-Si(19%)-C90m) and annealing without a-C deposition (G-Si(21%)-60m) are shown in figure 5.2. The developing masses and the ion currents of CO and CO<sub>2</sub> over the temperature range from 25 °C to 1500 °C for all samples listed in table 5.5 are depicted in SI (fig. 8.27). Regarding the mass development, the sample without a-C deposition shows a constant mass up to 650 °C with subsequent continuous mass decay. The samples with a-C deposition exhibit a mass loss at lower temperatures around 580 °C, which is more strongly pronounced for longer propene treatments. Around this temperature an additional ion current signal which can be assigned to CO and CO<sub>2</sub> appears for the propene treated samples. This indicates that the mass loss is correlated to the burning of carbon, which is different from that of the graphite substrate. Hence, it can be concluded that this carbon is generated during the propene treatment. When the material is further heated, the mass loss caused by the graphite burning is followed by a mass increase attributable to the oxidation of silicon to SiO<sub>2</sub>. Following, the silicon content can be estimated by  $m(\%)_{\text{Si}} = \frac{m(\%)_{\text{TG}}}{M_{\text{SiO}_2}} \cdot M_{\text{Si}}$ , with  $m(\%)_{\text{TG}}$  being the final mass evaluated by TG-MS and  $M_{\text{Si}}$  and  $M_{\text{SiO}_2}$  being the molar masses of silicon and SiO<sub>2</sub>, respectively. The resulting silicon contents are listed together with the contents obtained from EA in the SI (table 8.4). For 2 h silicon deposition the silicon contents vary between 17 and 21 wt.-% for EA and 20 – 23 wt.-% for TG-MS analysis. The sole exception is the sample which was exposed to air before a-C deposition, exhibiting a silicon content of 24 wt.-%.

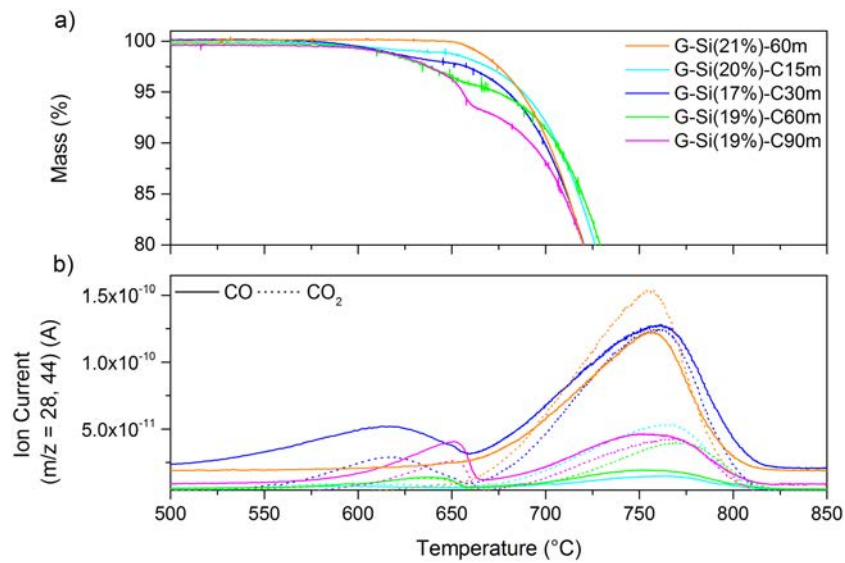


**Figure 5.2:** a) Sample mass and b) ion current for CO ( $m/z = 28$ , solid lines) and CO<sub>2</sub> ( $m/z = 44$ , dotted lines) as a function of temperature for samples treated for 15, 30, 60 and 90 min with C<sub>3</sub>H<sub>6</sub> and 60 min annealing under vacuum.

As shown in the previous chapter the silicon deposited at 485 °C is amorphous and it becomes crystalline (c-Si) when it is annealed at 800 °C. The powder XRD patterns of the samples listed in table 5.5 (fig. 5.3) all display the appearance of c-Si reflections. This is independent of the 800 °C treatment time or whether propene gas feed is applied. The reflections are slightly more pronounced for G-Si(19%)-C90m, G-Si(O)(24%)-C30m and G-C-Si(20%)-C30m, indicating a higher degree of silicon crystallinity. The sample G-Si(12%)-C30m exhibits less pronounced and broadened silicon reflections due to the lower silicon content.

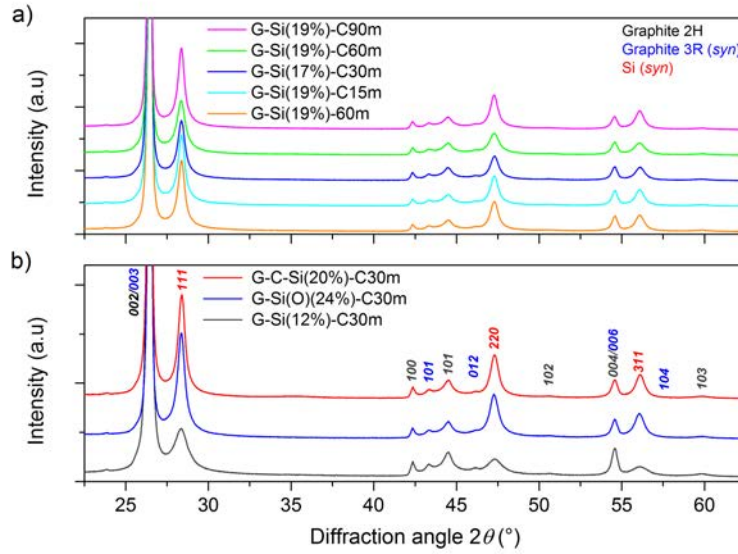


**Figure 5.3:** Powder XRD patterns for a) samples treated for 15, 30, 60 and 90 min with  $C_3H_6$  and 60 min annealing under vacuum and b) G-Si(12%)-C30m, G-Si(O)(24%)-C30m and G-C-Si(20%)-C30m.

A more precise impression of the deposited a-C can be obtained from Raman analysis. The D- and G-band region can be deconvoluted in five peaks for soot materials: G ( $\sim 1580\text{ cm}^{-1}$ ) caused by ideal graphitic lattice structures, D1 ( $\sim 1350\text{ cm}^{-1}$ ), D2 ( $\sim 1620\text{ cm}^{-1}$ ) and D4 ( $\sim 1200\text{ cm}^{-1}$ ) attributed to disordered graphitic lattice vibrations and D3 ( $\sim 1500\text{ cm}^{-1}$ ) ascribed to an a-C vibration mode.<sup>[230]</sup> Accordingly, the Raman spectra of the samples can be fitted as illustrated in figure 5.4 a). Regarding the D- and G-band region of the samples, with successive increasing propene treatment time all samples show an increase in the contribution of disordered and amorphous carbon bands compared to the annealed reference sample without propene treatment (G-Si(21%)-60m) (fig. 5.4 b). The D3 band integral in relation to the all-over integral from 1000 to  $2000\text{ cm}^{-1}$  is shown in figure 5.4 c). The D3 band integral increases with increasing propene treatment time, which indicates an increase in a-C content and is consistent with the observations from TG-MS analysis. The Raman spectra for 200 –  $3000\text{ cm}^{-1}$ , including those of the samples G-Si(O)(24%)-C30m and G-C-Si(20%)-C30m are plotted in SI (fig. 8.28).

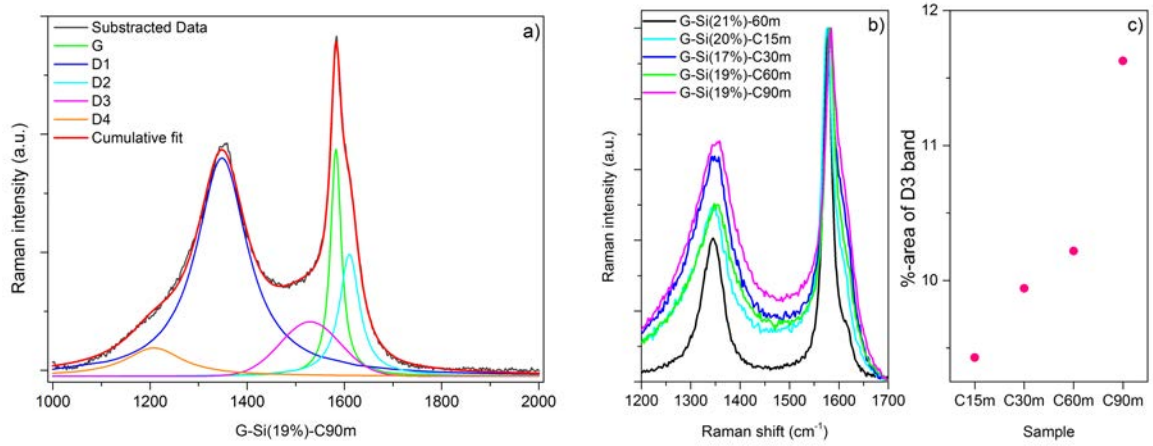


**Figure 5.4:** a) Example fitting of sample G-Si(19%)-C90m, b) Raman spectra of the samples treated for 15, 30, 60 and 90 min with C<sub>3</sub>H<sub>6</sub> and 60 min annealing under vacuum and c) percentage share of the D3 band integral of the samples obtained from 15, 30, 60 and 90 min C<sub>3</sub>H<sub>6</sub> treatment.

The SEM image of G-Si(19%)-60m (fig. 5.5 a) depicts a graphite flake with sintered silicon droplets. The sintering of a-Si deposited at 485 °C upon annealing at 800 °C leads to an increased droplet size and crystallinity, as shown in the previous chapter. Such sintering is also observable in the SEM images of G-Si(20%)-C15m, G-Si(17%)-C30m, G-Si(19%)-C60m and G-Si(19%)-C90m with 15 – 90 min propene treatment (fig. 5.5 b-e). However, neither the droplet shape, nor the droplet size correlate with the gas exposure or treatment time. This is due to inhomogeneous sintering of the silicon. The variation of the silicon sintering within one sample is illustrated in figure 5.6 a) and several pictures in the SI (fig. 8.29-8.32). The sample G-Si(19%)-C90m stands out due to big silicon agglomerates (fig. 5.5 e). This goes in line with the more pronounced silicon reflections observed in the related XRD pattern (fig. 5.3 a). Acquired at higher magnification, this sample reveals an abrasive surface structure on the silicon droplets (fig. 5.6 b), which could be attributed to a thicker coverage with a-C. This is in accordance with the exceptionally stronger mass decay observed in TG-MS analysis (fig. 5.2) and the increased contribution of the D3 band integral fitted in the Raman spectrum (fig. 5.4 c). As distinct from the other propene treated samples, the SEM images of G-C-Si(20%)-C30m, which was treated with propene before and after silicon deposition, show a remarkably homogeneous distribution of clearly defined silicon droplets (fig. 5.5 f) and 8.29 c).

To obtain a better impression of the a-C coverage several samples were investigated by TEM analysis. TEM images of the G-Si(12%)-C30m sample (fig. 5.7) reveal graphitic planes with polycrystalline silicon droplets, which are covered by an amorphous layer. This layer was identified by EDX mapping to consist of carbon (fig. 5.8). On average, an a-C layer thickness of ca. 3 nm was observed for this sample and no significant oxygen content was detectable. Hence, the 30 min propene treatment avoided the formation of a SiO<sub>x</sub> surface layer upon air exposure of the sample.

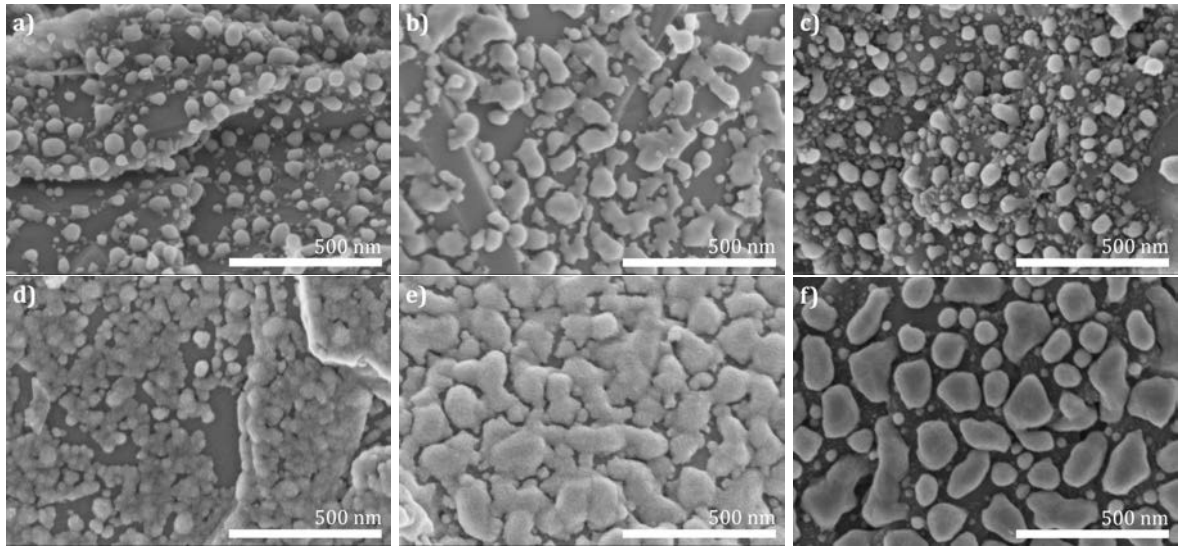


**Figure 5.5:** SEM images of a) G-Si(19%)-60m, b) G-Si(20%)-C15m, c) G-Si(17%)-C30m, d) G-Si(19%)-C60m, e) G-Si(19%)-C90m and f) G-C-Si(20%)-C30m.

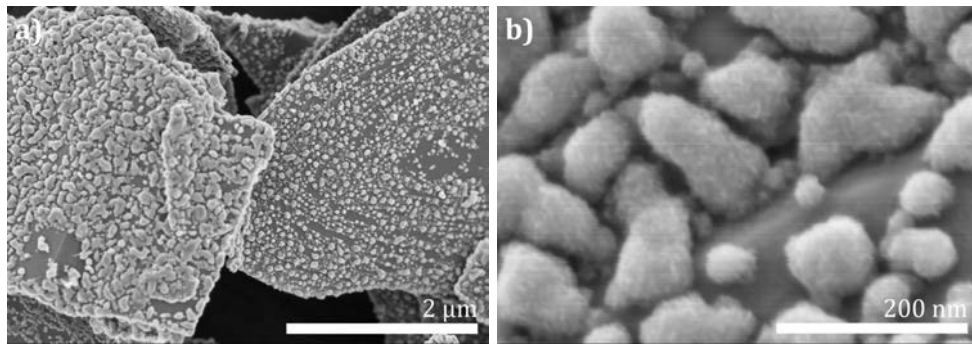


**Figure 5.6:** SEM images of a) G-Si(20%)-C15m with pronounced inhomogeneous silicon sintering on two graphite flakes and b) G-Si(19%)-C90m exhibiting abrasive-appearing silicon surface.

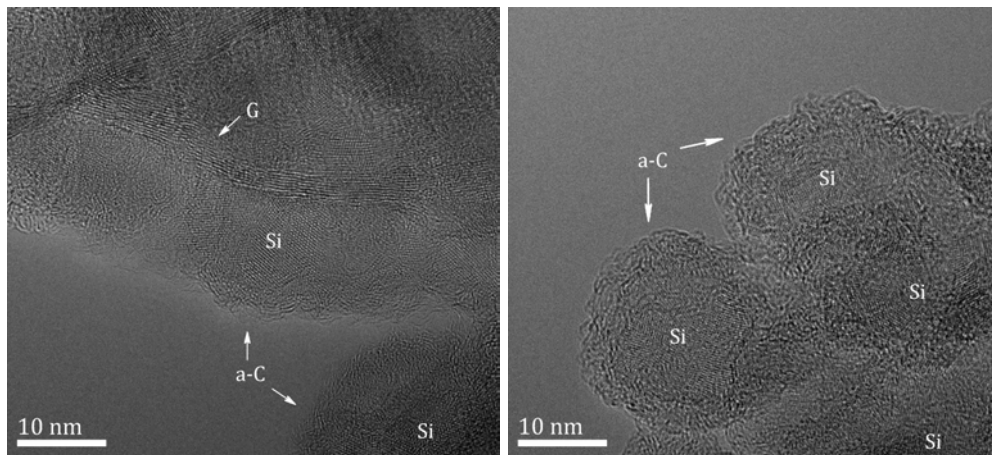


**Figure 5.7:** TEM images of G-Si(12%)-C30m.



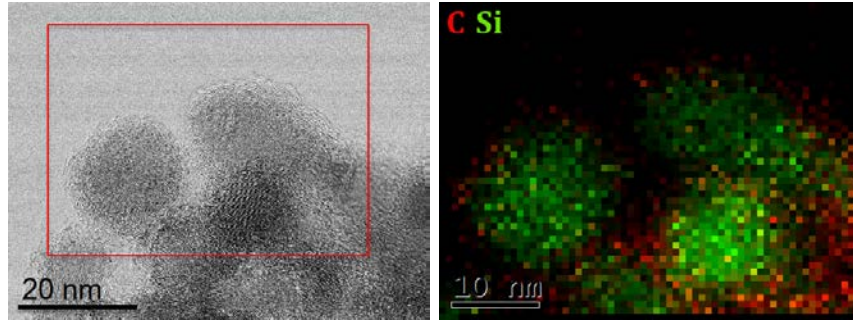


**Figure 5.8:** TEM image of G-Si(12%)-C30m with corresponding EDX elemental map of Si and C.

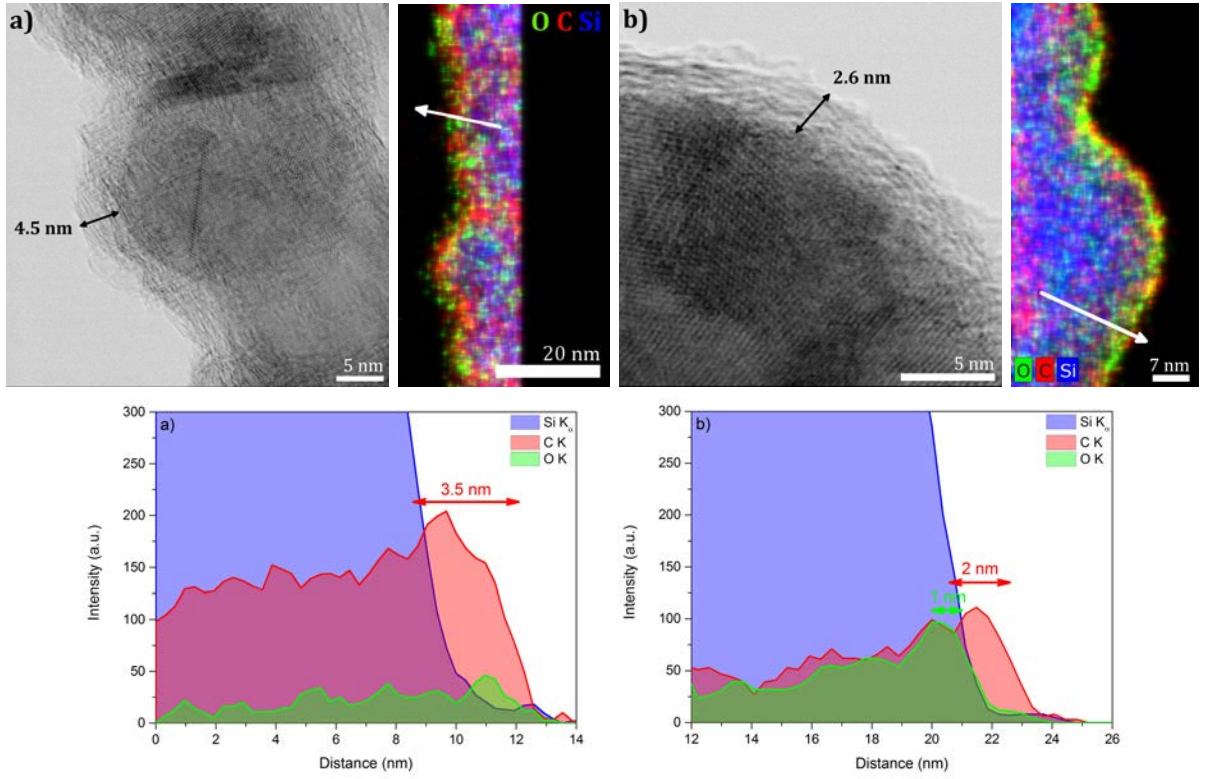


**Figure 5.9:** STEM BF images with EDX elemental map and line scan of a) G-Si(19%)-C60m (left) and b) G-Si(O)(24%)-C30m (right).

In agreement with this, the sample obtained from 60 min propene treatment (G-Si(19%)-C60m) does not exhibit a  $\text{SiO}_x$  layer either, as is depicted in the elemental map and EDX line scan in figure 5.9 a). In the respective STEM bright field (BF) image an a-C layer of 4.5 nm thickness was observed. In contrary, in the line scan an a-C layer of 3.5 nm thickness is identifiable. The difference of 1 nm can be attributed in a large part to an observed shrinkage of the a-C layer thickness during EDX investigation. The sample G-Si(O)(24%)-C30m was exposed to air for 60 h before the a-C was deposited. The related STEM BF image, elemental map and EDX line scan are shown in figure 5.9 b). For the G-Si(O)(24%)-C30m sample a clear oxygen signal was detectable, which is visible in the line scan as an oxygen-rich interphase of about 1 nm thickness

on the silicon surface below the a-C layer. The a-C surface layer thickness of 2.6 nm is similar to the a-C layer thickness of the sample G-Si(12%)-C30m, which also was treated with propene for 30 min. This indicates, firstly, that the deposition of a-C is reproducible and, secondly, that the propene treatment is capable to prevent the silicon surface from oxidation by air contact.

Summed up, a-C was deposited in various contents on graphite-silicon nanocomposites. The high propene treatment temperature led to sintering of the silicon deposit and therefore entailed an increase in the silicon crystallinity. The a-C content and layer thickness was controllable by the deposition time and the propene treatment was shown to avoid silicon surface oxidation upon air exposure.

### 5.3.2 Influence of the a-C coverage on the battery performance

To investigate the impact of the a-C coverage on the electrochemical performance of the batteries, anodes obtained from material treated for 15 min (G-Si(20%)-C15m), 30 min (G-Si(17%)-C30m), 60 min (G-Si(19%)-C60m) and 90 min (G-Si(19%)-C90m) with propene and the sample with 60 min annealing under vacuum (G-Si(21%)-60m) were cycled. The cycling raw data is plotted in the SI (fig. 8.33). The derived radar plot in figure 5.10 depicts seven expressive parameters of the cycling test. The comparison of the 3<sup>rd</sup>, 52<sup>nd</sup> and 102<sup>nd</sup> cycle gravimetric discharge capacity illustrates the capacity fade. It is clearly visible how much capacity is provided by the battery in the beginning and how much is lost after 50 and 100 cycles. A re-increase in the 103<sup>rd</sup> compared to the 102<sup>nd</sup> cycle gravimetric discharge capacity indicates that the capacity losses in the final capacity are at least partially reversible for slower C-rates. The capacity retention (CR) is the ratio of the final to the initial capacity and therefore is a direct measure of how much capacity is lost over cycling. The 1<sup>st</sup> cycle CE assigns the amount of charges lost in the very first cycle at C/20 and therefore reveals differences in the reaction of the fresh anode material with the electrolyte. The standard deviation of the CE ( $\sigma_{CE}$ ) is derived from the CEs generated at 1C, excluding all CE outliers above 120 %. It illustrates the steadiness of the CE over cycling. Higher values in  $\sigma_{CE}$  are an indication for either outliers in the CEs or occurring local decays in the CEs.

The initial gravimetric discharge capacities for the five samples are ordered according to their silicon content, i.e. samples with higher silicon content also provide a higher gravimetric capacity in the beginning of the cycling. However, the samples' capacities decay differently. While for the battery containing the uncovered nanocomposite (G-Si(21%)-60m) only 54 % of the initial capacity are maintained after 50 cycles, for the G-Si(19%)-C60m battery 75 % of the initial capacity are retained. In the 102<sup>nd</sup> cycle all batteries containing a-C covered samples exhibit similar capacities, except for the G-Si(17%)-C30m battery, which provides less capacity. When the current rate (C-rate) is reduced in the 103<sup>rd</sup> cycle the capacities of all batteries converge and re-increase, independent of the a-C coverage, indicating that the diverging capacity loss is not due to irreversible processes, but to kinetic hindrance. From the CRs it is visible that in

the mean the capacity decay is decreased for batteries containing a-C coated anodes. While the battery without a-C coverage on the nanocomposite shows a lower CR ( $\sim 37\%$ ), the samples with 15 and 60 min propene treatment provide the highest CRs ( $\sim 43\%$ ) in the row.

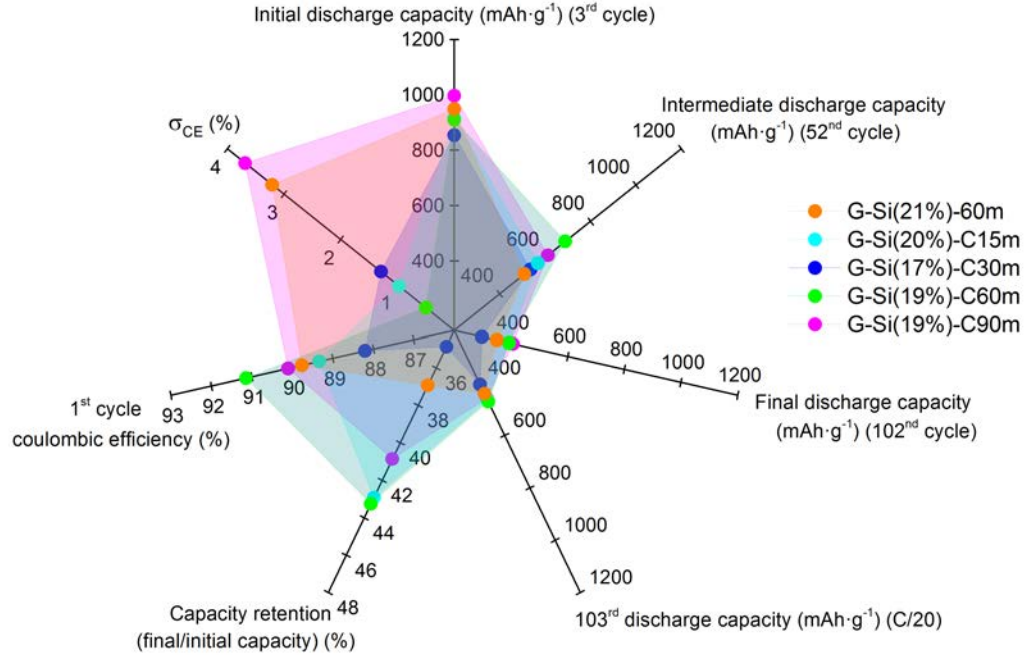


**Figure 5.10:** Radar plots of the performance of batteries containing anodes from  $C_3H_6$  treatment for 15 (G-Si(20%)-C15m), 30 (G-Si(17%)-C30m), 60 (G-Si(19%)-C60m) and 90 min G-Si(19%)-C90m) and the sample annealed under vacuum (G-Si(21%)-60m).

The 1<sup>st</sup> cycle CE values vary in a small region and without direct correlation to the propene treatment time. In the previous chapter it was shown that the 1<sup>st</sup> cycle CE correlates with the silicon coverage of the graphite surface. More precisely, the 1<sup>st</sup> cycle CE of pure graphite was low (81 %), while highly silicon covered graphite exhibited higher 1<sup>st</sup> cycle CE values (93 %). This is attributed to the formation of a stable solid electrolyte interphase (SEI) on graphite cycled in ethylene carbonate-based electrolytes in the 1<sup>st</sup> cycle, which does not occur in this manner on silicon.<sup>[147,200]</sup> The samples covered with a-C exhibit 1<sup>st</sup> cycle CEs ranging from 88 – 91 %. Hence, the a-C coverage does not seem to significantly influence the SEI formation in the 1<sup>st</sup> cycle. A high value in the  $\sigma_{CE}$  can be caused either by CE progressions with a strongly distinct minimum or a significant number of outliers between 100 – 120 %. The latter is caused either by a continuous current flow in the delithiation constant voltage protocol sequence (at 2 V) or by the failure to reach the 2 V border within the constant current protocol sequence. The G-Si(19%)-C90m battery exhibits plenty of these outliers in the first cycles, yielding in an unstable cycling performance. The annealed sample without a-C coverage (G-Si(21%)-60m) on the contrary exhibits a distinct CE loss around the 31<sup>st</sup> cycle (SI fig. 8.33). In the previous chapter this loss was characteristic for batteries containing anodes with highly crystalline silicon. However, it was derived from XRD analysis that, regarding the silicon crystallinity, the propene

treated samples do not differ from the annealed sample. This implies that the a-C coverage is capable to prevent the strong CE loss of batteries containing anodes with distinct silicon crystallinity.

In the radar plot resume in figure 5.11, the electrochemical performance of batteries containing the sample exposed to air before a-C coverage (G-Si(O)(24%)-C30m) and the sample treated with propene before and after silicon deposition (G-C-Si(20%)-C30m) are compared to the performance of the G-Si(17%)-C30m battery. In contrast to the G-Si(17%)-C30m nanocomposite, the sample exposed to air before a-C coverage exhibits a  $\text{SiO}_x$  surface layer on the silicon. Regarding the initial capacity, the oxidised sample surpasses the G-Si(17%)-C30m sample, however, this can be attributed to the higher silicon content. Moreover, both samples exhibit a similar decay and therefore a similar CR. The 1<sup>st</sup> cycle CE is higher for the oxidised sample, which may indicate a slightly different reactivity of the fresh anode towards the electrolyte. However, the G-Si(O)(24%)-C30m battery standard deviation of the CE ( $\sigma_{\text{CE}}$ ) is comparable to the other samples. Altogether, this is in accordance with the reported observation that the anode silicon surface oxidation does not have a significant negative effect on the battery cycling performance.<sup>[231]</sup> Compared to the battery containing silicon covered with a-C, the battery containing silicon encapsulated in a-C (G-C-Si(20%)-C30m) stands out due to its very high CR of nearly 48 %. The cycling raw data and the differential capacity plots recorded for all samples in the 2<sup>nd</sup> and 103<sup>rd</sup> cycle are given in SI (fig. 8.33, 8.34 and 8.35).

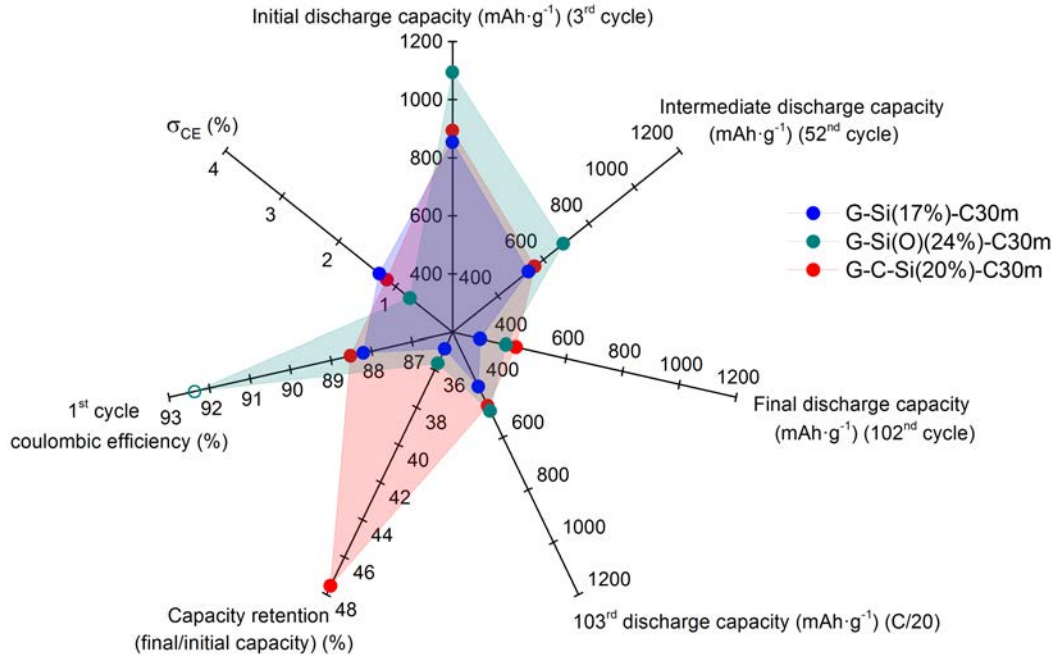


**Figure 5.11:** Radar plots of the performance of batteries containing anodes from  $\text{C}_3\text{H}_6$  treatment for 30 min (G-Si(17%)-C30m), the air exposed sample (G-Si(O)(24%)-C30m) and the twice  $\text{C}_3\text{H}_6$  treated sample (G-C-Si(20%)-C30m). The 1<sup>st</sup> cycle CE of the G-Si(O)(24%)-C30m battery was taken from a replica battery.

Figure 5.12 depicts the amount of capacity provided per wt.-% silicon, averaged over 100 cycles for batteries containing anodes from 15, 30, 60 and 90 min propene treatment, from the annealed sample and from the sample treated with propene before and after silicon deposition. The G-Si(19%)-C60m battery provides the highest averaged gravimetric discharge capacity. With  $1741 \text{ mAh} \cdot \text{g}_{(\text{Si})}^{-1}$  it provides around one and a half times the capacity supplied by the battery containing the uncovered silicon material (G-Si(21%)-60m,  $1112 \text{ mAh} \cdot \text{g}_{(\text{Si})}^{-1}$ ). Even though the G-C-Si(20%)-C30m battery exhibits the highest CR, it cannot achieve the highest gravimetric capacity per silicon, but  $1378 \text{ mAh} \cdot \text{g}_{(\text{Si})}^{-1}$ .

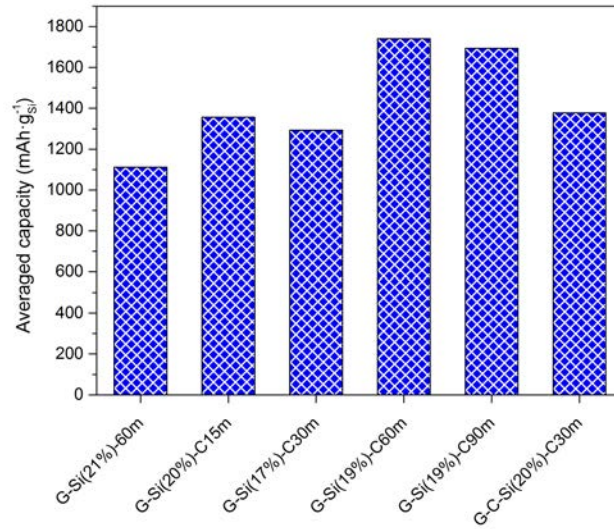


**Figure 5.12:** Averaged discharge capacity per silicon and cycle of batteries containing anodes from  $\text{C}_3\text{H}_6$  treatment for 15 (G-Si(20%)-C15m), 30 (G-Si(17%)-C30m), 60 (G-Si(19%)-C60m) and 90 min (G-Si(19%)-C90m), the sample annealed under vacuum (G-Si(21%)-60m) and the twice  $\text{C}_3\text{H}_6$  treated sample (G-C-Si(20%)-C30m).

The C-rate capability test of the a-C content variation series, G-Si(O)(24%)-C30m and G-C-Si(20%)-C30m is shown in figure 5.13. This test reveals how much of the initial capacity achieved at low C-rates can, firstly, be maintained when using faster C-rates and, secondly, be re-obtained after the stress test. During the C-rate capability test the C-rate is stepwise increased from C/10 to 10 C and reduced back to C/10 for the last set of cycles. A strong reduction in the capacity for increasing C-rates refers to sluggish lithiation kinetics, caused, for example, by low ion and electric conductivity. For evaluation of the capacity changes, the capacity is plotted in relation to the discharge capacity of the very first cycle. The annealed sample without a-C coverage (G-Si(21%)-60m) exhibits the lowest capacities for increased C-rates and shows the lowest capacity recovery when the C-rate is reduced back to C/10. This coincides with the improvement of the electrical conductivity of the anode materials reported for a-C coatings.<sup>[232]</sup> Among the propene treated nanocomposites, the G-Si(19%)-C60m battery provides the highest capacities under increased C-rates and the highest capacity recovery. This goes well in line with the previously observed superior performance of G-Si(19%)-C60m batteries

in regular cycling. The capacities of the other batteries are located in between the G-Si(21%)-60m and G-Si(19%)-C60m battery without identifiable trend.

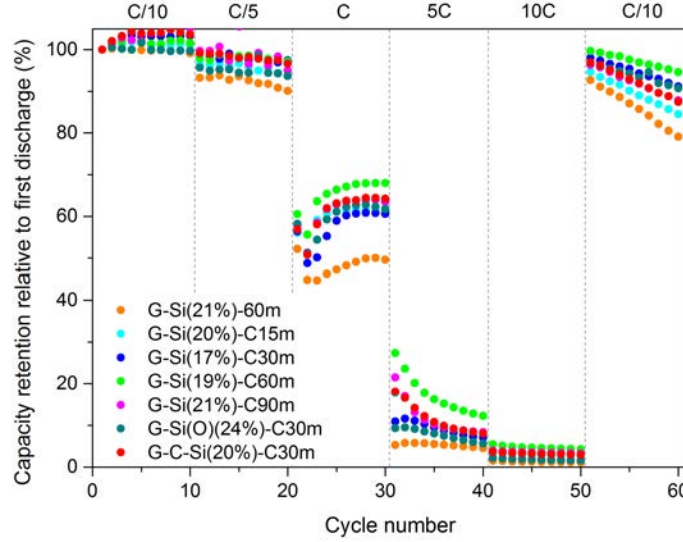


**Figure 5.13:** C-rate capability test of batteries containing anodes from  $C_3H_6$  treatment for 15 (G-Si(20%)-C15m), 30 (G-Si(17%)-C30m), 60 (G-Si(19%)-C60m) and 90 min (G-Si(19%)-C90m), the sample annealed under vacuum (G-Si(21%)-60m) and the twice  $C_3H_6$  treated sample (G-C-Si(20%)-C30m).

Altogether the deposited a-C layer had a positive effect on the battery performance. Especially the batteries containing G-Si(19%)-C60m anodes provided a high CR and the highest averaged discharge capacity per cycle and silicon content over 100 cycles. Also, the batteries comprising anodes made from twice propene treated material (G-C-Si(20%)-C30m) exhibited an outstandingly high CR. This improvement could neither be attributed to distinct differences in the 1<sup>st</sup> cycle SEI formation, nor to the prevention of the silicon surface oxidation. Considering the results from regular cycling tests and C-rate capability tests, the introduced a-C coverage more likely provided the enhancement in the role of a cohesive and conductive agent.

### 5.3.3 Evolution of the anode material upon electrochemical cycling

After cycling, a G-Si(19%)-60m battery with low CR, a G-Si(19%)-C60m battery with intermediate CR and a G-C-Si(20%)-C30m battery with the highest CR were dismantled in the discharged state and the anodes were evaluated using SEM. All anodes exhibit an irregular surface with darker and brighter areas, as depicted in figure 5.14 a) for the annealed sample without a-C coverage. Images of higher magnification of the dark and bright regions are shown in figure 5.14 b) and 5.14 c). The image of the brighter area reveals a rough surface structure, while the image of the darker area exhibits a flat surface with cracks. Comparable results were discussed in the previous chapter, where it was shown that this cracked layer grows with the cycle number and contains fluorine, phosphorous, oxygen, carbon and lithium, but no silicon.



It was identified as SEI, built up from electrolyte decomposition products and the silicon underneath the SEI is only detectable in the cracks or on the uncovered regions, like the bright areas.

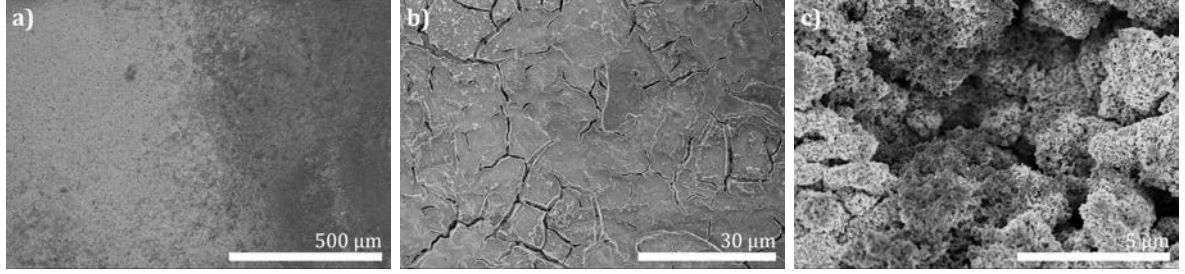


**Figure 5.14:** SEM images of a) a cycled G-Si(21%)-60m anode with images of higher magnification of b) the dark and c) the bright region.

After cycling, the anode obtained from the sample treated with propene for 60 min (G-Si(19%)-C60m) also exhibits an SEI with cracks. It does not cover the surface continuously, but is formed locally and the fluorine signal for these regions prevails the signal of silicon (fig. 5.15 a, b). Upon higher magnification the SEI with its cracks is clearly visible (fig. 5.15 c) and elemental mapping with an interaction depth of around 700 nm confirms that a silicon signal can only be acquired in the cracks (SI fig. 8.36). In between the SEI islands, on rougher regions (fig. 5.15 d), a silicon signal is detectable using EDX with the same acceleration voltage, which indicates a thinner SEI (SI fig. 8.37).

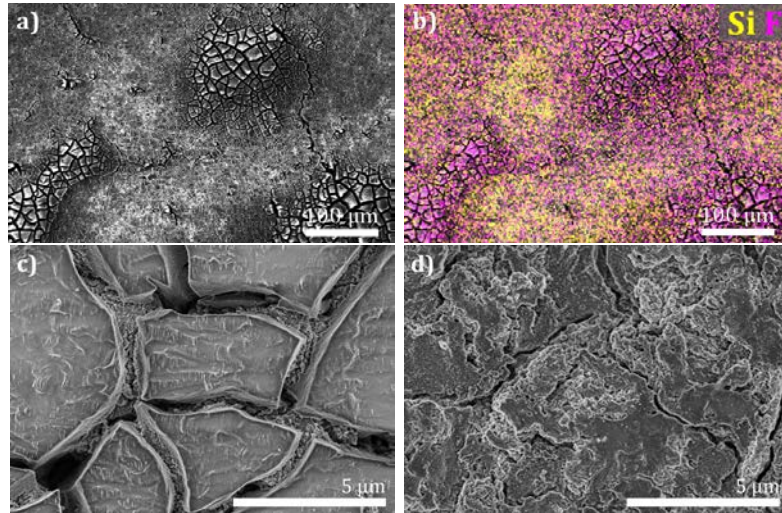


**Figure 5.15:** a) Secondary electron image with b) corresponding EDX elemental maps of silicon and fluorine (700 nm interaction depth) and c, d) SEM images of cycled G-Si(19%)-C60m anode.

For the sample treated with propene before and after silicon deposition (G-C-Si(20%)-C30m), which exhibited the highest CR, significantly less SEI is observed using SEM analysis. The cracked SEI layer appears thinner and the cracks exhibit a different shape as can be seen in figure 5.16 c) and in SI (fig. 8.38). Moreover, several spots on the anode surface appear

completely uncovered with SEI (fig. 5.16 d). An elemental map reveals more distributed silicon and fluorine signals over the surface (fig. 5.16 b). This supports the assumption that the formed SEI on this sample is thinner compared to the one formed on the G-Si(19%)-C60m anode. In turn this indicates that less SEI was formed, which is in accordance with the observed smaller capacity loss.

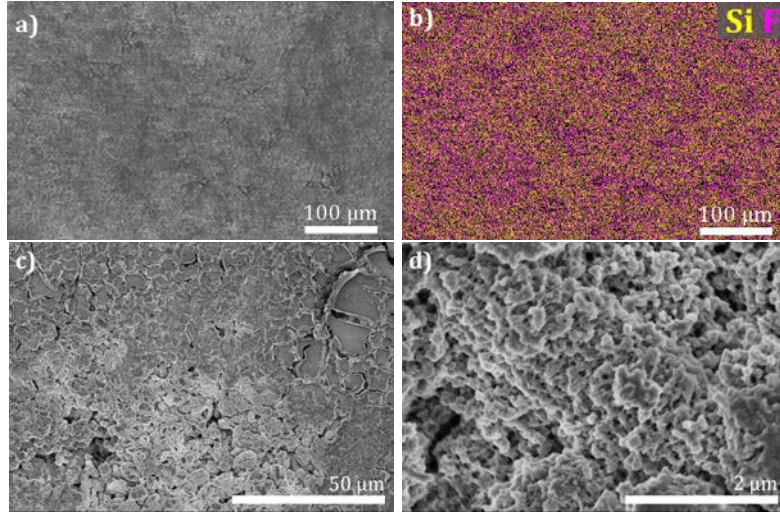


**Figure 5.16:** a) Secondary electron image with b) corresponding EDX elemental maps of silicon and fluorine (700 nm interaction depth) and c, d) SEM images of cycled G-C-Si(20%)-C30m anode.

Besides the SEI formation, the development of the a-C layer during cycling was of great interest. To explore the development of the a-C coverage, three cycled anodes were investigated using TEM. An anode obtained from G-Si(12%)-C30m was (dis-)charged only seven times to investigate the short-term changes (fig. 5.17). Therefore, a cycling protocol with a constant voltage sequence after each constant current charge and discharge sequence run at a current calculated appropriate to a C-rate of 1C was executed. The cycling raw data is plotted in SI (fig. 8.39). As can be seen in the high resolution (HR) TEM images (fig. 5.17 a, b) the materials original structure is preserved. This includes partially crystalline and amorphous silicon droplets being covered with an a-C layer of around 3 nm thickness. The elemental map in fig. 5.17 c) validates that the droplets contain silicon. The presence of c-Si reveals that the anode material was not completely lithiated, since after delithiation the crystalline silicon structure is destroyed.

The same material (G-Si(12%)-C30m) was (dis-)charged 27 times applying a current calculated appropriate to a C-rate of 1C in a constant current mode without a constant voltage sequence. The collected HRTEM image of the resulting material (fig. 5.18 a) depicts a mixed up structure. The initially polycrystalline silicon is amorphised and the original a-C surface coverage is now observed in fragments randomly distributed in the sample. Moreover, oxide species formed on the silicon during cycling as can be seen in the elemental mapping. This strongly suggests silicon-electrolyte contact during the cycling, leading to oxidation of the silicon. The shape



of the silicon also changed, so that the initial silicon spheres of around 10 nm diameter more resemble outstretched layers.

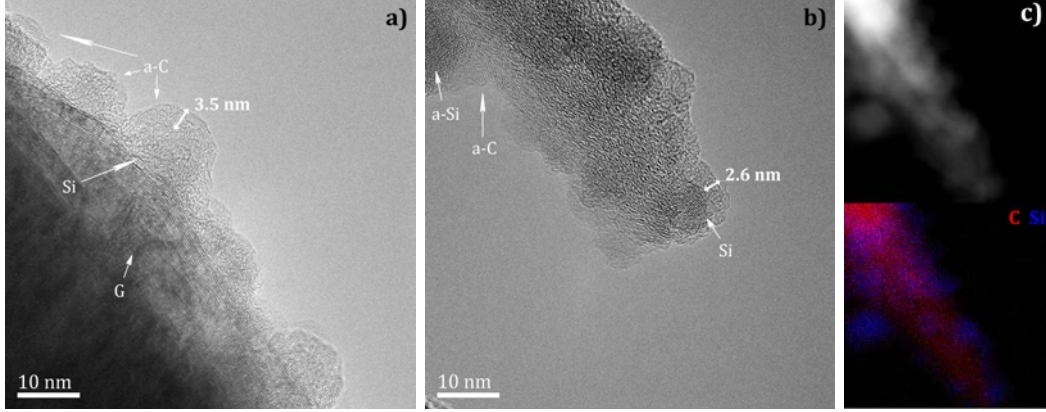


**Figure 5.17:** a, b) HRTEM and c) high-angle annular dark-field (HAADF) image with corresponding EDX elemental maps of carbon and silicon of G-Si(12%)-C30m material after 7 cycles.

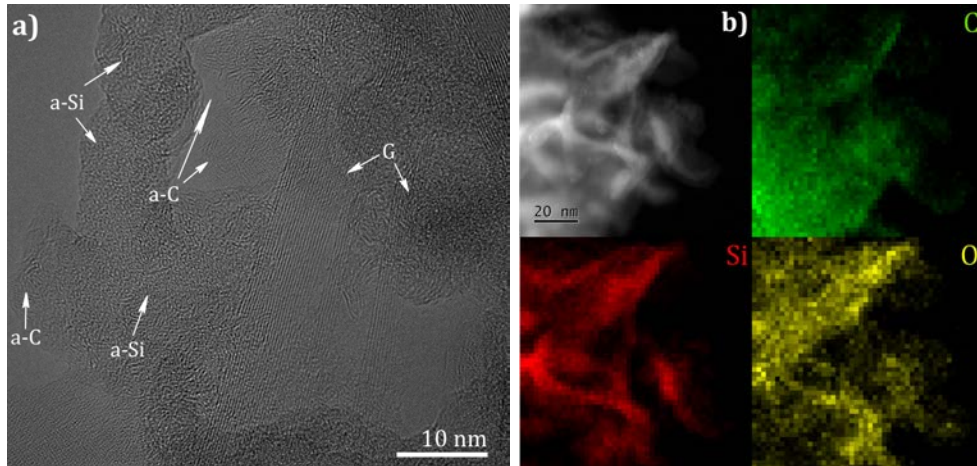


**Figure 5.18:** a) HRTEM and b) HAADF image with corresponding EDX elemental maps of carbon, silicon and oxygen of G-Si(12%)-C30m material after 27 cycles.

An STEM BF image of a G-Si(19%)-C60m anode cycled for 103 cycles, whose battery provided the best cycling performance, can be seen in figure 5.19 a). As observed for the previous anode material, the sample is mostly amorphous and no indication of a remaining a-C layer is detectable. Likewise, oxide species are formed on the silicon, indicating silicon-electrolyte interaction. Despite the deposited a-C layer was shown to be only maintained for a few cycles, the battery performance was improved compared to batteries containing nanocomposites which were not covered with a-C. This supports the assumption that the batteries stabilised capacity is not caused by a continuous silicon surface protection by the a-C, but it is very likely that the improved performance is caused by increased conductivity and cohesion of the anode material by blending of a-C with the silicon during cycling.

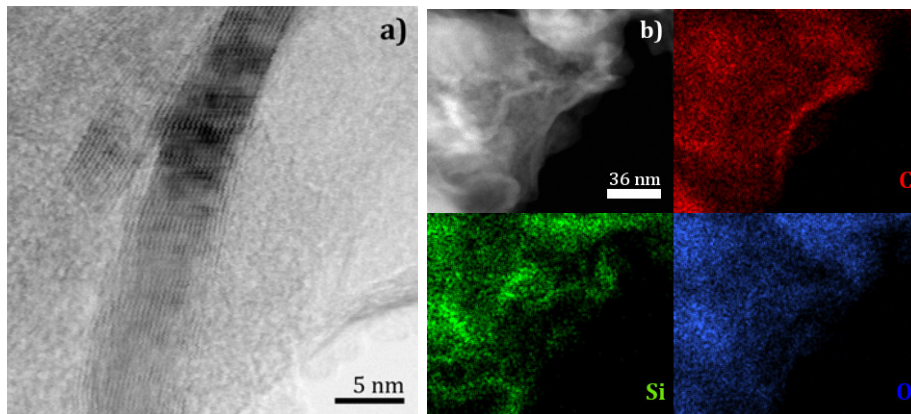


**Figure 5.19:** a) STEM BF and b) HAADF image with corresponding EDX elemental maps of carbon, silicon and oxygen of G-Si(19%)-C60m material after 103 cycles.

## 5.4 Conclusion

The combination of silane and propene pyrolysis in a rotating LPCVD setup opens a large variety of accessible syntheses of nanostructured silicon-amorphous carbon based nanocomposites, with the silicon and amorphous carbon (a-C) content being controllable by the deposition time. When the graphite-silicon nanocomposites were covered with a-C, the silicon sintered due to the high treatment temperature and was prevented from oxidation when exposed to air. By propene treatment of the graphite substrate before and again after silicon deposition also sintered silicon was obtained, which was assumed to be completely encapsulated in a-C. The cycling stability of batteries containing silicon-based anodes was improved by the coverage with a-C. Yet, the improvement did not increase proportionally with the propene treatment time, but in a range from 15 – 90 min propene treatment there was an optimum for batteries containing the sample treated with propene for 60 min (G-Si(19%)-C60m). This nanocomposite exhibited an a-C coverage of about 4.5 nm thickness, provided an outstanding averaged capacity over cycling and a significantly improved C-rate capability. Also, batteries containing anodes obtained from the a-C encapsulated silicon samples exhibited a significantly improved capacity retention after 100 cycles. This was concurrent with an observed decreased solid electrolyte interphase formation. Post-mortem TEM analysis of the a-C covered anode materials, however, revealed that this a-C coverage could not be maintained over a larger number of cycles. Hence, the improved battery performance could not be ascribed to silicon surface protection by a-C, but was rather caused by the insertion of the carbons beneficial properties, like conductivity and mechanical stability, through blending of the a-C inside the anode material during cycling.

## 6 Beyond anode material modification - the effect of battery parameters on LIB performance

### Abstract

To further extend the scope of lithium-ion batteries (LIBs), not only new electrode materials are investigated, but other battery parameters are also modified, e.g. the battery housing, the cycling protocol and the electrolyte composition. In this chapter selected criteria of the battery cycling protocol and battery setup were adapted and their effect on the battery cycling performance, the evolution of the anode material and the processes inside the battery were evaluated. Therefore, firstly, the impact of the constant voltage sequence in a constant current – constant voltage-based cycling protocol on the battery performance and the solid electrolyte interphase development was investigated. Secondly, the lucrativeness of a restricted charging protocol, which is based on bounded lithiation of the anode, was examined. Thirdly, anodes were cycled in a modified battery setup combining an adapted protocol, an in-house designed battery housing and an electrolyte with additive. The resulting severe changes of the battery performance were correlated with electrochemical processes using differential capacity analysis and the solid electrolyte interphase morphology and composition using post-mortem analysis. Moreover, it was investigated whether the improvements in battery performance obtained through anode material optimisation were amplified or attenuated by the battery parameter optimisation.

### 6.1 Introduction

The application of silicon-based anodes in lithium-ion batteries (LIBs) as an alternative to the commercial graphite-based anodes has been intensively studied.<sup>[18,19,21,43,69]</sup> This is attributed to the attractive properties of silicon, including its high theoretical capacity ( $3579 \text{ mAh} \cdot \text{g}^{-1}$ ), which exceeds the gravimetric capacity of graphite by nearly one order of magnitude, its appropriate lithiation potential, its abundant supply and its low toxicity.<sup>[46–48,56]</sup> While good progress has already been achieved regarding the mechanical stability of silicon-based anodes by nanostructuring of the material and hybridisation with conductive and buffering materials, such as carbon, the batteries still do not meet the desired cycling stability.<sup>[48,199]</sup> Although the batteries exhibit high initial capacities they suffer from continuous capacity loss during cycling, which

is mainly attributed to two processes: firstly, the ongoing formation of an unstable solid electrolyte interphase (SEI), and secondly, the irreversible accumulation of lithium-ions (Li-ions) in the silicon material.<sup>[233]</sup> To counteract this capacity decay two main approaches beyond the modification of the anode material exist, namely the adjustment of the battery cycling protocol and the addition of electrolyte additives.<sup>[164]</sup>

For the cycling of LIBs two protocol types are widely applied: constant current (CC) and constant current – constant voltage (CC-CV), which in turn can be further modified by adaption of the current density or the cut-off voltage.<sup>[231]</sup> In a CC-CV protocol the CC-sequence is usually applied until a certain potential is reached. Then the CV-sequence follows, for which the reached potential is maintained constant for a defined time, state of charge or residual current.<sup>[134,139]</sup> This allows to achieve almost full battery capacity, however, it also entails an increase of the charging time. For industrial application the (dis-)charging current densities prescribed by the current rate (C-rate) are aimed to be as high as possible to achieve fast charging times. The C-rate is given as the number of hours required for a full charge, so C/2 implies a complete charge in 2 h and 2 C in half an hour.<sup>[46]</sup> However, for CC-based protocols a continuous increase in the C-rate inevitably leads to capacity decay, since silicon lithiation is a diffusion controlled process.<sup>[231]</sup> Cui et al.<sup>[160]</sup> reported a drastic decrease of the capacity for increasing C-rates for a silicon-carbon nanofibre composite, namely  $1700 \text{ mAh} \cdot \text{g}^{-1}$  for C/15,  $1300 \text{ mAh} \cdot \text{g}^{-1}$  for C/5 and only  $800 \text{ mAh} \cdot \text{g}^{-1}$  for 1C. High C-rates cause the initial cycles to be stable, but low in capacity, because the silicon is not saturated with lithium. In this case, fresh silicon is lithiated continuously with each cycle, so that the decay is merely postponed. Moreover, an overestimated C-rate can cause lithium plating.<sup>[133]</sup> As opposed to this, it was reported that the C-rate also should not be too low for graphite containing anodes to avoid graphite exfoliation.<sup>[234]</sup> Hence, the C-rate needs to be adapted in such a way that the electrolyte decomposition leading to the formation of a passivating film is faster than the solvent co-intercalation.

Incomplete anode lithiation is a widely applied method to increase the battery cycling life, since the anode lithiation sequence is known to exhibit a significant influence on the LIB cycling stability.<sup>[132–134]</sup> Therefore, two major techniques are employed: firstly, battery cycling in a more restricted potential window, and secondly, restricting the depth of charge. Both methods aim at reducing the silicon expansion and avoiding the crystallisation of  $\text{Li}_{15}\text{Si}_4$ , which is associated with material stress.<sup>[47,53,157]</sup> Restricting the depth of charge requires the pre-definition of the charge being injected into the battery. For a cut-off criterion of about 50 % of the total battery capacity a very stable performance for 200 cycles was reported.<sup>[63,138,139]</sup> However, Lee et al.<sup>[123]</sup> documented for silicon powder-based anodes that this technique only postpones the battery failure. It was shown for batteries with differently set cycling capacities that with the continuous decrease of the gravimetric capacity an increase in the achievable cycle number was obtained for batteries with lower fixed capacities. It was demonstrated for the restricted charging that the initial c-Si was not completely amorphised in the first cycle, but gradually consumed with increasing cycle number. This implies that the aim to lithiate all silicon to only

small lithium contents from the beginning on was not achieved using this method. Aiming at a better control of the degree of silicon lithiation, the battery cycling potential window was suggested to be restricted. It was reported that the formation of  $c\text{-Li}_{15}\text{Si}_4$  was avoided and cycle life was prolonged when the lithiation cut-off potential of LIBs containing silicon-carbon-based anode materials was increased from 0 – 5 mV to 50 – 70 mV vs.  $\text{Li}/\text{Li}^+$ .<sup>[160,165,231]</sup> This equivalently leads to a reduction in the battery capacity.<sup>[235]</sup> An increase of the lithiation potential from 0.01 V to 0.1 V reduced the gravimetric capacity of a silicon-carbon nanofibre composite from  $2000 \text{ mAh} \cdot \text{g}^{-1}$  to  $1300 \text{ mAh} \cdot \text{g}^{-1}$ .<sup>[160]</sup> The capacity of  $1300 \text{ mAh} \cdot \text{g}^{-1}$  was reported to be stable over 47 cycles, while the capacity of  $2000 \text{ mAh} \cdot \text{g}^{-1}$  was stable over 30 cycles. When the number of cycles is multiplied by the capacity, the batteries provide an overall capacity of  $61.1 \text{ Ah} \cdot \text{g}^{-1}$  and  $60.0 \text{ Ah} \cdot \text{g}^{-1}$ . Hence, the overall provided capacity is equal for both methods. This could indicate, that the silicon-based batteries cannot outlast a specific overall capacity, independent of the applied protocol.

As mentioned, another approach to counteract the battery capacity decay is the application of electrolyte additives. They are intended to form a continuous passivation layer on the silicon anode surface, preventing the shortening of the battery cycle life caused by continuous electrolyte decomposition and Li-ion consumption during the cycling.<sup>[236]</sup> The addition of fluoroethylene carbonate (FEC) to the widely used electrolyte mixture based on lithium hexafluorophosphate ( $\text{LiPF}_6$ ) dispersed in mixtures of ethylene carbonate (EC), diethyl carbonate (DEC) and dimethyl carbonate (DMC) improved the cycling stability and coulombic efficiency (CE) of silicon and silicon-carbon-based LIBs.<sup>[129,130,237–244]</sup> The exact mode of operation of the FEC on the SEI improvement, however, is still under investigation. The reported FEC contents in  $\text{LiPF}_6\text{-EC/DEC}$  mixture electrolytes range from 3 – 25 wt.-% and the resulting SEI was reported to be smoother, more uniform and to exhibit fewer cracks, as illustrated in figure 6.1.<sup>[129,237,238,245]</sup> Furthermore, the SEI was observed to be thicker with FEC containing electrolyte and at the same time the anode surface film resistance was reported to be significantly lower.<sup>[130,239]</sup> Similar results were documented for batteries with  $\text{LiPF}_6\text{-EC/DEC(/DMC)}$  electrolyte mixtures containing 2 – 25 % FEC, where besides the capacity stabilisation, dense SEI formation and decreased electrolyte decomposition occurred.<sup>[240–242]</sup> Moreover, a decreased overvoltage for (de-)lithiation and the prevention of HF diffusion through the FEC derived SEI have been reported.<sup>[243,244]</sup>

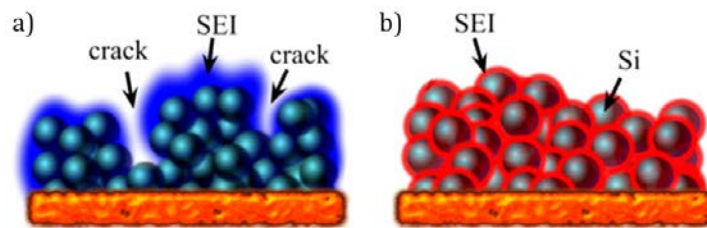


**Figure 6.1:** Illustration of SEI formed on silicon particles with  $\text{LiPF}_6\text{-EC/DEC}$  electrolyte mixture a) without FEC and b) with FEC.<sup>[129]</sup>

Moreover, the SEI exhibits another composition and undergoes less composition changes during cycling when FEC is added to the electrolyte.<sup>[127,246]</sup> While SEIs derived from FEC free electrolytes contain mainly carbon and oxygen species, attributable to EC and DEC decomposition products, SEIs derived from FEC containing electrolytes contain a larger amount of lithium fluoride (LiF) and, moreover, insoluble polymeric species.<sup>[129]</sup> The difference in the SEI composition is caused by the fact that the decomposition of FEC takes place at higher potentials and undergoes a different reductive decomposition reaction. In contrast to EC, the introduction of the fluorine in FEC leads to a drop in the highest occupied and lowest unoccupied molecular orbital energy levels of the former EC molecule, resulting in a higher reduction potential.<sup>[129,130]</sup> Therefore, FEC decomposes before EC and DEC are reduced. A reductive decomposition mechanism of FEC in 1 M LiPF<sub>6</sub> EC/ethyl methyl carbonate (EMC) was suggested by Jung et al.<sup>[131]</sup> (fig. 6.2). Several aspects are indicative of this mechanism. Firstly, formation of one mole CO<sub>2</sub> per mole FEC was observed. Secondly, the formation of a vinoxyl-radical is the most exergonic reaction<sup>[247]</sup>, and thirdly, the vinoxyl-radical constitutes a plausible reactant for the observed SEI components including the cross-linked polymers. However, the detailed reaction mechanism of the reductive decomposition of FEC is very complex and widely discussed in literature. A profound overview is given by Shkrob et al.<sup>[247]</sup> Independent of the detailed mechanism, whether one or two electron reduction, direct de-fluorination or initial ring opening, in most pathways reported a fluoride ion leaves the FEC molecule.<sup>[129,248]</sup>

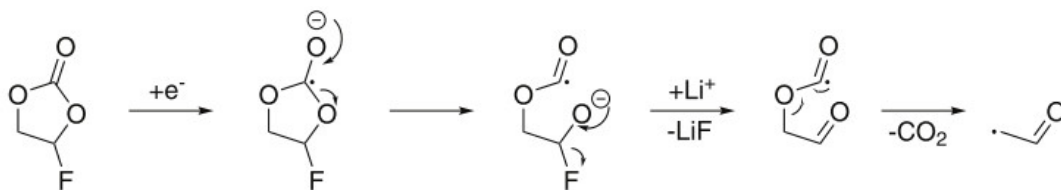


**Figure 6.2:** Proposed single electron reductive decomposition of FEC, resulting in a vinoxyl-radical, CO<sub>2</sub> and LiF.<sup>[131]</sup>

The resulting polymer, together with LiF, was reported to be responsible for the improved SEI stability.<sup>[130]</sup> LiF was attributed to stabilise the SEI through Li-F interactions in the SEI film component aggregates.<sup>[249]</sup> Herein, one fluorine atom was reported to be coordinated by approximately three lithium atoms. Another side effect of the fluoride formation during cycling is the elimination of Li<sub>x</sub>SiO<sub>y</sub> surface species, which are usually formed upon cycling in EC/DEC based electrolytes.<sup>[237,239,250]</sup> The SiO<sub>x</sub> is etched away, which was reported to increase the silicon reactivity. Furthermore, the thermal stability of fully lithiated nanosilicon-based batteries is enhanced from 153 to 200 °C with addition of FEC, due to polymerisation of FEC when it is in contact with Li<sub>x</sub>Si at elevated temperatures and thereby creates a robust "secondary SEI".<sup>[251]</sup> Regarding the optimum FEC content Wang et al.<sup>[130]</sup> reported 15 wt.-% FEC in 1 M LiPF<sub>6</sub> EC/DEC electrolyte exhibited the best performance in a series from 0 – 20 %. However, the FEC did not only affect the cycling stability, but also the C-rate capability, so that under higher currents (12.5 A · g<sup>-1</sup>) the capacity was nearly six times higher compared to FEC-free batteries.

Nevertheless, Jung et al. reported in a comparable study with 1 – 20 wt.-% FEC in a 1 M LiPF<sub>6</sub>-EC/EMC electrolyte mixture that the FEC was continuously consumed and that the capacity decayed suddenly as soon as the FEC was depleted.<sup>[131]</sup>

Therefore, the influence of the cycling protocol and the electrolyte on the anode materials developed in the former chapters is assessed in this chapter. More precisely, the effect of the lithiation CV-sequence in a CC-CV protocol, the supposed improvements of restricted silicon lithiation protocols and the influence of FEC on the battery performance and SEI formation are evaluated. Therefore, anodes of various properties, namely graphite/Si NP mixtures, silicon deposited by LPCVD on graphite and amorphous carbon covered graphite-silicon nanocomposite samples were cycled under distinct conditions in different electrolytes. Their electrochemical performance, the electrochemical processes and the SEI development were evaluated by comparison of the gravimetric capacities, overall capacities, differential capacity plots and post-mortem analysis.

## 6.2 Experimental

### 6.2.1 Graphite-silicon anode materials

The anode materials are listed in table 6.1. The silicon depositions were performed using an in-house designed LPCVD reactor setup comprised of a gas supply facility (N<sub>2</sub> and Ar, purity 99.999 %, Westfalen; SiH<sub>4</sub>, UHP, Air Liquide; C<sub>3</sub>H<sub>6</sub> containing 5 vol.-% 5.0 O<sub>2</sub>, 10 vol.-% 2.5 C<sub>3</sub>H<sub>6</sub> and 5.0 N<sub>2</sub> balance, Westfalen), a three zone hot wall oven (HTM Reetz GmbH), and a horizontally placed 1.2 m long by 4.5 cm in diameter quartz tube as main reaction chamber. All gases were dried and filtrated using a dry bed cartridge (MC200, MicroTorr). The depositions were performed using a rotary feedthrough motion quartz reactor insert (60 cm by 3.5 cm diameter) composed of a 10 cm baffled deposition chamber, reaction gas exhaust compartment, a glass frit, a quick connection holder and a rotary sealing (ALMA-M-KF-012-V-U, Alma) mounted on a KF40 “T” piece. Prior to deposition all gas lines were purged with N<sub>2</sub> at 2 l · min<sup>-1</sup> for 1 h. The reactor insert was typically filled with 1.5 g of graphite powder (KS6, Timcal) inserted inside the main reaction chamber and rotated at 2 rounds per minute. The main chamber absolute pressure was set to the required pressure and the oven heating zones were simultaneously heated from room temperature to the deposition temperature with a ramp of 5 °C · min<sup>-1</sup> under 10 sccm argon flow. The oven calibration revealed a  $T_{\text{sample}} = (20.80 + T_{\text{oven}} \cdot 0.99)$  (°C) correlation. In the following, given temperatures represent the set temperature ( $T_{\text{oven}}$ ). The setup was thermally stabilised for 30 min prior to deposition and cooled down to room temperature under a constant flow of argon after the deposition process. Silicon was deposited at 450, 485 or 550 °C, for 1 – 3 h, at 10 sccm SiH<sub>4</sub> flow. Carbon was deposited at 800 °C, for 1 h, at 9 mbar and 15 sccm C<sub>3</sub>H<sub>6</sub> flow. The products were ground in an agate mortar and stored inside an argon filled glove box (mBraun B790, O<sub>2</sub> ≤ 1 ppm Ionic

System Trace Oxygen Sensor Tos 3.0). The detailed powder characterisation can be found in the corresponding chapter listed in table 6.1.

**Table 6.1:** List of anode materials cycled in this chapter

sample	synthesis	properties
◇ G-SiNP-13% Si	graphite mixed with silicon	13 and 20 wt.-% silicon content
◇ G-SiNP-20% Si	nanoparticles	(see chapter 4)
◇ G-450C-18% Si	LPCVD SiH <sub>4</sub> at $T_{\text{oven}} = 450$ or	deposition of 18, 19 and 22 wt.-%
◇ G-485C-19% Si	485 °C for 2 h	amorphous silicon
◇ G-485C-22% Si		(see chapter 4)
◇ G-550C-13% Si	LPCVD SiH <sub>4</sub> at $T_{\text{oven}} = 550$ °C	deposition of 13, 22 and 30 wt.-%
◇ G-550C-22% Si	for 1, 2 and 3 h	crystalline silicon
◇ G-550C-30% Si		(see chapter 4)
◇ G-Si(19%)-C60m	LPCVD SiH <sub>4</sub> at $T_{\text{oven}} = 485$ °C	19 wt.-% polycrystalline silicon
	for 2 h at 1 mbar then C <sub>3</sub> H <sub>6</sub>	deposition covered with $\sim 4.5$ nm
	at $T_{\text{oven}} = 800$ °C for 1 h	a-C (see chapter 5)

### 6.2.2 Anode preparation and electrochemical tests

**Anode preparation** For the preparation of electrodes, polyacrylic acid (PAA,  $\leq 0.5$  % benzene, Sigma-Aldrich) was dispersed in an ethanol (Sigma-Aldrich) : 2-propanol ( $\geq 99.5$  %, Carl Roth) (6.25:1) mixture and stirred for 15 h. Then, carbon black (CB) (Super Conductive P, Alfa Aesar) and the ground sample were added (PAA : CB : sample = 1 : 1.5 : 10), stirred and treated in an ultrasonic bath. The prepared slurry was cast as a thin film on a 25  $\mu\text{m}$  thick copper foil (Cu58, bare, Schlenk) using a ZUA 2000 universal applicator (Zehntner) or a 4-sided film applicator (VF2169-013, 60 mm, TQC), respectively set to a film thickness of 120  $\mu\text{m}$ . The films containing silicon nanoparticles were produced under the same conditions using a mixture of KS6 and silicon nanopowder (Hongwu international group Ltd). Subsequently, the film was dried for 15 h at 80 °C in a vacuum oven (VTR 5022, Heraeus). Hereafter, anodes of 10 mm in diameter were punched out using a lever press, weighed and stored in an argon filled glovebox (mBraun B790, O<sub>2</sub>  $\leq 1$  ppm Ionic System Trace Oxygen Sensor Tos 3.0).

**Electrochemical testing** For the regular and the restricted lithiation battery tests (table 6.2 and 6.3) a modified stainless steel Swagelok tube fitting (fig. 6.3) was electrically insulated by a one-way 75  $\mu\text{m}$  Kapton foil (Dr. Dietrich Müller GmbH). The working electrode and counter electrode (metallic lithium, 10 mm diameter, Xiamen Tob New Energy Technology Co.) were sandwiched with two 25  $\mu\text{m}$  thick separators (C2500, Celgard Inc., USA) in between and wetted with 140  $\mu\text{l}$  of a solution of 1 M LiPF<sub>6</sub> dissolved in a mixture of ethylene carbonate : diethyl carbonate 1 : 1 wt.-% (Selectilyte LP40, Battery grade, BASF) electrolyte. The battery cell was sealed with nylon ferrules (Swagelok) on both sides inside the argon filled glovebox. For the modified battery testing 140  $\mu\text{l}$  of a solution of 1 M LiPF<sub>6</sub> dissolved in a mixture of ethylene carbonate, dimethyl carbonate and diethyl carbonate (EC:DMC:DEC = 1:1:1 wt.-%) (Selecti-



lyte LP71, BASF) mixed with 10 wt.-% fluoroethylene carbonate (FEC, 99 %, Sigma-Aldrich) were used as electrolyte and the batteries were cycled in a modified battery housing (fig. 6.3). The electrochemical measurements were carried out using a Biologic MPG-2 battery cyclier.

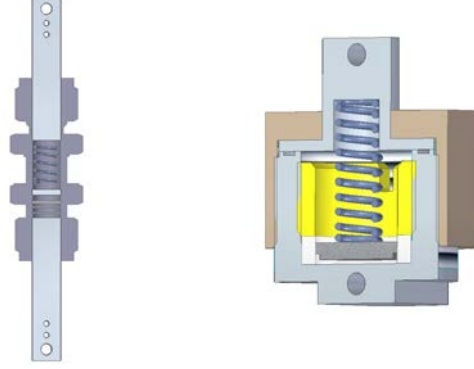


**Figure 6.3:** Illustration of the Swagelok (left) and self-designed (right) cell setup.

In the following tables (6.2-6.4) the cycling protocols are described. For the restricted charging protocol the charging, i.e. the anode lithiation, was reduced to 55 % of the batteries actual capacity. A detailed list of the batteries is given in SI (table 8.5).

**Table 6.2:** Cycling protocol and CC-CC-CV protocol

method	C-rate cycle 1-2; 103	C-rate cycle 3 -102	final lithiation potential (V)	CV- sequence (min)	final delithiation potential (V)	CV- sequence (min)
cycling	C/20	1C	0.005	90	2	60
CC-CC-CV	C/20	1C	0.005	-	2	60

**Table 6.3:** Restricted charging protocol

cycle	current (C-rate)	CV-sequence (min)	final delithiation potential (V)	CV-sequence (min)
1-5	0.13C	-	1.5	-
6-20	0.67C	-	1.5	-
21-35	1.70C	-	1.5	-
36-65	3.30C	-	1.5	-
66-80	1.70C	-	1.5	-
81-95	0.67C	-	1.5	-
96-100	0.13C	-	1.5	-

**Table 6.4:** Modified cycling protocol

cycle	current (C-rate)	final lithiation potential (V)	CV- sequence (current)	break (min)	final delithi- ation potential (V)	CV- sequence	break (min)
1	C/20	0.005	C/40	10	1.5	-	10
2	C/20	0.025	C/40	10	1.0	-	10
3-102	C/3	0.025	C/20	10	1.0	-	10
103	C/20	0.025	C/40	10	1.0	-	10

To calculate the gravimetric capacities of the anode materials the measured capacities were divided by the mass of the active material. Since the weight of the copper foil varies strongly while the mass of active material varies only slightly due to the casting process, the mass of the active material could not be accurately determined by weighing of the entire anode. Therefore, the active material was dissolved after cycling by ultrasonification in ethanol and the leftover copper foil was weighed. The difference to the anode weight prior to cycling, i.e. the amount of removed material, was set off against the binder and thereby resulted in the amount of active material, including graphite, silicon and carbon black. However, for anodes needed for post-mortem analysis this approach is not suitable. The capacity of these anodes was determined as follows: For new anode materials with unknown gravimetric capacity, the theoretical capacity was calculated based on  $372 \text{ mAh} \cdot \text{g}^{-1}$  gravimetric capacity for graphite and  $3579 \text{ mAh} \cdot \text{g}^{-1}$  for silicon. The anode was cycled following the cycling protocol in table 6.2 with the current congruous with the theoretical 1C C-rate, employing 50 instead of 100 cycles. Afterwards, the amount of active material was determined. The gravimetric discharge capacities of the subsequently cycled anodes were then pinned in the 5<sup>th</sup> cycle to the same gravimetric discharge capacity as the previously dispersed anode.

### 6.2.3 Post-mortem analysis

After electrochemical testing the batteries were disassembled inside the argon filled glove box, with the anodes being in the delithiated state. Then, the anodes were washed successively in four flasks filled with 3 ml DEC ( $\geq 99 \%$ , anhydrous, Sigma Aldrich) each and prepared for SEM analysis on a transfer holder which provides an airtight seal.

**Scanning Electron Microscopy** SEM images were acquired on a Hitachi S-4800 microscope using 1.5 kV accelerating voltage and 3 – 4 mm working distance. The anodes were mounted on conductive carbon tape (Plano) on a transfer holder. Energy dispersive X-ray (EDX) analysis was performed using a silicon drift detector (SDD).

## 6.3 Results and discussion

### 6.3.1 Influence of the "Constant Voltage" anode lithiation sequence in a "Constant Current – Constant Voltage" protocol

In the regular cycling protocol applied in this work one cycle consists of four steps:

- (1) anode lithiation applying a constant current until 5 mV are reached (CC-sequence)
- (2) application of 5 mV for 90 min (CV-sequence)
- (3) anode delithiation applying a constant current until 2 V are reached (CC-sequence)
- (4) application of 2 V for 60 min (CV-sequence)

To evaluate how the anode lithiation CV-sequence influences the battery performance and SEI formation, a reliably performing material (G-485C-19% Si) was cycled using the regular protocol (CVCV) and with skipped lithiation CV-sequence (CCV) (table 6.5). The cycling raw data (SI fig. 8.40) illustrates that the gravimetric discharge capacities in the first two cycles run with the current congruous with the theoretical C/20 C-rate are similar for the CVCV and CCV battery ( $925$  and  $903 \text{ mAh} \cdot \text{g}^{-1}$  in 2<sup>nd</sup> cycle). However, upon the 3<sup>rd</sup> cycle run at 1C the capacity of the CCV battery drops to  $512 \text{ mAh} \cdot \text{g}^{-1}$  while the CVCV battery maintains  $922 \text{ mAh} \cdot \text{g}^{-1}$ . This demonstrates the interplay of C-rate and protocol sequences. The anodes are lithiated to the same degree using the C/20 C-rate, independent of the application of a CV-sequence, but when lithiated faster, at 1C, the dismissal of the CV-sequence leads to a reduction in the capacity, e.g. the state of achieved charge. This indicates that for a C-rate of 1C in the CV-sequence significant amounts of charges are transferred when the potential is kept at 5 mV. Since for the slow lithiation at C/20 the capacities did not depend on the lithiation-CV sequence it is unlikely that these charges are transferred in side-reactions, but these charges are indeed involved in anode lithiation.

**Table 6.5:** CVCV and CCV cycling protocols

label	CC-lithiation	CV-lithiation	CC-delithiation	CV-delithiation
<b>CVCV</b>	1C	90 min	1C	60 min
<b>CCV</b>	1C	-	1C	60 min

The radar plot (fig. 6.4) illustrates seven expressive parameters of the cycling raw data plotted in the SI (fig. 8.40). The comparison of the 10<sup>th</sup>, 52<sup>nd</sup> and 102<sup>nd</sup> cycle gravimetric discharge capacity in the radar plot gives an impression of the capacity fade. Since the CCV battery exhibits a significant capacity instability after the C-rate increase in the 3<sup>rd</sup> cycle, the comparison starts with the 10<sup>th</sup> cycle. Besides the fact that the capacity is significantly reduced for the CCV battery over the whole testing, the comparison of these three axes reveals that while the CVCV battery capacity declines stronger in the first half of the cycling than in the second

half, it is the opposite case for the CCV battery. A capacity re-increase in the 103<sup>rd</sup> (C/20) compared to the 102<sup>nd</sup> (1C) cycle indicates that the capacity losses in the final capacity are at least partially reversible for slower C-rates. For the CCV battery this re-increase in capacity is significant, which supports the assumption that the low capacity in the previous cycles is mainly caused by kinetic hindrance and not by irreversible active material loss. Not only does the capacity of the CCV battery exceed the capacity of the CVCV battery in the 103<sup>rd</sup> cycle, but moreover, the CCV battery capacity reaches 60 % of the capacity achieved in the 2<sup>nd</sup> cycle, while the CVCV battery reaches only 48 %. This strongly suggests, that a significant amount of the anode material is not lithiated during the cycling at 1C and re-activated in the 103<sup>rd</sup> cycle for the CCV battery. The capacity retention (CR) is the ratio of the final to the initial capacity cycled at 1C and is therefore a direct indication for how much capacity is lost over cycling. The CVCV battery exhibits the higher CR, which indicates that the lithiation CV-sequence does not only increase the capacity, but also stabilise the capacity during the cycling at 1C. The 1<sup>st</sup> cycle coulombic efficiency (CE) illustrates the amount of charges lost in the very first cycle at C/20 and therefore reveals differences in the reaction of the fresh anode material with the electrolyte. The standard deviation of the CE ( $\sigma_{CE}$ ) is derived from the CE generated at 1C, excluding all CE outliers above 120 %. Both batteries exhibit similar values for these two characteristics, which is consistent with these two characteristics being more dependent on the anode properties than the cycling protocol.

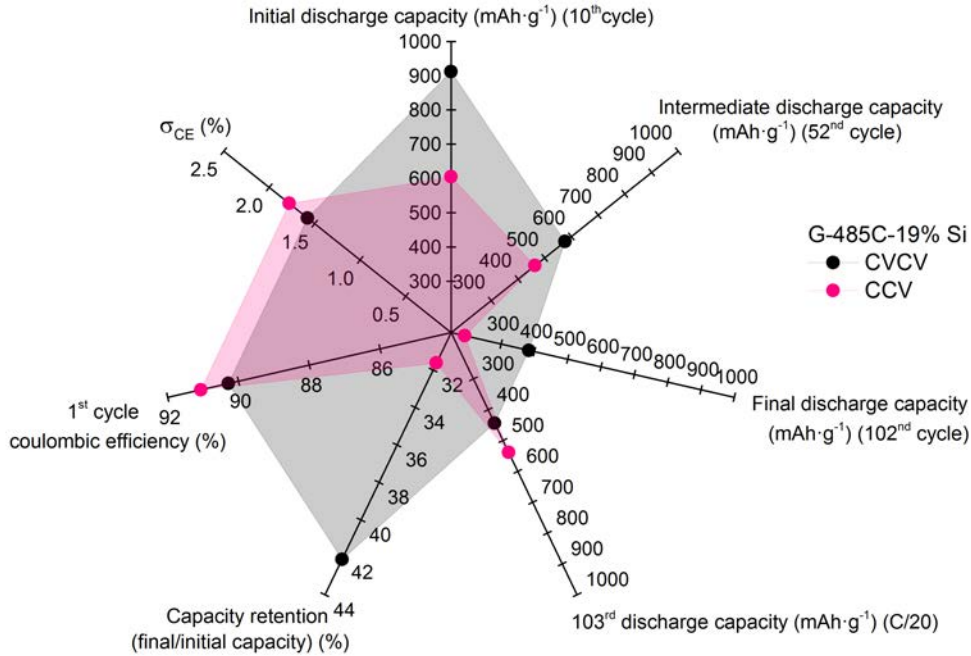


**Figure 6.4:** Radar plots of the performance of G-485C-19% Si batteries cycled with CVCV and CCV protocol.

The differential capacity plots (DCPs) in figure 6.5 depict the delithiation sequence of the CVCV and CCV batteries in the 2<sup>nd</sup> cycle run at C/20 and an overlay of the 3<sup>rd</sup> – 102<sup>nd</sup> cycle run

at 1C. In the 2<sup>nd</sup> cycle the peaks attributed to delithiation of graphite and silicon are clearly visible. The dominant peak at about 430 mV is attributed to the delithiation of c-Li<sub>15</sub>Si<sub>4</sub> while the broad peaks around 260 – 350 mV and 475 mV are attributed to the delithiation of a-Li<sub>2.0</sub>Si and a-Li<sub>3.5</sub>Si.<sup>[53,57,157,158]</sup> The DCP of the CCV battery is very similar to that of the CVCV battery, however, it shows a slightly decreased peak for the delithiation of c-Li<sub>15</sub>Si<sub>4</sub>, while the peaks attributed to the delithiation of the amorphous compounds are slightly increased. When the CVCV battery is cycled at 1C the peaks in the DCPs remain, but become ill-defined and are slightly shifted to higher potentials. For the CCV battery the peak attributed to the c-Li<sub>15</sub>Si<sub>4</sub> delithiation vanishes when the C-rate is increased to 1C. This non-appearance of delithiation indicates that c-Li<sub>15</sub>Si<sub>4</sub> is not formed to a detectable extent without the lithiation CV-sequence at higher C-rates. This corresponds to an insufficient lithiation of the anode and the observed decreased capacity. In literature, it is widely suggested to cycle silicon containing batteries without formation of c-Li<sub>15</sub>Si<sub>4</sub> to improve the battery performance.<sup>[47,53,157]</sup> The CCV battery, however, did not show a superior cycling performance compared to the CVCV battery.

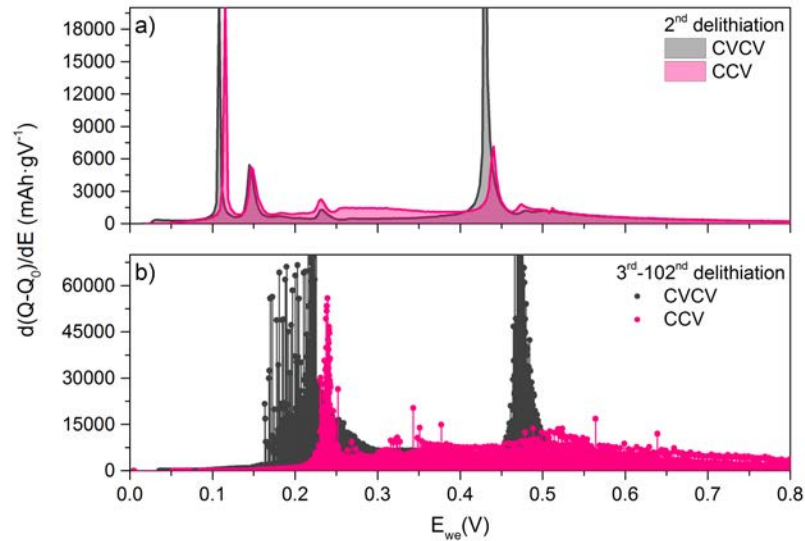


**Figure 6.5:** Differential capacity plots of the CVCV and CCV battery anode lithiation in the a) 2<sup>nd</sup> cycle and b) as an overlay of the 3<sup>rd</sup> – 102<sup>nd</sup> cycle.

SEM investigations of the cycled CVCV and CCV battery anodes reveal that a solid electrolyte interphase (SEI) is formed on both samples. The cracked SEI morphology (fig. 6.6 a, b), which was typically observed in this work for regularly cycled anodes (CVCV protocol) is less pronounced for the CCV battery anode (fig. 6.7 a, b). The cracked SEI is restricted to some areas on the CCV battery anode surface and it is thinner. The decreased thickness is confirmed by EDX measurements (fig. 6.7 d). With an interaction depth of 700 nm, silicon signals are detectable in areas with SEI coverage for the CCV battery anode, whereas for the CVCV battery anode silicon can only be detected in the cracks (fig. 6.6 d). Hence, the results indicate that the omission of the lithiation CV-sequence leads to less SEI formation.

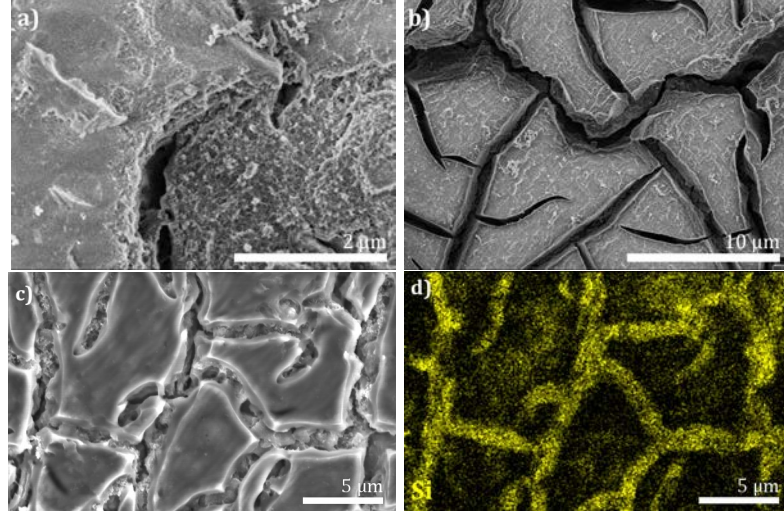


**Figure 6.6:** a, b) SEM images and c) secondary electron image with d) corresponding silicon elemental map of a CVCV battery anode.

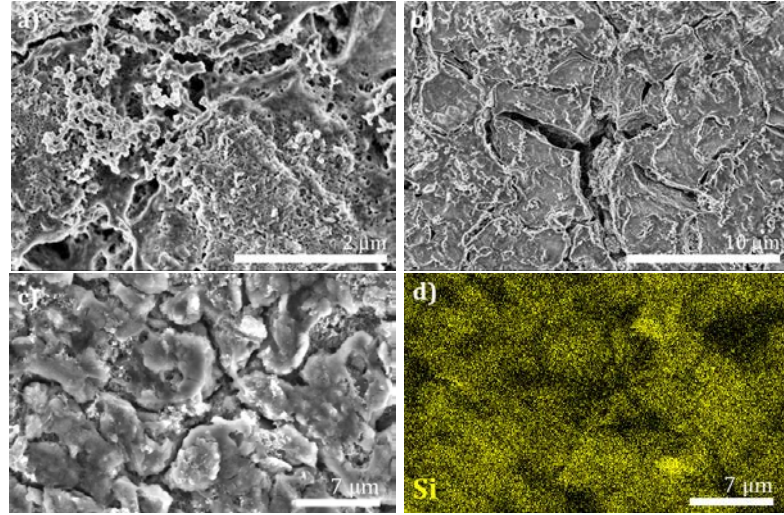


**Figure 6.7:** a, b) SEM images and c) secondary electron image with d) corresponding silicon elemental map of a CCV battery anode.

XPS analysis of a pristine anode and the cycled CVCV and CCV battery anodes exhibits a strongly reduced silicon signal for both cycled anodes. The respective XPS spectra of the cycled anodes are very similar and presented in SI (fig. 8.42). The C1s spectra exhibit C-C and C-H contributions from the graphite support and the carbon black. Moreover, at 289 eV a carbonate contribution is visible, which is likely caused by inorganic carbonates. The shoulder at higher binding energies further suggests C-F species. Despite the conformity of the spectra, a small decrease in fluorine (2.2 %) and phosphorous (0.4 %) content is observed for the CCV compared to the CVCV battery anode which goes in line with the observed decreased SEI formation detected using SEM and EDX.

Altogether upon battery cycling at a C-rate of 1C the omission of the anode lithiation CV-sequence led to a significant loss in capacity and the peak indicative for the formation of  $c\text{-Li}_{15}\text{Si}_4$  was absent in the differential capacity analysis. However, this did neither lead to an improvement in the overall battery capacity, nor in the capacity retention. Yet, SEM, EDX and XPS analysis suggested that less SEI was formed on the anode surface when the CV-sequence was omitted.

### 6.3.2 The effect of restricted charging on the battery performance

In this section selected samples, namely a graphite/Si NP mixture with 20 wt.-% silicon (G-SiNP-20% Si), graphite with a-Si deposition (G-450C-18% Si) and graphite with silicon deposition and additional a-C coverage (G-Si(19%)-C60m) were cycled using a restricted charging protocol. It differs in three characteristics from the regular cycling protocol used in this work as listed in table 6.3. Firstly, the anode lithiation (1<sup>st</sup> CC-sequence) is not restricted by a potential, but by the injected charges. Therefore, the lithiation currents were calculated with a hypothetical silicon capacity of  $1500 \text{ mAh} \cdot \text{g}^{-1}$  instead of  $3579 \text{ mAh} \cdot \text{g}^{-1}$ . Secondly, the CV-sequences are dismissed, and thirdly, the C-rate is varied. The gravimetric discharge capacities and CEs for the respective cycle and C-rate are presented in figure 6.8. The recorded gravimetric discharge capacities are bound to the fixed state of charge (SOC) of around 56 %, controlled by the applied current (table 6.6). The G-450C-18% Si battery provides the most stable performance with a CR of 99.6 % after 100 cycles. The G-SiNP-20% Si battery exhibits an equally high CR of 99.5 %, but suffers from capacity decay at higher C-rates, as clearly depicted by the CE. The G-Si(19%)-C60m battery undergoes slow but continuous capacity decay independent of the C-rate, leading to a CR of only 99.0 %. It is noteworthy that all samples show an outlier in the capacity and CE in the first cycle upon C-rate reduction. This might be attributed to the recovery of lithium trapped during cycling at the respectively higher C-rate. The initial gravimetric discharge capacity and CR obtained from the restricted lithiation cycling are compared to the respective values for the regular cycling protocol in table 6.6. The CR is more than doubled for the restricted lithiation protocol. However, the gravimetric capacities are close to the theoretical capacity of graphite ( $372 \text{ mAh} \cdot \text{g}^{-1}$ ). Regarding trends in the stability of the battery performance referring to the anode material for the two cycling protocols, for both methods the G-450C-18% Si provided the highest CR. However, the lowest CR was provided by the G-SiNP-20% Si battery for the regular cycling and by the G-Si(19%)-C60m for the restricted charging protocol. Even though the differences are small, this comparison displays how distinct evaluated characteristics for anode materials may vary with the cycling method.

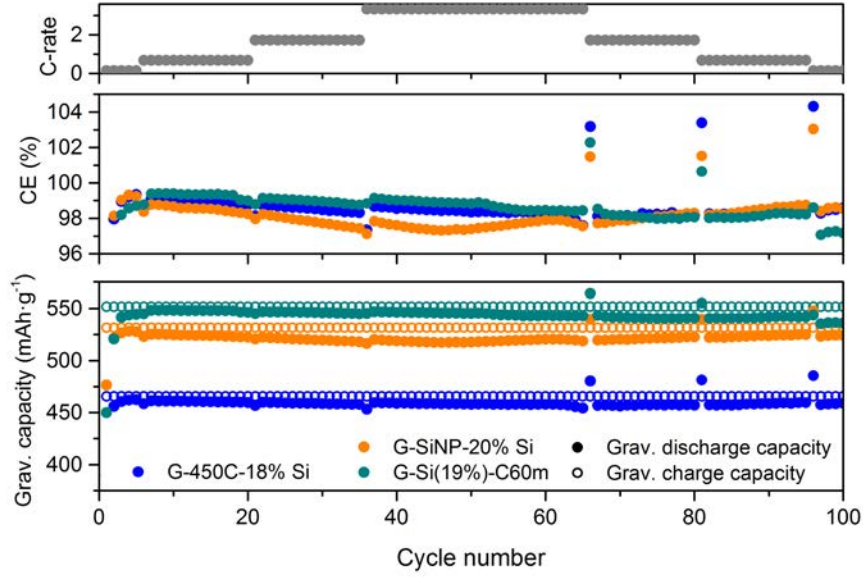


**Figure 6.8:** C-rate, coulombic efficiencies and gravimetric capacities as a function of the cycle number for G-450C-18% Si, G-SiNPs-20% Si and G-Si(19%)-C60m batteries cycled with a restricted charging protocol.

**Table 6.6:** Initial gravimetric discharge capacity ("capacity"), capacity retention (CR) and reached state of charge (SOC) for G-450C-18% Si, G-SiNP-20% Si and G-Si(19%)-C60m batteries cycled regularly with a C-rate of 1C and with restricted charging (C-rate 0.13C)

sample	regular (1C)		restricted (0.13C)		
	capacity (mAh · g <sup>-1</sup> )	CR (%)	capacity (mAh · g <sup>-1</sup> )	CR (%)	reached SOC (%)
G-450C-18% Si	886	44.6	461	99.6	52
G-SiNP-20% Si	910	41.2	526	99.5	58
G-Si(19%)-C60m	910	43.3	541	99.0	59

Whether the stable performance of the batteries cycled with the restricted charging protocol can compensate the low provided capacity, was evaluated on the basis of the overall capacity. Therefore, the capacities of all 100 cycles are added up, normalised per cycle and compared to the overall provided capacity of the regularly cycled batteries. In case of the G-450C-18% Si batteries (fig. 6.9 a) it is clearly visible that the integral of the curve for the regularly cycled battery is bigger than for the one which was cycled with lithiation restriction. The initial gravimetric capacity of the regularly cycled battery is almost two times bigger. Hence, despite the capacity decay, over 100 cycles a higher overall capacity was provided by the regularly cycled battery. The ratios of the overall capacities achieved by the batteries cycled with restricted charging and the regularly cycled batteries are plotted in figure 6.9 b). The G-SiNP-20% Si battery provides the lowest overall capacity for regular cycling and 89 % of this capacity can be provided by the restrictedly cycled battery. The batteries containing anodes obtained from LPCVD processes (G-450C-18% Si and G-Si(19%)-C60m) provide higher overall capacities in the regular cycling and the respective batteries cycled with restricted lithiation can only provide



75 and 80 % of the overall capacity. Hence, the efficiency of the restricted lithiation protocol depends on the anode material.

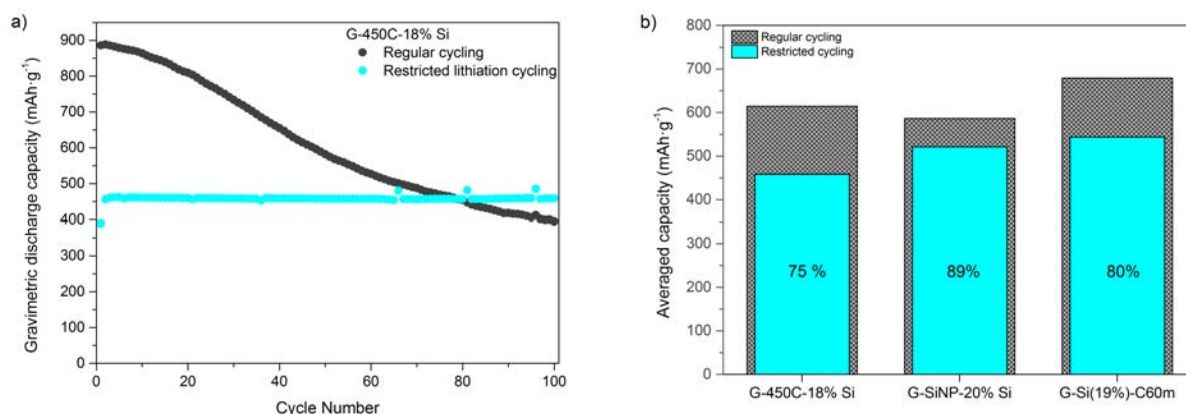


**Figure 6.9:** a) Gravimetric discharge capacity as a function of the cycle number for G-450C-18% Si batteries cycled regularly and with restricted charging and b) averaged capacity over 100 cycles for regularly and restrictedly cycled batteries.

The differential capacity plots (DCPs) of the 3<sup>rd</sup> and the 100<sup>th</sup> delithiation cycle of the G-450C-18% Si, G-SiNP-20% Si and G-Si(19%)-C60m batteries cycled with restricted lithiation are presented in figure 6.10. For all DCPs the peak attributed to the delithiation of c-Li<sub>15</sub>Si<sub>4</sub>, which usually appears at around 430 mV, is absent. This indicates that no c-Li<sub>15</sub>Si<sub>4</sub> is formed during the cycling. The broad peaks around 300 and 480 mV visible in the 3<sup>rd</sup> delithiation DCP are ascribed to delithiation of a-Li<sub>x</sub>Si compounds.<sup>[57,157]</sup> In the DCPs of the 100<sup>th</sup> delithiation sequence these peaks are still visible for the LPCVD generated samples. On the contrary, the G-SiNP-20% Si battery exhibits only very small and broad peaks. This indicates that the Si NPs are significantly less electrochemically active and goes in line with an observable lower potential onset of the DCP. If continuously less Si NPs are active, the battery reaches continuously lower lithiation potentials upon the uptake of the same amount of charges. Hence, upon lithiation lower potentials are reached (SI fig. 8.41 b) and the subsequent onset of the delithiation is shifted to lower potentials.

Concluding, the restricted charging cycling led to an increased cycling stability over 100 cycles. However, the gravimetric capacities of the batteries were low, so that the overall provided capacity was smaller than for the regularly cycled batteries. However, this might change if the cycle number is increased beyond 100 cycles. With an ongoing constant performance the overall capacity of the restrictedly cycled cells could surpass the overall capacity provided by the regularly cycled batteries. However, there are indications in literature that the restricted cycling protocol just postpones the capacity decay, so that the overall provided capacity of the battery remains similar only stretched over a higher number of cycles.<sup>[123,160]</sup>

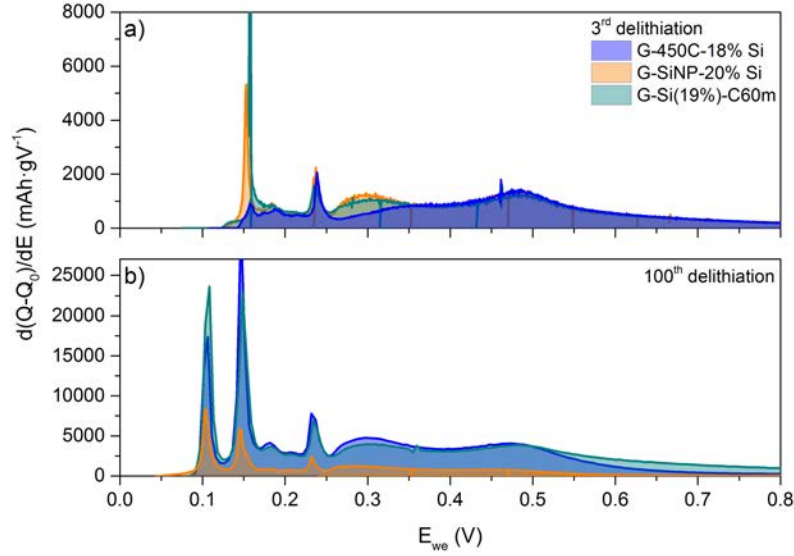


**Figure 6.10:** Differential capacity plots of a) 3<sup>rd</sup> and b) 100<sup>th</sup> delithiation of G-450C-18% Si, G-SiNP-20% Si and G-Si(19%)-C60m batteries, cycled with restricted charging.

### 6.3.3 Investigation of the influence of combined modified battery protocol, electrolyte and housing on the battery performance

Selected samples were cycled in a self-designed battery housing with a modified protocol and an electrolyte mixture containing dimethyl carbonate with 10 wt.-% fluoroethylene carbonate (FEC). The modified cycling protocol contains several parameters, which are considered helpful to promote a longer cycle life for silicon based batteries, including lower C-rates and a restricted cycling window (table 6.4).<sup>[165,231]</sup> Through comparison with the regularly cycled batteries it is evaluated how much the battery performance is affected by these battery parameters and whether the differences in performance between the synthesised anode materials are amplified or swallowed in the modified setup. The cycling raw data are presented in SI (fig. 8.43-8.46) for all samples, namely the batteries containing anodes made from graphite (G), from 2 h silicon deposition at 450 °C (G-450C-18% Si), 2 h silicon deposition at 485 °C (G-485C-22% Si), 1 h silicon deposition at 550 °C (G-550C-13% Si), 2 h silicon deposition at 550 °C (G-550C-22% Si), 3 h silicon deposition at 550 °C (G-550C-30% Si), graphite/Si NP mixture (G-SiNP-13% Si) and 2 h silicon deposition at 485 °C with 1 h amorphous carbon (a-C) coverage (G-Si(19%)-C60m). The overall capacities provided by the modified batteries in 100 cycles averaged per cycle and silicon are presented in figure 6.11. Moreover, they are compared to the capacities of the regularly cycled batteries. The G-550C-30% Si and G-Si(19%)-C60m batteries exhibit a decrease in the provided capacity. Accordingly, the modification of the battery setup is not suitable for batteries containing anodes with high silicon contents (~30 wt.-%) or anodes where the silicon is covered with amorphous carbon. For batteries containing anodes obtained from a-Si depositions (G-450C-18% Si and G-485C-22% Si) a capacity increase of 121 % and

107 % compared to the regularly cycled batteries, is observable. A more distinct increase of 143 – 188 %, is achieved for anodes obtained from c-Si depositions and the Si NP mixture.

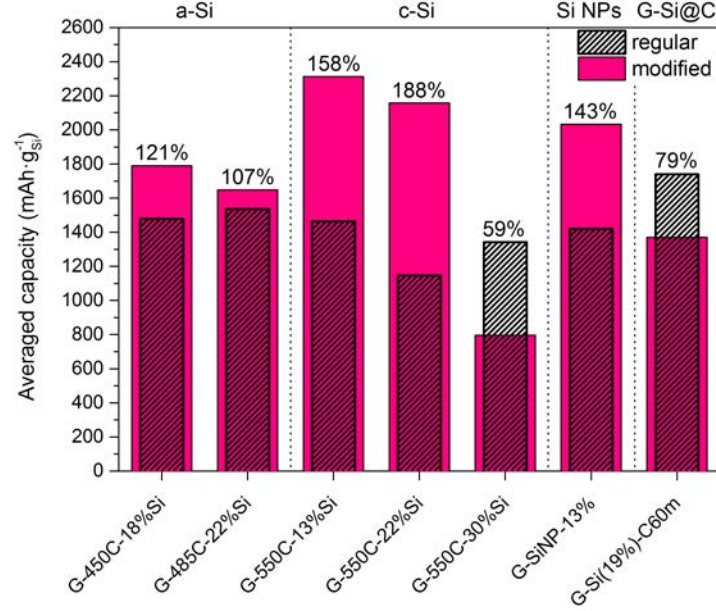


**Figure 6.11:** Gravimetric discharge capacity per mass silicon averaged over 100 cycles for batteries cycled regularly and in the modified setup. These include batteries of four categories: a-Si deposition (a-Si), c-Si deposition (c-Si), Si NP/graphite mixture (Si NPs) and a-C covered graphite-silicon nanocomposite (G-Si@C).

A clearer impression of the battery performances can be obtained from comparison of the corresponding radar plots. They depict seven expressive parameters of the cycling test. The comparison of the 3<sup>rd</sup>, 52<sup>nd</sup> and 102<sup>nd</sup> cycle gravimetric discharge capacity illustrates the capacity fade. It is clearly visible how much capacity is provided by the battery in the beginning and how much is lost after 50 and 100 cycles. A re-increase in the 103<sup>rd</sup> compared to the 102<sup>nd</sup> cycle gravimetric discharge capacity indicates that the capacity losses in the final capacity are at least partially reversible for slower C-rates. The capacity retention (CR) is the ratio of the final to the initial capacity and therefore a direct indication for how much capacity is lost over cycling. The 1<sup>st</sup> cycle coulombic efficiency (CE) gives the amount of charges lost in the very first cycle at C/20 and accordingly reveals differences in the reaction of the fresh anode material with the electrolyte. The standard deviation of the CE ( $\sigma_{CE}$ ) was derived from the CE generated at 1C, excluding all CE outliers above 120 %. It illustrates the steadiness of the CE over cycling. Higher values in  $\sigma_{CE}$  are an indication for either outliers in the CE or occurring local decays in the CE.

In figure 6.12, the radar plots of batteries containing anodes with 13 wt.-% (G-550C-13% Si) and 22 wt.-% c-Si deposition (G-550C-22% Si) and the reference graphite (G), cycled in the modified and in the regular setup are compared. When the reference graphite anode is cycled in the modified setup, its gravimetric discharge capacity is reduced from 346 mAh · g<sup>-1</sup> to

309  $\text{mAh} \cdot \text{g}^{-1}$  but its stability is maintained. The silicon containing batteries also exhibit lower initial gravimetric capacities in the modified setup, but at the same time a massive improvement in the capacity maintenance over cycling. The reduced initial capacities for all batteries are attributed to the decreased cycling potential window, i.e. a smaller degree of charging. The capacity of the 103<sup>rd</sup> cycle is increased less for the modified setup batteries than for the regularly cycled ones. This indicates that the lithiation is less kinetically hindered in the modified setup, for example due to a more conductive SEI, hence the capacity is less dependent on the C-rate. The improved capacity stability in the modified setup leads to a significantly increased CR from 49 % to 92 % for the G-550C-13% Si battery and from 32 % to 88 % for the G-550C-22% Si battery. The 1<sup>st</sup> cycle CE is significantly lower for the batteries cycled in the modified setup, which agrees well with the electrochemical processes reported for FEC in lithium-ion batteries. The contained FEC was reported to exhibit higher reductive potentials and therefore undergo chemical reactions before other organic electrolyte components do.<sup>[129,237,239]</sup> Hence, the reduced 1<sup>st</sup> cycle CEs for the modified setup batteries can be ascribed to FEC decomposition. The high standard deviation for the G battery cycled in the modified setup is caused by a significantly decreased CE to on average 92 % over the first 50 cycles. For the silicon containing batteries, the standard deviation of the CEs over cycling is not significantly affected by the modified setup, but it increases with higher silicon contents.

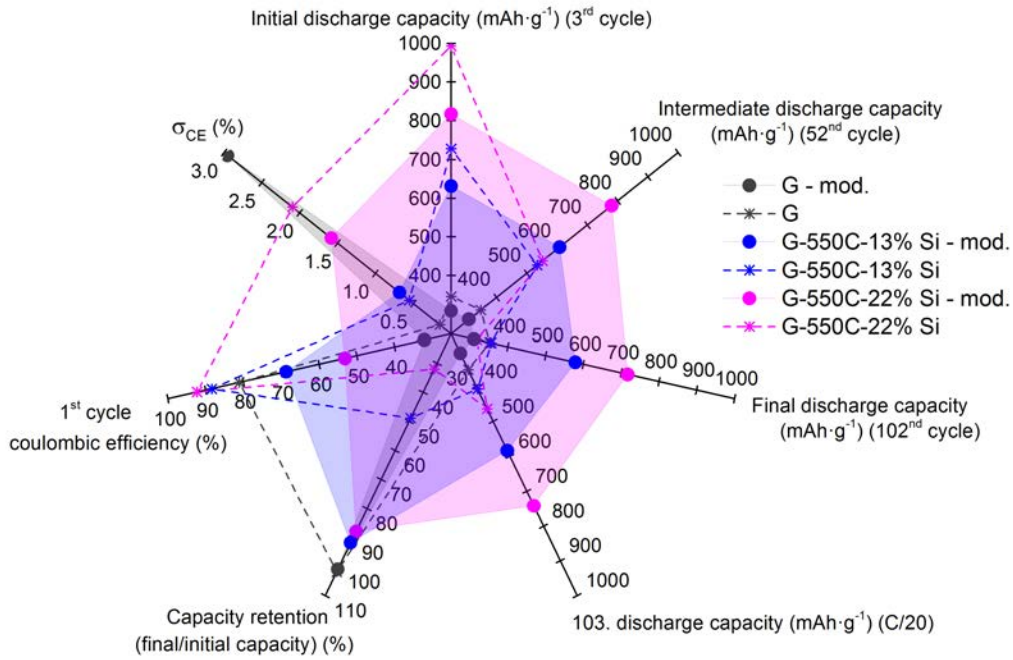


**Figure 6.12:** Radar plots of the performance of G, G-550C-13% Si and G-550C-22% Si batteries cycled in the regular and the modified (mod.) setup.

In figure 6.13, the performance of batteries containing 13 wt.-% c-Si deposition (G-550C-13% Si) and the graphite/Si NP mixture (G-SiNP-13% Si) with 13 wt.-% Si NPs are compared for the regular and modified setup. Again, both samples exhibit lower initial gravimetric capacities for

the modified setup, which can be maintained significantly longer, so the CR is increased from 49 % to 92 % for the c-Si deposition and 59 % to 85 % for the Si NP mixture. Consistent with the previous paragraph the 1<sup>st</sup> cycle CEs are significantly lower for the modified setup batteries and for the standard deviation of the CE no significant changes are observed. Notably, the battery with the LPCVD anode provides superior capacity and a higher CR compared to the Si NP-based battery, while in the regular setup the opposite trend was observed.

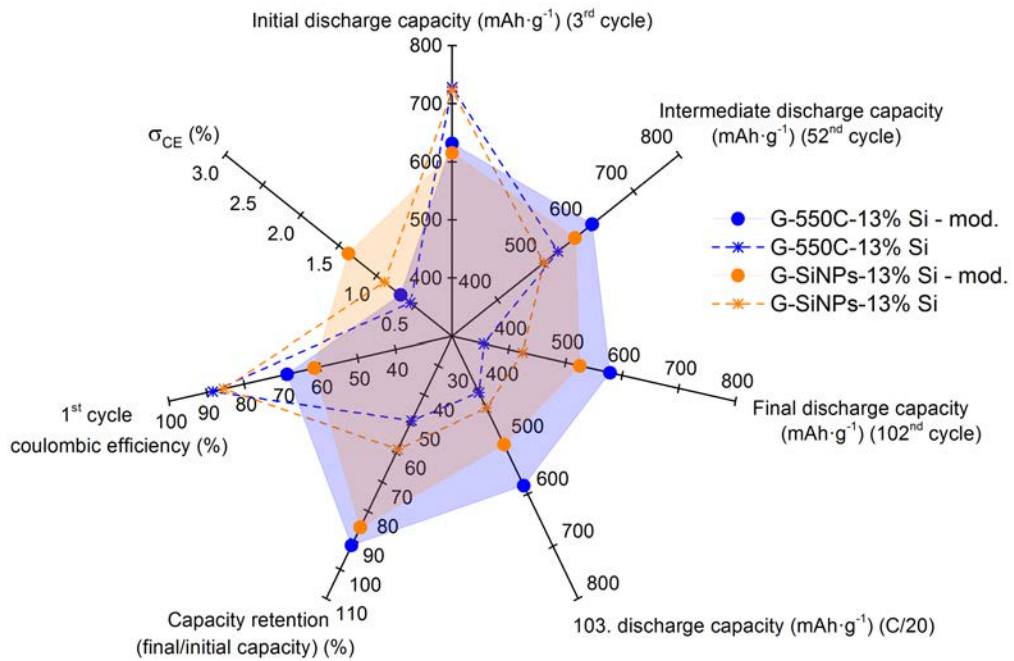


**Figure 6.13:** Radar plots of the performance of G-550C-13% Si and G-SiNP-13% Si batteries cycled in the regular and the modified (mod.) setup.

In figure 6.14, radar plots derived from cycling of batteries containing anodes obtained from silicon deposited at 450, 485 and 550 °C are compared in the regular and modified battery setup. The differences between modified and regularly cycled batteries are analogous to the previous samples. The CR is increased from 45 % to 81 % for the G-450C-18% Si battery, 42 % to 67 % for the G-485C-22% Si battery and 32 % to 88 % for the G-550C-22% Si battery. While no difference in the 1<sup>st</sup> cycle CE was observed for the varying deposition temperatures in the regular setup, the 1<sup>st</sup> cycle CEs is notably higher for the G-450C-18% Si battery in the modified setup. The standard deviation of the CE ( $\sigma_{CE}$ ) over cycling is nearly identical for the batteries cycled in the modified setup, while in the regular setup a small divergence was observed.

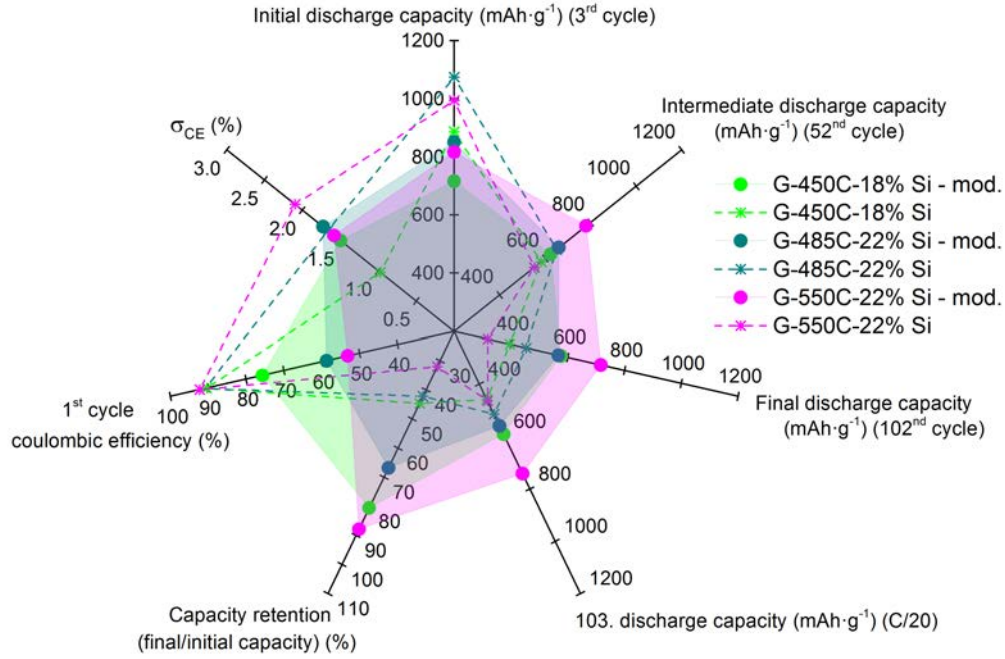


**Figure 6.14:** Radar plots of the performance of G-450C-18% Si, G-485C-22% Si and G-550C-22% Si batteries in the regular and the modified (mod.) setup. The 1<sup>st</sup> cycle CE of the regularly cycled G-485C-22% Si battery is taken from a replica (not marked with a star).

The differential capacity plots (DCPs) contain further information about the battery processes. In literature, a characteristic peak in the 1<sup>st</sup> cycle between 0.42 – 1.5 V is assigned to the reductive decomposition of FEC and the reduction of the native silicon oxide layer.<sup>[238,239,251]</sup> Similar reductive peaks were observed in the DCPs of the investigated batteries in the modified setup around 1 V as can be seen in SI figure 8.47. The effect of the modified setup on the 2<sup>nd</sup> and 103<sup>rd</sup> cycle DCPs is in the following exemplarily discussed for the G-550C-13% Si batteries, the 1<sup>st</sup> cycle DCP is presented in SI (fig. 8.48). In the 2<sup>nd</sup> cycle the cut-off voltage for the anode lithiation is increased from 5 to 25 mV for the modified cycling, as displayed in figure 6.15 a). The decreased lithiation entails a less pronounced oxidative peak at 450 mV, attributed to the delithiation of c-Li<sub>15</sub>Si<sub>4</sub><sup>[47,58,160,161]</sup>, as depicted in the delithiation sequence (fig. 6.15 c). This indicates a smaller degree of silicon lithiation, which is consistent with the observed decreased battery capacity. The 103<sup>rd</sup> cycle DCPs of the batteries cycled in regular and modified setup show more pronounced differences. The 103<sup>rd</sup> cycle lithiation DCP of the modified battery exhibits still notable peaks around 270 – 220, 85 and 50 mV, which are attributed to the formation of a-Li<sub>x</sub>Si and c-Li<sub>15</sub>Si<sub>4</sub> compounds (fig. 6.15 b).<sup>[57,157,158]</sup> In comparison to the 2<sup>nd</sup> cycle DCP, the peak intensities decreased only slightly. However, this is not the case for the battery cycled in the regular setup, which almost exclusively exhibits the typical graphite lithiation peaks (DCP of graphite see SI fig. 8.18). The significantly smaller silicon activity for the regularly cycled battery derived from the DCPs is in accordance with the observed low capacity (406 mAh·g<sup>-1</sup>) approaching the capacity of the graphite reference (352 mAh·g<sup>-1</sup>).

In contrast to this, the battery cycled in the modified setup with more pronounced peaks in the 103<sup>rd</sup> cycle DCP also maintained a capacity of  $584 \text{ mAh} \cdot \text{g}^{-1}$ .

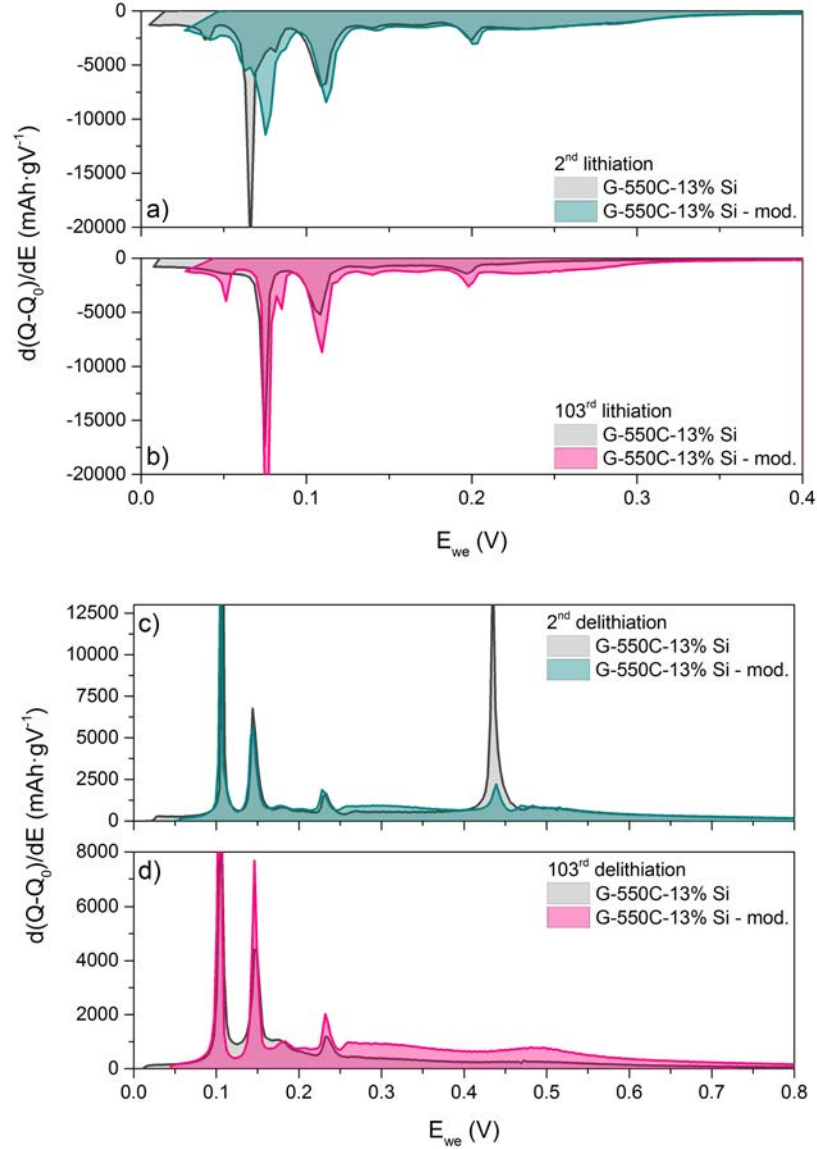


**Figure 6.15:** Differential capacity plots for a) 2<sup>nd</sup> and b) 103<sup>rd</sup> anode lithiation and c) 2<sup>nd</sup> and d) 103<sup>rd</sup> anode delithiation of G-550C-13%-Si batteries cycled in the regular and modified (mod.) setup.

In literature the improved cycling performance of batteries containing FEC is mostly ascribed to the impact of the FEC on the solid electrolyte interphase (SEI) formation. The images of the G-550C-22% Si anode cycled in the modified setup are compared to a regularly cycled G-550C-22% Si anode in figure 6.16. More images are shown in SI (fig. 8.49). The anode surface of the regularly cycled battery features irregular coverage with SEI, the SEI appears thick and exposes cracks. The surface of the anode cycled in the modified system containing FEC looks significantly different. The anode exhibits "dark" and "bright" regions on the



surface (fig. 6.16 b). A higher magnification of the dark regions reveals a desert rose-like surface structure, as shown in figure 6.16 c). Images of the bright areas expose a structured surface layer (fig. 6.16 d), which partially preserves the original morphology of the anode surface (fig. 6.16 e).

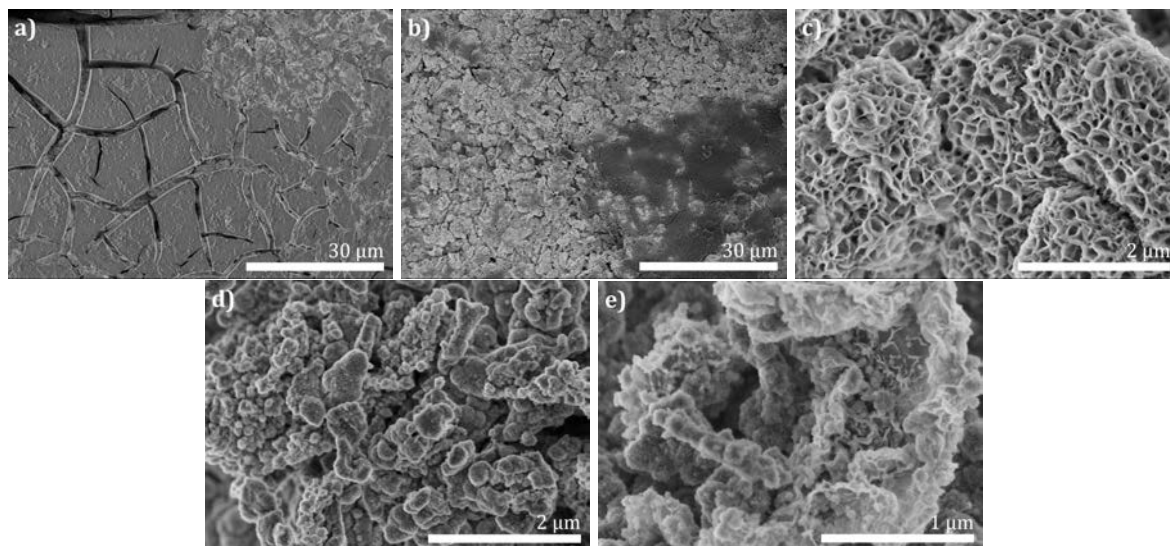


**Figure 6.16:** SEM images of G-550C-22% Si anodes cycled in the a) regular and b-e) modified setup.

The EDX spectra collected on "dark" and "bright" areas of the anode cycled in the modified setup are presented in figure 6.17. They are directly compared to the EDX spectra of the regularly cycled G-550C-22% Si anode, collected on the cracked SEI ("SEI") and in the cracks ("cracks"). No silicon signal, but carbon, oxygen, phosphorous and fluorine are detectable on the SEI formed during regular cycling using EDX analysis. Silicon is only detectable in the cracks between the SEI islands. Both EDX spectra, "SEI" and "dark", match regarding the absence of the silicon signal and vice versa the silicon signals of the "crack" spectrum matches with the silicon signal of the "bright" spectrum. Hence, the SEI formed in the dark areas with the desert rose-like structure shields the graphite-silicon nanocomposite like the SEI observed on the regularly cycled anode and from the bright areas a good silicon signal is acquired, comparable to the one collected in the cracks of the regularly cycled anode. Further comparison of the "dark" and "SEI" spectra demonstrates that for the anode cycled in the modified setup the phosphorous signal is dramatically increased and the carbon signal nearly vanished. Combined with the pronounced oxygen signal, this indicates that the desert rose-like structure contains mainly phosphate species. Despite the similar silicon signal, the residual EDX spectra of the "bright" and "crack" spots also exhibit differences. The anode cycled in the modified setup features a significantly increased fluorine signal, while carbon and oxygen are drastically decreased. This supports the reported increased LiF content of FEC-derived SEIs.<sup>[239]</sup> Furthermore, the decreased carbon signal suggests less EC and DEC decomposition products in the SEI.



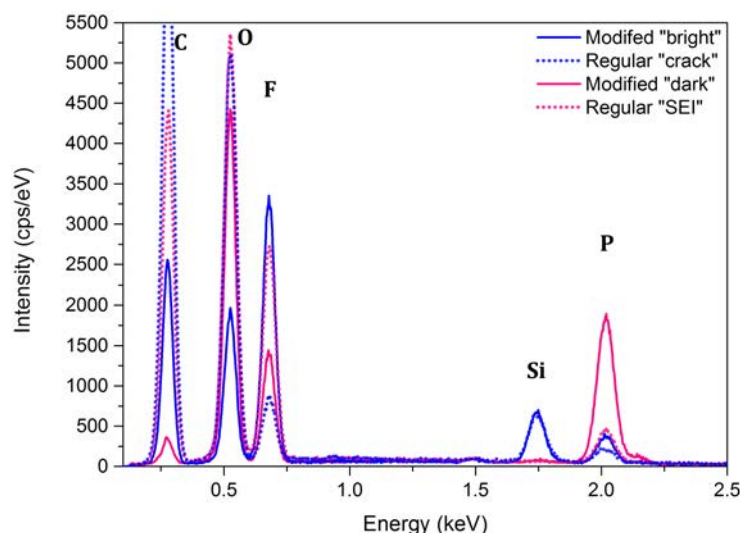


**Figure 6.17:** EDX spectra of G-550C-22% Si anodes cycled in regular (dotted lines) and modified (continuous lines) setup.

Altogether most batteries cycled in the modified system with adapted battery housing, protocol and electrolyte exhibited a drastic stabilisation of the capacity. Differential capacity analysis revealed that in batteries cycled in the modified setup the contained silicon is still electrochemically active in the 103<sup>rd</sup> cycle, in contrast to the silicon in regularly cycled batteries. This can be attributed in a large part to the addition of FEC to the electrolyte in the modified setup. The derived SEI was of different composition and featured different morphologies. Compared to the SEI derived in regularly cycled batteries the "modified" SEI contained significantly less carbon species and a desert rose-like structure being rich in phosphorous and oxygen.

## 6.4 Conclusion

In this chapter the influence of battery setup parameters beyond the anode material modification were investigated. The omission of the anode lithiation constant voltage (CV) sequence in a constant current – constant voltage (CC-CV) protocol was shown to have a significant effect on the battery capacity and cycling stability. Not only did the application of such a CV-sequence cause a more steady capacity performance and a higher capacity retention of the battery, but also it involved a significant increase in the battery capacity, caused by remaining anode lithiation. Incomplete lithiation after the CC-sequence appeared for graphite-silicon nanocomposite anodes cycled using currents corresponding to a current rate of 1C. At the same time less solid electrolyte interphase was observed on the anode surface for anodes cycled without a lithiation CV-sequence. A restricted charging protocol led to a stable battery capacity performance with capacity retentions of 99.0 – 99.6 % over 100 cycles, yet, only for gravimetric capacities close to the one of graphite. Therefore, the overall provided capacities over 100 cycles were smaller for

the batteries cycled with the restricted charging protocol compared to the ones cycled regularly. Even though the differences for distinct anode materials tested with the restricted charging protocol were minor, stability trends of the anode materials changed such that the usually stable performing amorphous carbon covered nanocomposite batteries provided the lowest capacity retention. This strongly suggested that electrochemical investigations carried out in different setups have to be compared carefully. By modifying the battery housing, the electrolyte and the cycling protocol at the same time a significant improvement of the battery performance was achieved, especially for samples containing crystalline silicon. This improved performance was mainly attributed to the modified solid electrolyte interphase formation. Batteries containing amorphous silicon deposition, which used to prevail regarding the overall capacity in the regular setup, were outdistanced by the batteries with crystalline silicon anodes when cycled in the modified battery setup. Hence, the battery performance is affected by the anode material as well as by the other battery parameters. However, these parameters have to be modulated iteratively, since cycling stabilisation through material adjustment does not necessarily persist in the modified setups and vice versa.

## 7 Summary and final conclusion

The last decades have been an eventful time for research in the field of lithium-ion batteries (LIBs) and silicon emerged as a potential anode material. Whether silicon can serve as a reliable anode material in LIBs was the vital point of the investigations presented in this work. More precisely, promising approaches to improve the electrochemical performance of silicon-based batteries were evaluated. This includes the modification of the silicon content, the alteration of the silicon morphology, the coverage of the silicon surface with carbon and modifications in the battery setup. Taken as a whole, the relevance of the material properties, testing conditions and the solid electrolyte interphase (SEI) formation on the battery performance were evaluated.

Graphite-silicon nanocomposites obtained from low pressure chemical vapour deposition of silicon on graphite flakes emerged with high reproducibility, facile tunability and cleanness of the synthesis method as the fundament for the silicon anode materials investigated in this work. Reliable modifications of the silicon deposit properties were achieved by the variation of the deposition parameters, i.e. the silane treatment time, temperature and pressure. An additional amorphous carbon (a-C) coverage of the nanocomposites was attained by pyrolysis of propene. The respectively obtained anodes were cycled with various protocols in different battery setups and analysed post-mortem to obtain a more thorough impression of the changes of the anodes during electrochemical (de-)lithiation.

Regarding the influence of the silicon properties on the battery performance the variation of the silicon content and crystallinity was investigated. As shown in chapter 4.3.2 an increase in the silicon content entailed an increase in the initial gravimetric capacity, so that batteries with 22 wt.-% silicon in the anode active material provided around  $1000 \text{ mAh} \cdot \text{g}^{-1}$ , which are desired in order to achieve a worthwhile improvement of the LIB capacity. However, with increasing silicon content the battery capacity also decayed stronger during cycling, such that after 100 cycles the capacities dropped nearly to the gravimetric capacity of graphite, independent of the initial capacity. To obtain a more thorough impression of the capability of the batteries presented in this work figure 7.1 depicts the comparison of the provided battery performances of selected batteries related to a model battery providing  $1000 \text{ mAh} \cdot \text{g}^{-1}$  without decay over 100 cycles. Whether the capacity decay can be avoided by modification of the silicon crystallinity, was investigated by adjustment of the silicon deposition temperature. It was shown that a higher degree of silicon crystallinity especially affected the batteries' coulombic efficiency (CE) in the first 40 cycles. Altogether the capacity decay was not completely avoided, but weakened for batteries containing amorphous silicon (a-Si) deposition, the most

for a-Si deposited at 485 °C. Two batteries comprising anodes from two hours depositions at 485 °C (G-485C-22% Si) and 550 °C (G-550C-22% Si), the latter resulting in crystalline silicon (c-Si) deposition, are compared on the scale of the model battery in figure 7.1. Both batteries provided equivalent, sufficiently high initial capacities, but the battery containing a-Si cycled more steadily, leading to a higher capacity retention (CR) after 100 cycles and a higher overall capacity.

The effect of the coverage of the graphite-silicon nanocomposite with a-C on the battery performance was discussed in chapter 5.3.2. Despite the finding that the high a-C deposition temperature generated highly crystalline silicon deposit and that a-C surface layer did not outlast the first quarter of the cycling, the cycling performance was improved for particular propene treatment times. Hence, a-C certainly did not serve as a continuous surface protection, but rather enhanced the anode properties by intermixing with the underlying nanocomposite. The observed battery performance improvements included stabilisation of the CE and, for some samples, an increased CR after 100 cycles compared to other batteries containing highly crystalline graphite-silicon nanocomposite anodes. In figure 7.1 the battery characteristics of a G-Si(19%)-C60m battery, which provided the highest capacity averaged over 100 cycles of the a-C deposition series, are presented. Despite the contained highly crystalline silicon this battery provided a performance comparable to the G-485C-22% Si battery comprising a-Si. Further, it was found that the deposited a-C layer needs to be controlled precisely, since the beneficial effect on the battery performance did not continuously increase with the a-C deposition time, but was maximum for an a-C layer thickness of 4.5 nm. An experiment with propene treatment before and after silicon deposition (G-C-Si(20%)-C30m) also resulted in anodes, which provided an improved battery CR as shown in figure 7.1. This indicates that innovative carbon-silicon nanocomposites deposited by CVD may represent a worthwhile material group to further the application of silicon-based anode materials in LIBs.

With regard to the battery cycling protocol parameters, in chapter 6.3.1 it was shown that the anode lithiation constant voltage sequence was of great relevance to achieve complete lithiation, and therefore higher capacities when the batteries were (dis-)charged in one hour. When the batteries were cycled with restricted lithiation to about 56 % state of charge, a stable performance over 100 cycles was achieved (chapter 6.3.2). Thereby, the CRs increased on average by 56.3 % to an average CR of 99.4 % after 100 cycles, as shown using the example of a G-Si(19%)-C60m battery in figure 7.1 (G-Si(19%)-C60m-rest.). However, when the provided charges were added up over 100 cycles, the overall capacities provided by the regularly cycled batteries were higher despite the capacity decay. This trend might change when the cycling is extended beyond 100 cycles or the state of charge is increased. These results demonstrate clearly that the various features of a battery performance strongly depend on the cycling protocol and that only the combination of several battery properties like the overall provided capacity, the gravimetric capacity, the CR and the CE give a real impression of the battery capability. To have a quick

overview over these parameters for various batteries at the same time radar plots proved to be a helpful tool.

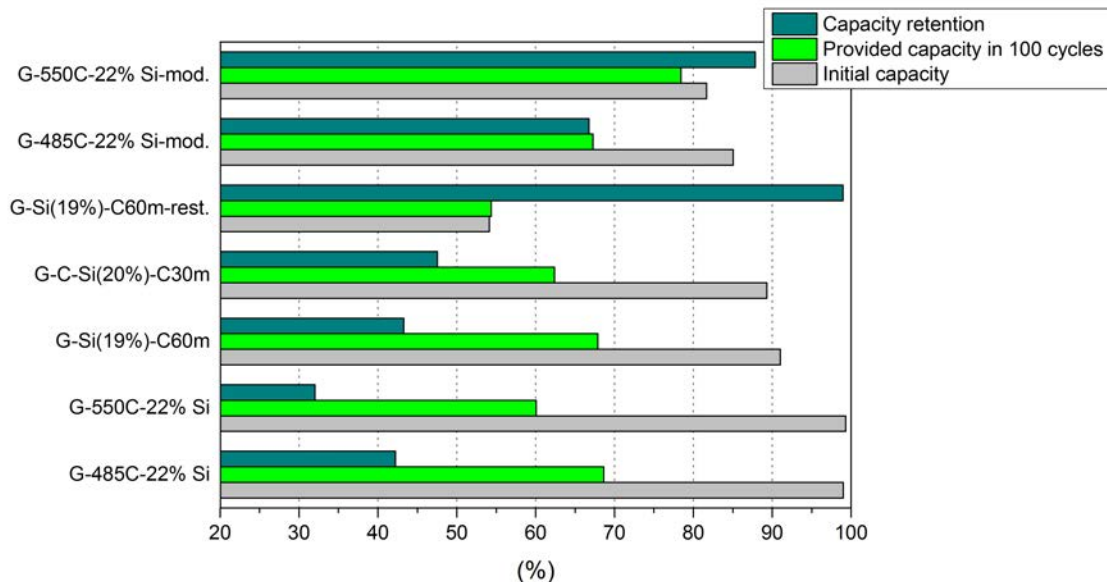


**Figure 7.1:** Initially (grey) and over 100 cycles (green) provided capacity on the scale of an ideal battery with stable  $1000 \text{ mAh} \cdot \text{g}^{-1}$  capacity. Selected samples cycled regularly, with restricted charging (-rest.) and in the modified setup with decreased C-rate (-mod.). Also shown is the capacity retention, i.e. ratio of final to initial capacity (dark cyan).

In chapter 4.3.3 an SEI layer of around 630 nm thickness was detected after 100 cycles on a regularly cycled anode obtained from a sample with 22 wt.-% a-Si. The identified SEI components oxygen, fluorine, lithium, carbon and phosphorous are very likely electrolyte decomposition products and their formation was conceivably responsible for the charge losses observed in the CE. Since the SEI thickness and the capacity decay increased with increasing cycle number it is also conceivable that the SEI formation contributed to the capacity loss by shielding the active material and generating overpotential. This was supported by the results in chapter 5.3.3 of the G-C-Si(20%)-C30m battery, which exhibited the highest CR after 100 cycles and at the same time showed less SEI formation. In chapter 6.3.3 the anodes were cycled in a modified setup with sparing protocol parameters and a different electrolyte composition. The overall capacities were increased up to 88 % over 100 cycles with the respective CRs increasing by a factor of around 1.5 to 2.5 up to 91.8 % for only slightly decreased initial capacities. These increases were mainly attributed to a modified SEI formation. The SEI exhibited another morphology and different elemental ratios, indicating different components. This outstanding improvement of the battery performance underlines the impact of the SEI on the battery cycling performance. However, the stabilisation was more pronounced for batteries containing c-Si, than for the ones with a-Si. Hence, the trends observed for the varied anode materials in the modified setup were different compared to the initial setup, such that the batteries containing c-Si (G-550C-22% Si-mod) showed a more stable performance than the ones containing a-Si (G-485C-22% Si-mod.)

(fig. 7.1). This indicates that the interplay of the anode material, the protocol and the electrolyte is not straightforward. An optimisation of the LIB can only be achieved by iterative variation and balancing of these three components.

Altogether plenty of material parameters can be adjusted which affect the battery cycling behaviour. At this, the pristine anode itself can be considered a precursor whose performance is strongly affected by the cycling parameters and the electrolyte. On the question of the suitability of silicon as a prospective anode material in LIBs, this work showed that for nanostructured silicons, which circumvent fragmentation during (de-)lithiation, indeed capacity stability improvements were achieved through anode material modifications and even more significant improvements in the battery CRs were obtained from electrolyte and protocol tuning. Hence, with some further research and in due consideration of the required charging times, silicon in combination with carbon could indeed serve as a reliable anode material for specific applications in portable or stationary devices.

## 8 Appendix

### 8.1 A Supporting information of chapter 3

The correlation between the set oven temperature ( $T_{\text{oven}}$ ) and the temperature measured by the thermocouples ( $T_{\text{sample}}$ ) is given in figure 8.1.

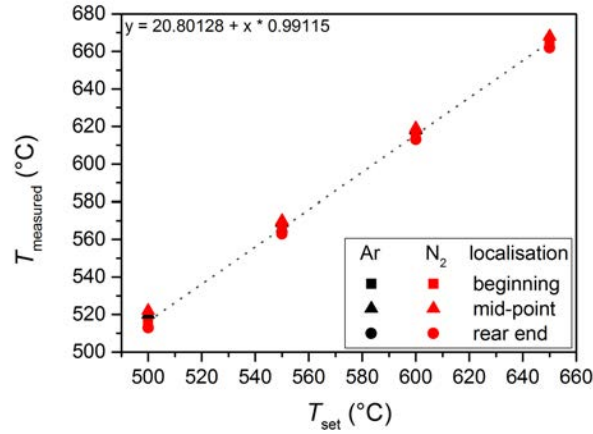


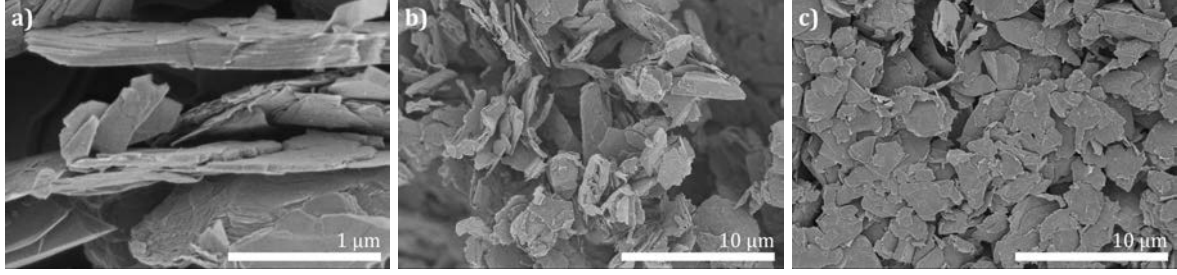
**Figure 8.1:** Temperature calibration with open Ar-flow of 650 sccm as well as N<sub>2</sub>-flow of 150 sccm at 100 mbar.

In table 8.1 the LPCVD parameters for all samples synthesised for chapter 3 are listed.

**Table 8.1:** List of samples for chapter 3 at  $p = 1$  mbar

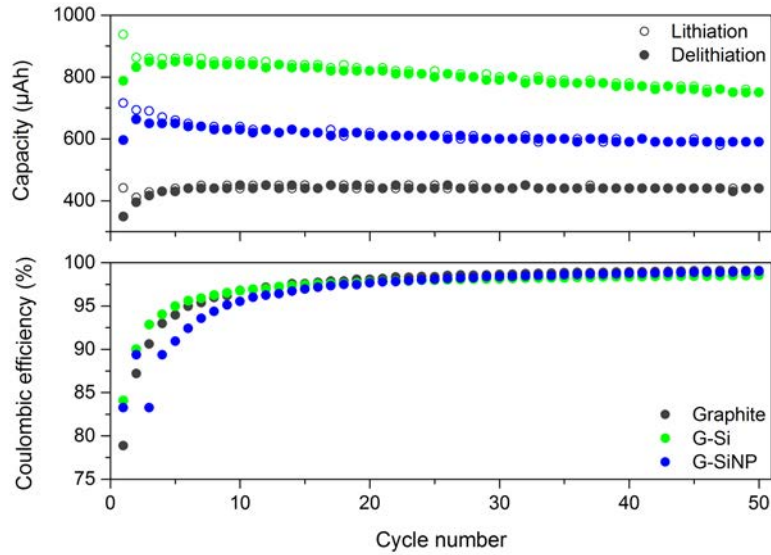
sample	substrate	$T_{\text{oven}}$ (°C)	$T_{\text{sample}}$ (°C)	$t$ (min)	$p$ (mbar)
G-Si-30m	Graphite (KS6)	550	566	30	1
G-Si	Graphite (KS6)	550	566	60	1
G-Si-5	Graphite (KS6)	550	566	60	5
G-Si-20	Graphite (KS6)	550	566	60	20
MWCNT-Si	MWCNTs	550	566	60	1
MWCNT-HTC-Si	MWCNT-HTC	550	566	60	1

SEM images of the pristine graphite are depicted in figure 8.2.



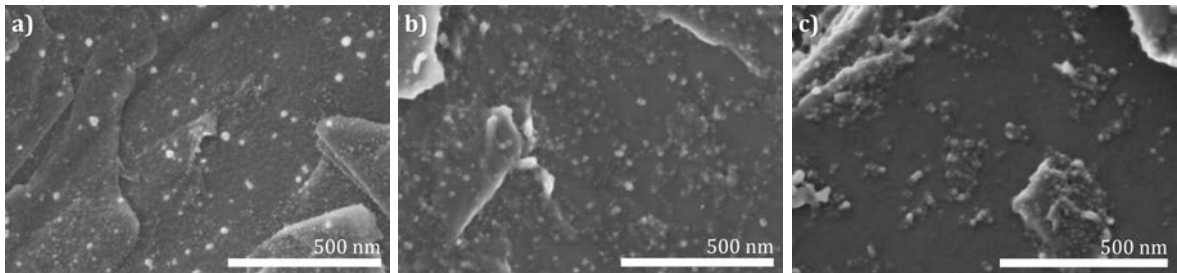
**Figure 8.2:** SEM images of graphite.

Figure 8.3 shows the lithiation and delithiation capacity and the coulombic efficiency of batteries containing anodes from the graphite reference, G-Si and G-SiNP for 50 cycles.



**Figure 8.3:** (De-)lithiation capacities and coulombic efficiencies vs. cycle number for graphite, G-Si and G-SiNP for 50 cycles.

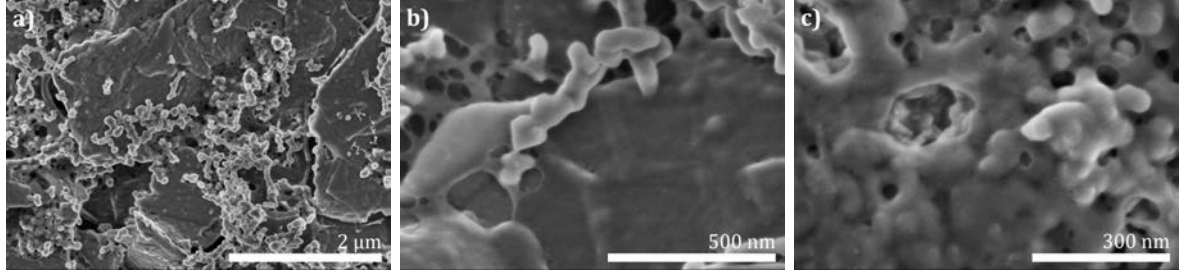
SEM images of G-Si anodes on regions with less silicon coverage after testing are shown in figure 8.4. The testing parameters include the exposure to OCV (a), 20 (dis-)charge cycles (b) and 50 (dis-)charge cycles (c).



**Figure 8.4:** SEM images of G-Si anodes after a) OCV b) 20 cycles and c) 50 cycles.

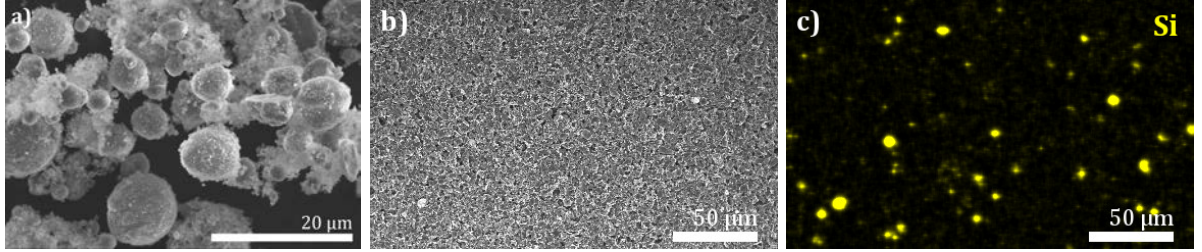


SEM images of the G-SiNP anode after 20 cycles are depicted in figure 8.5.



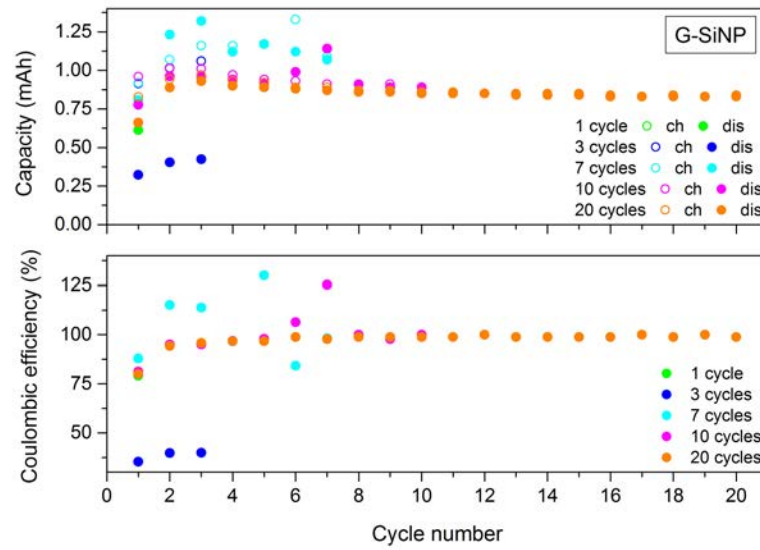
**Figure 8.5:** SEM images of the G-SiNP anode after 20 cycles.

In figure 8.6 a) an SEM image of the silicon nanoparticles, as received, is shown. In figure 8.6 b) an SEM image with the respective silicon elemental map (fig. 8.6 c) of the prepared G-SiNP anode is depicted.



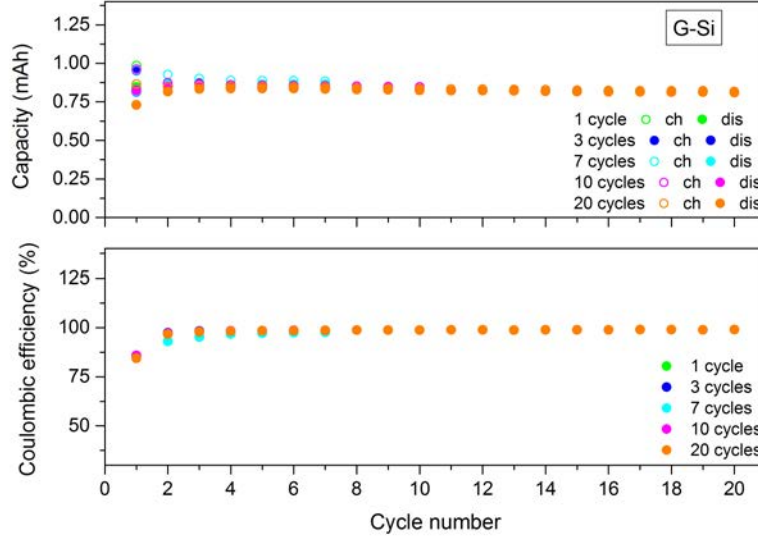
**Figure 8.6:** SEM images of a) Si NP reference powder and b) the G-SiNP anode with c) the respective silicon elemental map of the G-SiNP anode.

Figure 8.7 depicts the lithiation (ch) and delithiation (dis) capacities and the coulombic efficiencies of batteries containing G-SiNP anodes for 1, 3, 7, 10 and 20 cycles.



**Figure 8.7:** Charge (ch) and discharge (dis) capacities and coulombic efficiencies as a function of cycle number for G-Si batteries.

In figure 8.8 the lithiation (ch) and delithiation (dis) capacities and the coulombic efficiencies of batteries containing G-Si anodes for 1, 3, 7, 10 and 20 cycles are plotted.



**Figure 8.8:** Charge (ch) and discharge (dis) capacities and coulombic efficiencies as a function of cycle number for G-Si batteries.

## 8.2 B Supporting information of chapter 4

In table 8.2, all samples with the deposition parameters and silicon content determined by TG-MS and elemental analysis (EA) discussed in chapter 4 are listed.

**Table 8.2:** List of sample names, deposition parameters and ascertained silicon content

sample	$T_{\text{oven}}$ (°C)	$T_{\text{sample}}$ (°C)	$t$ (min)	$p$ (mbar)	Si wt.-% TG (mg)	Si wt.-% EA (mg)
G-435C-14% Si	435	452	240	1	14.7	14.3
G-450C-18% Si	450	477	120	1	18.1	17.6
G-450C-27% Si	450	477	180	1	29.1	26.8
G-450C-30% Si	450	477	240	1	33.8	30.1
G-485C-11% Si	485	502	60	1	10.9	10.9
G-485C-19% Si	485	502	120	1	20.6	18.9
G-485C-22% Si	485	502	120	1	22.3	22.0
G-485C-30% Si	485	502	180	1	35.8	30.2
G-510C-22% Si	510	526	120	1	24.6	21.9
G-550C-08% Si	550	566	30	1	6.5	7.6
G-550C-13% Si	550	566	60	1	14.6	12.7
G-550C-22% Si	550	566	120	1	24.0	21.5
G-550C-30% Si	550	566	180	1	30.9	29.9
G-800C <sup>a</sup> -21% Si	485	502	120	1	22.3	20.6

For a precise determination of the gravimetric capacity, replica anodes were dissolved and anodes of the same kind pinned to the same gravimetric capacity. The results are illustrated in figure 8.9. When the active material of one of the graphite reference anodes was dissolved after the capacity was measured, the gravimetric capacity was precisely determined. After standardising the other graphite anodes to the same gravimetric capacity, the plots in figure 8.9 b) are obtained. The same applies to the carbon black (CB) anodes.

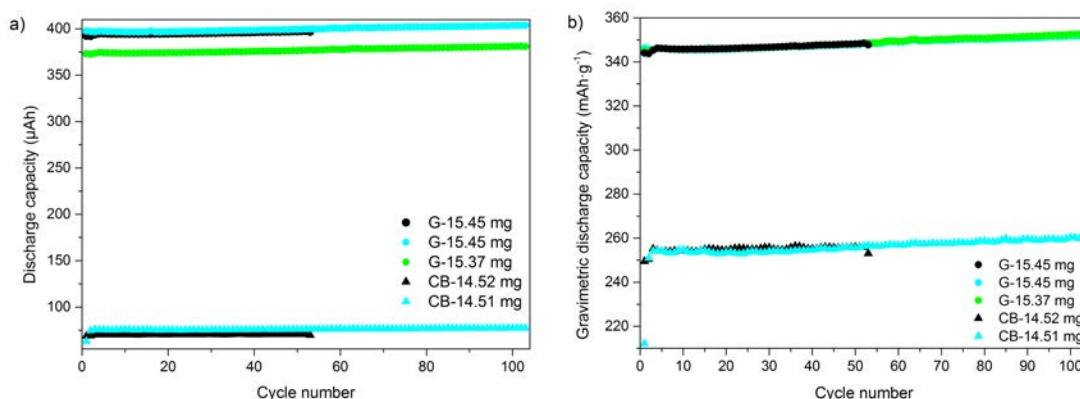


**Figure 8.9:** a) Discharge capacity and b) gravimetric discharge capacity as a function of the cycle number for graphite reference anodes containing carbon black (G) and carbon black anodes (CB).

The mass changes of all samples discussed in chapter 4 during TG-MS analysis are depicted in figure 8.10.

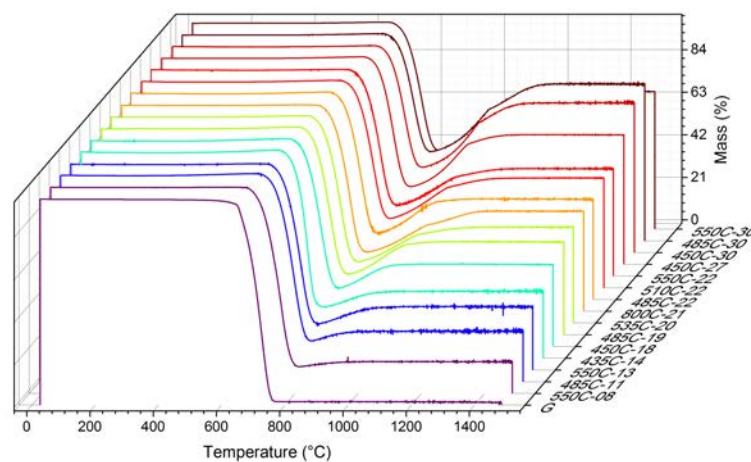


**Figure 8.10:** Mass (%) as a function of temperature ( $^{\circ}\text{C}$ ) for all samples discussed in chapter 4.

In figure 8.11, the evaluation of mass and CO<sub>2</sub>-ion current ( $m/z = 44$ ) as a function of the temperature are plotted for graphite (G) and samples obtained from graphite with 30, 60, 120 and 180 min of silicon deposition.

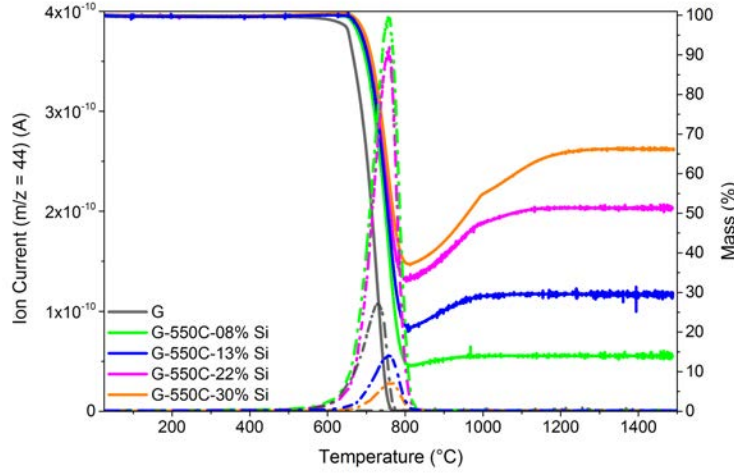


**Figure 8.11:** Mass (solid line) and ion current of CO<sub>2</sub> ( $m/z = 44$ ) (dashed line) as a function of temperature for graphite (G) and samples obtained from graphite with 30, 60, 120 and 180 min of silicon deposition.

XRD and SEM investigations of the sample G-550C-22% Si after TG-MS analysis are shown in figure 8.12. The XRD pattern exhibits reflections of cristobalite and the EDX analysis of the SEM images does not give a noteworthy carbon signal but sharp silicon and oxygen signals.

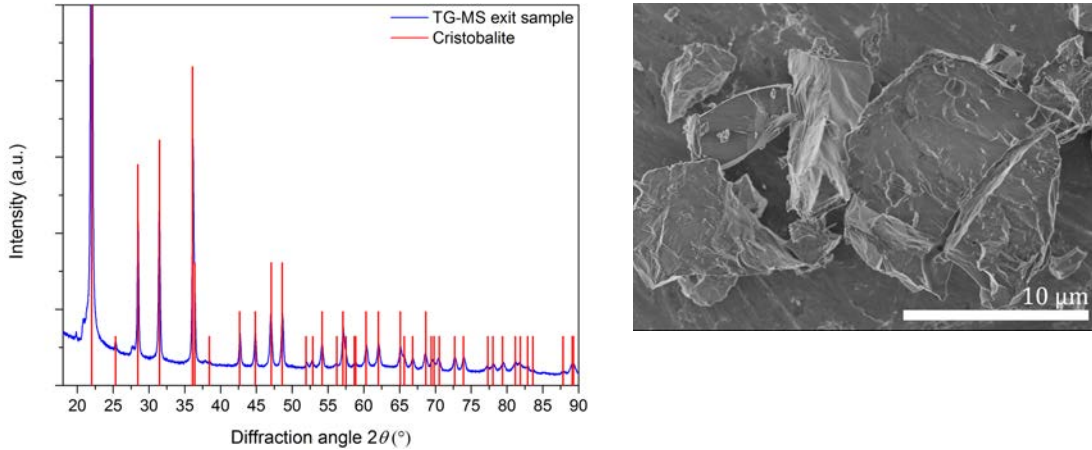


**Figure 8.12:** Left: powder XRD pattern; right: SEM image of the G-550C-22% Si sample after TG-MS analysis.

The crystalline volume fractions and silicon crystal domain sizes derived from Rietveld refinement for the samples G-550C-08% Si, G-550C-13% Si, G-550C-22% Si, G-550C-30% Si, G-510C-22% Si and G-800C<sup>a</sup>-21% Si, are plotted in figure 8.13.

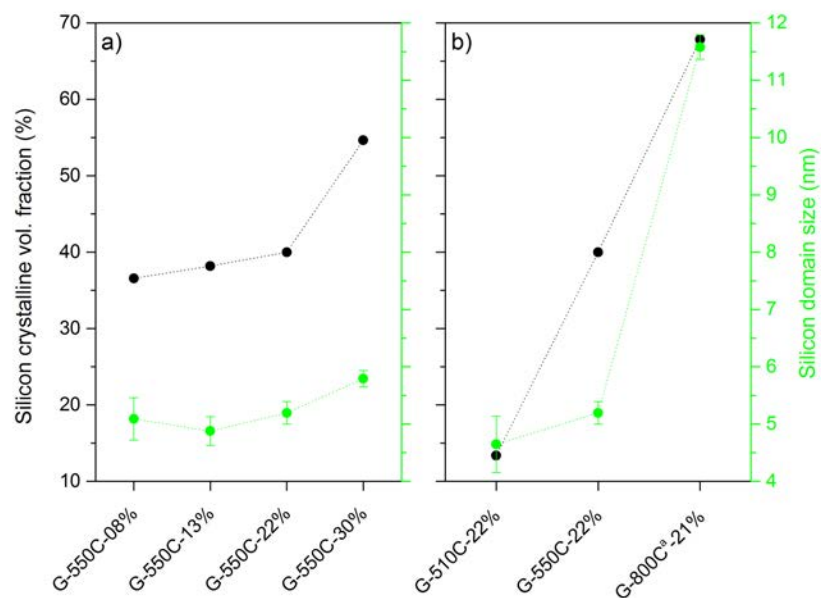


**Figure 8.13:** Values for a) the silicon crystalline volume fraction (black) and b) the silicon crystal domain size (green) derived from Rietveld refinement with error bars ( $3 \cdot \text{ESD}$ ).

In figure 8.14, the Raman spectra from 100 to 3000  $\text{cm}^{-1}$  normalised to the TO band are depicted for the samples discussed in section 3.3.1.

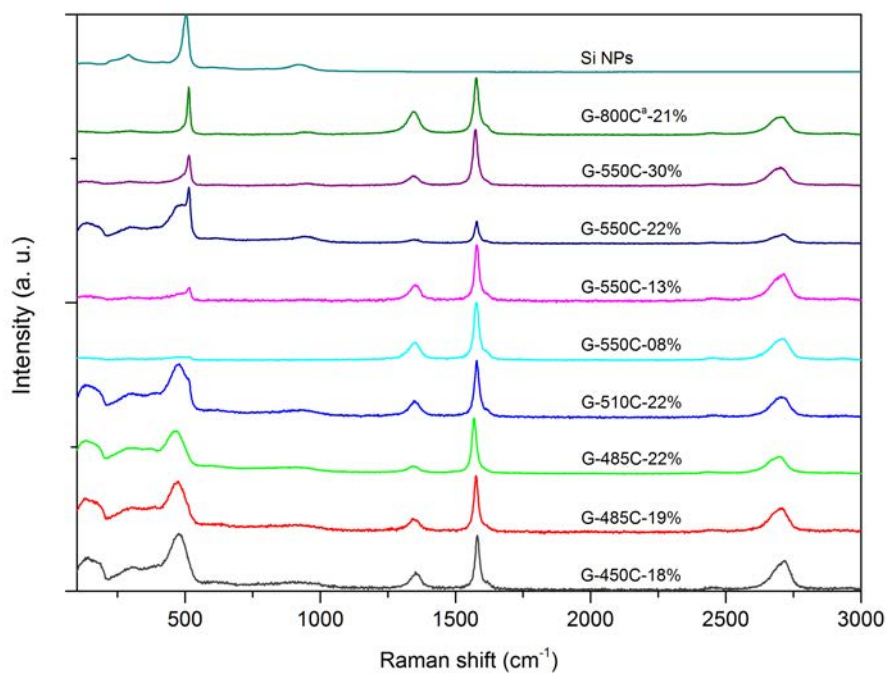


**Figure 8.14:** Normalized Raman spectra from 100 to 3000  $\text{cm}^{-1}$ .



In figure 8.15, the SEM images of the samples discussed in section 4.3.1 are given at lower magnification.

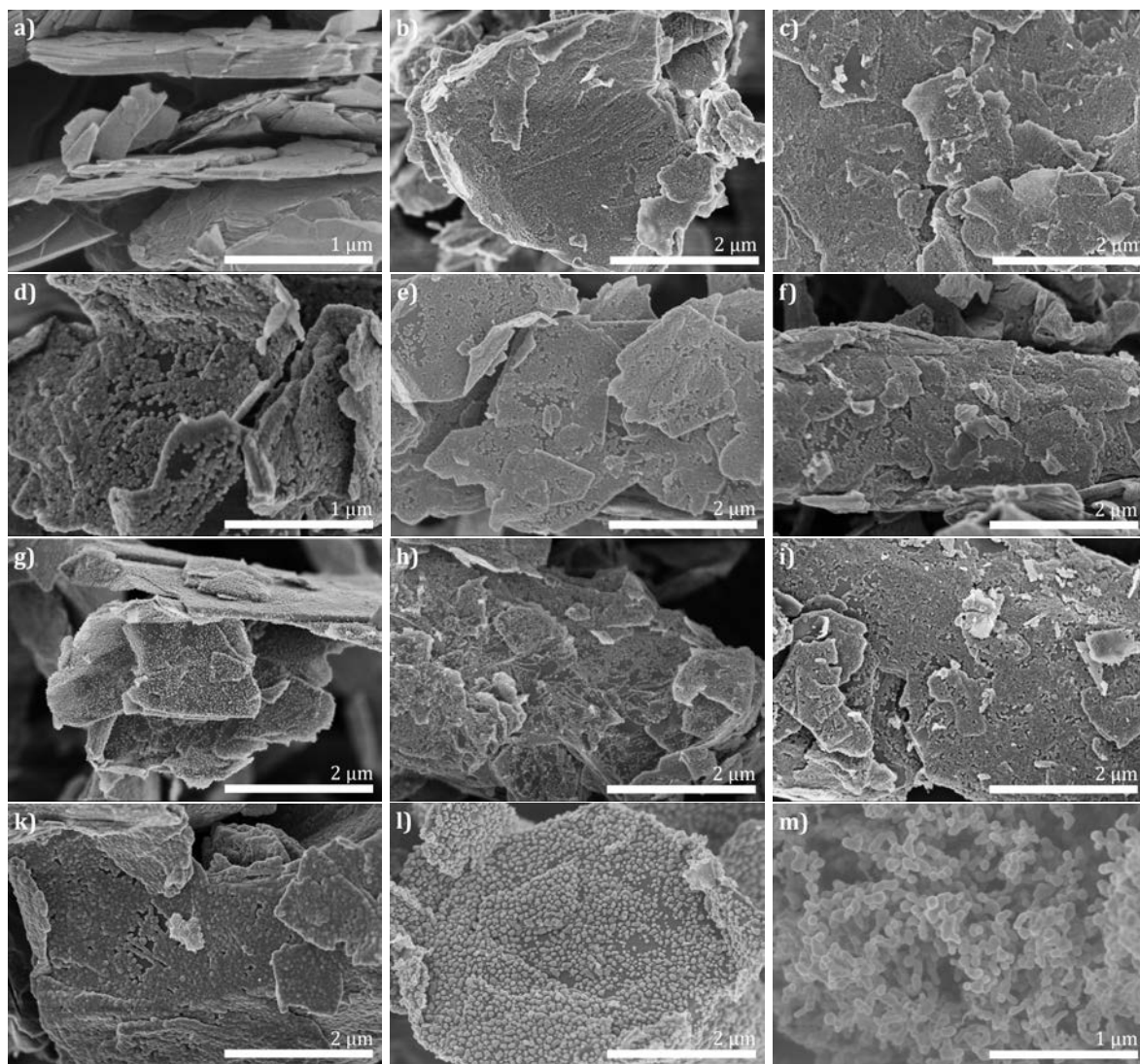


**Figure 8.15:** SEM images of a) G, b) G-435C-14% Si, c) G-450C-18% Si, d) G-485C-19% Si, e) G-485C-22% Si, f) G-485C-30% Si, g) G-550C-08% Si, h) G-550C-13% Si, i) G-550C-22% Si, k) G-550C-30% Si, l) G-800C<sup>a</sup>-21% Si and m) Si NPs.

Figures 8.16 and 8.17 show the raw data which form the basis of the radar plots of series B, C and D.

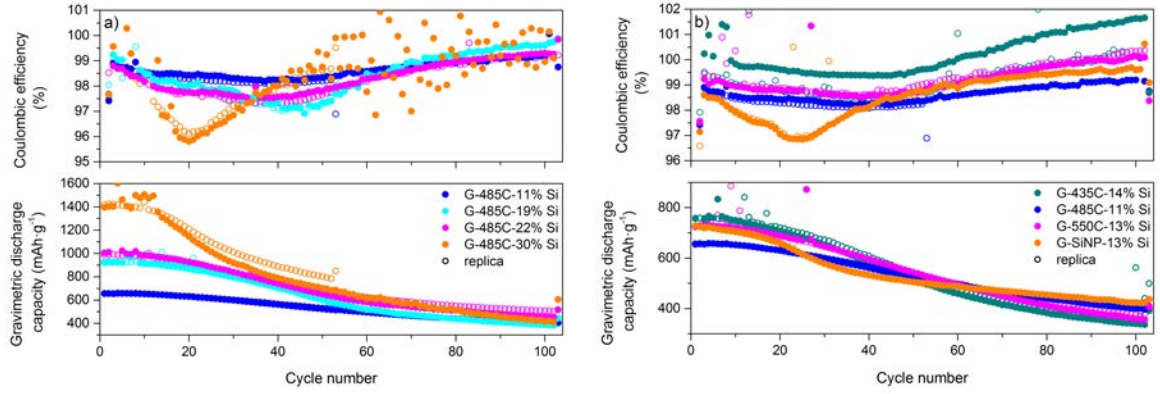


**Figure 8.16:** Gravimetric discharge capacity and CE as a function of the cycle number for a) series B and b) series C.

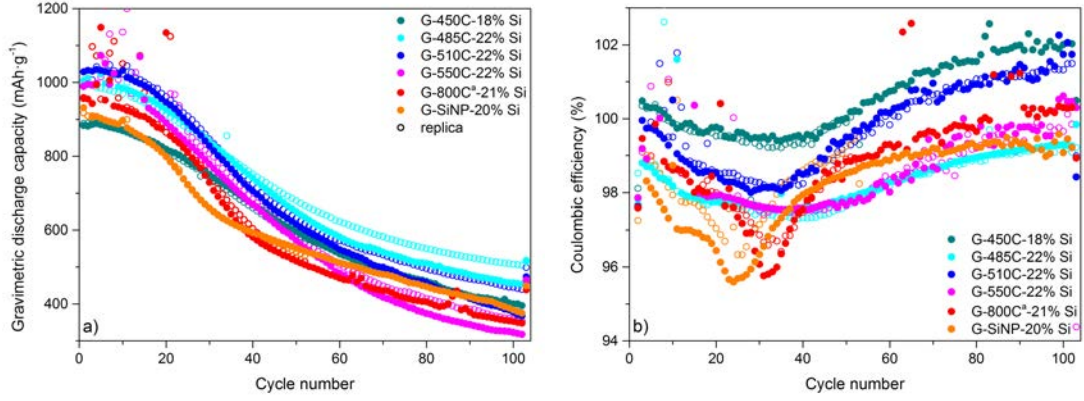


**Figure 8.17:** a) Gravimetric discharge capacity and b) CE as a function of the cycle number for series D.

In table 8.3 the samples used for the contour plot (fig. 4.14) with their gravimetric discharge capacities per silicon and cycle are listed.

**Table 8.3:** Gravimetric discharge capacity per silicon and cycle

sample	gravimetric discharge capacity (mAh · g <sub>Si</sub> <sup>-1</sup> )	sample	gravimetric discharge capacity (mAh · g <sub>Si</sub> <sup>-1</sup> )
G-435C-14% Si	1274	G-510C-22% Si	1407
G-450C-18% Si	1478	G-550C-08% Si	1198
G-485C-11% Si	1616	G-550C-13% Si	1463
G-485C-19% Si	1455	G-550C-22% Si	1147
G-485C-22% Si	1536	G-550C-30% Si	1342
G-485C-30% Si	1426	G-800C <sup>a</sup> -21% Si	1112

The differential capacity plots (DCPs) of batteries containing graphite reference anodes (8.18 a) and carbon black anodes (8.18 b) are depicted below.

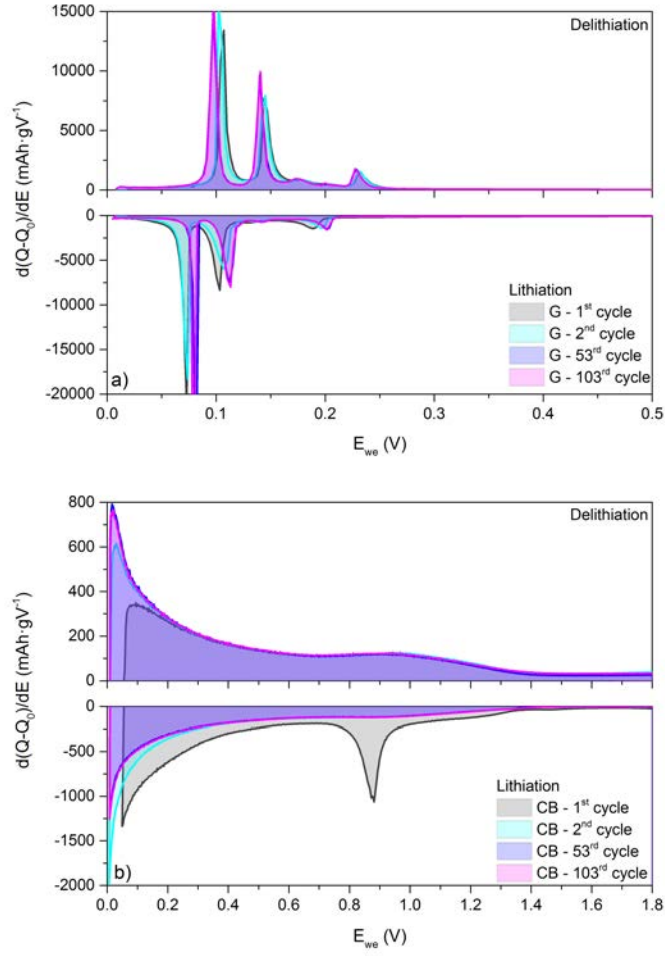


**Figure 8.18:** Differential capacity plots of batteries containing a) graphite reference anodes (G) and b) carbon black anodes (CB).

In the following, the DCPs of the 2<sup>nd</sup> cycle of series D (fig. 8.19), the 2<sup>nd</sup> and 103<sup>rd</sup> cycle of series B (fig. 8.20) and the 1<sup>st</sup> and 2<sup>nd</sup> cycle of series C (fig. 8.21) are depicted.

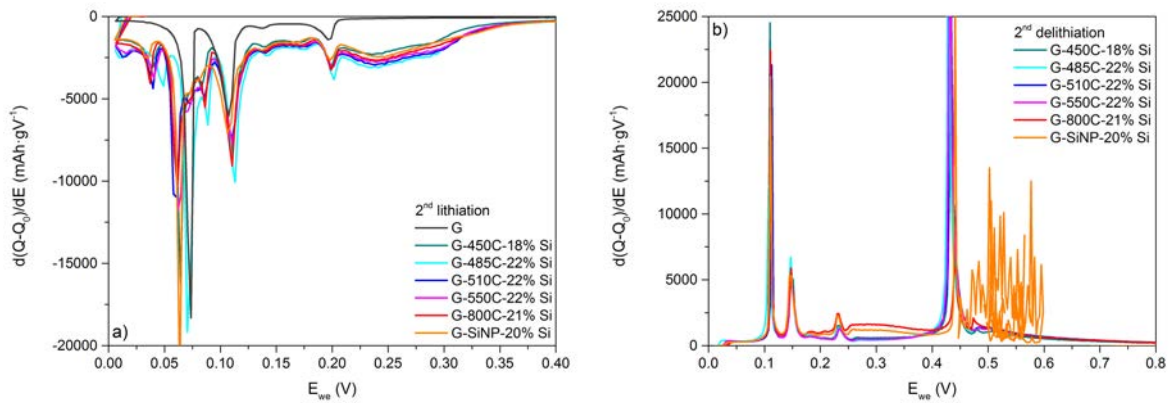


**Figure 8.19:** Differential capacity plots of the 2<sup>nd</sup> cycle a) lithiation and b) delithiation of batteries of series D.



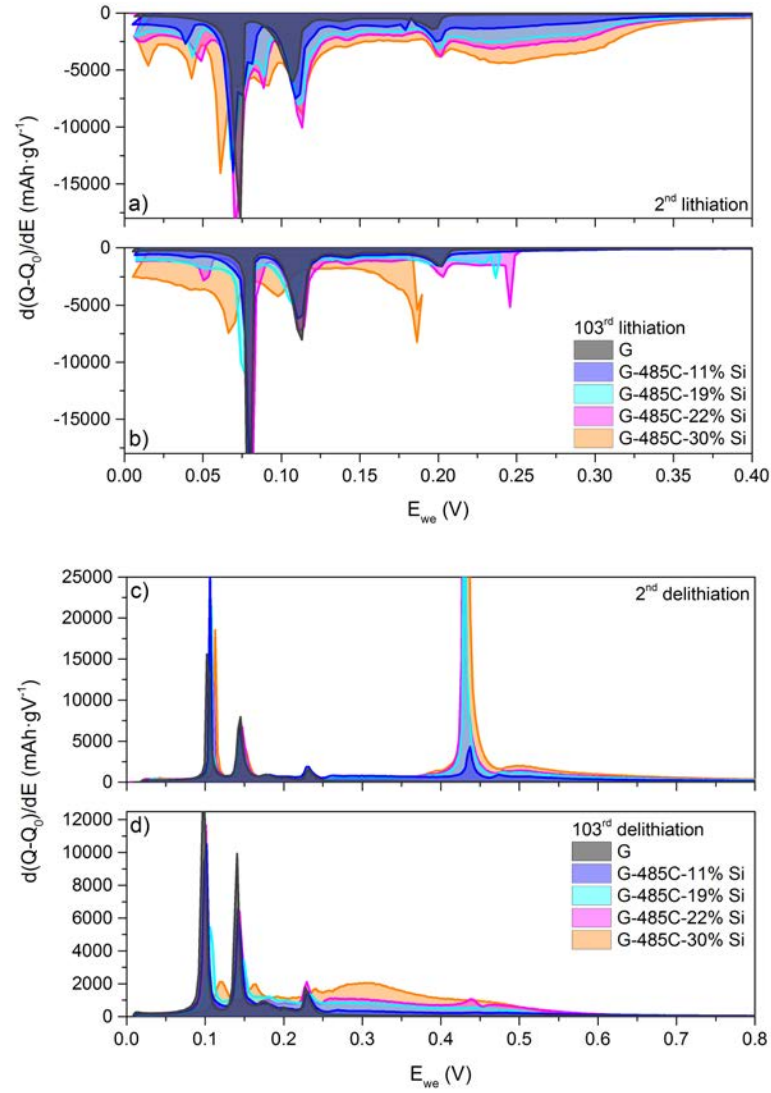


**Figure 8.20:** Differential capacity plots of the batteries of series B with a) 2<sup>nd</sup> lithiation, b) 103<sup>rd</sup> lithiation, c) 2<sup>nd</sup> delithiation and d) 103<sup>rd</sup> delithiation.

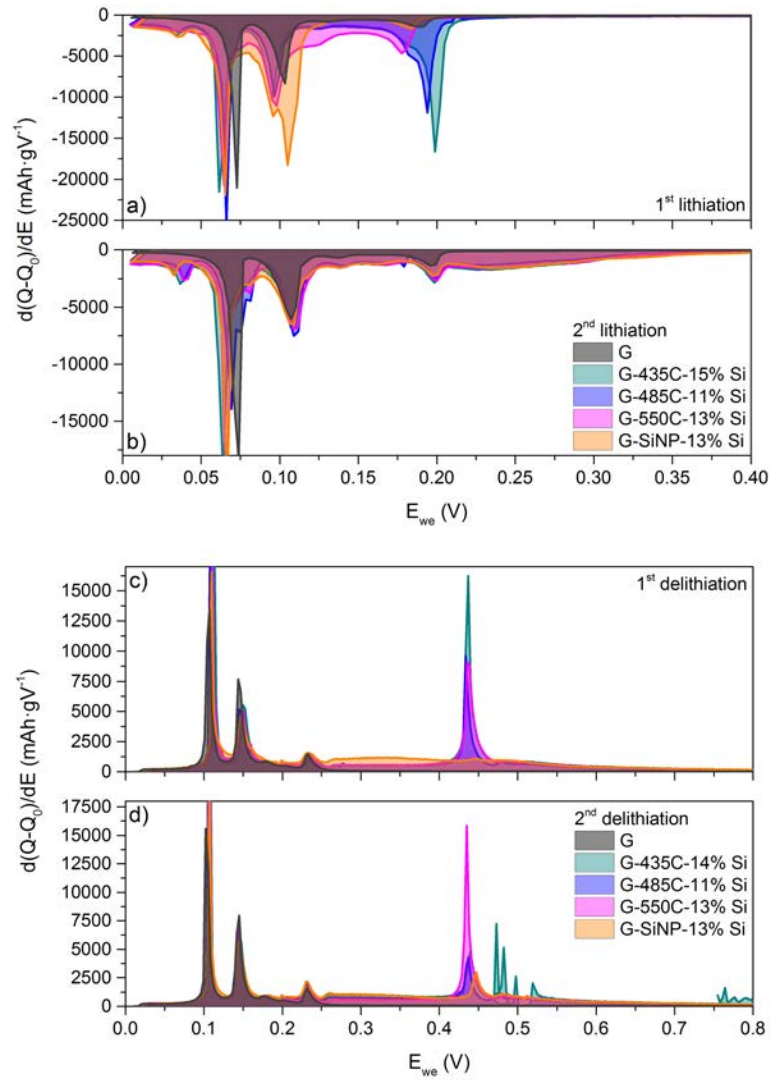


**Figure 8.21:** Differential capacity plots of the batteries of series C a) 1<sup>st</sup> lithiation, b) 2<sup>nd</sup> lithiation, c) 1<sup>st</sup> delithiation and d) 2<sup>nd</sup> delithiation.

In figure 8.22, the results of the C-rate capability tests on batteries containing graphite (G) and CB reference anodes, anodes of series C and anodes of series D are shown.

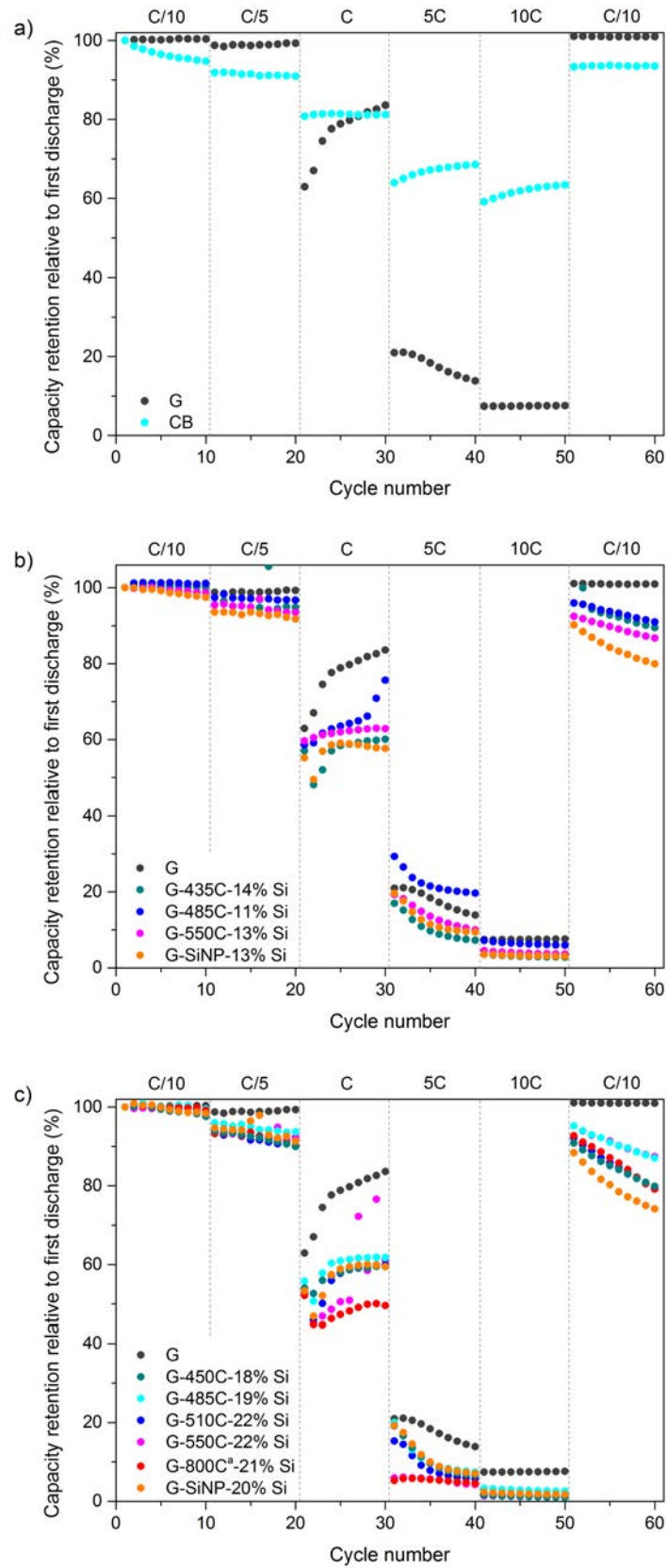


**Figure 8.22:** Capacity retention relative to first discharge as a function of the cycle number for C-rate variation protocol run on batteries containing a) G and CB reference anodes, b) anodes of series C and c) anodes of series D.

In figure 8.23, SEM images of a G-485C-19% Si anode after 103 cycles are depicted.

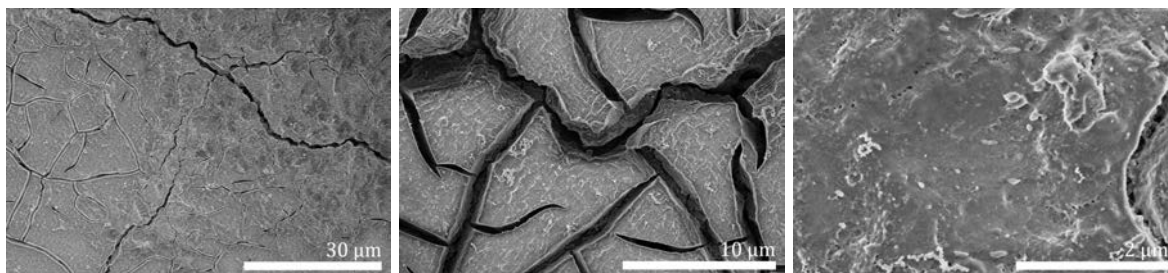


**Figure 8.23:** SEM images of G-485C-19% Si anode after 103 cycles.

In figure 8.24, SEM images of less SEI covered areas on G-550C-22% Si (a) and G-485C-19% Si (b, c) anodes after 103 cycles are shown.

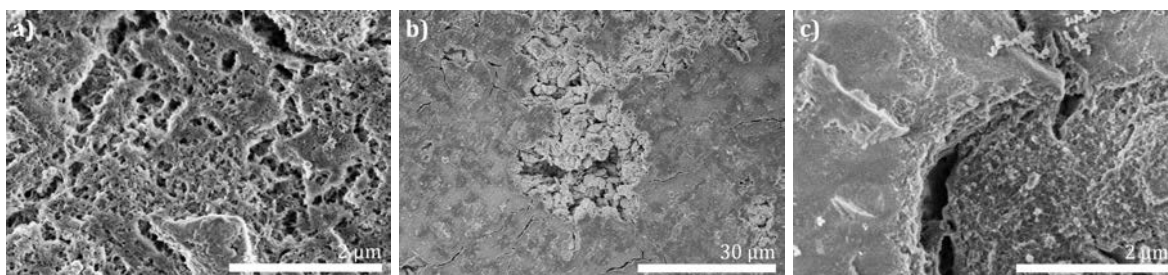


**Figure 8.24:** SEM images of a) G-550C-22% Si and b, c) G-485C-19% Si anode after 103 cycles.

In figure 8.25, SEM images of the cross section region of G-485C-19% Si after 103 cycles are shown.

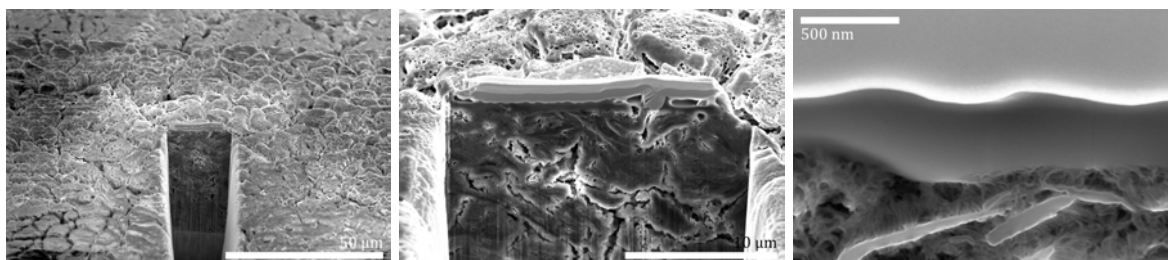


**Figure 8.25:** SEM images of cross section region of G-485C-19% Si anode after 103 cycles.

In figure 8.26 a), the EDX spectra for the cross section of the cycled G-485C-19% Si anode in spots A (SEI) and B (material) are plotted. Figure 8.26 b) presents the EDX spectrum of the graphite reference anode after 103 cycles.

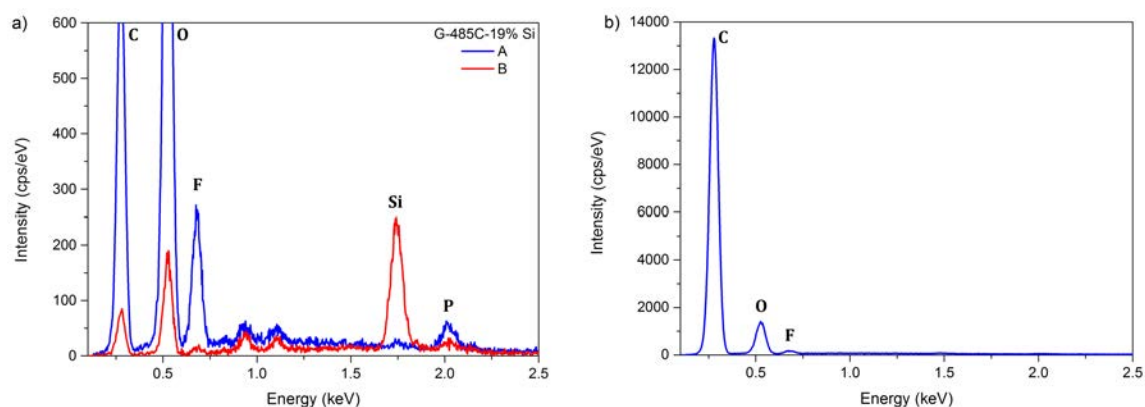


**Figure 8.26:** EDX spectra for a) the G-485C-19% Si anode cross section, spots A (SEI) and B (material), and b) the graphite reference anode after 103 cycles.

### 8.3 C Supporting information of chapter 5

In table 8.4, the silicon contents evaluated by TG-MS analysis and EA for all samples listed in table 5.5 are shown.

**Table 8.4:** Silicon contents evaluated by TG-MS analysis and EA

sample	EA	TGMS
	Si-wt. %	Si-wt. %
G-Si(21%)-60m	20.6	22.3
G-Si(20%)-C15m	19.7	21.5
G-Si(17%)-C30m	17.4	20.4
G-Si(19%)-C60m	19.4	19.7
G-Si(19%)-C90m	18.9	23.2
G-Si(12%)-C30m	12.4	13.0
G-Si(O)(24%)-C30m	24.0	26.6
G-C-Si(20%)-C30m	19.5	21.8

In figure 8.27, the mass development and the CO ( $m/z = 28$ ) and CO<sub>2</sub> ( $m/z = 44$ ) ion currents of the TG-MS analysis for all samples listed in table 5.5 are plotted.

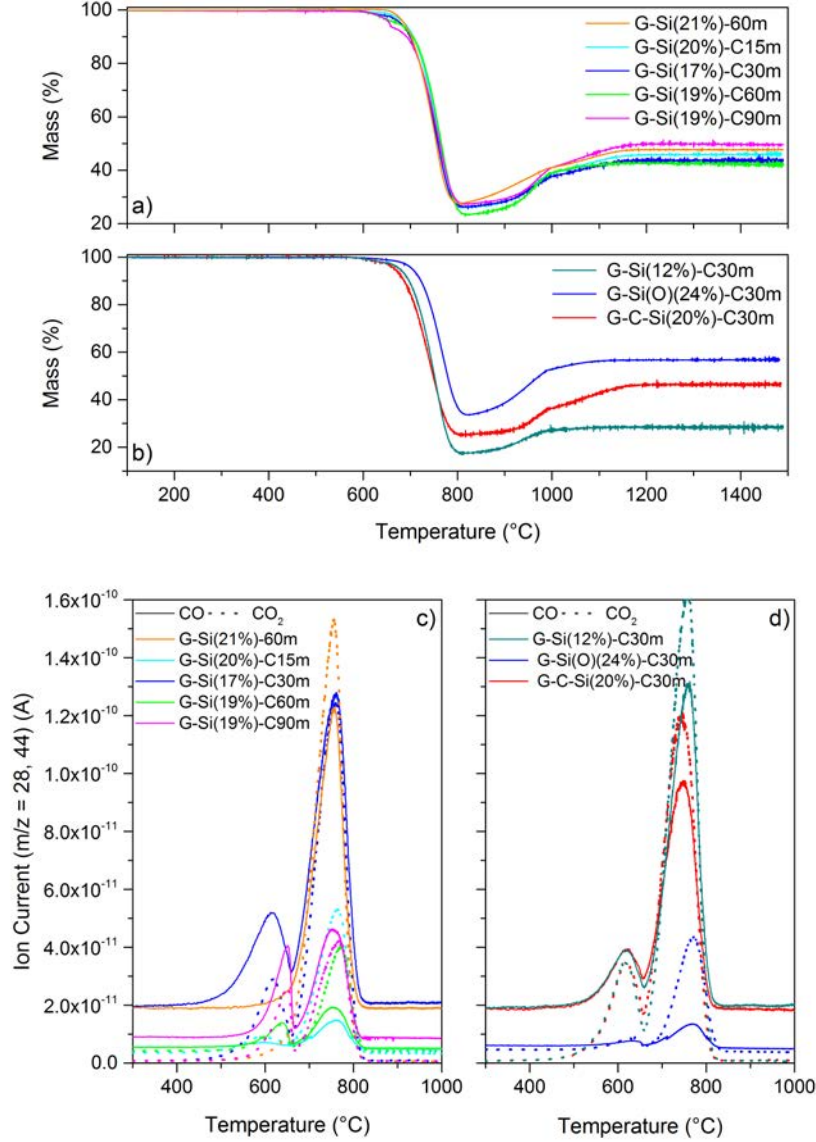


**Figure 8.27:** a, b) Mass and c, d) ion current for CO ( $m/z = 28$ , solid lines) and CO<sub>2</sub> ( $m/z = 44$ , dotted lines) as a function of temperature for G-Si(21%)-60m, G-Si(20%)-C15m, G-Si(17%)-C30m, G-Si(19%)-C60m, G-Si(19%)-C90m and b) G-Si(12%)-C30m, G-Si(O)(24%)-C30m and G-C-Si(20%)-C30m.



In figure 8.28, the Raman spectra from 200 – 3000  $\text{cm}^{-1}$  for G-Si(21%)-60m, G-Si(20%)-C15m, G-Si(17%)-C30m, G-Si(19%)-C60m, G-Si(19%)-C90m, G-Si(O)(24%)-C30m and G-C-Si(20%)-C30m normalised to the G-band are illustrated.

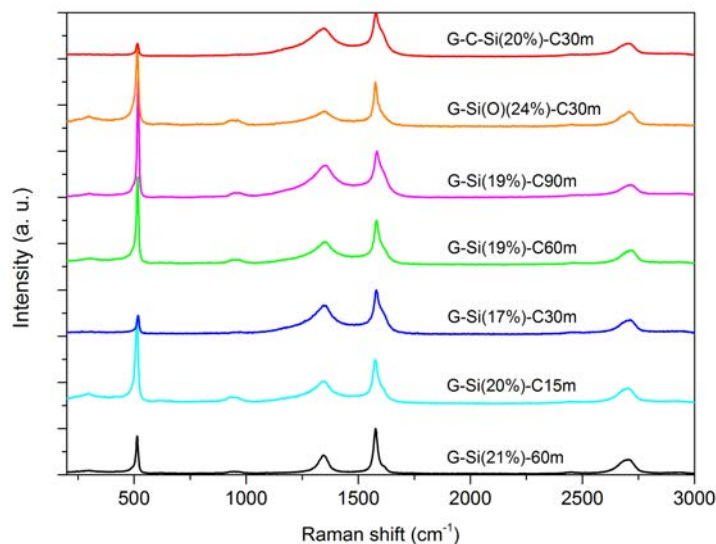


**Figure 8.28:** Raman spectra of G-Si(21%)-60m, G-Si(20%)-C15m, G-Si(17%)-C30m, G-Si(19%)-C60m, G-Si(19%)-C90m, G-Si(O)(24%)-C30m and G-C-Si(20%)-C30m.

SEM images of G-Si(21%)-60m, G-Si(20%)-C15m, G-Si(17%)-C30m, G-Si(19%)-C60m, G-Si(19%)-C90m and G-C-Si(20%)-C30m are shown in figure 8.29 – 8.32.

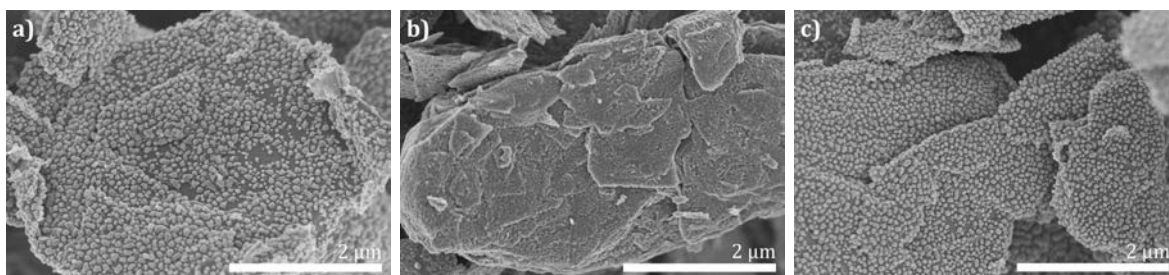


**Figure 8.29:** SEM images of a) G-Si(21%)-60m, b) G-Si(20%)-C15m and c) G-C-Si(20%)-C30m.

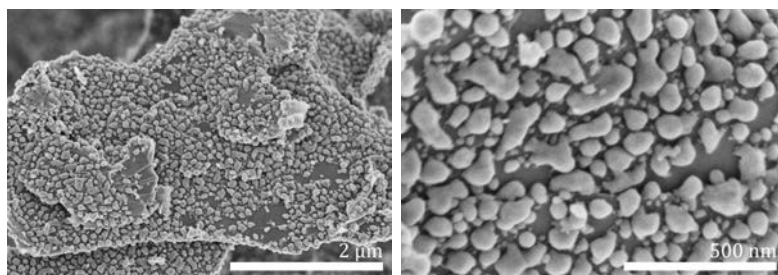


**Figure 8.30:** SEM images of G-Si(17%)-C30m.

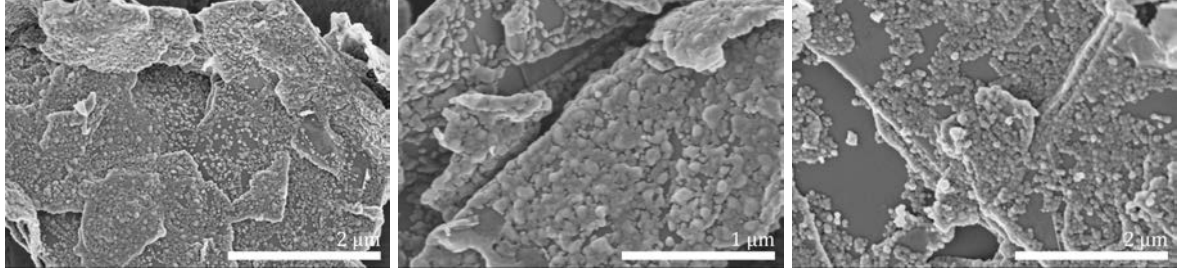


**Figure 8.31:** SEM images of G-Si(19%)-C60m.

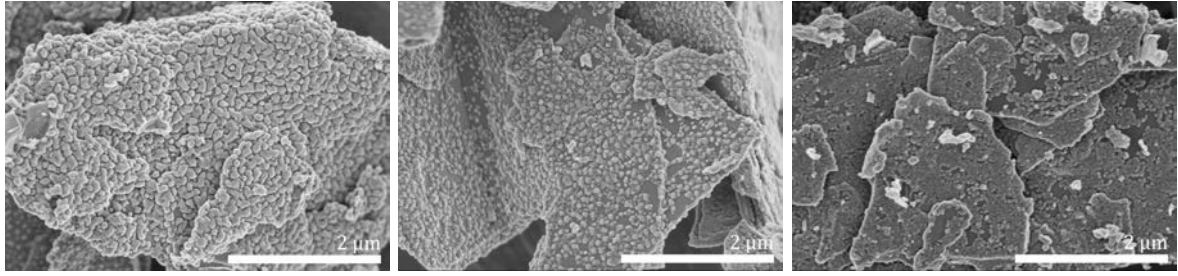


**Figure 8.32:** SEM images of G-Si(19%)-C90m.

The gravimetric discharge capacities and coulombic efficiencies of G-Si(21%)-60m, G-Si(20%)-C15m, G-Si(17%)-C30m, G-Si(19%)-C60m, G-Si(19%)-C90m, G-Si(O)(24%)-C30m and G-C-Si(20%)-C30m with replica as a function of the cycle number are plotted in figure 8.33.

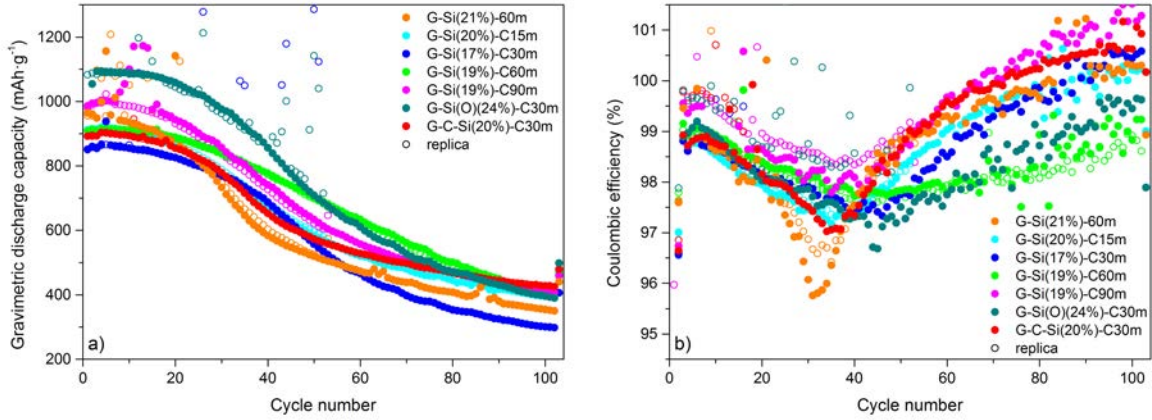


**Figure 8.33:** a) Gravimetric discharge capacity and b) CE as a function of the cycle number of G-Si(21%)-60m, G-Si(20%)-C15m, G-Si(17%)-C30m, G-Si(19%)-C60m, G-Si(19%)-C90m, G-Si(O)(24%)-C30m and G-C-Si(20%)-C30m batteries.



Differential capacity plots of the 2<sup>nd</sup> lithiation and delithiation of the G (graphite reference), G-Si(21%)-60m, G-Si(20%)-C15m, G-Si(17%)-C30m, G-Si(19%)-C60m, G-Si(19%)-C90m, G-Si(O)(24%)-C30m and G-C-Si(20%)-C30m batteries are depicted in figure 8.34.

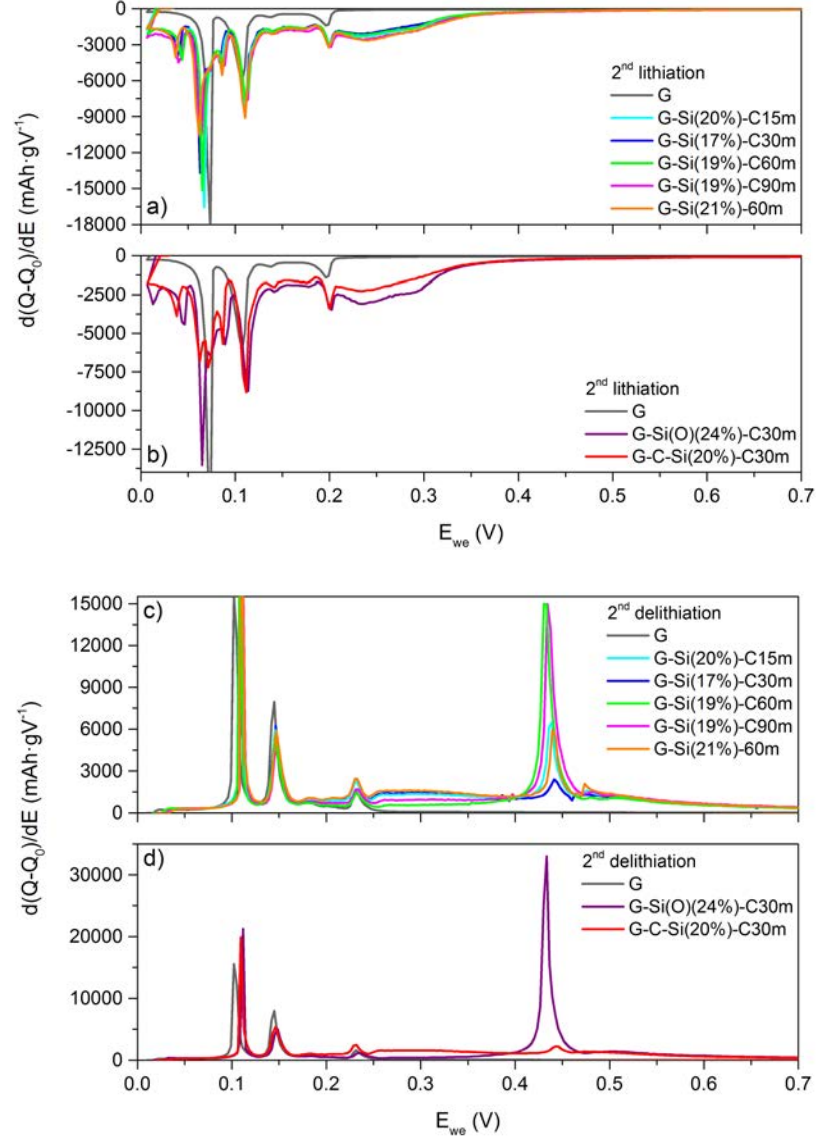


**Figure 8.34:** 2<sup>nd</sup> cycle lithiation (a,b) and delithiation (c,d) differential capacity plots of the G (graphite reference), G-Si(21%)-60m, G-Si(20%)-C15m, G-Si(17%)-C30m, G-Si(19%)-C60m, G-Si(19%)-C90m, G-Si(O)(24%)-C30m and G-C-Si(20%)-C30m batteries.

Differential capacity plots of the 103<sup>rd</sup> lithiation and delithiation of the G (graphite reference), G-Si(21%)-60m, G-Si(20%)-C15m, G-Si(17%)-C30m, G-Si(19%)-C60m, G-Si(19%)-C90m, G-Si(O)(24%)-C30m and G-C-Si(20%)-C30m batteries are shown in figure 8.35.

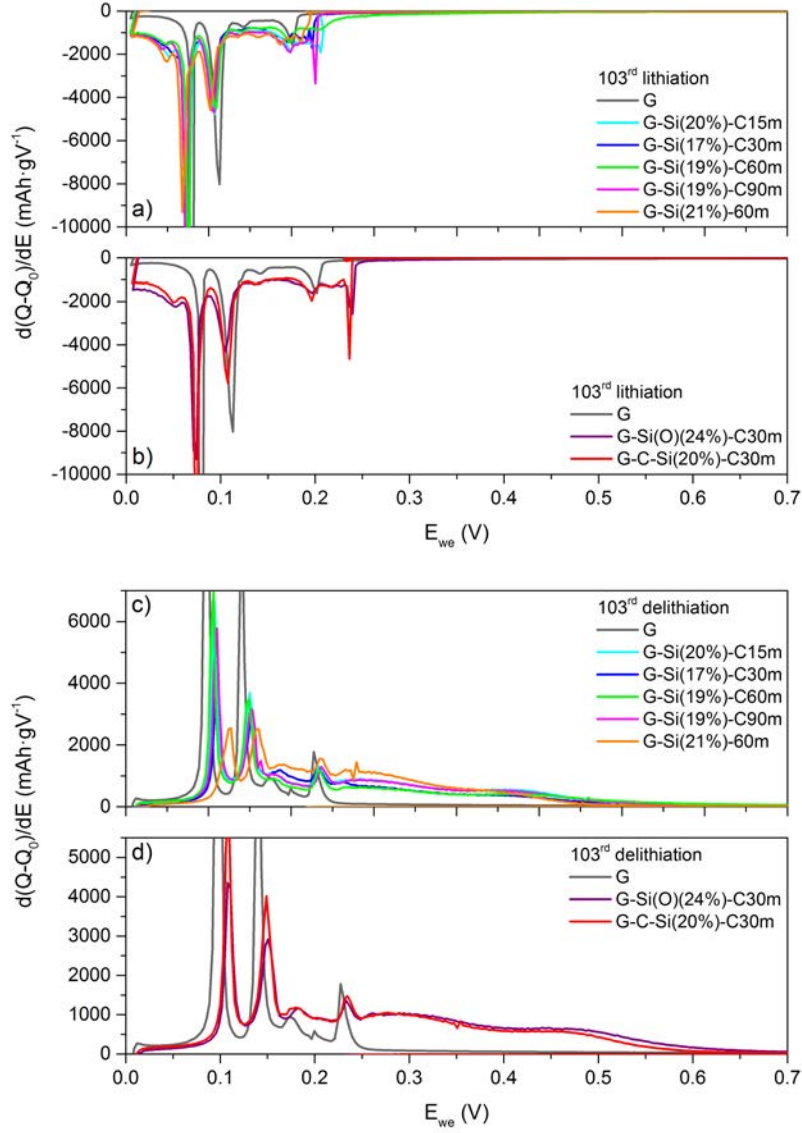


**Figure 8.35:** 103<sup>rd</sup> cycle lithiation (a,b) and delithiation (c,d) differential capacity plots of the G (graphite reference), G-Si(21%)-60m, G-Si(20%)-C15m, G-Si(17%)-C30m, G-Si(19%)-C60m, G-Si(19%)-C90m, G-Si(O)(24%)-C30m and G-C-Si(20%)-C30m batteries.

In figure 8.36 and 8.37, secondary electron images and the corresponding silicon and fluorine elemental maps of the cycled G-Si(19)-C60m anode for different spots on the anode surface are depicted.

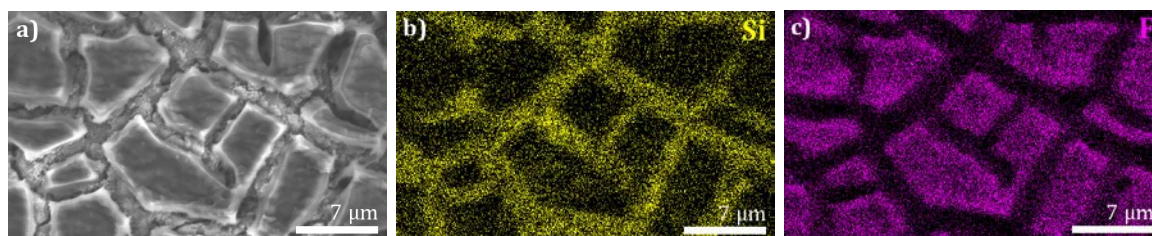


**Figure 8.36:** a) Secondary electron image and corresponding elemental maps of b) silicon and c) fluorine (700 nm interaction depth) of cycled G-Si(19)-C60m anode.

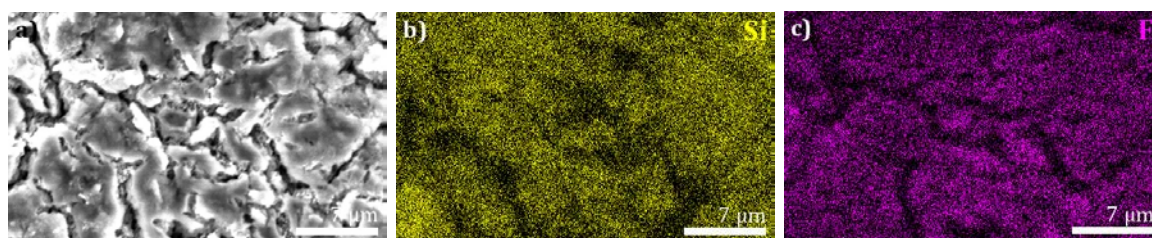


**Figure 8.37:** a) Secondary electron image and corresponding elemental maps of b) silicon and c) fluorine (700 nm interaction depth) of cycled G-Si(19)-C60m anode.

In figure 8.38 a-c), SEM images of the anode obtained from the twice propene treated sample (G-C-Si(20%)-C30m) after cycling are shown. The secondary electron image (8.38 d) and its corresponding elemental map of silicon and fluorine (8.38 e) were acquired on an anode region with more pronounced cracks.

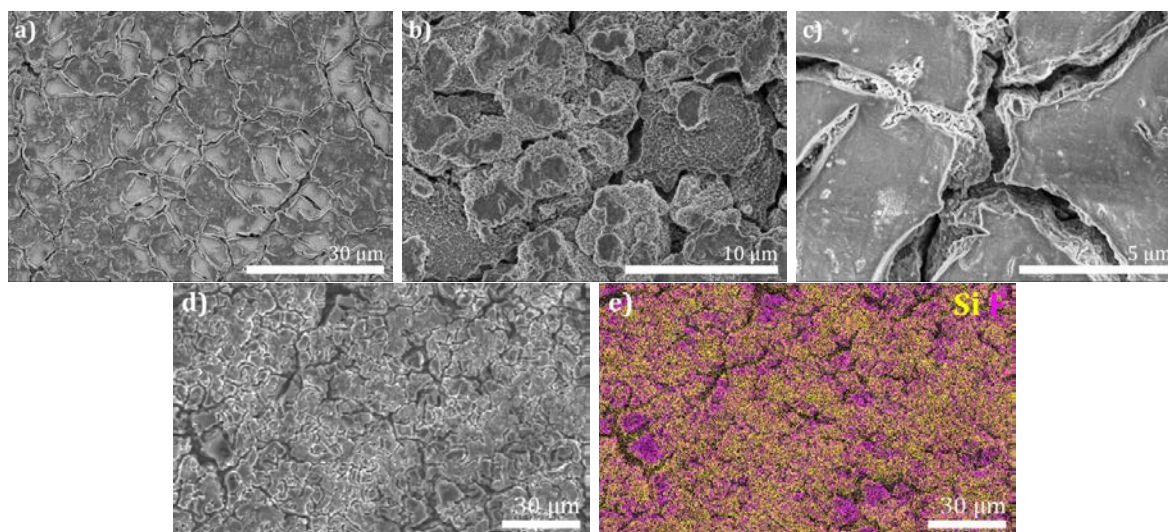


**Figure 8.38:** a,b,c) SEM images and d) secondary electron image with e) corresponding elemental maps of silicon and fluorine (700 nm interaction depth) of cycled G-C-Si(20%)-C30m anode.

In figure 8.39, the capacity and the coulombic efficiency of the G-Si(12%)-C30m batteries are plotted as a function of the cycle number. One battery was (dis-)charged 7 times (7 cycles) with a constant voltage sequence after each (dis-)charge (CC-CV protocol) and the other one was (dis-)charged 27 times (27 cycles) without a constant voltage sequence (CC protocol).

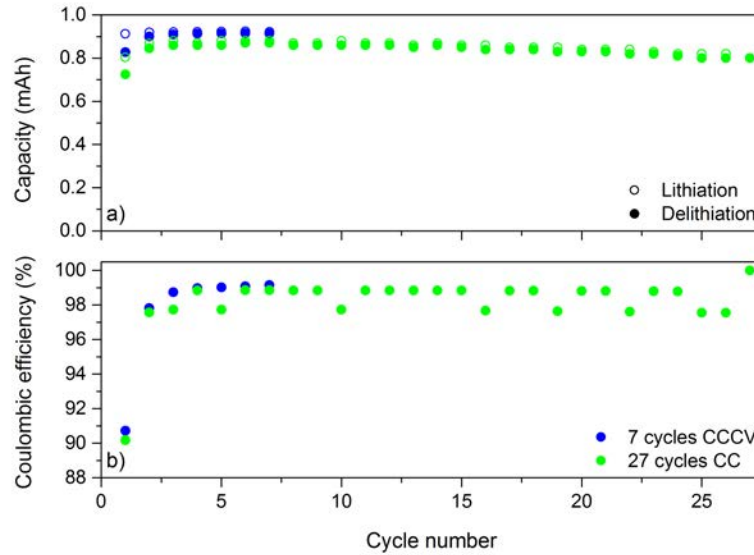


**Figure 8.39:** a) Capacity and b) coulombic efficiency as a function of the cycle number of G-Si(12%)-C30m batteries cycled for 7 cycles using a CC-CV protocol and 27 cycles using a CC protocol.

## 8.4 D Supporting information of chapter 6

In table 8.5, all batteries discussed in chapter 6 are listed with their synthesis parameters and battery setup.

**Table 8.5:** List of batteries tested in chapter 6 with reg. = regular, CCV = CC-CC-CV, mod. = modified and res. lith. = restricted lithiation protocol

label	LPCVD parameters	Si wt.-%	Electrolyte	battery setup	Protocol	m <sub>act</sub> (mg)	current 1C (μA)
G-450C-18% Si	SiH <sub>4</sub> , 450 °C, 2 h	◇ 18	LP40	reg.	reg.	-	904
		◇ 18	LP40	reg.	res. lith.	1.08	501
		◇ 18	LP71/FEC	mod.	mod.	1.06	863
G-485C-19% Si	SiH <sub>4</sub> , 485 °C 2 h	◇ 19	LP40	reg.	reg.	-	941
		◇ 19	LP40	reg.	CCV	1.01	1025
		◇ 19	LP40	reg.	CCV	-	1025
G-485C-22% Si	SiH <sub>4</sub> , 485 °C, 2 h	◇ 22	LP40	reg.	reg.	-	721
		◇ 22	LP71/FEC	mod.	mod.	0.54	515
G-550C-13% Si	SiH <sub>4</sub> , 550 °C, 1 h	◇ 13	LP40	reg.	reg.	1.45	1037
		◇ 13	LP71/FEC	mod.	mod.	1.62	857
G-550C-22% Si	SiH <sub>4</sub> , 550 °C, 2 h	◇ 22	LP40	reg.	reg.	-	1492
		◇ 22	LP71/FEC	mod.	mod.	-	1326
G-550C-30% Si	SiH <sub>4</sub> , 550 °C 3 h	◇ 30	LP40	reg.	reg.	-	1092
		◇ 30	LP71/FEC	mod.	mod.	0.94	1102
G-Si(19%)-C60m	SiH <sub>4</sub> , 485 °C, 2 h, C <sub>3</sub> H <sub>6</sub> , 800 °C, 1 h	◇ 19	LP40	reg.	reg.	-	954
		◇ 19	LP40	reg.	res. lith.	1.01	558
		◇ 19	LP71/FEC	mod.	mod.	1.04	951
G-SiNP-13% Si	-	◇ 13	LP40	reg.	reg.	-	773
		◇ 13	LP71/FEC	mod.	mod.	1.09	784
G-SiNP-20% Si	-	◇ 20	LP40	reg.	reg.	-	849
		◇ 20	LP40	reg.	res. lith.	0.84	445

In figure 8.40, the CE and gravimetric discharge capacity for the CVCV and CCV batteries are illustrated.

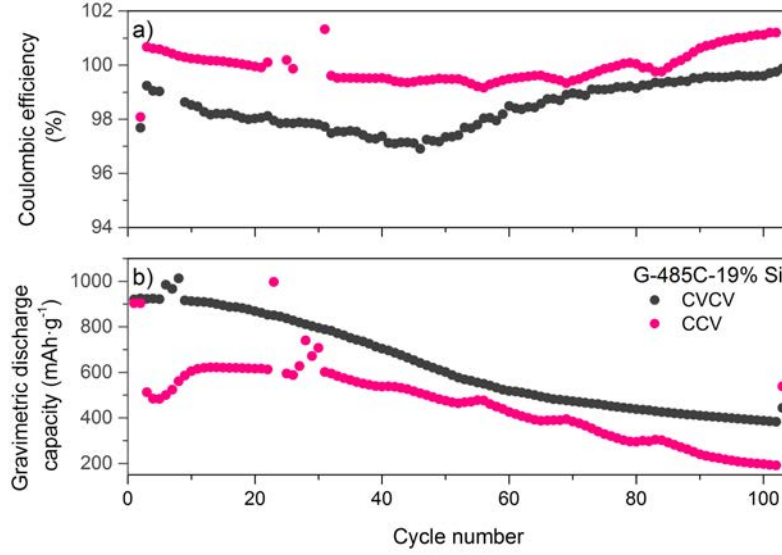


**Figure 8.40:** a) Coulombic efficiency and b) gravimetric discharge capacity as a function of the cycle number for the CVCV and CCV G-485C-19% Si batteries.

In figure 8.41, the differential capacity plots of the lithiation sequence in the 3<sup>rd</sup> and 100<sup>th</sup> cycle for batteries containing G-450C-18% Si, G-SiNP-20% Si and G-Si(19%)-C60m anodes, cycled with the restricted charging protocol are presented.

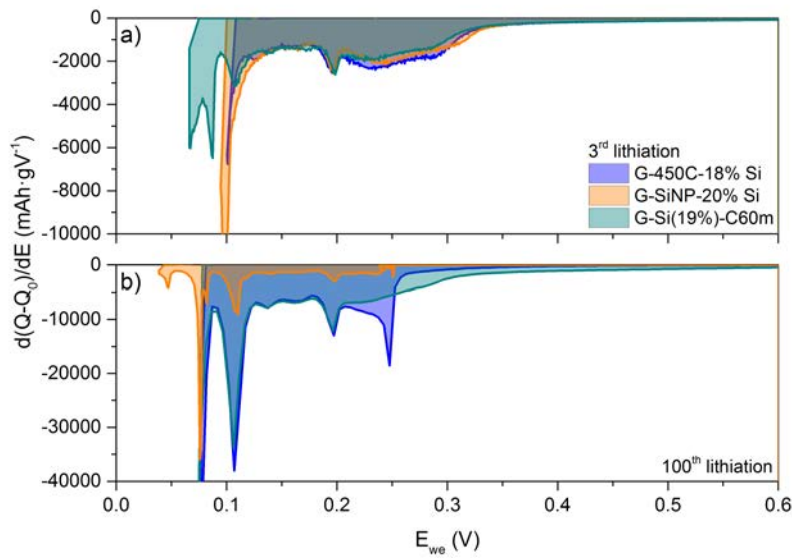


**Figure 8.41:** Differential capacity plots for batteries containing G-450C-18% Si, G-SiNP-20% Si and G-Si(19%)-C60m anodes, cycled with restricted lithiation; a) 3<sup>rd</sup>, b) 100<sup>th</sup> lithiation.



In figure 8.42, the C1s, O1s, P2p, F1s and Li1s XPS spectra of the anodes tested in the CVCV and CCV batteries are shown.

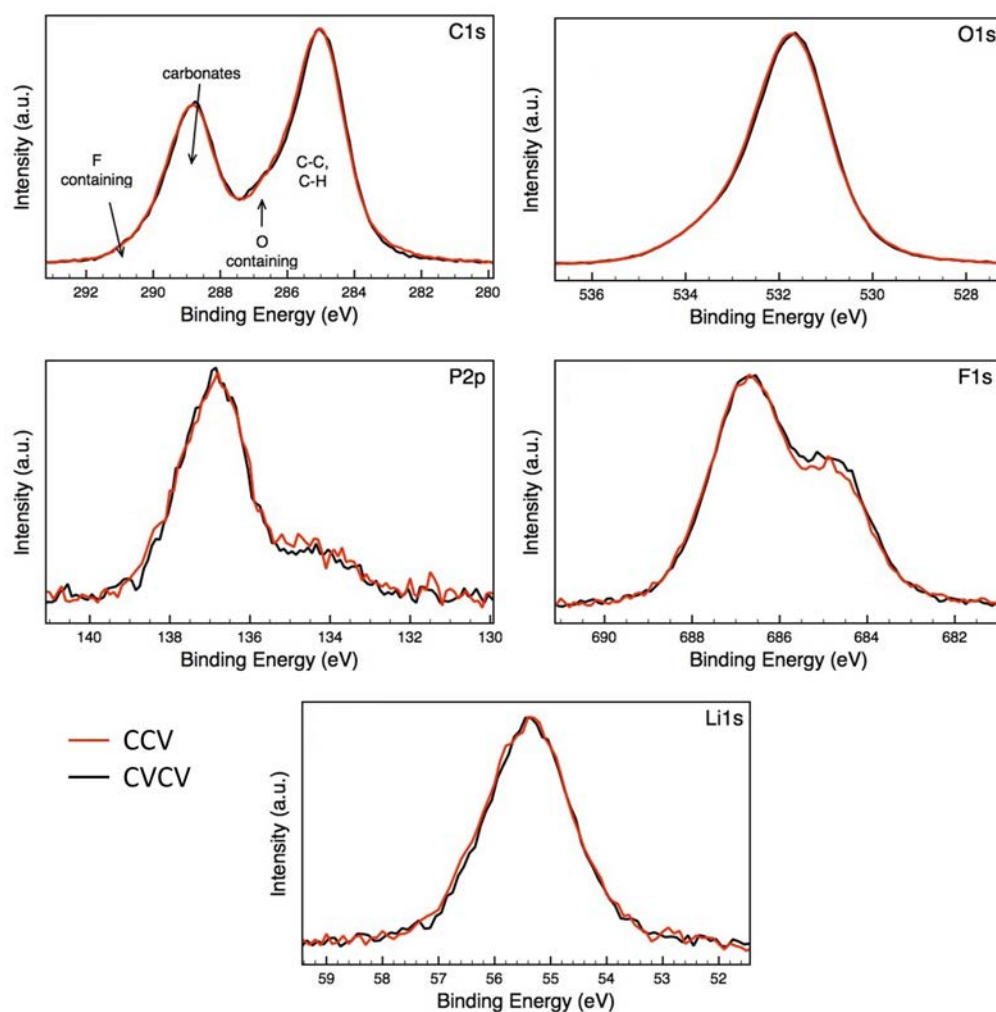


**Figure 8.42:** C1s, O1s, P2p, F1s and Li1s XPS spectra of the CCV (red) and CVCV (black) cycled battery anodes.

In figure 8.43 – 8.46, the gravimetric discharge capacity and coulombic efficiency as a function of the cycle number are illustrated for batteries containing graphite (G), G-450C-18% Si, G-485C-22% Si, G-550C-13% Si, G-550C-22% Si, G-550C-30% Si, G-SiNP-13% Si and G-Si(19%)-C60m anodes, cycled in the regular and the modified setup.

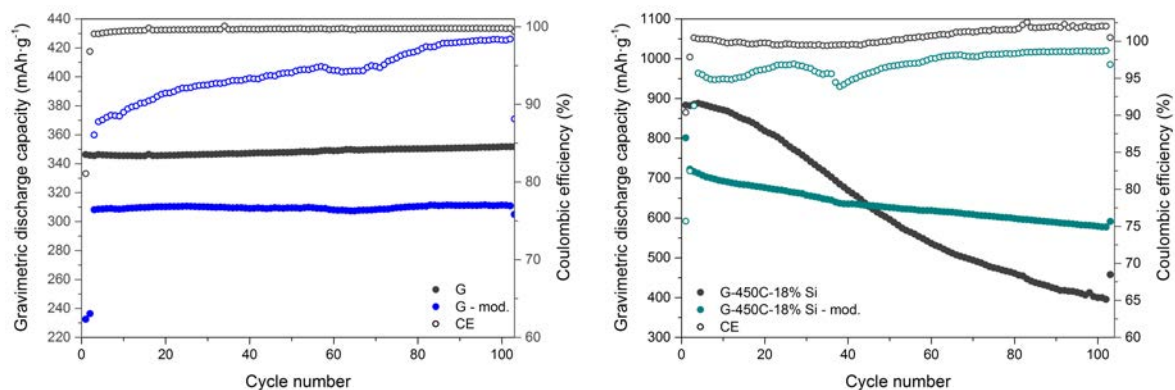


**Figure 8.43:** Gravimetric discharge capacity and coulombic efficiency as a function of the cycle number of the graphite (left) and G-450C-18% Si (right) batteries, cycled in regular and modified (mod.) setup.

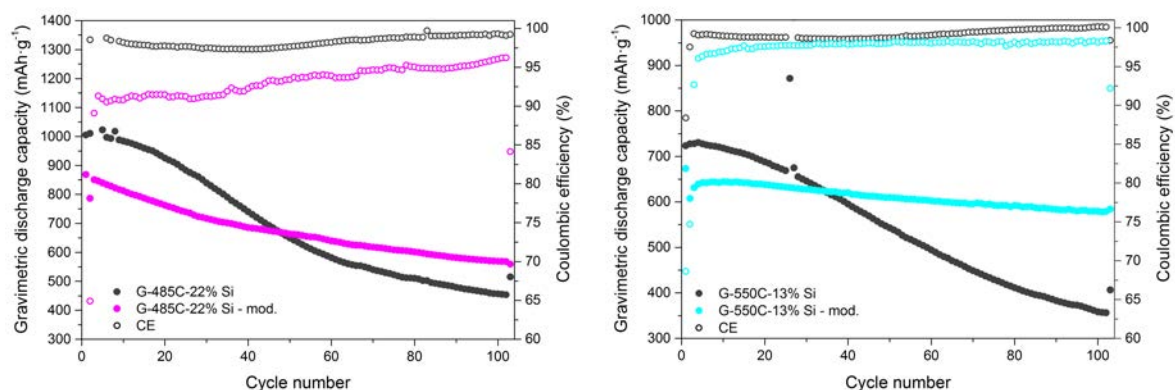


**Figure 8.44:** Gravimetric discharge capacity and coulombic efficiency as a function of the cycle number of the G-485C-22% Si (left) and G-550C-13% Si (right) batteries, cycled in regular and modified (mod.) setup.

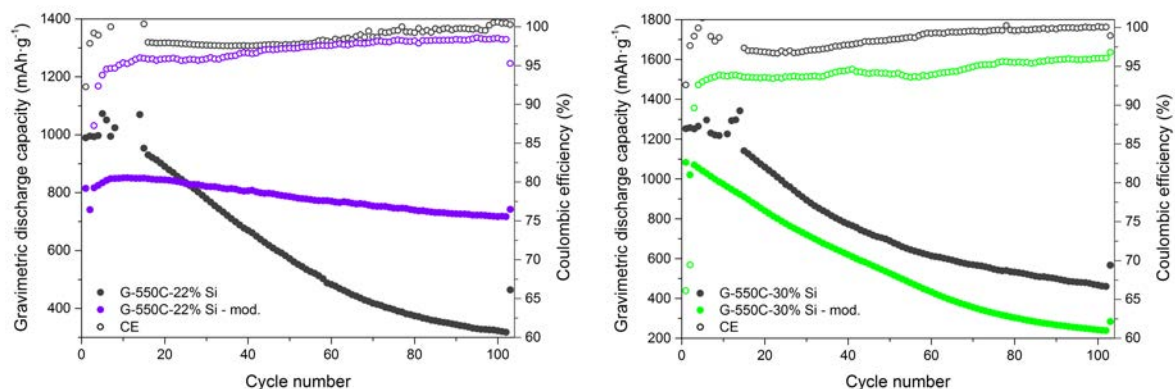


**Figure 8.45:** Gravimetric discharge capacity and coulombic efficiency as a function of the cycle number of the G-550C-22% Si (left) and G-550C-30% Si (right) batteries, cycled in regular and modified (mod.) setup.



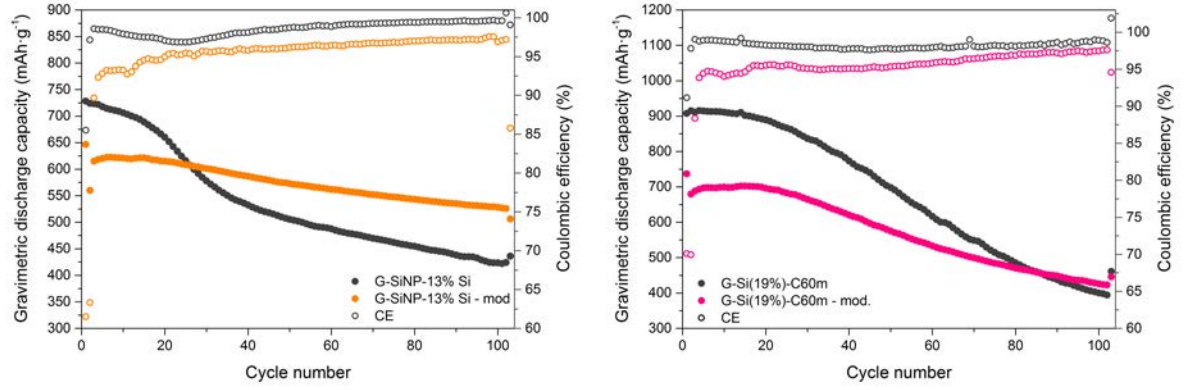


**Figure 8.46:** Gravimetric discharge capacity and coulombic efficiency as a function of the cycle number of the G-SiNP-13% Si (left) and G-Si(19%)-C60m (right) batteries, cycled in regular and modified (mod.) setup.

In figure 8.47, the differential capacity plots of the 1<sup>st</sup> anode lithiation sequence of G-450C-18% Si, G-485C-22% Si, G-550C-13% Si, G-550C-22% Si and G-SiNP-13% Si batteries, cycled in the regular and modified battery setup, are illustrated.

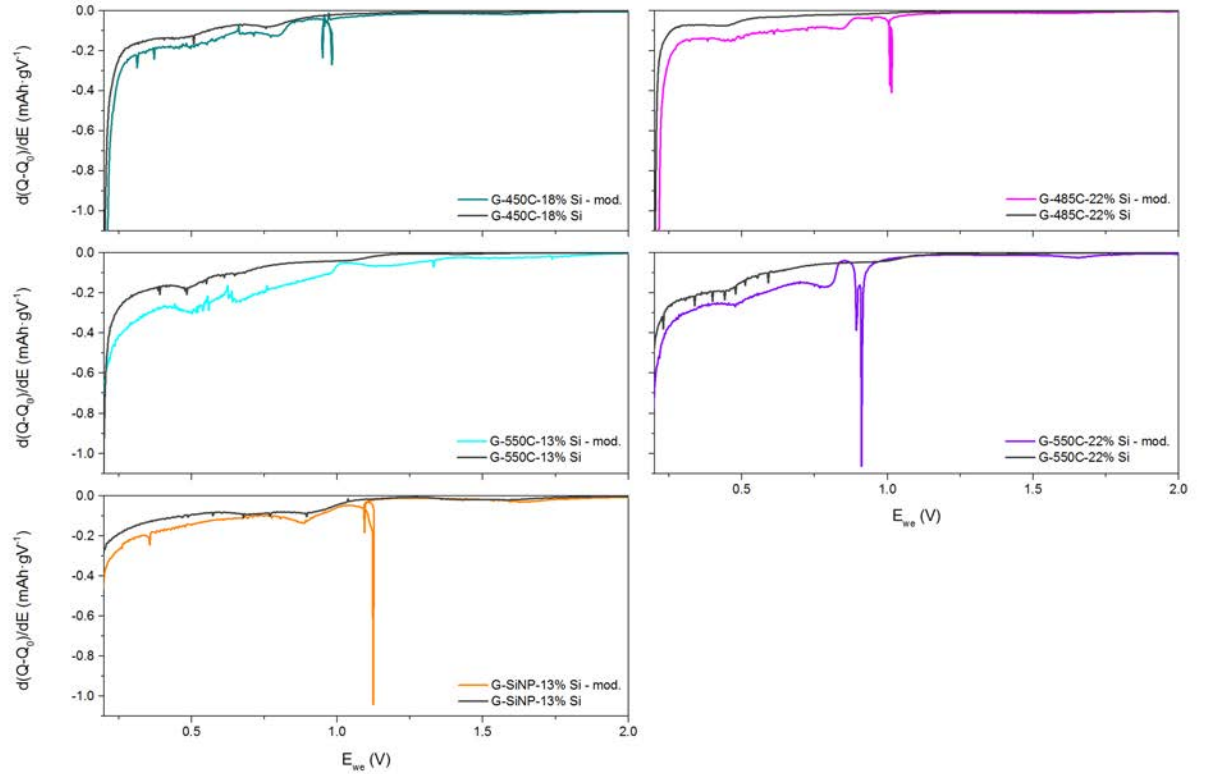


**Figure 8.47:** Differential capacity plots of 1<sup>st</sup> cycle anode lithiation of G-450C-18% Si, G-485C-22% Si, G-550C-13% Si, G-550C-22% Si and G-SiNP-13% Si batteries between 0.1 – 2.0 V cycled in the regular and modified (mod.) battery setup.

In figure 8.48, the differential capacity plots of the 1<sup>st</sup> cycle of G-550C-13% Si batteries, cycled in the regular and modified battery setup, are illustrated.

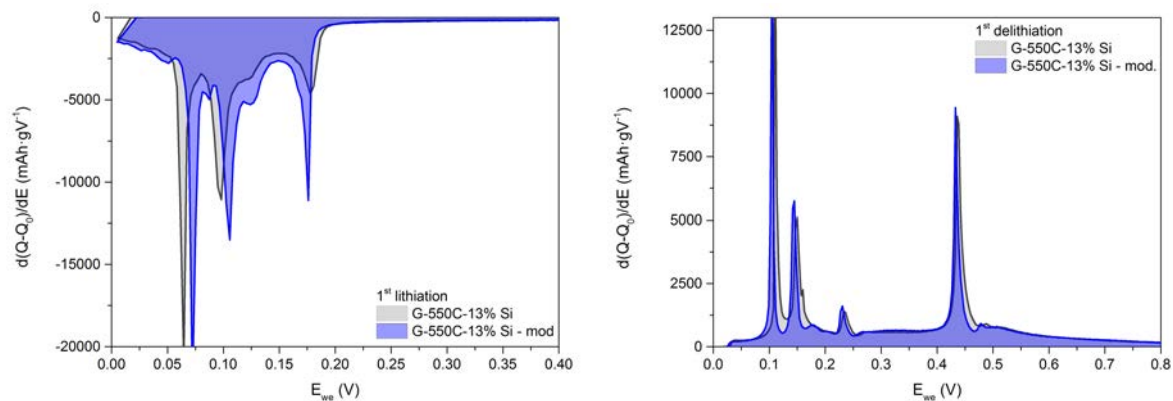


**Figure 8.48:** Differential capacity plots of the 1<sup>st</sup> cycle anode lithiation (left) and delithiation (right) of G-550C-13%-Si batteries, cycled in the regular and modified battery setup.

In figure 8.49, additional SEM images of the G-550C-22% Si anode cycled in the modified battery setup are depicted.

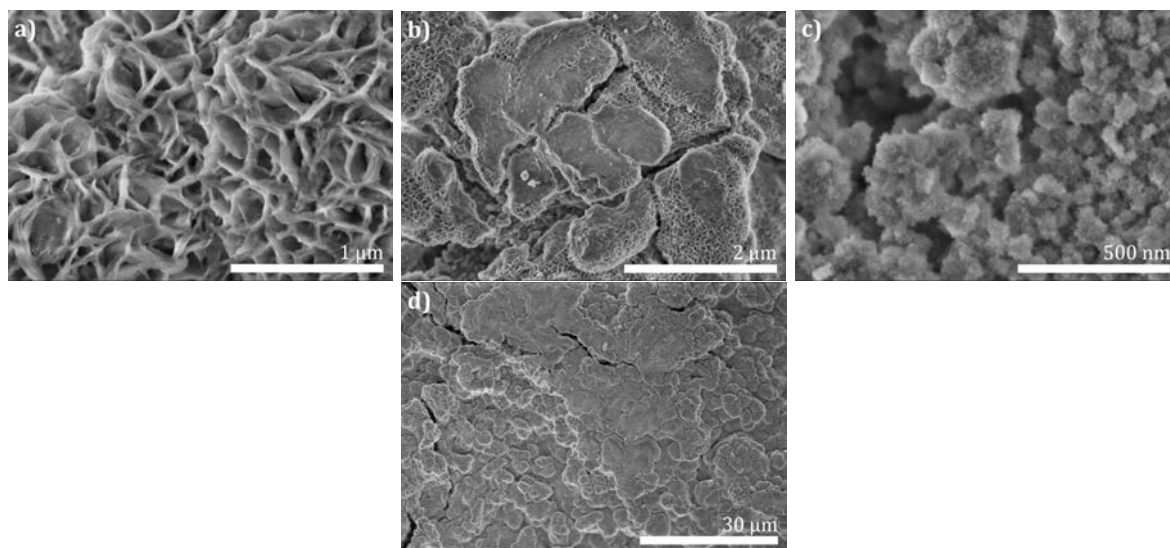


**Figure 8.49:** SEM images of G-550C-22% Si anode cycled in the modified battery setup.

# List of Figures

1.1	a) Ragone plot showing power density vs. energy density of different storage technologies adapted from ref. <sup>[10]</sup> ; b) History of the development of secondary batteries in view of energy density (dashed line represents progress 1930 – 2010 and solid line represents development of LIBs 1990 – 2010, adapted from ref. <sup>[6]</sup> ). . . . .	2
1.2	Schematic of a LIB cell comprised of a graphite anode and a LiCoO <sub>2</sub> cathode, separated by a membrane and liquid electrolyte. <sup>[11]</sup> . . . . .	3
1.3	Total specific capacity of a LIB as a function of the specific capacity of the anode for distinct cathodic specific capacities (Cc) based on eq. 2 (fig. adapted from ref. <sup>[21]</sup> ). . . . .	4
1.4	a) Schematic drawing of LiC <sub>6</sub> showing the AA layer stacking sequence and the $\alpha\alpha$ interlayer ordering of the intercalated lithium, b) view perpendicular to the basal plane of LiC <sub>6</sub> c) schematic galvanostatic curve for stage formation during electrochemical lithiation of graphite (adapted from ref. <sup>[12]</sup> ). . . . .	6
1.5	Li-Si phase diagram. <sup>[50]</sup> . . . . .	8
1.6	a) Diagram for cycling of a Li/Si electrochemical cell with 1 <sup>st</sup> lithiation (blue), 1 <sup>st</sup> delithiation (green) and 2 <sup>nd</sup> lithiation (red); a-Li <sub>y</sub> Si $\hat{=}$ fixed composition that coexists with c-Si, a-Li <sub>x</sub> Si $\hat{=}$ single-phase region of variable composition, Li <sub>2</sub> Si $\hat{=}$ fixed composition that coexists with Li <sub>15</sub> Si <sub>4</sub> during delithiation, Li <sub>15<math>\pm</math>w</sub> Si <sub>4</sub> $\hat{=}$ variable stoichiometry single-phase region <sup>[53]</sup> ; b) schematic view of the lithiation mechanism of an a-Si thin film. <sup>[68]</sup> . . . . .	9
1.7	Silicon anode failure mechanisms: (a) material pulverisation, (b) material vertical displacement and (c) continuous SEI growth. <sup>[81]</sup> . . . . .	10
1.8	Structural formula of a) ethylene carbonate (EC), b) diethyl carbonate (DEC), c) dimethyl carbonate (DMC), d) lithium hexafluorophosphate (LiPF <sub>6</sub> ) and e) fluoroethylene carbonate (FEC). . . . .	11
1.9	Schematic view of the mechanisms occurring at the surface of silicon nanoparticles: initial formation of the SEI, Li <sub>x</sub> Si, Li <sub>2</sub> O and Li <sub>x</sub> SiO <sub>y</sub> formation upon further lithiation and the partial reversibility upon delithiation (adapted from ref. <sup>[121]</sup> ). . . . .	14
1.10	Diagram of a) the cycle performance of ball-milled silicon with CMC-433 composition and b) the coulombic efficiency as a function of the cycle number. <sup>[123]</sup> . . . . .	16
1.11	Radar plot with a) individual stress factors for diverse battery categories <sup>[142]</sup> and b) battery data for varied electrolyte combinations in Li(Ni <sub>1/3</sub> Mn <sub>1/3</sub> Co <sub>1/3</sub> )O <sub>2</sub> /graphite pouch cells <sup>[143]</sup> . . . . .	17
1.12	Specific capacity as a function of the cycle number for Si/C electrodes in electrolytes containing 0, 1, 5, 10, 15 and 20 wt.-% FEC at current densities from 0.5 – 12.5 A · g <sup>-1</sup> to illustrate the C-rate capability. <sup>[130]</sup> . . . . .	17

1.13	a) Differential capacity plot of graphite <sup>[150]</sup> and b) reversible potential of a lithium-graphite-intercalation compound as a function of $x$ in $\text{Li}_x\text{C}_6$ . <sup>[153]</sup>	18
1.14	a) DCP of graphene-silicon nanocomposite <sup>[157]</sup> and first cycle DCPs of b) Si-NWs at different cutoff voltages of 10 mV (red), 70 mV (grey) and 150 mV (blue) and c) crystalline-amorphous core-shell Si-NWs (red) and single crystalline Si-NWs (green) <sup>[165]</sup> .	20
3.1	LPCVD reactor: a) picture of the hot wall LPCVD reactor with the rotary insert, b) picture of the deposition chamber of the rotary insert, c) scheme of the reactor and gas flow and d) picture of the quartz reactor insert connected to the rotary feedthrough sealing.	27
3.2	SEM images of a) MWCNTs, b) MWCNT-HTC and c) G before and a') MWCNTs-Si, b') MWCNT-HTC-Si and c') G-Si after silicon deposition.	30
3.3	a) STEM image of MWCNTs with silicon deposition (sample: MWCNT-HTC-Si) with b) respective silicon elemental map obtained from EDX.	31
3.4	SEM images of G-Si anodes after a) OCV b) 20 (dis-)charge cycles and c) 50 (dis-)charge cycles.	32
3.5	NEXAFS spectra of a) G-SiNP and b) G-Si anodes after OCV, 1, 3, 7, 10 and 20 cycles with silicon nanoparticle (Si NP) reference.	32
4.1	Summary of 1 <sup>st</sup> lithiation and subsequent cycling as suggested by McDowell et al. <sup>[67]</sup>	37
4.2	Graph of a) silicon content according to TG-MS and EA analysis for respective samples; b) silicon content according to TG-MS as a function of the silicon content according to EA.	43
4.3	Powder XRD patterns of sample series a) A and b) B.	44
4.4	Powder XRD patterns of sample series a) C and b) D with additional G-800C <sup>a</sup> -21% Si and G/Si NP mixture (G-SiNP-21% Si).	45
4.5	Raman spectra normalized to TO-band of sample series a) A and b) D with additional spectra of G-800C <sup>a</sup> -21% Si and Si NPs. For full range spectra see SI (fig. 8.14).	46
4.6	SEM images of a) G, b) G-435C-14% Si, c) G-450C-18% Si, d) G-485C-19% Si, e) G-485C-22% Si, f) G-485C-30% Si, g) G-550C-08% Si, h) G-550C-13% Si, i) G-550C-22% Si, k) G-550C-30% Si, l) G-800C <sup>a</sup> -21% Si and m) Si NPs.	47
4.7	BF-TEM images of the G-485C-22% Si cross section.	48
4.8	a) HRTEM image, b) HAADF image and STEM-EDX single element maps for c) carbon, d) silicon and e) oxygen of the G-485C-22% Si cross section.	48
4.9	Gravimetric discharge capacity and CE as a function of the cycle number for batteries containing anodes obtained from silicon deposited at 550 °C for 30 – 180 min (series A).	50
4.10	Radar plots of the performance of batteries containing anodes from silicon deposited at 550 °C for 30, 60, 120 and 180 min, leading to 8, 13, 22 and 30 wt.-% silicon content (series A).	51
4.11	Radar plots of the performance of batteries containing anodes from silicon deposited at 485 °C for 60, 120 and 180 min, leading to 11, 19, 22 and 30 wt.-% silicon content (series B). The 1 <sup>st</sup> cycle CE for G-485C-22% Si was taken from a replica battery.	52

4.12	Radar plots of the performance of batteries containing anodes from silicon deposited at 435 °C, 485 °C and 550 °C, resulting in ~13 wt.-% silicon content (series C) and additionally a graphite/Si NP mixture with 13 wt.-% silicon. . . . .	53
4.13	Radar plots of the performance of batteries containing anodes from silicon deposited at 450 °C, 485 °C, 510 °C and 550 °C, resulting in ~21 wt.-% silicon content (series D) with additional the sample annealed at 800 °C and a graphite/Si NP mixture with 20 wt.-% silicon. The 1 <sup>st</sup> cycle CE for G-485C-22% Si was taken from a replica battery. . . . .	55
4.14	Contour plot illustrating the gravimetric discharge capacity per silicon and cycle as a function of the silicon loading and the deposition temperature (dots = data points; dark areas indicate higher capacities, bright areas lower capacities). . . . .	55
4.15	Differential capacity plots of G-550C-22% Si batteries at 2 <sup>nd</sup> , 53 <sup>rd</sup> and 103 <sup>rd</sup> cycle for a) lithiation and b) delithiation. . . . .	56
4.16	Differential capacity plots of batteries containing anodes from silicon deposited at 550 °C for 30 – 180 min (series A): a) 2 <sup>nd</sup> lithiation, b) 103 <sup>rd</sup> lithiation, c) 2 <sup>nd</sup> delithiation and d) 103 <sup>rd</sup> delithiation. . . . .	57
4.17	Differential capacity plots of batteries containing anodes with ~21 wt.-% silicon (series D) in the 1 <sup>st</sup> cycle, a) lithiation of silicon deposited at 450, 485 and 510 °C, c) respective delithiation, b) lithiation of silicon deposited at 550 °C, annealed sample at 800 °C and graphite/Si NP mixture and d) respective delithiation. . . . .	59
4.18	Capacity retention relative to first discharge as a function of the cycle number for C-rate capability tests conducted on batteries containing silicon anodes obtained from silicon deposition at 550 °C for 30 – 180 min (series A) and at 485 °C for 60 – 180 min (series B). . . . .	60
4.19	SEM images of G-550C-22% Si anodes a, b) before cycling, c, d) after 52 cycles and e, f) after 103 cycles. . . . .	61
4.20	EDX spectra for spots A and B in SEM image 4.19 e). . . . .	62
4.21	a) Secondary electron image of G-485C-19% Si anode after 103 cycles and corresponding single element maps of b) silicon, c) fluorine and d) oxygen (700 nm interaction depth). . . . .	62
4.22	SEM image of the cross section of a G-485C-19% Si anode after 103 cycles. . . . .	63
4.23	SEM images of a graphite reference anode after 103 cycles. . . . .	64
5.1	Comparison of model predictions (lines) with experimental mole fraction profiles (symbols) of major species during propylene pyrolysis at 900 °C and 8 kPa. <sup>[226]</sup> . . . . .	69
5.2	a) Sample mass and b) ion current for CO (m/z = 28, solid lines) and CO <sub>2</sub> (m/z = 44, dotted lines) as a function of temperature for samples treated for 15, 30, 60 and 90 min with C <sub>3</sub> H <sub>6</sub> and 60 min annealing under vacuum. . . . .	75
5.3	Powder XRD patterns for a) samples treated for 15, 30, 60 and 90 min with C <sub>3</sub> H <sub>6</sub> and 60 min annealing under vacuum and b) G-Si(12%)-C30m, G-Si(O)(24%)-C30m and G-C-Si(20%)-C30m. . . . .	76
5.4	a) Example fitting of sample G-Si(19%)-C90m, b) Raman spectra of the samples treated for 15, 30, 60 and 90 min with C <sub>3</sub> H <sub>6</sub> and 60 min annealing under vacuum and c) percentage share of the D3 band integral of the samples obtained from 15, 30, 60 and 90 min C <sub>3</sub> H <sub>6</sub> treatment. . . . .	77

5.5	SEM images of a) G-Si(19%)-60m, b) G-Si(20%)-C15m, c) G-Si(17%)-C30m, d) G-Si(19%)-C60m, e) G-Si(19%)-C90m and f) G-C-Si(20%)-C30m. . . . .	78
5.6	SEM images of a) G-Si(20%)-C15m with pronounced inhomogeneous silicon sintering on two graphite flakes and b) G-Si(19%)-C90m exhibiting abrasive-appearing silicon surface. . . . .	78
5.7	TEM images of G-Si(12%)-C30m. . . . .	78
5.8	TEM image of G-Si(12%)-C30m with corresponding EDX elemental map of Si and C. . . . .	79
5.9	STEM BF images with EDX elemental map and line scan of a) G-Si(19%)-C60m (left) and b) G-Si(O)(24%)-C30m (right). . . . .	79
5.10	Radar plots of the performance of batteries containing anodes from C <sub>3</sub> H <sub>6</sub> treatment for 15 (G-Si(20%)-C15m), 30 (G-Si(17%)-C30m), 60 (G-Si(19%)-C60m) and 90 min G-Si(19%)-C90m) and the sample annealed under vacuum (G-Si(21%)-60m). . . . .	81
5.11	Radar plots of the performance of batteries containing anodes from C <sub>3</sub> H <sub>6</sub> treatment for 30 min (G-Si(17%)-C30m), the air exposed sample (G-Si(O)(24%)-C30m) and the twice C <sub>3</sub> H <sub>6</sub> treated sample (G-C-Si(20%)-C30m). The 1 <sup>st</sup> cycle CE of the G-Si(O)(24%)-C30m battery was taken from a replica battery. . . . .	82
5.12	Averaged discharge capacity per silicon and cycle of batteries containing anodes from C <sub>3</sub> H <sub>6</sub> treatment for 15 (G-Si(20%)-C15m), 30 (G-Si(17%)-C30m), 60 (G-Si(19%)-C60m) and 90 min (G-Si(19%)-C90m), the sample annealed under vacuum (G-Si(21%)-60m) and the twice C <sub>3</sub> H <sub>6</sub> treated sample (G-C-Si(20%)-C30m). . . . .	83
5.13	C-rate capability test of batteries containing anodes from C <sub>3</sub> H <sub>6</sub> treatment for 15 (G-Si(20%)-C15m), 30 (G-Si(17%)-C30m), 60 (G-Si(19%)-C60m) and 90 min (G-Si(19%)-C90m), the sample annealed under vacuum (G-Si(21%)-60m) and the twice C <sub>3</sub> H <sub>6</sub> treated sample (G-C-Si(20%)-C30m). . . . .	84
5.14	SEM images of a) a cycled G-Si(21%)-60m anode with images of higher magnification of b) the dark and c) the bright region. . . . .	85
5.15	a) Secondary electron image with b) corresponding EDX elemental maps of silicon and fluorine (700 nm interaction depth) and c, d) SEM images of cycled G-Si(19%)-C60m anode. . . . .	85
5.16	a) Secondary electron image with b) corresponding EDX elemental maps of silicon and fluorine (700 nm interaction depth) and c, d) SEM images of cycled G-C-Si(20%)-C30m anode. . . . .	86
5.17	a, b) HRTEM and c) high-angle annular dark-field (HAADF) image with corresponding EDX elemental maps of carbon and silicon of G-Si(12%)-C30m material after 7 cycles. . . . .	87
5.18	a) HRTEM and b) HAADF image with corresponding EDX elemental maps of carbon, silicon and oxygen of G-Si(12%)-C30m material after 27 cycles. . . . .	87
5.19	a) STEM BF and b) HAADF image with corresponding EDX elemental maps of carbon, silicon and oxygen of G-Si(19%)-C60m material after 103 cycles. . . . .	88
6.1	Illustration of SEI formed on silicon particles with LiPF <sub>6</sub> -EC/DEC electrolyte mixture a) without FEC and b) with FEC. <sup>[129]</sup> . . . . .	91
6.2	Proposed single electron reductive decomposition of FEC, resulting in a vinoxyl-radical, CO <sub>2</sub> and LiF. <sup>[131]</sup> . . . . .	92
6.3	Illustration of the Swagelok (left) and self-designed (right) cell setup. . . . .	95

6.4	Radar plots of the performance of G-485C-19% Si batteries cycled with CVCV and CCV protocol.	98
6.5	Differential capacity plots of the CVCV and CCV battery anode lithiation in the a) 2 <sup>nd</sup> cycle and b) as an overlay of the 3 <sup>rd</sup> – 102 <sup>nd</sup> cycle.	99
6.6	a, b) SEM images and c) secondary electron image with d) corresponding silicon elemental map of a CVCV battery anode.	100
6.7	a, b) SEM images and c) secondary electron image with d) corresponding silicon elemental map of a CCV battery anode.	100
6.8	C-rate, coulombic efficiencies and gravimetric capacities as a function of the cycle number for G-450C-18% Si, G-SiNPs-20% Si and G-Si(19%)-C60m batteries cycled with a restricted charging protocol.	102
6.9	a) Gravimetric discharge capacity as a function of the cycle number for G-450C-18% Si batteries cycled regularly and with restricted charging and b) averaged capacity over 100 cycles for regularly and restrictedly cycled batteries.	103
6.10	Differential capacity plots of a) 3 <sup>rd</sup> and b) 100 <sup>th</sup> delithiation of G-450C-18% Si, G-SiNP-20% Si and G-Si(19%)-C60m batteries, cycled with restricted charging.	104
6.11	Gravimetric discharge capacity per mass silicon averaged over 100 cycles for batteries cycled regularly and in the modified setup. These include batteries of four categories: a-Si deposition (a-Si), c-Si deposition (c-Si), Si NP/graphite mixture (Si NPs) and a-C covered graphite-silicon nanocomposite (G-Si@C).	105
6.12	Radar plots of the performance of G, G-550C-13% Si and G-550C-22% Si batteries cycled in the regular and the modified (mod.) setup.	106
6.13	Radar plots of the performance of G-550C-13% Si and G-SiNP-13% Si batteries cycled in the regular and the modified (mod.) setup.	107
6.14	Radar plots of the performance of G-450C-18% Si, G-485C-22% Si and G-550C-22% Si batteries in the regular and the modified (mod.) setup. The 1 <sup>st</sup> cycle CE of the regularly cycled G-485C-22% Si battery is taken from a replica (not marked with a star).	108
6.15	Differential capacity plots for a) 2 <sup>nd</sup> and b) 103 <sup>rd</sup> anode lithiation and c) 2 <sup>nd</sup> and d) 103 <sup>rd</sup> anode delithiation of G-550C-13%-Si batteries cycled in the regular and modified (mod.) setup.	109
6.16	SEM images of G-550C-22% Si anodes cycled in the a) regular and b-e) modified setup.	110
6.17	EDX spectra of G-550C-22% Si anodes cycled in regular (dotted lines) and modified (continuous lines) setup.	111
7.1	Initially (grey) and over 100 cycles (green) provided capacity on the scale of an ideal battery with stable 1000 mAh·g <sup>-1</sup> capacity. Selected samples cycled regularly, with restricted charging (-rest.) and in the modified setup with decreased C-rate (-mod.). Also shown is the capacity retention, i.e. ratio of final to initial capacity (dark cyan).	115
8.1	Temperature calibration with open Ar-flow of 650 sccm as well as N <sub>2</sub> -flow of 150 sccm at 100 mbar.	117
8.2	SEM images of graphite.	118
8.3	(De-)lithiation capacities and coulombic efficiencies vs. cycle number for graphite, G-Si and G-SiNP for 50 cycles.	118

8.4	SEM images of G-Si anodes after a) OCV b) 20 cycles and c) 50 cycles. . . . .	118
8.5	SEM images of the G-SiNP anode after 20 cycles. . . . .	119
8.6	SEM images of a) Si NP reference powder and b) the G-SiNP anode with c) the respective silicon elemental map of the G-SiNP anode. . . . .	119
8.7	Charge (ch) and discharge (dis) capacities and coulombic efficiencies as a function of cycle number for G-Si batteries. . . . .	119
8.8	Charge (ch) and discharge (dis) capacities and coulombic efficiencies as a function of cycle number for G-Si batteries. . . . .	120
8.9	a) Discharge capacity and b) gravimetric discharge capacity as a function of the cycle number for graphite reference anodes containing carbon black (G) and carbon black anodes (CB). . .	121
8.10	Mass (%) as a function of temperature ( $^{\circ}\text{C}$ ) for all samples discussed in chapter 4. . . . .	121
8.11	Mass (solid line) and ion current of $\text{CO}_2$ ( $m/z = 44$ ) (dashed line) as a function of temperature for graphite (G) and samples obtained from graphite with 30, 60, 120 and 180 min of silicon deposition. . . . .	122
8.12	Left: powder XRD pattern; right: SEM image of the G-550C-22% Si sample after TG-MS analysis. . . . .	122
8.13	Values for a) the silicon crystalline volume fraction (black) and b) the silicon crystal domain size (green) derived from Rietveld refinement with error bars ( $3 \cdot \text{ESD}$ ). . . . .	123
8.14	Normalized Raman spectra from 100 to $3000 \text{ cm}^{-1}$ . . . . .	123
8.15	SEM images of a) G, b) G-435C-14% Si, c) G-450C-18% Si, d) G-485C-19% Si, e) G-485C-22% Si, f) G-485C-30% Si, g) G-550C-08% Si, h) G-550C-13% Si, i) G-550C-22% Si, k) G-550C-30% Si, l) G-800C <sup>a</sup> -21% Si and m) Si NPs. . . . .	124
8.16	Gravimetric discharge capacity and CE as a function of the cycle number for a) series B and b) series C. . . . .	125
8.17	a) Gravimetric discharge capacity and b) CE as a function of the cycle number for series D. .	125
8.18	Differential capacity plots of batteries containing a) graphite reference anodes (G) and b) carbon black anodes (CB). . . . .	126
8.19	Differential capacity plots of the 2 <sup>nd</sup> cycle a) lithiation and b) delithiation of batteries of series D.	126
8.20	Differential capacity plots of the batteries of series B with a) 2 <sup>nd</sup> lithiation, b) 103 <sup>rd</sup> lithiation, c) 2 <sup>nd</sup> delithiation and d) 103 <sup>rd</sup> delithiation. . . . .	127
8.21	Differential capacity plots of the batteries of series C a) 1 <sup>st</sup> lithiation, b) 2 <sup>nd</sup> lithiation, c) 1 <sup>st</sup> delithiation and d) 2 <sup>nd</sup> delithiation. . . . .	128
8.22	Capacity retention relative to first discharge as a function of the cycle number for C-rate variation protocol run on batteries containing a) G and CB reference anodes, b) anodes of series C and c) anodes of series D. . . . .	129
8.23	SEM images of G-485C-19% Si anode after 103 cycles. . . . .	130
8.24	SEM images of a) G-550C-22% Si and b, c) G-485C-19% Si anode after 103 cycles. . . . .	130
8.25	SEM images of cross section region of G-485C-19% Si anode after 103 cycles. . . . .	130
8.26	EDX spectra for a) the G-485C-19% Si anode cross section, spots A (SEI) and B (material), and b) the graphite reference anode after 103 cycles. . . . .	131



8.27	a, b) Mass and c, d) ion current for CO ( $m/z = 28$ , solid lines) and CO <sub>2</sub> ( $m/z = 44$ , dotted lines) as a function of temperature for G-Si(21%)-60m, G-Si(20%)-C15m, G-Si(17%)-C30m, G-Si(19%)-C60m, G-Si(19%)-C90m and b) G-Si(12%)-C30m, G-Si(O)(24%)-C30m and G-C-Si(20%)-C30m. . . . .	132
8.28	Raman spectra of G-Si(21%)-60m, G-Si(20%)-C15m, G-Si(17%)-C30m, G-Si(19%)-C60m, G-Si(19%)-C90m, G-Si(O)(24%)-C30m and G-C-Si(20%)-C30m. . . . .	133
8.29	SEM images of a) G-Si(21%)-60m, b) G-Si(20%)-C15m and c) G-C-Si(20%)-C30m. . . . .	133
8.30	SEM images of G-Si(17%)-C30m. . . . .	133
8.31	SEM images of G-Si(19%)-C60m. . . . .	134
8.32	SEM images of G-Si(19%)-C90m. . . . .	134
8.33	a) Gravimetric discharge capacity and b) CE as a function of the cycle number of G-Si(21%)-60m, G-Si(20%)-C15m, G-Si(17%)-C30m, G-Si(19%)-C60m, G-Si(19%)-C90m, G-Si(O)(24%)-C30m and G-C-Si(20%)-C30m batteries. . . . .	134
8.34	2 <sup>nd</sup> cycle lithiation (a,b) and delithiation (c,d) differential capacity plots of the G (graphite reference), G-Si(21%)-60m, G-Si(20%)-C15m, G-Si(17%)-C30m, G-Si(19%)-C60m, G-Si(19%)-C90m, G-Si(O)(24%)-C30m and G-C-Si(20%)-C30m batteries. . . . .	135
8.35	103 <sup>rd</sup> cycle lithiation (a,b) and delithiation (c,d) differential capacity plots of the G (graphite reference), G-Si(21%)-60m, G-Si(20%)-C15m, G-Si(17%)-C30m, G-Si(19%)-C60m, G-Si(19%)-C90m, G-Si(O)(24%)-C30m and G-C-Si(20%)-C30m batteries. . . . .	136
8.36	a) Secondary electron image and corresponding elemental maps of b) silicon and c) fluorine (700 nm interaction depth) of cycled G-Si(19)-C60m anode. . . . .	137
8.37	a) Secondary electron image and corresponding elemental maps of b) silicon and c) fluorine (700 nm interaction depth) of cycled G-Si(19)-C60m anode. . . . .	137
8.38	a,b,c) SEM images and d) secondary electron image with e) corresponding elemental maps of silicon and fluorine (700 nm interaction depth) of cycled G-C-Si(20%)-C30m anode. . . . .	137
8.39	a) Capacity and b) coulombic efficiency as a function of the cycle number of G-Si(12%)-C30m batteries cycled for 7 cycles using a CC-CV protocol and 27 cycles using a CC protocol. . . . .	138
8.40	a) Coulombic efficiency and b) gravimetric discharge capacity as a function of the cycle number for the CVCV and CCV G-485-19% Si batteries. . . . .	140
8.41	Differential capacity plots for batteries containing G-450C-18% Si, G-SiNP-20% Si and G-Si(19%)-C60m anodes, cycled with restricted lithiation; a) 3 <sup>rd</sup> , b) 100 <sup>th</sup> lithiation. . . . .	140
8.42	C1s, O1s, P2p, F1s and Li1s XPS spectra of the CCV (red) and CVCV (black) cycled battery anodes. . . . .	141
8.43	Gravimetric discharge capacity and coulombic efficiency as a function of the cycle number of the graphite (left) and G-450C-18% Si (right) batteries, cycled in regular and modified (mod.) setup. . . . .	142
8.44	Gravimetric discharge capacity and coulombic efficiency as a function of the cycle number of the G-485C-22% Si (left) and G-550C-13% Si (right) batteries, cycled in regular and modified (mod.) setup. . . . .	142

8.45	Gravimetric discharge capacity and coulombic efficiency as a function of the cycle number of the G-550C-22% Si (left) and G-550C-30% Si (right) batteries, cycled in regular and modified (mod.) setup. . . . .	142
8.46	Gravimetric discharge capacity and coulombic efficiency as a function of the cycle number of the G-SiNP-13% Si (left) and G-Si(19%)-C60m (right) batteries, cycled in regular and modified (mod.) setup. . . . .	143
8.47	Differential capacity plots of 1 <sup>st</sup> cycle anode lithiation of G-450C-18% Si, G-485C-22% Si, G-550C-13% Si, G-550C-22% Si and G-SiNP-13% Si batteries between 0.1 – 2.0 V cycled in the regular and modified (mod.) battery setup. . . . .	143
8.48	Differential capacity plots of the 1 <sup>st</sup> cycle anode lithiation (left) and delithiation (right) of G-550C-13%-Si batteries, cycled in the regular and modified battery setup. . . . .	144
8.49	SEM images of G-550C-22% Si anode cycled in the modified battery setup. . . . .	144

# List of Tables

1.1	Characteristics of graphite and silicon as anode materials in LIBs (adapted from ref. [12,49]) . . . . .	7
1.2	Correlation of differential capacity plot peak positions (vs. Li/Li <sup>+</sup> ) and lithiation stages of graphite . . . . .	18
1.3	Correlation of differential capacity plot peak positions (vs. Li/Li <sup>+</sup> ) and lithiation processes of silicon; XRD <sup>1</sup> method involved capacity calculations for determination of the a-Li <sub>x</sub> Si stoichiometry . . . . .	20
3.1	Silicon content (wt.-%) from XRF analysis for depositions at 550 °C (standard error 8 %) . . . . .	30
4.1	XRD reference patterns . . . . .	39
4.2	Cycling protocol . . . . .	41
4.3	Current rate (C-rate) variation protocol applied between 5 mV and 2 V . . . . .	41
4.4	Sample series . . . . .	44
4.5	Overview over radar plot axes . . . . .	51
4.6	Near surface composition according to XPS (mol %) for G-485C-19% Si anodes before and after electrochemical testing . . . . .	63
5.1	List of sample names and varied deposition parameters . . . . .	71
5.2	XRD reference patterns . . . . .	71
5.3	Cycling protocol . . . . .	73
5.4	Current rate (C-rate) variation protocol applied between 5 mV and 2 V . . . . .	73
5.5	Classification of samples . . . . .	74
6.1	List of anode materials cycled in this chapter . . . . .	94
6.2	Cycling protocol and CC-CC-CV protocol . . . . .	95
6.3	Restricted charging protocol . . . . .	95
6.4	Modified cycling protocol . . . . .	96
6.5	CVCV and CCV cycling protocols . . . . .	97
6.6	Initial gravimetric discharge capacity ("capacity"), capacity retention (CR) and reached state of charge (SOC) for G-450C-18% Si, G-SiNP-20% Si and G-Si(19%)-C60m batteries cycled regularly with a C-rate of 1C and with restricted charging (C-rate 0.13C) . . . . .	102

8.1	List of samples for chapter 3 at $p = 1$ mbar . . . . .	117
8.2	List of sample names, deposition parameters and ascertained silicon content . .	120
8.3	Gravimetric discharge capacity per silicon and cycle . . . . .	125
8.4	Silicon contents evaluated by TG-MS analysis and EA . . . . .	131
8.5	List of batteries tested in chapter 6 with reg. = regular, CCV = CC-CC-CV, mod. = modified and res. lith. = restricted lithiation protocol . . . . .	139

# Bibliography

- [1] R. Schlögl, *Chemical Energy Storage*, **2013**, ISBN 978-3-11-026407-4.
- [2] J. Kim, Y. Suharto, T. U. Daim, *Journal of Energy Storage* **2017**, *11*, 25.
- [3] C. Wadia, P. Albertus, V. Srinivasan, *Journal of Power Sources* **2011**, *196*, 1593.
- [4] R. M. Dell, D. A. J. Rand, *Journal of Power Sources* **2001**, *100*, 2.
- [5] I. Hadjipaschalis, A. Poulikkas, V. Efthimiou, *Renewable and Sustainable Energy Reviews* **2009**, *13*, 1513.
- [6] C.-X. Zu, H. Li, *Energy & Environmental Science* **2011**, *4*, 2614.
- [7] G. Crabtree, E. Kócs, L. Trahey, *MRS Bulletin* **2015**, *40*, 1067.
- [8] C. K. Chan, H. Peng, G. Liu, K. McIlwrath, X. F. Zhang, R. A. Huggins, Y. Cui, *Nature Nanotechnology* **2008**, *3*, 31.
- [9] O. Schmidt, A. Hawkes, A. Gambhir, I. Staffell, *Nature Energy* **2017**, *2*, 17110.
- [10] J. W. Tester, Presentation: Energy Transfer, Conversion and Storage - Toolbox 5, **2017**.
- [11] S. Zhang, K. Zhao, T. Zhu, J. Li, *Progress in Materials Science* **2017**, *89*, 479.
- [12] M. Winter, J. O. Besenhard, M. E. Spahr, P. Novák, *Advanced Materials* **1998**, *10*, 725.
- [13] N.-S. Choi, Z. Chen, S. A. Freunberger, X. Ji, Y.-K. Sun, K. Amine, G. Yushin, L. F. Nazar, J. Cho, P. G. Bruce, *Angewandte Chemie - International Edition* **2012**, *51*, 9994.
- [14] X. H. Liu, Y. Liu, A. Kushima, S. Zhang, T. Zhu, J. Li, J. Y. Huang, *Advanced Energy Materials* **2012**, *2*, 722.
- [15] P. Arora, R. E. White, M. Doyle, *Journal of The Electrochemical Society* **1998**, *145*, 3647.
- [16] V. Manev, I. Naidenov, B. Puresheva, G. Pistoia, *Journal of Power Sources* **1995**, *57*, 133.
- [17] United States Council for Automotive Research, Appendix G USABC Criteria for Advanced Battery Technologies, **2018**.
- [18] X. Zuo, J. Zhu, P. Müller-Buschbaum, Y.-J. Cheng, *Nano Energy* **2017**, *31*, 113.

- [19] U. Kasavajjula, C. Wang, A. J. Appleby, *Journal of Power Sources* **2007**, *163*, 1003.
- [20] M. Yoshio, T. Tsumura, N. Dimov, *Journal of Power Sources* **2005**, *146*, 10.
- [21] J. K. Lee, C. Oh, N. Kim, J.-Y. Hwang, Y.-K. Sun, *Journal of Materials Chemistry A* **2016**, *4*, 5366.
- [22] D. S. Su, R. Schlögl, *ChemSusChem* **2010**, *3*, 136.
- [23] W. Müller-Warmuth, R. Schöllhorn, *Progress in Intercalation Research*, **1994**, ISBN 978-94-010-4385-4.
- [24] J. O. Besenhard, H. P. Fritz, *Angewandte Chemie International Edition in English* **1983**, *22*, 950.
- [25] M. Drüe, M. Seyring, M. Rettenmayr, *Journal of Power Sources* **2017**, *353*, 58.
- [26] V. Aravindan, Y.-S. Lee, S. Madhavi, *Advanced Energy Materials* **2015**, *5*, 1402225.
- [27] K. Zaghib, G. Nadeau, K. Kinoshita, *Journal of Power Sources* **2001**, *98*, 97.
- [28] T. Tran, K. Kinoshita, *Journal of Electroanalytical Chemistry* **1995**, *386*, 221.
- [29] W. Kohs, H. J. Santner, F. Hofer, H. Schröttner, J. Doninger, I. Barsukov, H. Buqa, J. H. Albering, K.-C. Möller, J. O. Besenhard, M. Winter, *Journal of Power Sources* **2003**, *119-121*, 528.
- [30] J. Sangster, *Journal of Phase Equilibria and Diffusion* **2007**, *28*, 561.
- [31] K. Persson, V. A. Sethuraman, L. J. Hardwick, Y. Hinuma, Y. S. Meng, A. van der Ven, V. Srinivasan, R. Kostecki, G. Ceder, *Journal of Physical Chemistry Letters* **2010**, *1*, 1176.
- [32] K. Zaghib, F. Brochu, A. Guerfi, K. Kinoshita, *Journal of Power Sources* **2001**, *103*, 140.
- [33] M. Winter, P. Novák, A. Monnier, *Journal of The Electrochemical Society* **1998**, *145*, 428.
- [34] X. Y. Song, K. Kinoshita, T. D. Tran, *Journal of The Electrochemical Society* **1996**, *143*, L120.
- [35] J. Rossat-Mignod, D. Fruchart, M. J. Moran, J. W. Milliken, J. E. Fischer, *Synthetic Metals* **1980**, *2*, 143.
- [36] R. Fong, U. von Sacken, J. R. Dahn, *Journal of The Electrochemical Society* **1990**, *137*, 2009.
- [37] J. O. Besenhard, M. Winter, J. Yang, W. Biberacher, *Journal of Power Sources* **1995**, *54*, 228.

- 
- [38] M. E. Spahr, T. Palladino, H. Wilhelm, A. Würsig, D. Goers, H. Buqa, M. Holzapfel, P. Novák, *Journal of The Electrochemical Society* **2004**, *151*, A1383.
- [39] R. Yazami, Y. F. Reynier, *Electrochimica Acta* **2002**, *47*, 1217.
- [40] M. N. Richard, J. R. Dahn, *Journal of The Electrochemical Society* **1999**, *146*, 2068.
- [41] M. D. Levi, C. Wang, D. Aurbach, *Journal of The Electrochemical Society* **2004**, *151*, A781.
- [42] Z. Chen, Y. Qin, Y. Ren, W. Lu, C. Orendorff, E. P. Roth, K. Amine, *Energy & Environmental Science* **2011**, *4*, 4023.
- [43] B. Liang, Y. Liu, Y. Xu, *Journal of Power Sources* **2014**, *267*, 469.
- [44] S.-C. Lai, *Journal of The Electrochemical Society* **1976**, *123*, 1196.
- [45] A. F. Hollemann, N. Wiberg, *Lehrbuch der Anorganischen Chemie*, **2007**, ISBN 978-3-11-017770-1.
- [46] N. Nitta, G. Yushin, *Particle and Particle Systems Characterization* **2014**, *31*, 317.
- [47] M. N. Obrovac, L. Christensen, *Electrochemical and Solid-State Letters* **2004**, *7*, A93.
- [48] M. Ashuri, Q. He, L. L. Shaw, *Nanoscale* **2016**, *8*, 74.
- [49] M. N. Obrovac, V. L. Chevrier, *Chemical Reviews* **2014**, *114*, 11444.
- [50] H. Okamoto, *Journal of Phase Equilibria and Diffusion* **2009**, *30*, 118.
- [51] V. L. Chevrier, J. W. Zwanziger, J. R. Dahn, *Journal of Alloys and Compounds* **2010**, *496*, 25.
- [52] P. Limthongkul, Y.-I. Jang, N. J. Dudney, Y.-M. Chiang, *Journal of Power Sources* **2003**, *119-121*, 604.
- [53] J. Li, J. R. Dahn, *Journal of The Electrochemical Society* **2007**, *154*, A156.
- [54] X. H. Liu, J. W. Wang, S. Huang, F. Fan, X. Huang, Y. Liu, S. Krylyuk, J. Yoo, S. A. Dayeh, A. V. Davydov, S. X. Mao, S. T. Picraux, S. Zhang, J. Li, T. Zhu, J. Y. Huang, *Nature Nanotechnology* **2012**, *7*, 749.
- [55] M. T. McDowell, S. W. Lee, W. D. Nix, Y. Cui, *Advanced Materials* **2013**, *25*, 4966.
- [56] B. Key, R. Bhattacharyya, M. Morcrette, V. Seznéc, J.-M. Tarascon, C. P. Grey, *Journal of The American Chemical Society* **2009**, *131*, 9239.
- [57] K. Ogata, E. Salager, C. J. Kerr, A. E. Fraser, C. Ducati, A. J. Morris, S. Hofmann, C. P. Grey, *Nature Communications* **2014**, *5*, 1.

- [58] T. D. Hatchard, J. R. Dahn, *Journal of The Electrochemical Society* **2004**, *151*, A838.
- [59] B. Key, M. Morcrette, J.-M. Tarascon, C. P. Grey, *Journal of The American Chemical Society* **2011**, *133*, 503.
- [60] V. L. Chevrier, J. R. Dahn, *Journal of The Electrochemical Society* **2009**, *156*, A454.
- [61] M. Gauthier, J. Danet, B. Lestriez, L. Roué, D. Guyomard, P. Moreau, *Journal of Power Sources* **2013**, *227*, 237.
- [62] B.-K. Seidlhofer, B. Jerliu, M. Trapp, E. Hüger, S. Risse, R. Cubitt, H. Schmidt, R. Steitz, M. Ballauff, *ACS Nano* **2016**, *10*, 7458.
- [63] J. Yin, M. Wada, K. Yamamoto, Y. Kitano, S. Tanase, T. Sakai, *Journal of The Electrochemical Society* **2006**, *153*, A472.
- [64] D. Rehnlund, F. Lindgren, S. Böhme, T. Nordh, Y. Zou, J. Pettersson, U. Bexell, M. Boman, K. Edström, L. Nyholm, *Energy & Environmental Science* **2017**, *10*, 1350.
- [65] N. Ding, J. Xu, Y. X. Yao, G. Wegner, X. Fang, C. H. Chen, I. Lieberwirth, *Solid State Ionics* **2009**, *180*, 222.
- [66] J. H. Ryu, J. W. Kim, Y.-E. Sung, S. M. Oh, *Electrochemical and Solid-State Letters* **2004**, *7*, A306.
- [67] M. T. McDowell, S. W. Lee, J. T. Harris, B. A. Korgel, C. Wang, W. D. Nix, Y. Cui, *Nano Letters* **2013**, *13*, 758.
- [68] A. Bordes, E. De Vito, C. Haon, C. Secouard, A. Montani, P. Marcus, *ACS Applied Materials & Interfaces* **2015**, *7*, 27853.
- [69] J.-Y. Li, Q. Xu, G. Li, Y.-X. Yin, L.-J. Wan, Y.-G. Guo, *Materials Chemistry Frontiers* **2017**, *1*, 1691.
- [70] M. N. Obrovac, L. J. Krause, *Journal of The Electrochemical Society* **2007**, *154*, A103.
- [71] D. Y. W. Yu, M. Zhao, H. E. Hoster, *ChemElectroChem* **2015**, *2*, 1090.
- [72] L. Y. Beaulieu, K. W. Eberman, R. L. Turner, L. J. Krause, J. R. Dahn, *Electrochemical and Solid-State Letters* **2001**, *4*, A137.
- [73] P. Hovington, M. Dontigny, A. Guerfi, J. Trottier, M. Lagacé, A. Mauger, C. M. Julien, K. Zaghib, *Journal of Power Sources* **2014**, *248*, 457.
- [74] J. Gonzalez, K. Sun, M. Huang, J. Lambros, S. Dillon, I. Chasiotis, *Journal of Power Sources* **2014**, *269*, 334.
- [75] F. Wang, L. Wu, B. Key, X.-Q. Yang, C. P. Grey, Y. Zhu, J. Graetz, *Advanced Energy Materials* **2013**, *3*, 1324.



- 
- [76] X. H. Liu, L. Zhong, S. Huang, S. X. Mao, T. Zhu, J. Y. Huang, *ACS Nano* **2012**, *6*, 1522.
- [77] T. L. Kulova, A. M. Skundin, Y. V. Pleskov, O. I. Kon'kov, *Chemical and Biochemical Engineering Quarterly* **2007**, *21*, 83.
- [78] T. L. Kulova, A. M. Skundin, Y. V. Pleskov, E. I. Terukov, O. I. Kon'kov, *Journal of Electroanalytical Chemistry* **2007**, *600*, 217.
- [79] J. P. Maranchi, A. F. Hepp, P. N. Kumta, *Electrochemical and Solid-State Letters* **2003**, *6*, A198.
- [80] S. Ohara, J. Suzuki, K. Sekine, T. Takamura, *Journal of Power Sources* **2003**, *119-121*, 591.
- [81] H. Wu, Y. Cui, *Nano Today* **2012**, *7*, 414.
- [82] A. Tranchot, H. Idrissi, P.-X. Thivel, L. Roué, *Journal of Power Sources* **2016**, *330*, 253.
- [83] H. Li, X. Huang, L. Chen, G. Zhou, Z. Zhang, D. Yu, Y. J. Mo, N. Pei, *Solid State Ionics* **2000**, *135*, 181.
- [84] J. B. Goodenough, Y. Kim, *Chemistry of Materials* **2010**, *22*, 587.
- [85] I. A. Profatillova, N.-S. Choi, K. H. Yew, W.-U. Choi, *Solid State Ionics* **2008**, *179*, 2399.
- [86] S.-I. Lee, U.-H. Jung, Y.-S. Kim, M.-H. Kim, D.-J. Ahn, H.-S. Chun, *Korean Journal of Chemical Engineering* **2002**, *19*, 638.
- [87] K. Xu, *Chemical Reviews* **2004**, *104*, 4303.
- [88] S. E. Sloop, J. K. Pugh, J. B. Kerr, K. Kinoshita, *Electrochemical and Solid-State Letters* **2001**, *4*, A42.
- [89] K. Tasaki, K. Kanda, S. Nakamura, M. Ue, *Journal of The Electrochemical Society* **2003**, *150*, A1628.
- [90] Y. Matsuda, T. Fukushima, H. Hashimoto, R. Arakawa, *Journal of The Electrochemical Society* **2002**, *149*, A1045.
- [91] M. Shakourian-Fard, G. Kamath, S. K. R. S. Sankaranarayanan, *ChemPhysChem* **2016**, *17*, 2916.
- [92] W. Cui, Y. Lansac, H. Lee, S.-T. Hong, Y. H. Jang, *Physical Chemistry Chemical Physics* **2016**, *18*, 23607.
- [93] X. Bogle, R. Vazquez, S. Greenbaum, A. von Wald Cresce, K. Xu, *The Journal of Physical Chemistry Letters* **2013**, *4*, 1664.

- [94] K. Xu, Y. Lam, S. S. Zhang, T. R. Jow, T. B. Curtis, *Journal of Physical Chemistry C* **2007**, *111*, 7411.
- [95] B. Jiang, V. Ponnuchamy, Y. Shen, X. Yang, K. Yuan, V. Vetere, S. Mossa, I. Skarmoutsos, Y. Zhang, J. Zheng, *The Journal of Physical Chemistry Letters* **2016**, *7*, 3554.
- [96] M. Gauthier, T. J. Carney, A. Grimaud, L. Giordano, N. Pour, H.-H. Chang, D. P. Fenning, S. F. Lux, O. Paschos, C. Bauer, F. Maglia, S. Lupart, P. Lamp, Y. Shao-Horn, *The Journal of Physical Chemistry Letters* **2015**, *6*, 4653.
- [97] A. M. Haregewoin, E. G. Leggesse, J.-C. Jiang, F.-M. Wang, B.-J. Hwang, S. D. Lin, *Electrochimica Acta* **2014**, *136*, 274.
- [98] P. Verma, P. Maire, P. Novák, *Electrochimica Acta* **2010**, *55*, 6332.
- [99] H. Bryngelsson, M. Stjerndahl, T. Gustafsson, K. Edström, *Journal of Power Sources* **2007**, *174*, 970.
- [100] S. Bhattacharya, A. R. Riahi, A. T. Alpas, *Scripta Materialia* **2011**, *64*, 165.
- [101] F. Holtstiege, A. Wilken, M. Winter, T. Placke, *Physical Chemistry Chemical Physics* **2017**, *19*, 25905.
- [102] A. J. Smith, J. C. Burns, S. Trussler, J. R. Dahn, *Journal of The Electrochemical Society* **2010**, *157*, A196.
- [103] S. Menkin, D. Golodnitsky, E. Peled, *Electrochemistry Communications* **2009**, *11*, 1789.
- [104] D. Aurbach, Y. Ein-Eli, B. Markovsky, A. Zaban, S. Luski, Y. Carmeli, H. Yamin, *Journal of The Electrochemical Society* **1995**, *142*, 2882.
- [105] R. Imhof, P. Novák, *Journal of The Electrochemical Society* **1998**, *145*, 1081.
- [106] D. Goers, M. Holzapfel, W. Scheifele, E. Lehmann, P. Vontobel, P. Novák, *Journal of Power Sources* **2004**, *130*, 221.
- [107] Y. Domi, M. Ochida, S. Tsubouchi, H. Nakagawa, T. Yamanaka, T. Doi, T. Abe, Z. Ogumi, *The Journal of Physical Chemistry C* **2011**, *115*, 25484.
- [108] D. Bar-Tow, E. Peled, L. Burstein, *Journal of The Electrochemical Society* **1999**, *146*, 824.
- [109] S. Zhang, M. S. Ding, K. Xu, J. Allen, T. R. Jow, *Electrochemical and Solid-State Letters* **2001**, *4*, A206.
- [110] A. M. Andersson, A. Henningson, H. Siegbahn, U. Jansson, K. Edström, *Journal of Power Sources* **2003**, *119-121*, 522.
- [111] A. L. Michan, M. Leskes, C. P. Grey, *Chemistry of Materials* **2016**, *28*, 385.

- 
- [112] E. Peled, D. B. Tow, A. Merson, L. Burstein, *Journal of New Materials for Electrochemical Systems* **2000**, 3, 321.
- [113] E. Peled, D. Bar Tow, A. Merson, A. Gladkich, L. Burstein, D. Golodnitsky, *Journal of Power Sources* **2001**, 97-98, 52.
- [114] D. Aurbach, *Journal of Power Sources* **2000**, 89, 206.
- [115] D. Aurbach, E. Zinigrad, Y. Cohen, H. Teller, *Solid State Ionics* **2002**, 148, 405.
- [116] J. Zheng, H. Zheng, R. Wang, L. Ben, W. Lu, L. Chen, L. Chen, H. Li, *Physical Chemistry Chemical Physics* **2014**, 16, 13229.
- [117] N. Delpuech, N. Dupré, D. Mazouzi, J. Gaubicher, P. Moreau, J. S. Bridel, D. Guyomard, B. Lestriez, *Electrochemistry Communications* **2013**, 33, 72.
- [118] D. Mazouzi, N. Delpuech, Y. Oumellal, M. Gauthier, M. Cerbelaud, J. Gaubicher, N. Dupré, P. Moreau, D. Guyomard, L. Roué, B. Lestriez, *Journal of Power Sources* **2012**, 220, 180.
- [119] C. K. Chan, R. Ruffo, S. S. Hong, Y. Cui, *Journal of Power Sources* **2009**, 189, 1132.
- [120] D. E. Arreaga-Salas, A. K. Sra, K. Roodenko, Y. J. Chabal, C. L. Hinkle, *The Journal of Physical Chemistry C* **2012**, 116, 9072.
- [121] B. Philippe, R. Dedryvère, J. Allouche, F. Lindgren, M. Gorgoi, H. Rensmo, D. Gonbeau, K. Edström, *Chemistry of Materials* **2012**, 24, 1107.
- [122] B. Philippe, R. Dedryvère, M. Gorgoi, H. Rensmo, D. Gonbeau, K. Edström, *Chemistry of Materials* **2013**, 25, 394.
- [123] P.-K. Lee, Y. Li, D. Y. W. Yu, *Journal of The Electrochemical Society* **2017**, 164, A6206.
- [124] J. Li, J. Wang, J. Yang, X. Ma, S. Lu, *Journal of Alloys and Compounds* **2016**, 688, 1072.
- [125] Y.-S. Hu, R. Demir-Cakan, M.-M. Titirici, J.-O. Müller, R. Schlögl, M. Antonietti, J. Maier, *Angewandte Chemie - International Edition* **2008**, 47, 1645.
- [126] L. Luo, P. Zhao, H. Yang, B. Liu, J.-G. Zhang, Y. Cui, G. Yu, S. Zhang, C.-M. Wang, *Nano Letters* **2015**, 15, 7016.
- [127] B. T. Young, D. R. Heskett, C. C. Nguyen, M. Nie, J. C. Woicik, B. L. Lucht, *ACS Applied Materials & Interfaces* **2015**, 7, 20004.
- [128] F.-H. Du, K.-X. Wang, J.-S. Chen, *Journal of Materials Chemistry A* **2016**, 4, 32.
- [129] C. Xu, F. Lindgren, B. Philippe, M. Gorgoi, F. Björefors, K. Edström, T. Gustafsson, *Chemistry of Materials* **2015**, 27, 2591.

- [130] W. Wang, S. Yang, *Journal of Alloys and Compounds* **2017**, 695, 3249.
- [131] R. Jung, M. Metzger, D. Haering, S. Solchenbach, C. Marino, N. Tsiouvaras, C. Stinner, H. A. Gasteiger, *Journal of The Electrochemical Society* **2016**, 163, A1705.
- [132] M. A. Monem, K. Trad, N. Omar, O. Hegazy, B. Mantels, G. Mulder, P. Van den Bossche, J. Van Mierlo, *Applied Energy* **2015**, 152, 143.
- [133] P. Keil, A. Jossen, *Journal of Energy Storage* **2016**, 6, 125.
- [134] N. Dimov, K. Fukuda, T. Umeno, S. Kugino, M. Yoshio, *Journal of Power Sources* **2003**, 114, 88.
- [135] W.-J. Zhang, *Journal of Power Sources* **2011**, 196, 13.
- [136] H. Li, X. Huang, L. Chen, Z. Wu, Y. Liang, *Electrochemical and Solid-State Letters* **1999**, 2, 547.
- [137] H. Jung, M. Park, Y.-G. Yoon, G.-B. Kim, S.-K. Joo, *Journal of Power Sources* **2003**, 115, 346.
- [138] S. Iwamura, H. Nishihara, T. Kyotani, *Journal of Power Sources* **2013**, 222, 400.
- [139] M. Holzapfel, H. Buqa, W. Scheifele, P. Novák, F.-M. Petrat, *Chemical Communications* **2005**, 1566.
- [140] H. Jung, M. Park, S. H. Han, H. Lim, S.-K. Joo, *Solid State Communications* **2003**, 125, 387.
- [141] P. Nikolaidis, A. Poulikkas, *Journal of Power Technologies* **2017**, 97, 220.
- [142] V. Svoboda, H. Wenzl, R. Kaiser, A. Jossen, I. Baring-Gould, J. Manwell, P. Lundsager, H. Bindner, T. Cronin, P. Nørgård, A. Ruddell, A. Perujo, K. Douglas, C. Rodrigues, A. Joyce, S. Tselepis, N. van der Borg, F. Nieuwenhout, N. Wilmot, F. Mattera, D. U. Sauer, *Solar Energy* **2007**, 81, 1409.
- [143] J. Xia, J. E. Harlow, R. Petibon, J. C. Burns, L. P. Chen, J. R. Dahn, *Journal of The Electrochemical Society* **2014**, 161, A547.
- [144] Á. G. Miranda, C. W. Hong, *Applied Energy* **2013**, 111, 681.
- [145] H. Y. Tran, C. Täubert, M. Wohlfahrt-Mehrens, *Progress in Solid State Chemistry* **2014**, 42, 118.
- [146] H. Buqa, D. Goers, M. Holzapfel, M. E. Spahr, P. Novák, *Journal of The Electrochemical Society* **2005**, 152, A474.
- [147] M. Holzapfel, H. Buqa, L. J. Hardwick, M. Hahn, A. Würsig, W. Scheifele, P. Novák, R. Kötz, C. Veit, F.-M. Petrat, *Electrochimica Acta* **2006**, 52, 973.

- 
- [148] T. Schott, J. L. Gómez-Cámer, P. Novák, S. Trabesinger, *Journal of The Electrochemical Society* **2017**, *164*, A190.
- [149] A. J. Smith, J. R. Dahn, *Journal of The Electrochemical Society* **2012**, *159*, A290.
- [150] L. Mickelson, H. Castro, E. Switzer, C. Friesen, *Journal of The Electrochemical Society* **2014**, *161*, A2121.
- [151] J. Shim, K. A. Striebel, *Journal of Power Sources* **2004**, *130*, 247.
- [152] S. S. Zhang, K. Xu, T. R. Jow, *Electrochimica Acta* **2002**, *48*, 241.
- [153] T. Ohzuku, Y. Iwakoshi, K. Sawai, *Journal of The Electrochemical Society* **1993**, *140*, 2490.
- [154] J. R. Dahn, *Physical Review B* **1991**, *44*, 9170.
- [155] J. R. Dahn, R. Fong, M. J. Spoon, *Physical Review B* **1990**, *42*, 6424.
- [156] M. D. Levi, C. Wang, J. S. Gnanaraj, D. Aurbach, *Journal of Power Sources* **2003**, *119-121*, 538.
- [157] F. Maroni, R. Raccichini, A. Birrozzi, G. Carbonari, R. Tossici, F. Croce, R. Marassi, F. Nobili, *Journal of Power Sources* **2014**, *269*, 873.
- [158] M. J. Loveridge, M. J. Lain, Q. Huang, C. Wan, A. J. Roberts, G. S. Pappas, R. Bhagat, *Physical Chemistry Chemical Physics* **2016**, *18*, 30677.
- [159] M. K. Datta, P. N. Kumta, *Journal of Power Sources* **2006**, *158*, 557.
- [160] L.-F. Cui, Y. Yang, C.-M. Hsu, Y. Cui, *Nano Letters* **2009**, *9*, 3370.
- [161] L. Baggetto, R. A. H. Niessen, F. Roozehoom, P. H. L. Notten, *Advanced Functional Materials* **2008**, *18*, 1057.
- [162] V. L. Chevrier, L. Liu, D. B. Le, J. Lund, B. Molla, K. Reimer, L. J. Krause, L. D. Jensen, E. Figgemeier, K. W. Eberman, *Journal of The Electrochemical Society* **2014**, *161*, A783.
- [163] Y. N. Jo, Y. Kim, J. S. Kim, J. H. Song, K. J. Kim, C. Y. Kwag, D. J. Lee, C. W. Park, Y. J. Kim, *Journal of Power Sources* **2010**, *195*, 6031.
- [164] M. Klett, J. A. Gilbert, K. Z. Pupek, S. E. Trask, D. P. Abraham, *Journal of The Electrochemical Society* **2017**, *164*, A6095.
- [165] L.-F. Cui, R. Ruffo, C. K. Chan, H. Peng, Y. Cui, *Nano Letters* **2009**, *9*, 491.
- [166] K. L. Choy, *Progression in Materials Science* **2003**, *48*, 57.
- [167] J. D. Joannopoulos, G. Lucovsky, *The Physics of Hydrogenated Amorphous Silcion I*, **1984**, ISBN 978-3-540-38741-1.

- [168] T. R. Hogness, T. L. Wilson, W. C. Johnson, *Journal of The American Chemical Society* **1936**, *58*, 108.
- [169] R. F. C. Farrow, *Journal of The Electrochemical Society* **1974**, *121*, 899.
- [170] J. H. Purnell, R. Walsh, *The Royal Society* **1966**, *293*, 543.
- [171] R. Robertson, D. Hils, H. Chatham, A. Gallagher, *Applied Physics Letters* **1983**, *43*, 544.
- [172] V. L. Dalal, *Thin Solid Films* **2001**, *395*, 173.
- [173] V. Cocheteau, E. Scheid, P. Mur, T. Billon, B. Caussat, *Applied Surface Science* **2008**, *254*, 2927.
- [174] V. Cocheteau, P. Mur, T. Billon, E. Scheid, B. Caussat, *Chemical Engineering Journal* **2008**, *140*, 600.
- [175] S. Lombardo, B. De Salvo, C. Gerardi, T. Baron, *Microelectronic Engineering* **2004**, *72*, 388.
- [176] I. Zahi, P. Mur, P. Blaise, A. Estève, M. D. Rouhani, H. Vergnes, B. Caussat, *Thin Solid Films* **2011**, *519*, 7650.
- [177] A. T. Voutsas, M. K. Hatalis, *Journal of The Electrochemical Society* **1992**, *139*, 2659.
- [178] M. Hirose, *Journal de Physique Colloques* **1981**, *42*, C4 705.
- [179] S. Bourderau, T. Brousse, D. M. Schleich, *Journal of Power Sources* **1999**, *81-82*, 233.
- [180] M. Uehara, J. Suzuki, K. Tamura, K. Sekine, T. Takamura, *Journal of Power Sources* **2005**, *146*, 441.
- [181] T. Takamura, M. Uehara, J. Suzuki, K. Sekine, K. Tamura, *Journal of Power Sources* **2006**, *158*, 1401.
- [182] W.-R. Liu, Z.-Z. Guo, W.-S. Young, D.-T. Shieh, H.-C. Wu, M.-H. Yang, N.-L. Wu, *Journal of Power Sources* **2005**, *140*, 139.
- [183] L.-F. Cui, L. Hu, J. W. Choi, Y. Cui, *ACS Nano* **2010**, *4*, 3671.
- [184] K. Evanoff, J. Benson, M. Schauer, I. Kovalenko, D. Lashmore, W. J. Ready, G. Yushin, *ACS Nano* **2012**, *6*, 9837.
- [185] N. Coppey, L. Noé, M. Monthieux, B. Caussat, *Chemical Engineering Research and Design* **2013**, *91*, 2491.
- [186] W. Wang, P. N. Kumta, *ACS Nano* **2010**, *4*, 2233.
- [187] A. Gohier, B. Laïk, K.-H. Kim, J.-L. Maurice, J.-P. Pereira-Ramos, C. S. Cojocar, P. T. Van, *Advanced Materials* **2012**, *24*, 2592.

- 
- [188] M. Ko, S. Chae, S. Jeong, P. Oh, J. Cho, *ACS Nano* **2014**, *8*, 8591.
- [189] M. Alias, O. Crosnier, I. Sandu, G. Jestin, A. Papadimopoulos, F. Le Cras, D. M. Schleich, T. Brousse, *Journal of Power Sources* **2007**, *174*, 900.
- [190] M. Holzapfel, H. Buqa, F. Krumeich, P. Novák, F.-M. Petrat, C. Veit, *Electrochemical and Solid-State Letters* **2005**, *8*, A516.
- [191] J. L. Gómez-Cámer, C. Bünzli, M. M. Hantel, T. Poux, P. Novák, *Carbon* **2016**, *105*, 42.
- [192] S. Brunauer, P. H. Emmett, E. Teller, *Journal of The American Chemical Society* **1938**, *60*, 309.
- [193] M. K. Hatalis, D. W. Greve, *Journal of Applied Physics* **1988**, *63*, 2260.
- [194] Y. Yao, M. T. McDowell, I. Ryu, H. Wu, N. Liu, L. Hu, W. D. Nix, Y. Cui, *Nano Letters* **2011**, *11*, 2949.
- [195] J. E. Krzanowski, S. Palacín, A. Gutiérrez, F. Schäfers, M. Mertin, J. L. Endrino, L. Soriano, *Scripta Materialia* **2007**, *56*, 1011.
- [196] M. Kasrai, W. N. Lennard, R. W. Brunner, G. M. Bancroft, J. A. Bardwell, K. H. Tan, *Applied Surface Science* **1996**, *99*, 303.
- [197] M. Yamada, A. Inaba, A. Ueda, K. Matsumoto, T. Iwasaki, T. Ohzuku, *Journal of The Electrochemical Society* **2012**, *159*, A1630.
- [198] V. Mastelaro, A. M. Flank, M. C. A. Fantini, D. R. S. Bittencourt, M. N. P. Carreño, I. Pereyra, *Journal of Applied Physics* **1996**, *79*, 1324.
- [199] M. L. Terranova, S. Orlanducci, E. Tamburri, V. Guglielmotti, M. Rossi, *Journal of Power Sources* **2014**, *246*, 167.
- [200] M. W. Forney, R. A. Dileo, A. Raisanen, M. J. Ganter, J. W. Staub, R. E. Rogers, R. D. Ridgley, B. J. Landi, *Journal of Power Sources* **2013**, *228*, 270.
- [201] R. Epur, M. K. Datta, P. N. Kumta, *Electrochimica Acta* **2012**, *85*, 680.
- [202] Z. Du, S. Zhang, Y. Liu, J. Zhao, R. Lin, T. Jiang, *Journal of Materials Chemistry* **2012**, *22*, 11636.
- [203] J. W. Wang, Y. He, F. Fan, X. H. Liu, S. Xia, Y. Liu, C. T. Harris, H. Li, J. Y. Huang, S. X. Mao, T. Zhu, *Nano Letters* **2013**, *13*, 709.
- [204] J. Graetz, C. C. Ahn, R. Yazami, B. Fultz, *Electrochemical and Solid-State Letters* **2003**, *6*, A194.
- [205] S. Misra, N. Liu, J. Nelson, S. S. Hong, Y. Cui, M. F. Toney, *ACS Nano* **2012**, *6*, 5465.

- [206] J. J. Yeh, I. Lindau, *Atomic Data and Nuclear Data Tables* **1985**, *32*, 1.
- [207] Z. Li, W. Li, Y. Jiang, H. Cai, Y. Gong, J. He, *Journal of Raman Spectroscopy* **2011**, *42*, 415.
- [208] C. Vichery, V. Le Nader, C. Frantz, Y. Zhang, J. Michler, L. Philippe, *Physical Chemistry Chemical Physics* **2014**, *16*, 22222.
- [209] C. Smit, R. A. C. M. M. van Swaaij, H. Donker, A. M. H. N. Petit, W. M. M. Kessels, M. C. M. van de Sanden, *Journal of Applied Physics* **2003**, *94*, 3582.
- [210] W. Li, D. Xia, H. Wang, X. Zhao, *Journal of Non-Crystalline Solids* **2010**, *356*, 2552.
- [211] M. Kosović, O. Gamulin, M. Balarin, M. Ivanda, V. Derek, D. Ristić, M. Marciuš, M. Ristić, *Journal of Raman Spectroscopy* **2014**, *45*, 470.
- [212] A. Cetinel, N. Artunç, G. Sahin, E. Tarhan, *International Journal of Modern Physics B* **2015**, *29*, 1550093.
- [213] P. Mishra, K. P. Jain, *Physical Review B* **2001**, *64*, 733041.
- [214] N. Dimov, S. Kugino, M. Yoshio, *Electrochimica Acta* **2003**, *48*, 1579.
- [215] G. Sandu, L. Brassart, J.-F. Gohy, T. Pardoën, S. Melinte, A. Vlad, *ACS Nano* **2014**, *8*, 9427.
- [216] T. D. Bogart, D. Oka, X. Lu, M. Gu, C. Wang, B. A. Korgel, *ACS Nano* **2014**, *8*, 915.
- [217] G. Zhao, L. Zhang, Y. Meng, N. Zhang, K. Sun, *Materials Letters* **2013**, *96*, 170.
- [218] F. Zhang, X. Yang, Y. Xie, N. Yi, Y. Huang, Y. Chen, *Carbon* **2015**, *82*, 161.
- [219] Z.-F. Li, H. Zhang, Q. Liu, Y. Liu, L. Stanciu, J. Xie, *ACS Applied Materials & Interfaces* **2014**, *6*, 5996.
- [220] B. Gattu, R. Epur, P. H. Jampani, R. Kuruba, M. K. Datta, P. N. Kumta, *The Journal of Physical Chemistry C* **2017**, *121*, 9662.
- [221] A. Magasinski, P. Dixon, B. Hertzberg, A. Kvit, J. Ayala, G. Yushin, *Nature Materials* **2010**, *9*, 353.
- [222] K. Evanoff, A. Magasinski, J. Yang, G. Yushin, *Advanced Energy Materials* **2011**, *1*, 495.
- [223] J. Xie, G. Wang, Y. Huo, S. Zhang, G. Cao, X. Zhao, *Electrochimica Acta* **2014**, *135*, 94.
- [224] M. Ko, S. Chae, J. Ma, N. Kim, H.-W. Lee, Y. Cui, J. Cho, *Nature Energy* **2016**, *1*, 1.
- [225] R. Yi, F. Dai, M. L. Gordin, H. Sohn, D. Wang, *Advanced Energy Materials* **2013**, *3*, 1507.



- 
- [226] K. Norinaga, O. Deutschmann, *Industrial & Engineering Chemistry Research* **2007**, *46*, 3547.
- [227] T. Kasukabe, H. Nishihara, S. Iwamura, T. Kyotani, *Journal of Power Sources* **2016**, *319*, 99.
- [228] J. Xiao, W. Xu, D. Wang, D. Choi, W. Wang, X. Li, G. L. Graff, J. Liu, J.-G. Zhang, *Journal of The Electrochemical Society* **2010**, *157*, A1047.
- [229] M. K. Datta, J. Maranchi, S. J. Chung, R. Epur, K. Kadakia, P. Jampani, P. N. Kumta, *Electrochimica Acta* **2011**, *56*, 4717.
- [230] A. Sadezky, H. Muckenhuber, H. Grothe, R. Niessner, U. Pöschl, *Carbon* **2005**, *43*, 1731.
- [231] Y. Eker, K. Kierzek, E. Raymundo-Piñero, J. Machnikowski, F. Béguin, *Electrochimica Acta* **2010**, *55*, 729.
- [232] J. D. Wilcox, M. M. Doeff, M. Marcinek, R. Kostecki, *Journal of The Electrochemical Society* **2007**, *154*, A389.
- [233] N. Dimov, M. Yoshio, *Journal of Power Sources* **2007**, *174*, 607.
- [234] W. Maerkele, C.-Y. Lu, P. Novák, *Journal of The Electrochemical Society* **2011**, *158*, A1478.
- [235] K. Kierzek, J. Machnikowski, *Electrochimica Acta* **2016**, *192*, 475.
- [236] R. Deshpande, M. Verbrugge, Y.-T. Cheng, J. Wang, P. Liu, *Journal of The Electrochemical Society* **2012**, *159*, A1730.
- [237] M. Sina, J. Alvarado, H. Shobukawa, C. Alexander, V. Manichev, L. Feldman, T. Gustafsson, K. J. Stevenson, Y. S. Meng, *Advanced Materials Interfaces* **2016**, *3*, 1600438.
- [238] N.-S. Choi, K. H. Yew, K. Y. Lee, M. Sung, H. Kim, S.-S. Kim, *Journal of Power Sources* **2006**, *161*, 1254.
- [239] K. Schroder, J. Alvarado, T. A. Yersak, J. Li, N. Dudney, L. J. Webb, Y. S. Meng, K. J. Stevenson, *Chemistry of Materials* **2015**, *27*, 5531.
- [240] W.-J. Tang, W.-J. Peng, G.-C. Yan, H.-J. Guo, X.-H. Li, Y. Zhou, *Ionics* **2017**, *23*, 3281.
- [241] S. Dalavi, P. Guduru, B. L. Lucht, *Journal of The Electrochemical Society* **2012**, *159*, A642.
- [242] X. Chen, X. Li, D. Mei, J. Feng, M. Y. Hu, J. Hu, M. Engelhard, J. Zheng, W. Xu, J. Xiao, J. Liu, J.-G. Zhang, *ChemSusChem* **2014**, *7*, 549.
- [243] T. Jaumann, J. Balach, M. Klose, S. Oswald, U. Langklotz, A. Michaelis, J. Eckert, L. Giebeler, *Physical Chemistry Chemical Physics* **2015**, *17*, 24956.

- [244] V. Etacheri, O. Haik, Y. Goffer, G. A. Roberts, I. C. Stefan, R. Fasching, D. Aurbach, *Langmuir* **2012**, *28*, 965.
- [245] J. G. Lee, J. Kim, J. B. Lee, H. Park, H.-S. Kim, J. H. Ryu, D. S. Jung, E. K. Kim, S. M. Oh, *Journal of The Electrochemical Society* **2017**, *164*, A6103.
- [246] M. Nie, D. P. Abraham, Y. Chen, A. Bose, B. L. Lucht, *The Journal of Physical Chemistry C* **2013**, *117*, 13403.
- [247] I. A. Shkrob, J. F. Wishart, D. P. Abraham, *The Journal of Physical Chemistry C* **2015**, *119*, 14954.
- [248] J. M. Martínez de la Hoz, P. B. Balbuena, *Physical Chemistry Chemical Physics* **2014**, *16*, 17091.
- [249] Y. Okuno, K. Ushirogata, K. Sodeyama, Y. Tateyama, *Physical Chemistry Chemical Physics* **2016**, *18*, 8643.
- [250] H. Nakai, T. Kubota, A. Kita, A. Kawashima, *Journal of The Electrochemical Society* **2011**, *158*, A798.
- [251] I. A. Profatilova, C. Stock, A. Schmitz, S. Passerini, M. Winter, *Journal of Power Sources* **2013**, *222*, 140.